http://researchcommons.waikato.ac.nz/

Research Commons at the University of Waikato

Copyright Statement:

The digital copy of this thesis is protected by the Copyright Act 1994 (New Zealand).

The thesis may be consulted by you, provided you comply with the provisions of the Act and the following conditions of use:

- Any use you make of these documents or images must be for research or private study purposes only, and you may not make them available to any other person.
- Authors control the copyright of their thesis. You will recognise the author's right to be identified as the author of the thesis, and due acknowledgement will be made to the author where appropriate.
- You will obtain the author's permission before publishing any material from the thesis.

Microstructure Dual-Refinement and Mechanical Properties Manipulation of TiBw/TA15(Si) Composites by Thermo-mechanical Processing and Heat Treatment

A thesis

submitted in fulfilment

of the requirements for the degree

of

Doctor of Philosophy in Materials Processing and Engineering

at

The University of Waikato

by

Rui Zhang

THE UNIVERSITY OF
WAIKATO
Te Whare Wānanga o Waikato

Year of submission

2024

Abstract

Titanium matrix composites with near-α titanium alloy as the matrix exhibit high specific strength and good high-temperature strength. However, the thermo-mechanical processing is limited by the brittleness of the reinforcement, making it difficult to refine the grain size and control the silicide precipitates. The present work aims to prepare titanium matrix composites with refined grain size and silicide particles. To this end, network-architecture TiBw/TA15(Si) composites were prepared using low-energy ball milling and vacuum hot-pressing. After refining the initial lamellar microstructure of the material through a solid solution treatment, the evolution of the TA15(Si) matrix and TiBw reinforcement during the hot deformation were studied. Ideal thermo-mechanical processing parameters in dual-phase region for TiBw/TA15(Si) composites after solid solution treatment was obtained, and the strain distribution in the compressive sample was revealed. Subsequently, TiBw/TA15(Si) composites with fine grains and dispersed silicide particles were obtained using solid solution treatment and isothermal hot-pressing, achieving a simultaneous improvement in room temperature strength and ductility. The influence mechanism of solid solution treatment on the microstructure and properties of the material was analyzed. Finally, TiBw/TA15(Si) composites with different lamellar content and morphologies were obtained through heat treatment of the deformed material. The effect of heat treatment on the microstructure of the material and the influence of different microstructures on the room temperature and high-temperature tensile mechanical behaviors of the material were discussed.

After compositional design through thermodynamic calculation, TiBw/TA15(Si) composites with different Si and Zr contents and a network architecture were prepared by low-energy ball milling and vacuum hot-pressing sintering using spherical TA15 coarse powder and TiB_2, ZrB_2, and Si fine powders. Silicide particles precipitated on the α/β interfaces in the matrix, and the precipitation amount increased with the increase of Si and Zr element contents. The tensile strength of materials with different compositions ranged from 1012 MPa to 1120 MPa, and the elongation ranged from 1.2% to 6.7%. When the Si content was between 0.3 wt.% and 1.0 wt.% and the Zr content was between 0.3 wt.% and 1.0 wt.%, the materials exhibited good strength and plasticity. By observing the microstructures of different materials subjected to heat treatment at 960°C to

1040°C for 30 min followed by quenching, it was found that silicide particles can be completely dissolved below β transformation temperature when the Si content is below 0.5 wt.%, which is suitable for microstructure control in dual-phase region. Considering the comprehensive mechanical properties and silicide dissolution temperature, a composite with a chemical composition of 3.4 vol.% TiBw/TA15-0.3 wt.%Si was selected for the study of dual-phase region thermo-mechanical processing and microstructure control.

After the solid solution treatment in single-phase region, the initial microstructure of TiBw/TA15(Si) was refined, after that, the high-temperature deformation behavior of the material was studied. The hot compression tests were conducted in dual-phase region at temperatures ranging from 870°C to 950°C and strain rates ranging from 1 s^{-1} to 0.001 s^{-1}. It was found that the compressive stress-strain curves of the composite in this range exhibited dynamic recrystallization features, and the compressive stress decreased with increasing deformation temperature and decreasing strain rate. Except for the fully lath overheated-microstructure observed at 950°C / 1 s^{-1}, the deformation microstructure of the material under the remaining conditions consisted of equiaxed α grains and residual α/β laths. The microstructure became finer with lower deformation temperature and higher strain rate. Higher recrystallization degree was observed below 910°C at lower strain rates, while the opposite was observed above 910°C. Observation of the microstructure produced by different deformation degrees revealed that the formation of equiaxed grains in the material involved three steps: α/β lath distortion, formation of boundaries within α/β laths, and lath decomposition. The activation energy for hot deformation of the TiBw/TA15(Si) composite after single-phase solid solution pretreatment was determined to be 623 kJ/mol. Based on the constructed processing map, the ideal deformation parameters were determined to be in the temperature range of 900°C to 950°C and strain rates of 0.01 s^{-1} to 0.001 s^{-1}.

The orientation distribution of TiBw reinforcements during high-temperature plastic deformation in materials has been studied. The rotational behavior of TiBw reinforcements during deformation was analyzed, revealing that the orientation distribution of the reinforcements is influenced by the direction and magnitude of the principal strain applied to the material. The direction of the principal strain determines the principal directions of covariance matrix for the reinforcement's

orientation distribution, while the magnitude of the principal strain determines the parameters in the probability density function. Based on these findings, a method was proposed to calculate the local plastic deformation in materials using the orientation distribution of TiBw reinforcements. Error analysis through computer simulations showed that this method exhibited good accuracy in the range of 20% to 80% compression strain. Using this method, the strain distribution in hot-deformed TiBw/TA15(Si) composites was analyzed, and the accuracy of the calculations was confirmed by comparing them with the deformation of the network structure of TiBw.

Based on the results of hot compression tests, TiBw/TA15(Si) composites were subjected to a solid solution treatment followed by isothermal hot pressing at 920 °C and a strain rate of 0.003 s^{-1} with 75% height reduction. This process yielded a microstructure with fine equiaxed α grains and dispersed fine silicide particles, with an average grain size of 1.6 μm and particle size of 70 μm, respectively, achieving a dual-refinement of both α grains and silicide particles. The composite exhibited a yield strength of 1100 MPa and an elongation of 7.7%. A comparison showed that the solid solution pretreatment led to finer grains and more dispersed silicide particles in the material after isothermal hot pressing, resulting in a significant increase in yield strength.

Heat treatment of the hot-pressed composite in the range of 980 °C to 1050 °C revealed that higher temperatures led to higher contents of α/β laths and coarser microstructures, while faster cooling rates resulted in finer lath structures. Water quenching after the heat treatment at 1010 °C for 30 min produced excellent room temperature strength and ductility, with a tensile strength of 1350 MPa and an elongation of 6.7%. Slip trace analysis and transmission electron microscopy analysis revealed that the equiaxed microstructure in the material facilitated multi-system slip, enhancing deformation uniformity. The prismatic slip in lamellar microstructure obtained with air cooling was suppressed by the Burgers orientation relationship, the strain-softening of the lamellae resulted in deformation dominated by single-system slip and strain localization. The transformed β phase obtained through water quenching exhibited limited deformability, which was primarily accommodated by the prismatic slip of primary α laths. High-temperature tensile tests under different conditions showed that decreasing the deformation temperature,

increasing the strain rate, refining the grain size, and decreasing the α/β lath content transform the deformation mechanism into grain boundary sliding, which significantly enhances the deformability of TiBw/TA15(Si) composites. The composite with fine equiaxed microstructure could achieve an elongation up to 348% at 800 °C and a strain rate of 0.0003 s^{-1}, which showed a good potential for superplastic forming at low temperatures.

Keywords: Titanium matrix composites; Thermo-mechanical processing; Microstructure refinement; Heat-treatment manipulation; Deformation behaviors

List of Publications

I: Publications in international journals

Publications related to this thesis

[1] **Rui Zhang**, Shuai Wang, Xin Chen, Qi An, Lujun Huang, Lin Geng, Fei Yang. Significantly Enhanced Superplasticity of TiBw/near-α Ti Composite: Microstructure Tailoring and Deformation Mechanisms[J]. ***Materials Science and Engineering A***, 2022, 853: 143772. **Corresponding to the contents in section 6.5.**

[2] **Rui Zhang**, Shuai Wang, Weihang Lu, Fengbo Sun, Lujun Huang, Leandro Bolzoni, Lin Geng, Fei Yang. Enhancing Microstructure Refinement and Strengthening Efficiency of TiBw/Near α-Ti Composites by Combining Solid-Solution Treatment with Hot Processing[J]. ***Composites Part B: Engineering***, 2023, 257: 110696. **Corresponding to the contents in sections 5.2, 5.3, 5.4, and 6.2.**

Co-publications during PhD research

[3] **Rui Zhang**, Lujun Huang, Qi An, Lin Geng, Bo Wang, Yang Jiao. The Hyperbolic Constitutive Equations and Modified Dynamic Material Model of TiBw/Ti-6.5Al-2.5Zr-1Mo-1V-0.5Si Composites[J]. ***Materials Science and Engineering A***, 2019, 776: 138329.

[4] **Rui Zhang**, Lujun Huang, Xiangxu Zhao, Lin Geng, Shuai Wang, Shan Jiang. Influence of Deformation Parameters and Network Structure to the Microstructure Evolution and Flow Stress of TiBw/Ti64 Composite. ***Materials Science and Engineering A***, 2021, 809: 140997.

[5] Shan Jiang, Lujun Huang, Xiang Gao, Gang Liu, **Rui Zhang**, Qi An, Shuai Wang, Lin Geng. Interstitial Carbon Induced FCC-Ti Exhibiting Ultrahigh Strength in a Ti37Nb28Mo28-C7 Complex Concentrated Alloy. ***Acta Materialia***, 2021, 203: 116456.

[6] Fengbo Sun, **Rui Zhang**, Yu Zhang, Fanchao Meng, Zishuo Ma, Lujun Huang, Lin Geng. Revealing Hot Deformation Behavior of Ti2C-Ti Composite and Associated Dynamic Recrystallization Mechanism of Ceramic Matrix. ***Materials Characterization***, 2023, 204: 113236.

II: Applied & granted patents

[1] Lujun Huang, **Rui Zhang**, Yang Bao, Lin Geng, Xiping Cui, Junchao Zheng, Shan Jiang, A high performance and machine-friendly titanium-based composite for 700 °C applications. **Granting No.: ZL201810077839.3.**

[2] Lujun Huang, **Rui Zhang**, Qi Aan, Shuai Wang, Xin Chen, Fengbo Sun, Run Chen, Lin Geng, A titanium matrix composite with superplasticity and its superplastic forming method. **Granting No.: ZL202111551773.5.**

[3] Lujun Huang, **Rui Zhang**, Shuai Wang, Shuai Wang, Shan Jiang, Qi An, Fengbo Sun, Xiping Cui, Lin Geng, A method to measure the local strain in short-fiber reinforced composites. **Application No.: CN202210189555.X**.

III: Contributions to international conferences

[1] **Rui Zhang**, Lujun Huang, The Thermal Compression Behavior and Dynamic Modeling of TiBw/Ti-6Al-2.5Zr-1Mo-1V-0.5Si Composite. *9th International Conference on Physical and Numerical Simulation of Materials Processing*, Oct. 2019, Moscow, Russia, **Oral presentation**.

[2] **Rui Zhang**, Lujun Huang, Fei Yang, Significantly Refined Microstructure of TiBw/TA15(Si) Composites by Single-Pass Hot Pressing with Prior Heat-treatment, *The 11th Pacific Rim International Conference on Advanced Materials and Processing*. Nov. 2023, Jeju, Korea, **Oral presentation**.

Acknowledgements

I would like to express my sincere gratitude to my PhD supervisor Associate Professor Fei Yang for his guidance and kind support throughout the fulfillment of my PhD degree.

I would like to express my sincere gratitude to my co supervisors Professor Lujun Huang and Associate Professor Leandro Bolzoni for providing a firm support throughout the pursuit of my PhD degree.

I would like to acknowledge the supports and beneficial discussions from my coworkers Junqi Liu, Jingnan Ma and Yutao Zhai.

I would like to thank everyone who directly or indirectly contributed to the preparation of this thesis.

Table of Contents

Abstract ..... **I**

List of Publications ..... **V**

Acknowledgements ..... **VII**

Table of Contents ..... **VIII**

List of abbreviations ..... **XIII**

List of figures ..... **XIV**

List of tables ..... **XXV**

Chapter 1 Introduction **1**

Chapter 2 Literature review **5**

2.1 Discontinuously reinforced titanium matrix composites 5

2.1.1 Porperties of titanium matrix 5

2.1.2 Preparation of DRTMCs 9

2.1.3 Architectures design of DRTMCs 13

2.1.4 In-situ TiBw reinforcements in titanium matrix composites 18

2.2 Hot deformation of titanium matrix composites 21

2.2.1 Behaviors of titanium matrix in hot deformation 22

2.2.2 Behaviors of TiBw in thermo-mechanical processing 26

2.2.3 Microstructure evolution of titanium matrix composites 29

2.2.4 Optimization of thermo-mechanical processing parameters 32

2.2.5 Heat treatment manipulation of microstructure and mechanical property 34

2.3 Research gap 36

2.4 Hypothesis, research objectives, and structure of thesis 37

Chapter 3 Methodology and experimental materials 40

3.1 Research methodology 40

3.2 Raw materials 42

3.3 Analysis methodology 43

3.3.1 Phase analysis 43

3.3.2 Microstructrue characterization 43

3.4 Mechanical properties measurement 44

3.4.1 Room temperature tensile test 44

3.4.2 High temperature tensile test 45

3.4.3 Hot compression test 46

Chapter 4 Preparation and composition optimization of TiBw/TA15(Si) composites 47

4.1 Introduction 47

4.2 Composition design and preparation of TiBw/TA15(Si) composites 47

4.2.1 Composition design of TiBw/TA15(Si) composites 47

4.2.2 Sintering procedure design and materials preparation of TiBw/TA15(Si) composites 50

4.3 Room temperature tensile tests of TiBw/TA15(Si) composites 57

4.4 Microstructure evolution of TiBw/TA15(Si) at high temperatures 60

4.5 Summary 63

Chapter 5 Hot deformation constitutive equations and strain distributions of TiBw/TA15(Si) composites 65

5.1 Introduction 65

5.2 Solid-solution treatment prior to hot deformation 65

5.3 Microstructure evolution during hot compression tests 68

5.4 Constitutive equations and processing maps of TiBw/TA15(Si) composites 78

5.4.1 Constructing the constitutive equations 78

5.4.2 Constructing the processing map 81

5.5 Influence of hot deformation to orientations of TiBw 84

5.5.1 Influence of hot deformation to the orientation of a single TiBw 84

5.5.2 Influence of principal directions of strain to orientations of TiBw 88

5.5.3 Influence of principal strains to orientations of TiBw 91

5.5.4 Calculating local strain tensor with orientations of TiBw..... 94

5.5.5 Error analysis by simulations 96

5.6 Quantitative analysis of strain in TiBw/TA15(Si) composites..... 100

5.6.1 Plastic strain in hot rolled TiBw/TA15(Si) composites..... 100

5.6.2 Strain distribution in hot compressed TiBw/TA15(Si) composites 103

5.6.3 Validation of calculated strain by the deformation of TiBw networks 107

5.7 Summary 109

Chapter 6 Microstructure and mechanical properties regulation of TiBw/TA15(Si) composites by thermo-mechanical processing and heat treatment 112

6.1 Introduction 112

6.2 Microstructure refinement of TiBw/TA15(Si) composites by isothermal hot-pressing 113

6.2.1 Microstructure evolution of TiBw/TA15(Si) composites after isothermal hot-pressing 113

6.2.2 Tensile properties of as-pressed TiBw/TA15(Si) composites 122

6.2.3 Fractography of as-pressed TiBw/TA15(Si) composites 126

6.3 Influence of heat treatment to microstructure of TiBw/TA15(Si) composites 128

6.4 Influence of heat treatment to tensile behaviors of TiBw/TA15(Si) composites 142

6.4.1 Tensile properties of TiBw/TA15(Si) composites after heat treatment 142

6.4.2 Room temperature tensile behaviors of TiBw/TA15(Si) composites 147

6.4.3 Slip trace of TiBw/TA15(Si) composites after room temperature tesnile testing 151

6.4.4 Slip activation of TiBw/TA15(Si) composites during room temperature tensile testing..... 158

6.4.5 Dislocation configuration of TiBw/TA15(Si) composites after tensile testing..... 164

6.5 High temperature tensile behaviors of TiBw/TA15(Si) composites 168

6.5.1 High temperature tensile properties of TiBw/TA15(Si) composites 169

6.5.2 Hot tensile microstructure evolution of TiBw/TA15(Si) composites 171

6.5.3 Activation energy and strain rate sensitivity of TiBw/TA15(Si) composites..... 180

6.5.4 Tensile deformation mechanism of TiB/TA15(Si) composites .. 180

6.6 Summary 186

Chapter 7 Conclusions and perspectives.....189

Reference.....193

List of abbreviations

In alphabetical order

AC: Air cooling

BCC: Body centered cubic

BOR: Burgers orientation relationship

BSE: Back scattered electron

CD: Compression direction

CDRX: Continuous dynamic recrystallization

CRTMCs: Continuously reinforced titanium matrix composites

CT: Computer-aided tomography

DDRX: Discontinuous dynamic recrystallization

DIC: Digital image correlation

DMM: Dynamic materials modeling

DRTMCs: Discontinuously reinforced titanium matrix composites

DRV: Dynamic recovery

DRX: Dynamic recrystallization

EBSD: Electron backscatter diffraction

EDS: Energy-dispersive X-Ray spectroscopy

FFT: Fast Fourier transformation

GBS: Grain boundary sliding

GND: Geometrically necessary dislocation

HAADF: High-angle annular dark field

HIP: Hot isostatic pressing

HRTEM: High resolution transmission microscopy

H-S: Hashin-Shtrickman

MLE: Maximum likelihood estimation

ND: Normal direction

RD: Rolling direction or radial direction

RE: Rare earth

SAED: Selective area electron diffraction

SE: Secondary electron

SEM: Scanning electron microscopy

SPS: Sparkling plasma sintering

SSD: Statistically stored dislocation

TEM: Transmission electron microscopy

TMCs: Titanium matrix composites

VME: von-Mises equivalent

WEDM: Wire electrical discharge machining

XRD: X-ray diffractometer

List of figures

Fig. 2.1 Crystal structures and Burgers relationship of titanium[41] (a) Crystal structure of α-Ti, (b) crystal structure of β-Ti, (c) Burgers relationship and orientation of lamellae 5

Fig. 2.2 Typical microstructures of titanium alloys [46] (a) Widmanstätten microstructure, (b) basketweave microstructure, (c) bimodal microstructure, (d) equiaxed microstructure 8

Fig. 2.3 Room temperature tensile properties of TiBw/Ti composites with different architectures [69], (a) reinforcements distributed uniformly, (b) reinforcements distributed in network architecture (c) Tensile properties of different TiBw/Ti composites..... 14

Fig. 2.4 Preparation methods of TiBw/titanium composites with typical architectures [70–72], (a) TMCs with network architecture (b) TMCs with layered architecture, (c) TMCs with gradient architecture 15

Fig. 2.5 The schematic diagram of the load bearing effect of TiBw in composites [82], (a) force equilibrium in TiBw reinforcements, (b) the distribution of normal stress in TiBw below the critical aspect ratio, (c) the distribution of normal stress in TiBw above the critical aspect ratio, (d) – (f) force equilibrium in TiBw tilting away from the loading direction..... 19

Fig. 2.6 The globularization mechanism of α/β lath in dual-phase titanium alloy [87,88], (a) lamellar microstructure bending after thermal processing, (b) globularization of lamellar microstructure after thermo-mechanical processing and annealing, (c) Three stages of lamellae globularization..... 25

Fig. 2.7 Rotation of TiBw with the hot deformation of composites [91]..... 27

Fig. 2.8 Typical microstructures of TiBw/Ti composites after thermo-mechanical processing below β transformation temperature [99–101], (a) laminated TiBw/TA15-Ti composite after hot rolling, (b)TiBw/TA15composite after hot rolling, (c) (TiBw+La_2O_3)/Ti composite after solid-solution and hot

compression 30

Fig. 2.9The typical processing map and microstructures obtained at different deformation conditions [108]..... 34

Fig. 2.10 Schematic diagram of the structure of the present thesis 39

Fig. 3.1 Sample dimensions for room temperature tensile testing (unit: mm) 44

Fig. 3.2 Sample dimensions for high temperature tensile testing (unit: mm)..... 46

Fig. 4.1 Phase fraction of TiBw/TA15(Si) with the change of element composition, (a)-(e) phase compositions of composites at different temperatures with varying chemical compositions, (f) β transformation temperatures and silicide dissolution temperatures of composites with different chemical compositions 49

Fig. 4.2 Preparation method and morphologies of powder mixture by low-energy ball milling, (a) raw materials and ball milling process, (b) mixture powders in low magnification, (c) surface morphology of the mixed powder..... 51

Fig. 4.3 Schematic diagrams of the consolidation process of TiBw/TA15(Si) composites (a) powder mixture，(b) in-situ reaction and element diffusion after heating, (c) densification after applying load, (d) formation of room-temperature microstructure after cooling..... 52

Fig. 4.4 The diffusion degree of different elements in TA15 powder during consolidation, (a) Zr element, (b) Si element 54

Fig. 4.5 Microstructures and element distributions of as-sintered TiBw/TA15(Si) composites, (a) Microstructure of as-sintered TiBw/TA15(Si) composites at low magnification, (b) precipitation of silicide in composites with different compositions: (b1) Si0.3Zr2.3, (b2) Si0.3Zr3.0, (b3) Si0.3Zr4.0, (b4) Si1.0Zr2.3, (c) element distribution in the as-sintered composite 55

Fig. 4.6 TEM micrographs of silicide particles in as-sintered TiBw/TA15(Si) composites (a), (d) High-Angle Annular Dark Field (HAADF) imaging, (b), (e)

element distribution in silicide particles, (c), (f) Selected Area Electron Diffraction (SAED) patterns of silicide particles..... 56

Fig. 4.7 Fractured tensile samples and typical tensile stress-strain curves of TiBw/TA15(Si) (a) macroscopic morphologies of fractured specimens with different compositions, (b) typical stress-strain curves of composites with different compositions..... 57

Fig. 4.8 SEM micrographs of fracture surfaces and side-faces of TiBwTA15(Si) composites, (a), (b) Si0.5Zr2.3 and Si0.3Zr3 fracture surfaces in low magnifications, (c) Si0.5Zr2.3 fracture surface in high magnification, (d) Si0.5Zr2.3 fracture side face in low magnification, (e) Si0.5Zr2.3 fracture side face in high magnification 60

Fig. 4.9 TiBw/TA15(Si) with different Si contents after quenched from temperatures (a) Si0.3Zr2.3, (b) Si0.5Zr2.3, (c) Si1.0Zr2.3, subfigures 1 – 3 are obtained at 980 °C，1020 °C and 1040 °C, respectively..... 61

Fig. 4.10 TiBw/TA15(Si) with different Zr contents after quenched from temperatures, (a) Si0.3Zr2.3, (b) Si0.3Zr3.0, (c) Si0.3Zr4.0, subfigures 1 and 2 are 960 °C and 980 °C, respectively 62

Fig. 5.1 Microstructures and element distribution maps of TiBw/TA15(Si) composites before and after solution treatment, (a), (b): S-Ti, (c), (d): ST-Ti67

Fig. 5.2 Crystal orientations in TiBw/TA15(Si) before and after solid-solution treatment (a) orientation map of α phase in S-Ti, (b) prior β grains reconstructed from (a), (c) orientation distribution of TiBw in S-Ti, (d) orientation map of α phase in ST-Ti, (e) prior β grains reconstructed from (d), (f) orientation distribution of TiBw in ST-Ti 68

Fig. 5.3 Results of high-temperature compression tests of TiBw/TA15(Si) composites (a) schematic diagram of the hot compression procedure, (b) macroscopic morphologies of samples after hot compression, (c) – (g) true stress-true strain curves obtained at different conditions: (c) 870 °C, (d) 890 °C, (e) 910 °C, (f) 930 °C, (g) 950 °C..... 69

Fig. 5.4 Microstructures of ST-Ti deformed under different temperatures, at a rate of 1 s^{-1} (a) 870 °C in low magnification, (b) 910 °C in low magnification, (c) 950 °C in low magnification, (d) 870 °C in high magnification, (e) 910 °C in high magnification 71

Fig. 5.5 Microstructures of ST-Ti deformed under different temperatures, at a rate of 0.1 s^{-1}, (a), (d) 870 °C, low and high magnifications, (b), (e) 910 °C, low and high magnifications, (c), (f) 950 °C low and high magnifications..... 73

Fig. 5.6 Microstructures of S-Ti and ST-Ti deformed under different temperatures, at the rates of 0.01 s^{-1} and 0.001 s^{-1}, (a) – (e) microstructures of ST-Ti after deformation at different conditions, (f) microstructure of S-Ti after deformed at 910 °C / 0.01 s^{-1}..... 74

Fig. 5.7 Microstructures of ST-Ti deformed at 910 °C / 0.1 s^{-1}, with varying deformation degrees, (a) deformation degree of different samples, (b) ε=2.5%, (c) ε=5%, (d), (g) ε=10%, (e), (h) ε=20%, (f), (i) ε=40%..... 76

Fig. 5.8 Schematic diagram of microstructure evolution of TiBw/TA15(Si) composites during hot deformation, (a) – (c) microstructure evolution during hot deformation, (d) – (f) the decomposition of lamellar microstructure 77

Fig. 5.9 The calculated and experimental values of Z parameters in logarithm coordinate..... 81

Fig. 5.10 Processing map of ST-Ti in the range of 870 °C – 950 °C, 1 s^{-1} – 0.001 s^{-1} 84

Fig. 5.11 The definition of orientation vectors 85

Fig. 5.12 The changing of orientation distribution of TiBw during deformation (a) Initial state, orientation vectors uniformly distributed, (b) orientation vectors after deformation but before normalization, (c) orientation vectors after normalization 88

Fig. 5.13 The 3-dimensional distribution of TiBw probability density, (a) probability density distribution of orientation vectors on the orientation sphere, (b) the

probability density after projected to the xy plane..... 89

Fig. 5.14 Definition of tilting angles of TiBw 92

Fig. 5.15 The procedure for simulated error analysis 96

Fig. 5.16 Results of the simulated error analysis. (a)-(c): The misorientations between the principal axes of calculated and the exerted strain, (a) average misorientation at different conditions; (b) misorientation distribution at different Δh when n=200; (c) misorientation scatterplot in axis-angle space when Δh=0.8 and n=200; (d)-(f) The error between the magnifications of calculated strains and exerted strains: (d) Average error at different conditions, (e) error distribution at different Δh when n=200, (f) interval with good confidence when n=200 97

Fig. 5.17 The microstructures of TiBw/Ti composites (a) before and (b) after the hot-rolling, and the pole figures of the (010) surface of TiB (c) before and (d) after the hot-rolling 101

Fig. 5.18 Process of calculating the deformation status of TiBw/TA15(Si) after hot rolling, (a) gather the fiber orientations, (b) calculate the principal directions, (c) calculate the principal strains, (d) calculate the strain tensor in the sample frame 102

Fig. 5.19 Area for EBSD data collection of the compressive sample, (a) cross-section of the sample, (b) – (d) TiBw orientations in different regions of the sample, (e) orientations of α phase in the data collection area 104

Fig. 5.20 Approach for strain distribution reconstruction in compressive sample 104

Fig. 5.21 Strain distribution near the center of hot compressive sample, (a) the distribution of different strain components, (b) the distribution of VME strain 106

Fig. 5.22 Comparison of calculated strains the network deformations in different regions of compressive sample, (a) The morphologies of deformed network

structures, the corresponding $[010]_{TiB}$ pole figures, and the calculated strain at different points on the compressive sample. (b) The locations of the selected points on the sample. (c) The comparison of ε_{yy} / ε_{xx} measured from the deformed network structures and calculated with fiber orientations, error bars reveal the standard deviations of the measured values 108

Fig. 6.1 Schematic diagram of isothermal hot pressing of TiBw/TA15(Si) composite 114

Fig. 6.2 Microstructures in TiBw/TA15(Si) composites after isothermal hot pressing, (a) center of SP-Ti billet in low magnification, (b) center of STP-Ti billet in low magnification, (c) center of SP-Ti billet in high magnification, (d) center of STP-Ti billet in high magnification, (e), edge of STP-Ti billet in high magnification 115

Fig. 6.3 TEM analysis of silicide particles in the composite after isothermal hot pressing, (a) – (c) silicide particles in β-phase of SP-Ti, (d) – (f) silicide particles in STP-Ti 116

Fig. 6.4 Crystal orientations of α phase in composites after isothermal hot pressing (a) SP-Ti, orientation distribution map of α phase, (b) STP-Ti, orientation distribution map of α phase, (c) SP-Ti, pole figures of α phase, (d) STP-Ti, pole figures of α phase 117

Fig. 6.5 Dislocation densities in SP-Ti and SPT-Ti, (a) dislocation density map in SP-Ti, (b) dislocation density map in STP-Ti, (c) dislocation density distribution in SP-Ti, (d) dislocation density distribution in STP-Ti 119

Fig. 6.6 Schematic diagram of element diffusion and lath breakdown during isothermal hot pressing, (a) The diffusion tendency of β stabilization elements in β phase, (b) and (c) the recrystallized microstructures at different conditions: (b) diffusion distance of β stabilizers greater than lath width, (c) diffusion distance of β stabilizers smaller than lath width 120

Fig. 6.7 Room temperature tensile properties of S-Ti, SP-Ti and STP-Ti, (a) typical stress-strain curves, (b) typical true stress-true strain curves and strain hardening rates 123

Fig. 6.8 Fracture side-faces of S-Ti, ST-Ti and STP-Ti: (a) and (d) S-Ti, (b) and (e) STP-Ti, (c) and (f) SP-Ti..... 126

Fig. 6.9 Fracture surfaces of S-Ti, ST-Ti and STP-Ti, (a), (d) S-Ti，(b), (e) STP-Ti，(g), (f) SP-Ti..... 128

Fig. 6.10 Schematic diagram of heat-treatment procedures..... 129

Fig. 6.11 Microstructures of STP-Ti underwent heat-treatment and air-cooling, (a), (b) 980 °C / 30 min / AC, (c), (d) 1010 °C / 30 min / AC, (e), (f) 1050 °C / 30 min / AC..... 130

Fig. 6.12 Microstructures of STP-Ti after 1010 °C / 30 min treatment and water quenching, (a) low magnification, (b) high magnification 132

Fig. 6.13 TEM analysis of STP-1010AC, (a) equiaxed α grains and lamellar microstructures, bright field imaging, (b) α/β interfaces, bright field imaging, (c) – (e) HRTEM images and FFT patterns of interfaces between β phase, α laths and equiaxed α grains..... 133

Fig. 6.14 TEM analysis of STP-1010WQ, (a) equiaxed α grains and nearby transformed β phase, bright field imaging, (b) distribution of Mo at low magnification, (c) distribution of Mo in transformed β phase, (d) SAED pattern in transformed β phase, (e) transformed β phase in bright field imaging, (f) α' phase in transformed β phase, HRTEM imaging and corresponding FFT pattern 134

Fig. 6.15 XRD patterns of TiBw/TA15(Si) composites with different treatment 136

Fig. 6.16 EBSD analysis of STP-980AC, (a) orientation map of α-Ti, (b) residual α grains after reconstruction of original β grains, (c) orientation map of original β grains..... 137

Fig. 6.17 Pole figures and grain size distribution of α phase, residual α phase after reconstruction, and prior β phase in STP-980AC 138

Fig. 6.18 EBSD analysis of STP-1010AC, (a) orientation map of α-Ti, (b) residual

α grains after reconstruction of original β grains, (c) orientation map of original β grains 139

Fig. 6.19 Pole figures and grain size distribution of α phase, residual α phase after reconstruction, and prior β phase in STP-1010AC 140

Fig. 6.20 EBSD analysis of STP-1050AC, (a) orientation map of α-Ti, (b) orientation map of original β grains, (c) Pole figures and grain size distribution of α phase and prior β phase in STP-1050AC 142

Fig. 6.21 Room temperature tensile properties of TiBw/TA15(Si) with different treatments, (a) typical stress-strain curves, (b) room temperature tensile properties 143

Fig. 6.22 Relationship between f_{Lath} and $\Delta\sigma_{Lath}$ 145

Fig. 6.23 Strain hardening and uniform deformation capabilities of TiBw/TA15(Si) after different treatments, (a) typical true stress-true strain curves, (b) comparison between total elongation and uniform elongation 147

Fig. 6.24 DIC analysis of S-Ti and STP-Ti during room temperature tensile tests, (a) local strain distribution in S-Ti at different tensile strain, (b) average strain and strain near fracture point in S-Ti, (c) local strain distribution in STP-Ti at different tensile strain, (d) average strain and strain near fracture point in STP-Ti 148

Fig. 6.25 DIC analysis of STP-1010AC and STP-1010WQ during room temperature tensile tests, (a) local strain distribution in STP-1010AC at different tensile strain, (b) average strain and strain near fracture point in STP-1010AC, (c) local strain distribution in STP-1010WQ at different tensile strain, (d) average strain and strain near fracture point in STP-1010WQ 150

Fig. 6.26 BSE images of fracture side-faces of STP-980AC after room temperature tensile test, (a) low magnification morphology, (b), (c) slip traces, (d), (e) polished surface 152

Fig. 6.27 BSE images of fracture side-faces of STP-1010AC after room temperature

tensile test, (a) low magnification morphology, (b), (c) slip traces, (d), (e) polished surface 153

Fig. 6.28 BSE images of fracture side-faces of STP-1050AC after room temperature tensile test, (a) low magnification morphology, (b), (c) slip traces, (d), (e) polished surface 154

Fig. 6.29 BSE images of fracture side-faces of STP-1010WQ after room temperature tensile test, (a) low magnification morphology, (b), (c) slip traces, (d), (e) polished surface 155

Fig. 6.30 Schematic diagrams of plastic deformation behaviors of lamellar microstructures, (a) softening mechanism of lamellae, (b) slip systems in lamellar microstructures..... 157

Fig. 6.31 Activation of slip systems in STP-Ti during room temperature tensile tests, (a) orientation map of α grains and the most favored slip direction for each system, (b) slip traces on the fracture side face, (c) the frequency of slip system activation..... 160

Fig. 6.32 Activation of slip systems in STP-1010AC during room temperature tensile tests, (a) orientation map of α grains and the most favored slip direction for each system, (b), (c), slip traces in the lamellar microstructures, (d) – (f) slip traces in equiaxed α grains, (g) the frequency of slip system activation161

Fig. 6.33 Activation of slip systems in STP-1010WQ during room temperature tensile tests, (a) orientation map of α grains and the most favored slip direction for each system, (b) – (d), slip traces in the transformed β phase, (e), (f) slip traces in equiaxed α grains, (g) the frequency of slip system activation 162

Fig. 6.34 TEM micrographs of STP-Ti after room temperature tensile test, (a), (b) α grains in different regions, (c) dislocations near TiBw, (d) dislocations hindered by grain boundary, (e) dislocations around the silicide particle 165

Fig. 6.35 TEM micrographs of STP-1010AC after room temperature tensile test, (a) bright field imaging at low magnification, (b) dislocations in grain 1, (c) dislocations in grain 2, (d) dislocations in lath structure, (e) dislocations in

grain 3 166

Fig. 6.36 TEM micrographs of STP-1010WQ after room temperature tensile test, (a) bright field imaging at low magnification, (b) two-beam condition with g=[0001], (c) slip traces in the equiaxed α grain, (d) transformed β phase in high magnification, (e) <c+a> type dislocations in equiaxed α grains under two-beam condition 168

Fig. 6.37 Fractured samples and high temperature tensile stress-strain curves of STP-Ti, (a) tensile specimens after testing, (b) – (d) stress-strain curves at conditions, (b) 700 °C, (c) 750 °C, (d) 800 °C 169

Fig. 6.38 Fractured samples and high temperature tensile stress-strain curves of STP-980AC, (a) tensile specimens after testing, (b) – (d) stress-strain curves at conditions, (b) 700 °C, (c) 750 °C, (d) 800 °C 169

Fig. 6.39 Typical macroscopic and microscopic morphologies of samples with type 1 curves, (a) macroscopic morphology, (b) a typical type 1 stress-strain curve, (c) – (e) typical deformation microstructures at the positions marked in (a), subfigures 1 and 2 are corresponding STP-Ti and STP-980AC, respectively 172

Fig. 6.40 Typical macroscopic and microscopic morphologies of samples with type 2 stress-strain curves, (a) macroscopic morphology, (b) a typical type 1 stress-strain curve, (c) – (e) typical deformation microstructures at the positions marked in (a), subfigures 1 and 2 are corresponding STP-Ti and STP-980AC, respectively 174

Fig. 6.41 Typical macroscopic and microscopic morphologies of samples with type 3 stress-strain curves, (a) macroscopic morphology, (b) a typical type 1 stress-strain curve, (c) – (e) typical deformation microstructures at the positions marked in (a), subfigures 1 and 2 are corresponding STP-Ti and STP-980AC, respectively 176

Fig. 6.42 Second-electron images, GND density maps and distribution histograms of samples tested with different conditions, (a) – (c) STP-Ti, 800 °C / 0.0003 s^{-1}, (d) – (f) STP-Ti, 750 / 0.001 s^{-1}, (g) – (i) STP-980AC, 750 °C / 0.001 s^{-1}

..... 179

Fig. 6.43 Strain rate sensitivity of composites at different temperatures, expressed in line slopes, (a) STP-Ti, (b) STP-980AC 182

Fig. 6.44 Schematic diagram of the mechanisms of plastic deformation and defects nucleation for composites with different initial microstructures at different conditions. 186

List of tables

Table 3.1 Interstitial element contents in TA15 spherical powder (wt.%)..... 43

Table 4.1 The compositions for phase calculations in JMatPro..... 48

Table 4.2 The compositions and denotations of prepared composites..... 50

Table 4.3 Tensile strengths of TiBw/TA15(Si) with different Zr and Si contents.. 58

Table 4.4 Tensile elongations of TiBw/TA15(Si) with different Zr and Si contents 58

Table 4.5 Volume fraction of β_T in composites with different Si contents 62

Table 5.1 Peak stresses of ST-Ti deformed at different conditions (MPa)..... 79

Table 5.2 Materials constants of the constitutive equation 80

Table 5.3 Flow stresses of ST-Ti under different conditions at true strain=0.4 83

Table 6.1 Properties of dislocations of different slip systems in α-Ti.....119

Table 6.2 Tensile properties of S-Ti, SP-Ti, STP-Ti and TA15 alloy [104]..... 123

Table 6.3 Denotations and corresponding heat treatment procedures 129

Table 6.4 Room temperature tensile properties of TiBw/TA15(Si) with different treatments..... 143

Table 6.5 Strengthening effects in heat-treated and air-cooled materials 145

Table 6.6 Slip systems and corresponding relative CRSS in α-Ti [155]..... 159

Table 6.7 High temperature tensile peak stresses of materials under different conditions / MPa 170

Table 6.8 High temperature tensile elongations of materials under different

conditions / % 171

Table 6.9 Strain rate sensitivities and apparent activation energies of different materials [166] 183

Chapter 1 Introduction

Titanium and titanium alloys have high specific strength and stiffness, excellent high-temperature mechanical properties, corrosion resistance, and biocompatibility, and are widely used in aerospace, shipbuilding, sports, and biomedical fields [1-5]. Compared to steels, titanium alloys are capable of achieving similar strength and service temperatures with 40% less weight. Though having higher densities than light-weighted alloys like aluminum and magnesium, titanium alloys provide 1.5-2 times higher strength and stiffness, while also having higher service temperatures. As the result, titanium alloys are commonly used to manufacture compressor blades, turbine discs, nozzles for aerospace engines, as well as structural components such as frames and skins for aircraft bodies and wings [1, 4, 6-9]. The use of titanium alloy components effectively reduces the weight of aircraft, decreasing flight costs while improving aircraft performance, providing ample space for aircraft design and manufacturing. Therefore, the proportion of titanium alloy components in newly developed aircraft has gradually increased in recent years.

Titanium alloys exhibit a significant decrease in strength and durability above 650 °C, as well as poor oxidation resistances. Therefore, 650°C is generally considered the upper temperature limit for traditional titanium alloys [9-14]. With the increasing requirements for aircraft speed and maneuverability, aircraft components face harsh service environments with strong vibrations, high overloads, and poor heat dissipation, posing multidimensional challenges to the material's room-temperature and high-temperature performance. Nickel, iron, cobalt, or tungsten-based superalloys, as well as titanium-aluminum or titanium-aluminum-niobium alloys are common alternatives of titanium alloys for service temperatures higher than 650 °C. Superalloys have excellent thermal strength which can be used at temperatures close to 1000°C, while possessing excellent weldability and machinability. However, excessive using of superalloy components significantly increases the weight of aircrafts [15-18]. Ordered structures and strong atomic bonds in titanium-aluminum and titanium-aluminum-niobium alloys significantly hinder dislocation slip, making them lightweighted while exhibiting excellent high-temperature performance [19-21]. However, the room-temperature brittleness, poor weldability and formability of titanium-aluminum alloys and titanium-aluminum-

niobium alloys limit their engineering applications.

Titanium Matrix Composites (TMCs), which are composed of titanium alloy matrix and non-metallic reinforcements, have gained attention in both scientific and industrial fields due to their potential application in aerospace applications. Titanium matrix composites combine the toughness of titanium alloys with the high strength and stiffness of non-metallic reinforcements. Moreover, the performance of TMCs can be designed according to specific requirements [22-25]. Depending on the type and distribution of reinforcements, titanium matrix composites can be classified as Continuously Reinforced Titanium Matrix Composites (CRTMCs), such as carbon fiber-reinforced titanium matrix composites, and Discontinuously Reinforced Titanium Matrix Composites (DRTMCs), such as composites reinforced with silicon carbide particles or titanium boride whiskers (TiB whiskers, TiBw). Continuously reinforced titanium matrix composites have extremely high specific strength and excellent high-temperature durability but exhibit strong anisotropy, making them suitable only for unidirectional tensile loading. Discontinuously reinforced titanium matrix composites have outstanding comprehensive properties and exhibit good isotropy, allowing them to serve under complex loads.

TiBw reinforcements formed by in-situ reaction, due to their excellent load transfer capability, superior interfacial bonding strength, and small difference in thermal expansion coefficient with the titanium alloy matrix, have become the most commonly used reinforcements in DRTMCs [26]. Traditional discontinuously reinforced composites pursue a uniform reinforcement distribution, which makes cracks prone to propagate continuously along the reinforcements, leading to brittle fracture [25,27,28]. Huang et al. [29,30] designed a DRTMCs in which TiBw reinforcements were distributed in a network architecture. The inhomogeneously-distributed reinforcements effectively constrained the grain growth in the titanium matrix, while guided the cracks propagating along the network structure, fully utilized the plasticity of the matrix. Therefore, DRTMCs with a network-like distribution of reinforcements not only possess good room-temperature and high-temperature strength, but also exhibit good room-temperature ductility, greatly expanding the industrial applications of DRTMCs. Based upon the ideal of non-

uniform reinforcement distribution, Jiao et al. [31-33] fabricated DRTMCs with a multi-scale reinforcements architecture by introducing Si element into the matrix. By forming the first-level network-structure with TiBw reinforcements and the secondary-level network-structure with nanoscale silicide particles, the composites exhibited excellent room-temperature and high-temperature strength. In the meanwhile, the addition of Si element further enhanced the resistance to creep and oxidation of the composites, which makes DRTMCs with two-level network structure excellent candidates for long-term service at elevated temperature.

DRTMCs with network structures have good formability, which can be processed into complex components through techniques such as hot rolling, hot forging, and hot extrusion. The hot deformation behaviors of DRTMCs are determined by both the flow behaviors of the metal matrix and the displacement, rotation, and damage of the reinforcements. Additionally, the dislocations movements are also impacted by ceramic reinforcements [34,35], and the interface between the reinforcements and the matrix can alter the material's dynamic and static recrystallization behaviors [36,37]. Therefore, the thermo-mechanical processing of TMCs is more complicated than monolithic alloys. Improper deformation parameters can result in unfavorable microstructures or micro-defects, significantly impacting the performance of composites [38,39]. The thermo-mechanical processing of DRTMCs is typically carried out above the β transformation temperature of the titanium matrix, with reduced deformation rate and controlled deformation degree to protect the reinforcements. However, both high deformation temperatures and lowered deformation degree leads to inadequate microstructure refinement, resulting in poor mechanical performances. Additionally, the laminated microstructure resulting from thermo-mechanical processing in the single-phase region can hardly be tailored by heat-treatment, which allowing only simple strength-plasticity exchange, thereby failing to meet the requirements.

To solve the aforementioned problems, this study aims to design and fabricate a high-temperature DRTMCs suitable for microstructure tailoring in dual-phase region. To this end, near-α TA15 alloy containing Si and reinforced by TiBw was taken as an example. By combining the solid solution treatment above β transformation temperature with the thermo-mechanical processing in the dual-

phase region, this study aims to obtain both refined α grains and refined and dispersed silicide particles, achieving a dual refinement of microstructure, obtaining both excellent comprehensive properties and good heat-treatment controllability to meet different requirements.

Chapter 2 Literature review

2.1 Discontinuously reinforced titanium matrix composites

2.1.1 Porperties of titanium matrix

Titanium is the 22nd element with a relative atomic mass of 47.88. The density of titanium is 4.5 g/cm^3 at room temperature, and the linear expansion coefficient is 8.6×10^{-6}/°C [40]. Under thermodynamic equilibrium, pure titanium has two crystal structures. At room temperature, titanium has a close-packed hexagonal structure known as α-Ti, as shown in Fig. 2.1 (a). The space group of α-Ti is P63/mmc, with the lattice constants a=b=0.295 nm, c=0.468 nm, and α=β=90°, γ=120°. When the temperature exceeds 885 °C, pure titanium undergoes a transition to a body-centered cubic (BCC) structure known as β-Ti, as shown in Fig. 2.1 (b).

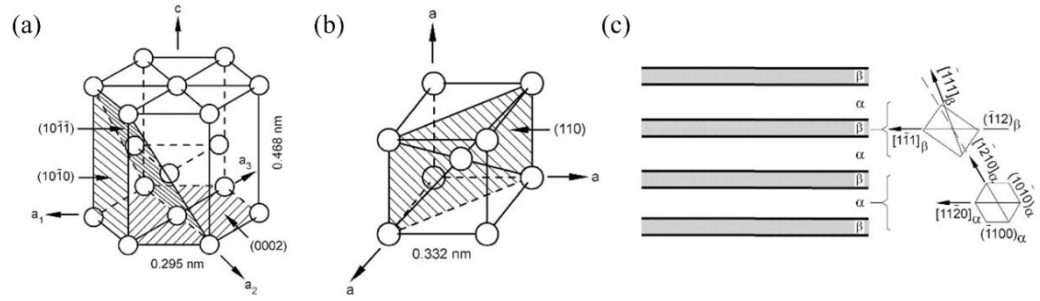

Fig. 2.1 Crystal structures and Burgers relationship of titanium[41]
(a) Crystal structure of α-Ti, (b) crystal structure of β-Ti,
(c) Burgers relationship and orientation of lamellae

The space group of β-Ti is Im-3m, with theoretical lattice constants of a=b=c=0.332 nm, and α=β=γ=90° at room temperature. The transformation between the α and β phases follows a specific orientation relationship: $\{0001\}_\alpha \parallel \{110\}_\beta$ and $\langle 11\text{-}20\rangle_\alpha \parallel \langle 111\rangle_\beta$, known as the Burgers Orientation Relationship (BOR). Both diffusion-induced phase transformations at low cooling rates and shear-induced phase transformations at high cooling rates follow the BOR. Since $\{110\}_\beta$ contains six different crystal planes, and each plane has two possible $\langle 11\text{-}20\rangle_\alpha \parallel \langle 111\rangle_\beta$ relationships, there are a total of 12 different variants of BOR. Unaffected by other factors, the β→α phase transformation randomly selects among the 12 variants. However, if influenced factors such as stress and lattice distortion, the β→α transformation is more likely to occur with a specific variants, known as variant selection. During the phase transformation, α grains usually nucleate at β grain

boundaries and grow in a cluster-like manner into the interior of β grains, eventually contacting each other to form lamellar structures. The α layers within the same cluster belong to the same BOR variant, and α/β interfaces are parallel to $\{1\text{-}100\}_{\alpha}$ planes, as shown in Fig. 2.1 (c) [41].

Generally, it is believed that there are four slip systems in α-Ti: <11-20> direction on the (0001) plane with the Burgers vector <a>, known as basal slip. <11-20> direction on the {1-100} plane with the Burgers vector <a>, known as prismatic slip; <11-20> direction on the {10-11} plane with the Burgers vector <a>, known as type <a> pyramidal slip; and <11-23> direction on the {10-11} plane with the Burgers vector <c+a>, known as type <c+a> pyramidal slip. Although <11-23> direction on the {1-122} plane (known as type II pyramidal slip) has also been reported [42], it is less common at room temperature. The c/a ratio of pure Ti, which is 1.59, is smaller than the theoretical value of 1.63 for close-packed hexagonal structure, making prismatic slips of α-Ti easier to be activated than basal slips. Substitutional solution elements with smaller atomic radius than Ti, such as Al, and interstitial solution elements, such as O, increase the c/a ratio of α-Ti, making the activation of basal slip easier [43]. Basal slip, prismatic slip, and type <a> pyramidal slip are unable to accommodate the deformation along c-axis, as the result, the activation of type <c+a> pyramidal slip is necessary for the plastic deformation of α-Ti. However, dislocations of <c+a> type have higher energy than the type <a> counterparts, and type <c+a> pyramidal slip is difficult to activate at room temperature. As the result, α-Ti has a poor room temperature plastic deformability compared to metals with cubic crystal structures, such as iron and aluminum. β-Ti has three common slip systems, the slip planes are {110}, {112}, and {123}, respectively, and slip direction is <111>. The activation of {110} and {112} planes are most common at room temperature. Compared to α-Ti, β-Ti does not have significant difficult slip directions, therefore exhibits better plasticity.

The elastic modules of α-Ti exhibit strong heterogeneity, which is 145 GPa along c-axis and 100 GPa along a-axis. When randomly oriented, α-Ti exhibits an average elastic module of 105 GPa. [44] The elastic modules of β-Ti is lower than α-Ti, which is about 80 GPa. [45]

The alloying elements of titanium can be categorized into α-stabilizers, β-stabilizers,

and neutral elements based on their influence on phase transformation temperatures. Common α-stabilizers including Al, O, and N. The addition of α-stabilizers can improve high-temperature stability and room temperature strength of titanium alloys, but excessive α-stabilizer content can lead to room temperature brittleness. Common β-stabilizers including V, Mo, Fe, and Nb. The addition of β-stabilizers in titanium alloys can stabilize the β phase at room temperature, refine grain size, and enhance the plasticity of the alloy. However, excessive addition of β-stabilizers can result in decreased high-temperature performance and increased density. Neutral elements, such as Zr and Sn, are commonly used to improve material strength and high-temperature performance of titanium alloys. Additionally, rare earth (RE) elements like Nd and La can be added to reduce the interstitial atom content in titanium alloys, while Si can be added to enhance the high-temperature durability. Based on the equivalent content of α-stabilizers and β-stabilizers, titanium alloys can be classified into near-α titanium alloys, α+β titanium alloys, and near-β titanium alloys. Near-α titanium alloys exhibit good high-temperature phase stability and maintain decent strength above 500 °C, but are unsensitive to heat treatments. α+β titanium alloys have good room temperature strength and plasticity, as well as favorable high-temperature performance, making them the most widely produced and used type of titanium alloy. Near-β titanium alloys exhibit good heat treatment sensitivity. High volume fraction of meta-stable β phase can be obtained in near-β titanium alloys by solid-solutioning and quenching. Following by aging treatment, dispersed nano-scale α phases can be precipitated within β grains, significantly improving the strength of materials. Near-β titanium alloys can achieve room temperature strengths of over 1500 MPa with good ductility, but softens significantly at elevated temperatures. Although near-β titanium alloys have excellent room temperature performance, the high production cost limits the usage to high-end industries.

Common microstructures in near-α and α+β titanium alloys include Widmanstätten microstructure, basketweave microstructure, equiaxed microstructure, and bimodal microstructure, as shown in Fig. 2.2 [46]. The Widmanstätten and basketweave microstructure are collectively referred to as lamellar microstructures, which are obtained when titanium alloys are cooled above the β transition temperature. The Widmanstätten microstructure is typically formed through slow cooling and is

commonly observed in as-cast and as-sintered alloys. Widmanstätten microstructure features coarse α/β lamellar surrounded by grain boundary α phase. Above the β transformation temperature, the titanium alloy is consisted of equiaxed β grains. Due to the disordered atomic arrangement at β grain boundaries, interstitial elements such as oxygen and nitrogen tend to accumulate at grain boundaries. As the result, phase transformation occurs first at the grain boundaries while cooling, forming a continuous grain boundary α phase. Subsequently, the α lamellae nucleates along the grain boundary α phase and grow into the interior of β grains, ultimately forming the Widmanstätten microstructure. The basketweave microstructure is typically obtained by subjecting the titanium alloy to significant plastic deformation above the β transformation temperature. Basketweave microstructure is characterized by the absence of grain boundary α phase, and the presence of intertwined α/β lamellar structures. In materials with lamellar structures, the width of the α/β lamellae is mainly determined by the alloy composition and cooling rate. Higher cooling rates result in a nucleation rate of α lamellae, leading to refined microstructures.

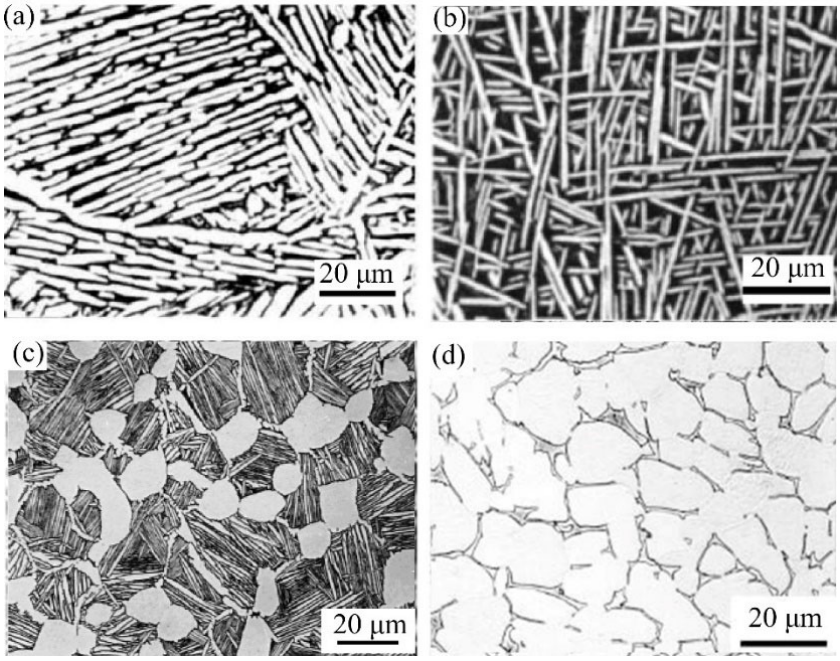

Fig. 2.2 Typical microstructures of titanium alloys [46]
(a) Widmanstätten microstructure, (b) basketweave microstructure,
(c) bimodal microstructure, (d) equiaxed microstructure

Equiaxed and bimodal microstructures are obtained through the recrystallization of severely deformed titanium matrix. The recrystallization can be either static, carried

out by annealing above the recrystallization temperature, or dynamic, which happens during the hot deformation. If the material is slowly cooled to room temperature after recrystallization, an equiaxed microstructure composed of equiaxed α grains and intergranular β phase can be obtained. If the material is rapidly cooled to room temperature, a bimodal microstructure composed of α/β lamellar and equiaxed α grains at triple junctions can be obtained. Equiaxed and bimodal microstructures are usually distinguished based on the content of α/β lamellae. The microstructure is considered as equiaxed if the volume fraction of α/β lamellae is less than 50%, and bimodal if more than 50%. The content of α/β lamellae can be controlled by the temperature of recrystallization annealing. Titanium alloys with different microstructures exhibit different mechanical properties. The Widmanstätten microstructure has poor strength and ductility due to the presence of continuous brittle grain boundary α and coarse microstructure, which make it unfavorable. The strength of the basketweave microstructure is determined by the lamellar width and the size of the original β grains. Refinement of the lamellar structure can enhance material strength, while refinement of the original β grains can improve material ductility. Additionally, basketweave microstructure exhibit good high-temperature durability. Equiaxed microstructure typically have low strength but good room-temperature ductility. At elevated temperatures, titanium alloys with equiaxed microstructure deforms with grain boundary sliding, resulting in poor high-temperature durability. However, grain boundary sliding can also be used for superplastic forming. Bimodal microstructure have good strength, ductility, and high-cycle fatigue performance, as well as good fracture toughness. However, their high-temperature durability is inferior to that of lamellar microstructure materials.

2.1.2 Preparation of DRTMCs

Composites are materials that combine two or more different materials in order to achieve superior performance that unachievable with a single material. The industrial application of composite began in the mid-20th century with glass fiber reinforced polymer matrix composites. By combining high-strength, high-stiffness yet brittle glass fibers with plastic but weak polymers, composites with excellent strength, stiffness, and toughness were obtained [22]. The emergence of composites brought revolutionary changes to materials design, leading to the rapid development

of polymer and metal matrix composites using glass fibers, carbon fibers, and silicon carbide (SiC) fibers as reinforcements. Titanium matrix composites were first fabricated during this period. Following the examples of polymer matrix composites, titanium matrix composites used continuous fibers as reinforcements in the early period, typically carbon fibers or SiC fibers. Due to the low density (approximately 1.7 g/cm^3 for carbon fibers, and 3.1 g/cm^3 for silicon carbide fibers), high elastic modulus (about 300 GPa for carbon fibers, and 450 GPa for SiC fibers), and good high-temperature strength [47, 48]. As the result, CRTMCs exhibit extremely high specific strength and specific stiffness in the fiber alignment direction, with the room temperature tensile strength exceeding 1900 MPa and the elastic modulus exceeding 230 GPa. Moreover, the service temperature of CRTMCs reach over 700°C. However, since continuous fibers can only bear unidirectional tensile loads, the transverse tensile strength (approximately 300 MPa) and compressive strength (approximately 600 MPa) of CRTMCs are poor [49], resulting in strong anisotropic mechanical properties. Additionally, to protect the continuity and integrity of the fibers, CRTMCs can barely be machined or welded. Furthermore, CRTMCs face challenges such as high reinforcement costs, complex fabrication processes, and difficulties in controlling interfacial reactions. As a result, the application of CRTMCs is relatively limited.

In order to reduce the anisotropy and improve the formability of TMCs, ex-situ particle reinforcements such as SiC particles or Ti_2C particles were used as the alternatives of continuous fibers [50-52]. DRTMCs with ex-situ reinforcements are commonly produced by powder metallurgy. The reinforcements are mixed with titanium alloy powder and compacted to approximately 85% of the theoretical density through cold isostatic pressing. The green compact is then densified through vacuum sintering. Due to the high reactivity of titanium, controlling the reaction between the reinforcements and the titanium matrix is challenging. Nevertheless, the reactivity of titanium also enables the preparation of reinforcements with in-situ reaction. By adding elements like C or B, reinforcements such as titanium carbide particles (TiCp) or titanium boride whiskers (TiBw) can be produced by the in-situ reactions with Ti. In-situ reinforcements have good thermostability, good interfacial bonding, and ideal mechanical properties. DRTMCs with in-situ reinforcements can be prepared with various methods, including powder metallurgy, self-consumable

arc melting, and additive manufacturing.

Powder metallurgy involves mixing the reactants of reinforcements and titanium alloy powder with ball-milling, followed by sintering to obtain a dense compact. Graphite powder is often used to generate TiCp reinforcements [53], while boron powder [54] and TiB2 powder [29] are used to form TiBw. B4C powder is employed to produce hybrid TiBw+TiCp reinforcements [55, 56]. Common sintering methods include vacuum hot pressing, hot isostatic pressing, and spark plasma sintering. Vacuum hot pressing is a traditional powder metallurgy technique where the powder mixture is placed in a furnace and densified in vacuum with hydraulic press at elevated temperatures. TMCs fabricated by vacuum hot pressing has low O and N content, high relative density and complete reaction, the mass of the produced compact can weight over 100 kg. However, the slow heating and cooling rates (less than 10 °C/min) in results in coarse grain size and limited control over reinforcement morphology. Typically, TiCp and TiBw reinforcements in TMCs fabricated by vacuum hot pressing have sizes ranging from 5 μm to 10 μm, while the α/β lamellar structure in the matrix ranges from 10 μm to 20 μm. Heat treatment or thermal mechanical processing is often required to obtain good performance.

Hot isostatic pressing (HIP) is a sintering process for titanium matrix composites where the powder mixture is encapsulated in a metal container, vacuum-sealed, and subjected to elevated temperatures and isostatic pressure using an inert gas to promote densification [57]. HIP allows for a densification pressure over 100 MPa, resulting in good density. The size and shape of the HIP-fabricated compacts are determined by the furnace dimensions and the shape of capsule, enabling the production of complex near-net-shaped components, reducing the materials waste and risk of reinforcement damage during forming and machining. However, the use of steel capsules in HIP is limited by the Ti-Fe eutectic reaction, which restricts the sintering temperature to below 1085 °C, leading to insufficient densification and incomplete reinforcement reaction. To overcome the eutectic reaction, a two-step sintering process which involves an initial low-temperature sintering using stainless steel capsule, followed by the removal of the container and subsequent sintering using HIP, is usually employed. Alternatively, titanium capsule can be used to avoid the eutectic reaction. However, both approaches increase the cost of material

fabrication [58]. The vacuum level during HIP sintering depends on the vacuum achieved during capsule sealing. Inadequate degassing can result in residual gases in the container, leading to oxidation of the titanium alloy matrix and residual pores in the composites, which may induce brittleness [59]. Similar to hot pressing, the heating and cooling rates in HIP are relatively slow, resulting in similar microstructural features. However, due to the higher sintering pressures, TMCs fabricated by HIP generally have higher relative density and superior mechanical properties compared to those produced by vacuum hot pressing.

Spark plasma sintering (SPS) is a sintering process where the powder is placed in a vacuum or inert gas environment, then heated by plasma produced by high-frequency current. [59–61]. SPS exhibits rapid heating and cooling rates, reaching up to 10 °C/s. The short thermal exposure time allows for the formation of fine-grained titanium alloy matrices, resulting in improved properties in the as-sintered state. The rapid cooling rate also suppresses reactions between reinforcements and the matrix, deviating the material behavior from thermodynamic equilibrium. This enables the incorporation of reinforcements such as diamond, carbon nanotubes, and titanium boride nanowires that are not obtainable through conventional methods, significantly expanding the choices of reinforcement for TMCs. However, the thickness of the produced compacts is typically limited to less than 20 mm due to equipment power and plasma excitation requirements. The short densification time also poses a risk of incomplete densification in the material.

Consumable electrode arc melting is a preparation method for TMCs where raw materials are first compressed into electrode rods, then melted by arc under a protective atmosphere and solidify into ingots [62,63]. Compared to powder metallurgy methods, arc melting involves a melting-solidification process, allowing for long-range diffusion of elements in the liquid phase, which makes the addition of alloying elements with high melting points and low diffusivity possible. Through consumable electrode arc melting, rare earth elements such as Nd and La can be added to the composite, forming dispersed nanoparticles like La_2O_3, achieving grain refinement and dispersion strengthening. However, the microstructure of composites prepared with arc melting is coarse, and the distribution of reinforcements cannot be controlled. As a result, the mechanical properties of the

as-cast materials are typically poor and require subsequent thermal-mechanical processing.

Additive manufacturing is a novel fabrication method that deposits materials in a layer-by-layer manner, enabling the production of components with complex shapes. Common additive manufacturing techniques for TMCs including laser deposition [64,65], selective laser melting [66,67], and selective electron beam melting [68]. Laser deposition is achieved by melting premade powder or wire using laser and spraying them onto a substrate, solidifying into the component. Selective laser melting and electron beam melting construct the components by first spreading the composite powder or mixed powder in layers, then sintering with localized laser beam or an electron beam. Laser deposition has low costs and can be used to fabricate graded structures, but the dimensional accuracy of the component is low. Selective laser melting offers high precision, but the rapid heating and cooling rates of the laser beam result in significant thermal stresses within the component. Therefore, the fabrication of TMCs by selective laser melting and electron beam melting has narrow processing windows, undesirable processing parameters can lead to deformation and cracking of components, which may induce brittleness. Selective electron beam melting is performed in a vacuum chamber, using defocused electron beam irradiation, metal powders can be preheated, and the solidified component can be in-situ heat-treated. Therefore, Selective electron beam melting has low thermal stress, and need no support structures. However, the fabrication and equipment cost for selective electron beam melting is higher than that of selective laser melting.

2.1.3 Architectures design of DRTMCs

DRTMCs offer good specific strength and stiffness, isotropic properties, and excellent high-temperature performance. Besides, DRTMCs can be subjected to machining and hot forming, making them promising candidates for industrial applications. Influenced by dispersion strengthening theory, early designs of DRTMCs typically pursued a uniform distribution of reinforcements. However, due to the properties of ceramics like high strength, high hardness, and brittleness, cracks tend to initiate in ceramic reinforcements and propagate rapidly by connecting the cracks in adjacent reinforcements. As a result, DRTMCs with

uniformly distributed reinforcements exhibit poor room-temperature ductility, with tensile elongation typically below 2%, and demonstrate macroscopic brittleness upon fracture. Therefore, improving the room-temperature ductility of DRTMCs is important to achieving industrial applications [25,27].

Inspired by the Hashin-Shtrikman (H-S) model, Huang et al. [69] first proposed a design approach for TMCs which distribute the reinforcements in a network architecture. As shown in Fig. 2.3 (b), TiBw reinforcements are enriched in network architecture regions. The network architecture TiBw/Ti composite exhibits excellent room-temperature ductility while maintaining good strength at both room and high temperatures. The network architecture composite with 5 vol.% TiBw content exhibited an elongation exceeding 8%, which is more than three times higher compared to the uniform counterpart. Fracture surface observations of the tensile specimens revealed that cracks in network architecture TiBw/Ti composite propagate along TiBw-rich regions, traversing a large number of high-strength TiBw reinforcements and high-toughness titanium alloy matrix, effectively utilizing the material's ductility.

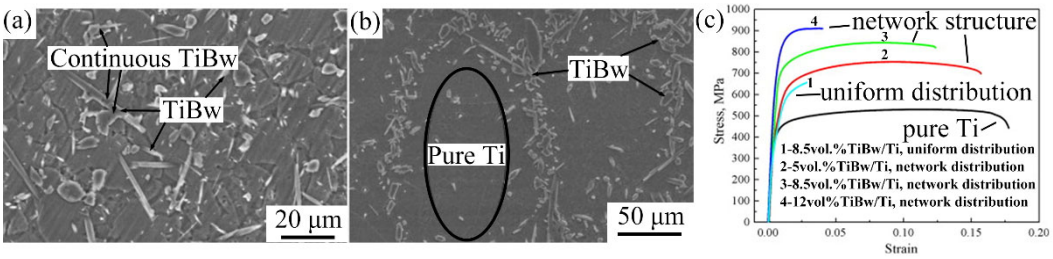

Fig. 2.3 Room temperature tensile properties of TiBw/Ti composites with different architectures [69], (a) reinforcements distributed uniformly, (b) reinforcements distributed in network architecture (c) Tensile properties of different TiBw/Ti composites

The excellent mechanical performance of TMCs with network architecture demonstrates that the design of TMCs does not need to blindly pursue uniform reinforcement distribution. This idea opens up a new dimension for the design of TMCs. Subsequently, researchers have extensively investigated the configuration design of TMCs. Recently, the most researched configurations for DRTMCs include network architectures (including multi-level network architecture), layered architecture, and gradient architecture. The fabrication methods for DRTMCs with typical configurations are illustrated in Fig. 2.4 [70-72].

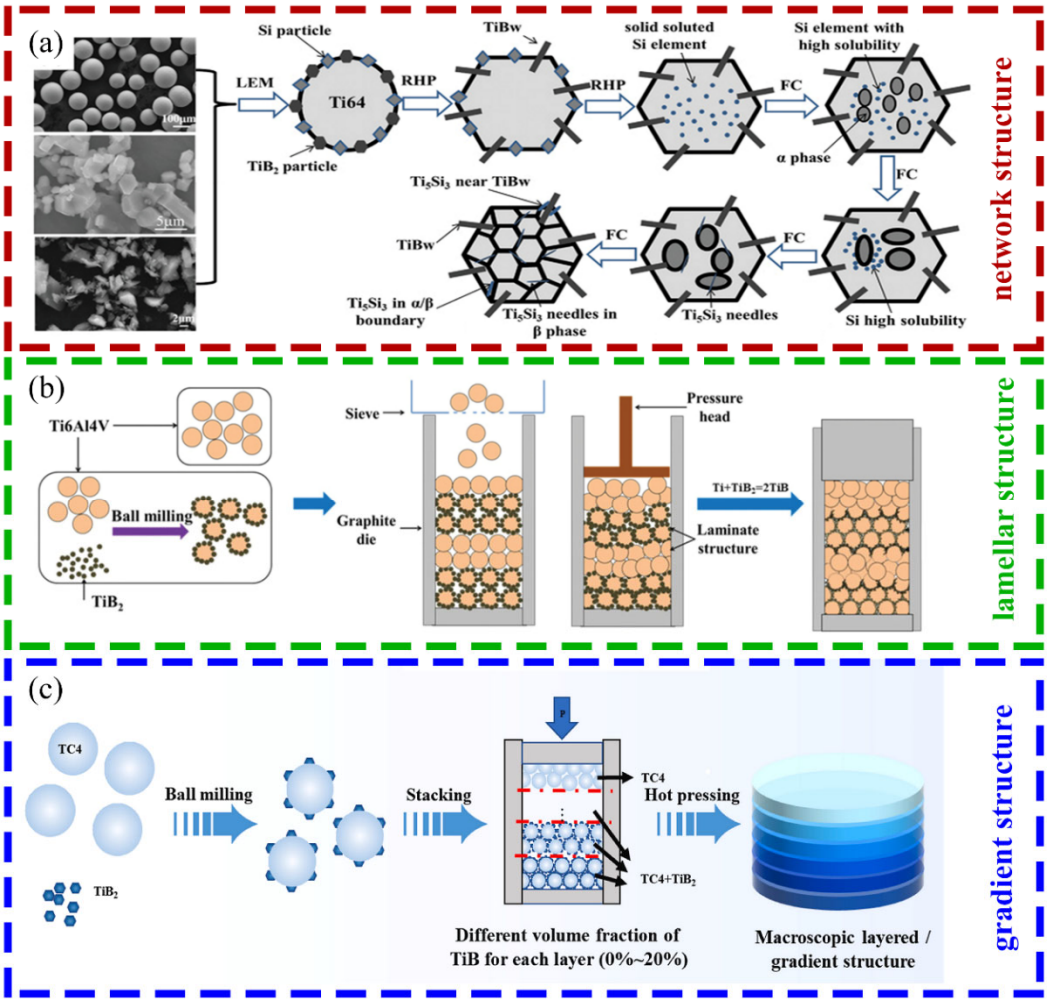

Fig. 2.4 Preparation methods of TiBw/titanium composites with typical architectures [70–72], (a) TMCs with network architecture (b) TMCs with layered architecture, (c) TMCs with gradient architecture

(1) TMCs with network architectures. Network architecture is the most extensively studied configuration for TMCs. The microstructure of TMCs with network architecture consists of regions enriched with reinforcements that distributed in a network manner, and reinforcements-lean regions that encapsulated within the network. TMCs with network architecture are typically fabricated using powder metallurgy techniques. Titanium alloy powders with diameters ranging from tens to hundreds of micrometers are mixed with ceramic powders ranging from a few nanometers to a few micrometers in diameter through low-energy ball milling. This process ensures the uniform embedment of ceramic powders onto the spherical titanium alloy powders. Subsequently, the material is densified using methods such as hot pressing, hot isostatic pressing, or spark plasma sintering. The network architecture is formed by in-situ reaction of reinforcements on the surface of the spherical titanium alloy powders. The network distribution of reinforcements

not only provides strengthening effects but also restricts grain growth within the matrix. As a result, TMCs with network architecture exhibit excellent strength and ductility without the need for grain refinement through thermal processing, making them highly suitable for near-net-shape manufacturing processes.

On the basis of network architecture TiBw/TC4 composite, Jiao et al. [70,73] discovered that the addition of Si can result in the precipitation of nanoscale Ti_5Si_3 silicide particles at the α/β phase interface in the matrix, thus creating a secondary network structure. Two-scale network architecture TMCs exhibit excellent high-temperature strength and creep resistance. Compared to the unreinforced titanium alloy matrix, the steady-state creep rate of the TMCs with two-scale network architecture is reduced by two orders of magnitude. Replacing the matrix with TA15 or Ti65 near-α titanium alloys on the basis of the TMCs with two-scale network architecture, the precipitation phase transforms into a more stable $(Ti,Zr)_xSi_y$ ternary silicide, further enhancing the high-temperature performance of the material [74,75].Based on the TMCs with two-scale network architecture, a design concept of multi-level and multi-scale reinforcement is derived, where micron-sized ceramic reinforcements form a primary structure to stabilize grain boundaries, nanoscale silicide particles form a secondary structure to stabilize phase boundaries, and dispersed rare earth nano-oxides strengthen the matrix. TiBw/Ti55 composites designed and fabricated based on this concept exhibit excellent high-temperature creep resistance, potentially raising the service temperature of DRTMCs to 700 °C [33], thereby partially replacing superalloys and achieving significant weight reduction in engines for aerospace applications. Huang et al. [76], based on the concept of network architecture, obtained TiB nanowires (TiBnw) with an extremely high aspect ratio utilizing spark plasma sintering technique. TiBnw exhibits improved strengthening efficiency due to its high aspect ratio and refined size, while retaining good flexibility. As a result, TiBnw reinforced TMCs show enhanced room-temperature strength and ductility compared to traditional network architecture TMCs, offering a new designing route of flexible network architectures.

(2) Laminate structured TMCs. Laminate structured TMCs are heterogeneous materials composed of TMCs layers and titanium alloys layers. Applying network architecture within the composite layers, it is possible to fabricate laminate-

structured TMCs with a secondary network architecture. There are several methods for the preparation of laminate structured TMCs. Common approaches include diffusion bonding, where titanium alloy and TMCs thin sheets are stacked and bonded to form a bulk material [77], and powder layering, where titanium alloy powder and mixture powder of titanium alloys and ceramics are stacked and consolidated through sintering to achieve densification [71]. Laminate structured TMCs combine the strength of titanium matrix composites with the ductility of titanium alloys. The layer interfaces within these composites serve as crack propagation channels, allowing the material to deflect cracks for multiple times prior to fracture, thus obtaining good toughness. Diffusion-bonded laminate composites exhibit straight composite-alloy interfaces, but the presence of oxide layers and porosity at the interfaces, combined with lower bonding strength, makes cracks more likely to propagate along the bonding interfaces. Laminate composites fabricated with powder metallurgy techniques have relatively tortuous interfaces but exhibit good interfacial bonding. Wang et al. [78] improved the powder layering method, resulting in laminate-network-structured TMCs with controllable layer thickness and flat interfaces. These composites exhibit superior bending fracture toughness, surpassing both titanium alloys and TMCs.

(3) Gradient-structured TMCs. Gradient-structured TMCs refer to TMCs in which the volume fraction of the reinforcement gradually increases or decreases from the surface to the interior. The design objective of gradient structures is to achieve different functionalities by exhibiting different properties on the material's surface and interior. For instance, to achieve high wear resistance on the surface and high toughness internally, a design with a higher volume fraction of the reinforcement on the surface and a lower volume fraction internally would be employed. The design with a gradient change in the volume fraction of the reinforcement avoids abrupt changes in the internal stress and strain state, reducing interfacial effects and preventing the interfacial failure that often encountered in traditional heterogeneous materials. Gradient-structured TMCs are typically fabricated using powder metallurgy or additive manufacturing techniques. In powder metallurgy, a series of alloy-ceramic mixed powders with different ceramic contents are prepared, followed by layer-by-layer stacking according to the reinforcement content, and finally sintered to achieve a dense bulk material [72].

Additive manufacturing involves laser melting of alloy powders and ceramic powders, followed by deposition, gradually adjusting the composition of the melted material to obtain the desired gradient structure [79].

2.1.4 In-situ TiBw reinforcements in titanium matrix composites

TiB is one of the most common in-situ reinforcements in TMCs. It is typically formed through in-situ reactions between the titanium matrix and boron sources such as boron powder, TiB_2 powder or VB_2 powder. TiB has a density of 4.59 g/cm3, an elastic modulus of approximately 440 GPa, and a linear thermal expansion coefficient of 8.6×10^{-6} /°C [80]. Compared to other common reinforcing phases in TMCs, TiB exhibits a lower density, higher elastic modulus, excellent toughness, and a thermal expansion coefficient similar to that of titanium. Therefore, TiB is considered to be the optimal reinforcement for titanium matrix composites [26]. TiB has orthorhombic crystal structure with a space group of Pnma and lattice parameters a = 0.612 nm, b = 0.306 nm, c = 0.456 nm, and $\alpha = \beta = \gamma = 90°$.

The morphology of in-situ formed TiB reinforcements is determined by the diffusion rates of boron atoms in different directions. Due to the significant anisotropy of the TiB crystal structure, boron atoms diffuse fastest along the [010] direction, followed by the [001] direction, and slowest along the [100] direction. As a result, TiB formed by in-situ reaction in TMCs often exhibit short rod-like morphology and known as TiB whiskers (TiBw). Additionally, the diffusion rates of boron atoms along different directions are also influenced by temperature, as the result, the aspect ratio of TiBw can be controlled by controlling sintering temperatures. Huang et al. [81] found that when preparing TiBw/TC4 composites using TiB_2 as the boron source, TiBw with diameters in the range of a few hundred nanometers and high aspect ratios were obtained at sintering temperatures of 1000 °C and 1100 °C. At sintering temperatures of 1200 °C and 1300 °C, the diameter of TiBw increased to 2 μm – 5 μm, and the aspect ratio no longer significantly changed with temperature. Furthermore, prolonging the holding time did not alter the morphology of TiBw.

Due to the fibrous shape of TiBw reinforcements, the applied load in the matrix alloy is transmitted to the reinforcements in the form of shear stress, thereby

strengthening the material. The strengthening effect of TiBw reinforcements in TMCs can be estimated using shear-lag models. The load transfer is influenced by factors such as the content, size, and aspect ratio of TiBw, and the direction of loading. The stress distribution in TiBw reinforcements within TMCs is illustrated in Fig. 2.5 [82].

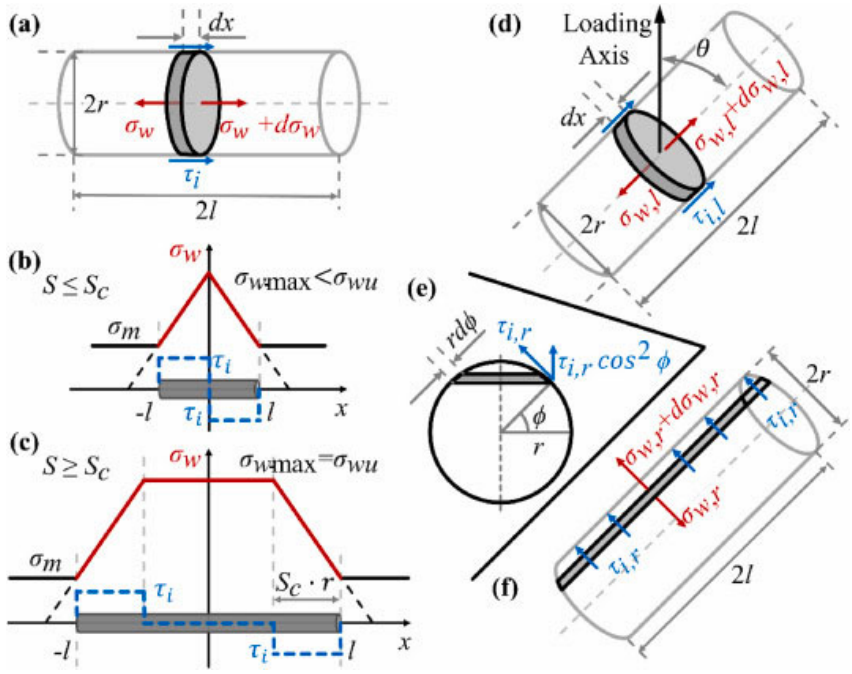

Fig. 2.5 The schematic diagram of the load bearing effect of TiBw in composites [82], (a) force equilibrium in TiBw reinforcements, (b) the distribution of normal stress in TiBw below the critical aspect ratio, (c) the distribution of normal stress in TiBw above the critical aspect ratio, (d) – (f) force equilibrium in TiBw tilting away from the loading direction

When the direction of the reinforcement aligns with the direction of applied stress in the material, the force equilibrium within a unit length dx of a single reinforcement with a radius of r is depicted in Fig. 2.5 (a). At the interface between the matrix and the reinforcement exists a uniform shear stress τ_i, while within the reinforcement, the magnitude of the tensile stress in the negative direction is σ_w, and in the positive direction, it is σ_w+dσ_w. Thus, force equilibrium can be expressed as:

$$-d\sigma_w = \tau_i \cdot \frac{2}{r} \cdot dx \tag{2-1}$$

Le et al. [82] proposed that the stress distribution in the reinforcement is determined by its aspect ratio, which can be divided into two conditions depended on whether

it is higher or lower than the critical aspect ratio S_C. The critical aspect ratio S_C can be calculated by the strength of the reinforcement σ_{wu} and the strength of the matrix σ_m:

$$S_C = \frac{\sigma_{wu}}{\sigma_m} - 1 \tag{2-2}$$

The distribution of normal stress is shown as Fig. 2.5 (b) when the aspect ratio of the reinforcement is smaller than S_C, which obeys:

$$\overline{\sigma}_w = \sigma_m \left(1 + \frac{S}{2}\right) \tag{2-3}$$

In which $\bar{\sigma}_w$ is the average stress in the reinforcement and S is the aspect ratio of the reinforcement. When the aspect ratio of reinforcement is larger than S_C, the distribution of normal stress is shown as Fig. 2.5 (c), which obeys:

$$\overline{\sigma}_w = \frac{S_C}{2S}\left(\sigma_{wu} - \sigma_m\right) \tag{2-4}$$

Via equation 1-3 and 1-4, it can be seen that the reinforcement with larger aspect ratio exhibit higher load-bearing capability, which lead to higher strengthening efficiency. When the reinforcement is aligned in different directions with the loading direction, the force equilibrium within the reinforcement is shown as Fig. 2.5 (d) – (f), and the critical aspect ratio of reinforcement becomes:

$$S_C = \frac{\sigma_{wu}}{\sigma_m \cos\theta} - 1 \tag{2-5}$$

In which θ is the misalignment angle between the reinforcement and the loading direction. If the aspect ratio of the reinforcement is smaller than S_C, the average stress in the reinforcement can be calculated with:

$$\overline{\sigma}_w = \sigma_m \left[1 + \frac{S}{2}\cos^2\theta + \left(1 + \frac{1}{S}\right)\left(1 + \frac{4}{3\pi}\right)\frac{\sin^2\theta}{2}\right] \tag{2-6}$$

Otherwise, the average stress in the reinforcement can be calculated by:

$$\begin{aligned}\overline{\sigma}_w = \sigma_{wu}\cos\theta\left(1-\frac{S_C}{2S}\right)+ \\ \sigma_m\left[\left(\frac{3}{2}-\frac{2}{3\pi}\right)\frac{\sin^2\theta}{2}+\frac{1}{S}\left(\frac{S_C\cos^2\theta}{2}\right)+\frac{\sin^2\theta}{2}-\frac{2\sin^2\theta}{3\pi}\right]\end{aligned} \tag{2-7}$$

Equation 1-6 and 1-7 shows that the reinforcement with lower misalignment angle with the loading directions exhibit better strengthening efficiency. Since the aspect ratio S and misalignment angle θ of each reinforcement are different, the total strengthening effect of reinforcements should be calculated from the probability density function of aspect ratio of reinforcements $h(S)$ and the misalignment angle $g(\theta)$:

$$\begin{aligned}\Delta\sigma_w(\theta,S) = \frac{V_w}{S_{mean}}\left[\int_1^{S_C}\int_0^{\pi/2}\overline{\sigma}_w(S,\theta)\cdot g(\theta)\cdot Sh(S)\,d\theta dS\right. \\ \left.+\int_{S_C}^{\infty}\int_0^{\pi/2}\overline{\sigma}_w(S,\theta)\cdot g(\theta)\cdot Sh(S)\,d\theta dS\right]\end{aligned} \tag{2-8}$$

In which V_w is the volume fraction of the reinforcement, and S_{mean} is the average aspect ratio of reinforcements. Equation 1-8 can not only calculate the strengthening effect of TiBw to TMCs, but also guide the composites' preparation and processing.

2.2 Hot deformation of titanium matrix composites

One of the significant advantages of DRTMCs, compared to the continuously reinforced counterparts, is their capability for plastic forming through thermal processing. Techniques such as hot rolling, hot forging, and hot extrusion can be employed to form DRTMCs into sheets, rods, and even components with complex geometries. Thermal processing not only facilitates material forming but also changes the microstructure, thereby influencing mechanical properties. TMCs are consisted of titanium alloy matrix with good ductility and ceramic reinforcements that hard to be deformed. Consequently, the distribution of microscopic stresses and strains within composites is complex, making them susceptible to defects such as

voids and microcracks caused by reinforcement cracking or interface debonding. Compared to titanium alloys, the microstructural evolution during thermal processing is more complicated TMCs, and the thermal processing window is narrower. Therefore, thorough research is necessary to understand the thermal processing behaviors and mechanisms of TMCs. This section summarizes the research findings on the hot deformation behaviors and mechanisms of DRTMCs, with a particular focus on the progress in studying the two-phase region thermo-mechanical processing of TiBw-reinforced near α-titanium matrix composites.

2.2.1 Behaviors of titanium matrix in hot deformation

During the thermal processing of TMCs, plastic deformation occurs in the titanium alloy matrix, resulting in grain deformation and rotation, as well as the introduction of a large number of dislocations within the matrix. This leads to phenomena such as dynamic recovery (DRV) and dynamic recrystallization (DRX). In the process of DRV, dislocations with opposite-sign cancel each other out, and those with same-sign arrange into low-angle grain boundaries, thereby reducing the elastic strain energy within the crystals. The DRV process does not have an incubation period and occurs simultaneously with high-temperature plastic deformation. DRX in the titanium alloy matrix can manifest as continuous dynamic recrystallization (CDRX), where subgrains within the crystals gradually engulf dislocations and increase their misorientation angles, eventually forming recrystallized grains. It can also manifest as discontinuous dynamic recrystallization (DDRX), where recrystallized grains nucleate at grain boundaries and grow into neighboring grains. DRX has an incubation period and requires a relatively high dislocation density in the material to trigger. Both DRV and DRX consume dislocations within the matrix, change the microstructure, and affect the mechanical properties of the composite.

The proportion of α and β phases, dislocation mobility, and stability of the α/β interface in the titanium alloy matrix are all temperature-dependent, thus the thermal processing temperature significantly affects the hot deformation behaviors of TMCs. Above the β transformation temperature, the matrix is in body-centered cubic crystal structure, and thermal processing within this temperature range is referred to as single-phase region thermal processing. In the single-phase region, the titanium alloy matrix has abundant slip systems and high dislocation mobility,

resulting in lower flow stress and better plasticity. The self-diffusion coefficient of the β phase is three orders of magnitude higher than that of the α phase, leading to a high DRV rate during thermal processing, making DRX difficult and resulting in rapid grain growth, making it difficult to obtain fine grains. The microstructure of the matrix after thermal processing in the β phase region is mainly determined by the β→α phase transformation process and the morphology of the original β grains. If the dislocation density in the matrix is low after thermal processing, the α phase primarily nucleates at the grain boundaries of the β grains during cooling and grows through the migration of α/β semi-coherent interfaces. A fully lamellar microstructure with Burgers orientation between α and β phase is obtained under this condition. If the dislocation density in the matrix is high after thermal processing, the α phase will nucleate within the original β grains with the assistance of high-density dislocations and grow through the migration of non-coherent interfaces. Under this condition, there is no orientation relationship between the α phase that formed by the β→α phase transformation and the original β phase, and a near-equiaxed microstructure is obtained after cooling. The formation of a near-equiaxed microstructure requires low thermal processing temperatures and high strain rates. For example, in the case of the TC4 alloy, a near-equiaxed microstructure can only be formed at strain rates above 1 s^{-1} when the thermal processing temperature is 1000 °C. Since it is often necessary to control the strain rate in TMCs to prevent the fracture of reinforcements, it is easier to obtain a lamellar microstructure rather than equiaxed microstructure. The distribution of lamellar microstructure in the matrix depends on the morphology of the original β grains. At lower thermal processing temperatures and higher strain rates, the original β grains tend to exhibit an equiaxed shape due to DRX, while at higher temperatures and lower strain rates, β grains tend to elongate due to plastic deformation. In titanium alloys subjected to thermal processing in the single-phase region, the α phase lamellae tend to precipitate following specific variant selection based on the Burgers orientation relationship. Hua et al. [86] found that reducing the elastic strain energy generated during thermal processing is the main driving force for variant selection in the α phase.

Below the β transformation temperature, both the hexagonal α phase and the body-centered cubic β phase exist in the matrix, and thermal processing in this

temperature range is referred to as dual-phase region thermal processing. The dual-phase region thermal processing temperature is relatively low, resulting in poor dislocation mobility, combining with the fewer dislocation system in α phase, a higher flow stress and poorer deformability is obtained in dual-phase region, making it prone to reinforcement fracturing and macroscopic cracking. However, the rapid accumulation of dislocations in the dual-phase region makes DRX more likely to be triggered. Besides, both the α and β phases restrict the coarsening of each other, which makes the microstructure refinement easier achievable in the dual-phase region. Since the TMCs are often prepared above β transformation temperature, the lamellar microstructure is a common initial microstructure before thermal processing. Therefore, the microstructure evolution of TMCs during hot deformation is mainly determined by the refinement process of α/β lamellae in the matrix.

The lamellar refinement during the dual-phase region thermal processing consists of two steps: lamellar bending and lamellar spheroidization, as shown in Fig. 2.6 [87, 88]. When the strain is low (less than 0.3), dislocations tend to be aligned within the α/β lamellae, causing lamellar distortion. The direction and degree of lamellar distortion are influenced by the relative orientation between the lamellae cluster and the deformation direction, lamellae aligned parallel to the compression direction are more prone to bending. Lamellar distortion is generally believed to be induced by the local rigid rotation, which introduces low-angle and high-angle grain boundaries into lamellae, disrupting the integrity of lamellae and providing conditions for spheroidization.

Lamellar spheroidization can be divided into three stages: the formation of high-energy defects, lamellar structure instability and decomposition, and grain growth. The latter two stages can be either achieved dynamically during thermal processing or achieved statically through annealing. High-energy defects refer to interfaces, twinning, distortions, and other structures generated by DRV, DRX, local shearing, and crystal rotation. The accumulation of high-energy defects leads to the generation of a large number of substructures within the lamellae, causing the loss of α/β interface coherency, and changing the microstructure from elastic-energy-dominated to interfacial-energy-dominated. As the result, the lamellar

microstructure becomes unstable and gradually spheroidizes to reduce interfacial energy. For example, the α/β interfaces with high curvature (such as the ends of lamellae) will expand under interfacial tension, leading to spheroidization or cylindricalization of the lamellae. The presence of grain boundaries or subgrain boundaries within the lamellae will transform into equilibrium triple junctions, leading to the decomposition of lamellae. The specific form of lamellar decomposition is influenced by lamellar orientation, aspect ratio, and diffusion mode. Lamellae within a same cluster often exhibit similar spheroidization behaviors due to the similarity in orientation, morphology, and stress state, resulting in similar crystal orientations after spheroidization, which forms microtextured zone. Under the Oswald ripening effect, the grain boundaries of coarse grains will migrate towards the fine grains, causing the coarse grains to further grow at the consumption the fine grains, ultimately achieving a uniform equiaxed microstructure and completing the spheroidization.

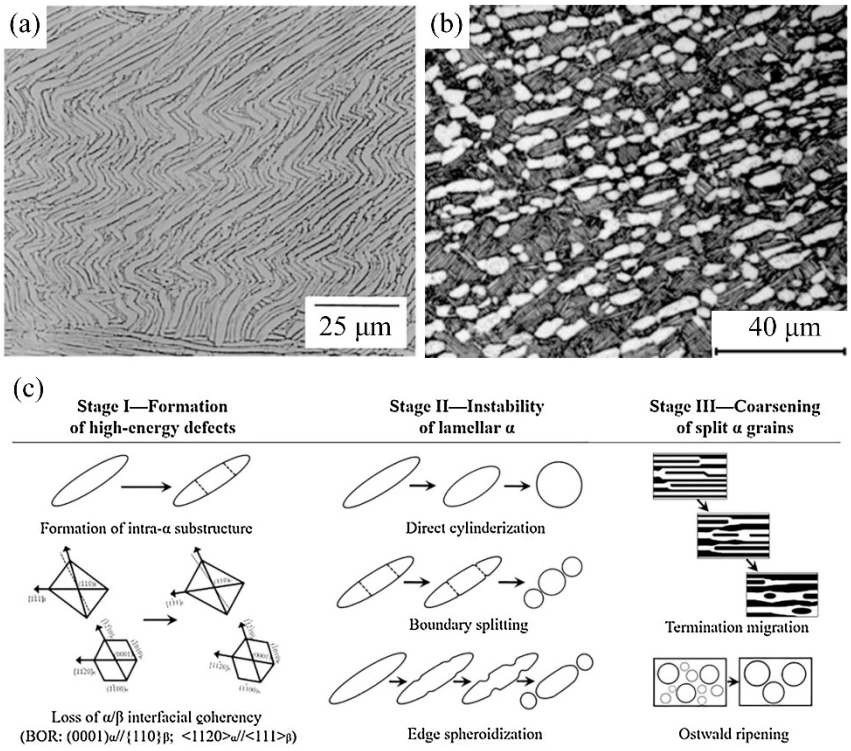

Fig. 2.6 The globularization mechanism of α/β lath in dual-phase titanium alloy [87,88], (a) lamellar microstructure bending after thermal processing, (b) globularization of lamellar microstructure after thermo-mechanical processing and annealing, (c) Three stages of lamellae globularization

In addition to the above-mentioned microstructure evolution mechanisms, which occur both in titanium alloys and TMCs, the reinforcements in TMCs can also

influence the microstructure of the matrix, resulting in distinct microstructures in TMCs. Since the ceramic reinforcements can hardly be deformed, dislocations in the matrix tend to accumulate near the reinforcements, resulting in a higher driving force for recrystallization. At the same time, the interface between the reinforcements and the matrix provides heterogeneous nucleation sites for recrystallization grains, reducing the critical nucleation energy near the reinforcements. Combined, the recrystallization grains are more likely to form near the reinforcements in TMCs [36, 37]. This phenomenon is particularly pronounced in TMCs with network architecture after single-phase region thermo-mechanical processing, where the reinforcements-lean regions lack nucleation sites, and the reinforcements-rich regions have high DRX tendency. As a result, numerous small equiaxed grains can be observed near network structured reinforcements, which encapsules the lamellar matrix, forming a unique heterogeneous microstructure [90].

2.2.2 Behaviors of TiBw in thermo-mechanical processing

The TiBw reinforcements have limited plastic deformability, during thermo-mechanical processing of TMCs, TiBw primarily accommodate the plastic strain by rigid rotation towards the flow direction of the titanium alloy matrix. However, plastic deformation cannot be accommodated completely by rigid rotation, therefore the strain mismatch between the matrix and reinforcements leads to stress concentration, which eventually causes the fracture and reduction of aspect ratio of reinforcements. Guo et al. [91] proposed that the rotation of a single TiBw reinforcement during hot deformation approximately follows the relationship depicted in Fig. 2.7. Assuming that after rotation, the projected dimensions of the reinforcement in the horizontal direction change from l to nl, and in the vertical direction change from H to H/n, the relationship between the tilting angle of the reinforcement before and after deformation can be written as:

$$\tan\theta = \frac{dy'}{dx'} = \frac{n^{-1}dy}{ndx} = n^{-2}\tan\alpha \tag{2-9}$$

In which α and θ are the tilting angle of the reinforcement before and after deformation, respectively. dy and dy' are the projected dimensions of the reinforcement on the vertical direction before and after deformation, respectively.

dx and *dx′* are the projected dimensions of the reinforcement on the horizontal direction before and after deformation, respectively.

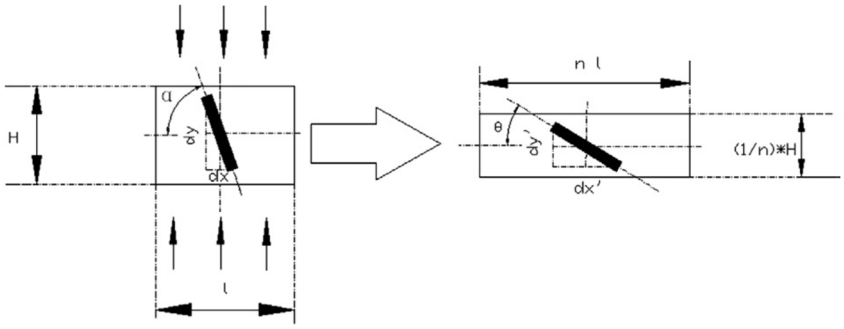

Fig. 2.7 Rotation of TiBw with the hot deformation of composites [91]

Equation 1-9 indicates that the reinforcements rotate towards the stretched direction of the composite after thermal processing, and the inclination angle before and after rotation can be expressed using simple trigonometric functions. Assuming that the initial direction of the reinforcements is completely random, the probability density distribution of the angle between the reinforcement and the horizontal direction after deformation $P(\theta)$ follows:

$$P(\theta) = \frac{2}{\pi} \cdot \frac{1}{n^2 \sin^2 \theta + n^{-2} \cos^2 \theta} \tag{2-10}$$

Equation 1-10 shows that when n > 1, $P(\theta)$ reaches its maximum value at $\theta = 0$, indicating that the reinforcements tend to align along the stretched direction of the material after thermal processing. According to Equations 1-6 and 1-7, it is known that the strengthening effectiveness of TiBw reinforcements is optimal when the loading direction is parallel to the reinforcement. Therefore, TiBw reinforcements in TMCs after thermal processing exhibits higher strengthening effectiveness along the stretched direction of the composites, and lower effectiveness in other directions. Experimental evidence confirms that Equation 1-10 describes the orientation distribution of TiBw reinforcements in TMCs after hot rolling with good accuracy. When combined with the shear-lag model, Equation 1-10 can be used to predict the strengthening effect of TiBw reinforcements in the hot-rolled TMCs [92–96].

Whether the reinforcements fracture during the thermo-mechanical processing primarily depends on the stress state of the reinforcements during deformation. As

indicated by Equations 1-3 and 1-4, higher reinforcements aspect ratios and higher matrix strength result in higher stress within the reinforcements, making them more vulnerable to fracture. Kelly et al. [97] suggested that in the plastic deformation of composites, the reinforcements will fracture if their aspect ratio exceeds a critical value. This critical aspect ratio, denoted as AR_C, can be calculated using the following equation:

$$AR_C = \frac{\sigma_{fb}}{2\tau_m} \tag{2-11}$$

In which σ_{th} is the fracture strength of reinforcement, and τ_m is the shear strength of the matrix. It can be inferred that the critical aspect ratio for reinforcement fracture decreases as the strength of the matrix increases. Both reducing the deformation temperature and increasing the strain rate led to higher flow stresses in the material, making the reinforcement more prone to fracture at lower deformation temperatures and higher strain rates. This finding aligns with the research results of Wang et al. [90] and Wang et al. [98]. Wang et al. [90] compared the microstructures of TiBw/TA15 composites in the sintered state and after hot rolling at different temperatures. They found that the aspect ratio of the reinforcement was highest in the as-sintered state, reaching 10.3. However, after hot rolling at 900 °C, 1000 °C, and 1100 °C with a height reduction of 60%, the aspect ratio of the reinforcement decreased to 3.47, 4.90, and 7.22, respectively. Wang et al. [98] also discovered that in TiBw/Ti60 composites, lower strain rates resulted in more intact reinforcements during hot compression deformation. Additionally, excessive strain can also lead to reinforcement fracture. Zhao et al. [39] observed a decrease in the aspect ratio of TiBw reinforcements in TMCs with increasing forging ratios. After forging at 1050 °C with height reductions of 60%, 75%, and 85%, the average aspect ratios of TiBw decreased from 11 to 9, 5.5, and 4.5, respectively.

As mentioned in section 1.2.4, TiBw reinforcements with higher aspect ratios lead to better strengthening effectiveness. Therefore, excessive fracture of the reinforcements during thermal processing can potentially result in a declined mechanical performance. Wang et al. [90] conducted tensile tests on TiBw/TA15 composites in the as-sintered state and after hot rolling at 900 °C, 1000 °C, and

1100 °C. They found that the tensile strength of the as-rolled composites at room temperature was higher than that of the as-sintered composites. However, with the increase of temperature, the strength of the as-rolled composites rapidly decreased, among which the most significant decline was observed in the composites rolled at 900 °C. Wang et al. attributed this to the severe fracture of TiBw reinforcements in the composite after rolling at 900 °C. The fracture of TiBw lead to a significant reduction of the load-bearing effect. At high temperatures, the titanium alloy matrix was softened, and the strengthening contribution of grain refinement and dislocation accumulation became less significant, making strengthening brought by TiBw dominative. Hence, the strength of composites with low reinforcements aspect ratio reduced rapidly with the increase of temperature. Besides, reinforcement fracture can also introduce microcracks into the composite, leading to local stress concentration and crack initiation, thereby reducing the fatigue life of the composites.

2.2.3 Microstructure evolution of titanium matrix composites

As previously described, thermo-mechanical processing of TMCs in the dual-phase region effectively refines the titanium alloy matrix and aligns the TiBw reinforcements, enhancing the matrix strength while enabling higher strengthening efficiency of the reinforcements. This contributes to improved mechanical properties of the TMCs. Larger deformation and higher strain rates facilitate the rapid accumulation of dislocations, leading to significant matrix refinement. However, these conditions also increase the flow stress during thermo-mechanical processing, making the TiBw reinforcements more susceptible to fracture. Considering the limitations of TiBw reinforcements, the thermo-mechanical processing parameters for TiBw-reinforced TMCs in the dual-phase region should taking both the effects of matrix refinement and reinforcement fracture into account. The target for thermo-mechanical processing is no longer solely on achieving uniform and fine equiaxed or bimodal microstructures, but rather on seeking optimal overall performance. The typical dual-phase region thermo-mechanical processing microstructures of TiBw-reinforced TMCs reported in the literature are shown in Fig. 2.8 [99–101].

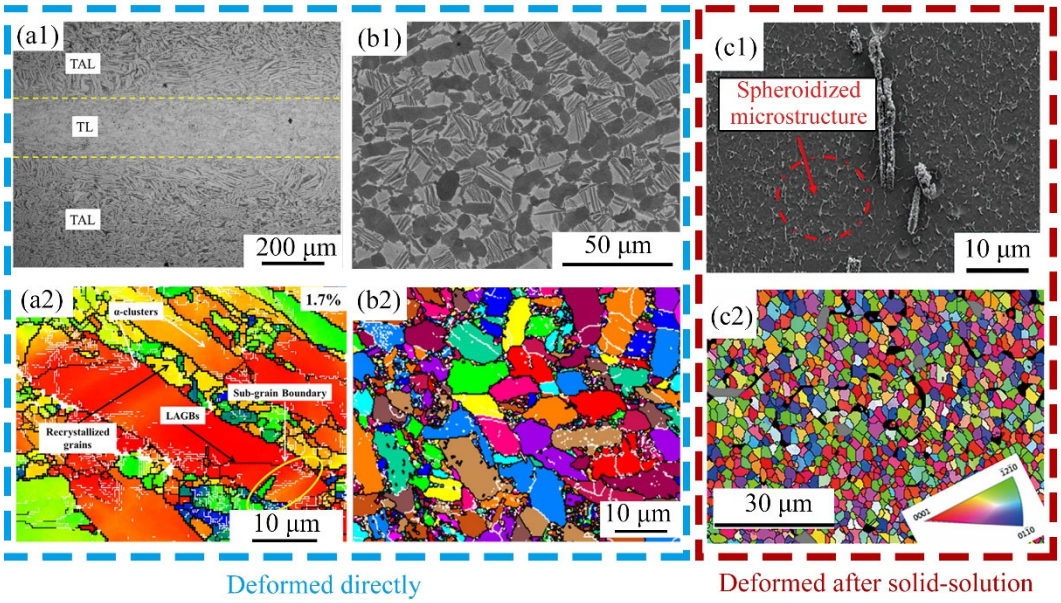

Fig. 2.8 Typical microstructures of TiBw/Ti composites after thermo-mechanical processing below β transformation temperature [99–101], (a) laminated TiBw/TA15-Ti composite after hot rolling, (b)TiBw/TA15composite after hot rolling, (c) (TiBw+La_2O_3)/Ti composite after solid-solution and hot compression

Fig. 2.8 (a) shows the microstructure obtained by Wang et al. [101] through hot rolling of a network-lamellated TiBw/TA15-Ti composite at 950 °C with a height reduction of 50%. Due to the relatively low deformation degree, the coarse lamellar structure in the as-sintered TA15 was not fully globularized, and recrystallized grains occurs only near the α/β phase boundaries. This resulted in a microstructure consisted of fine equiaxed α grains surrounding the coarse columnar primary α phase. Such microstructures often appear in TMCs after dual-phase region thermo-mechanical processing, where the dynamic recrystallization and globularization of lamellar microstructures are insufficient. For example, Sun et al. [102] conducted high-temperature compression on a TiBw-reinforced near-α TMCs at 950 °C/0.1 s^{-1} and found a significant increase in the amount of columnar α phase compared to 900 °C/0.1 s^{-1} conditions.

For TMCs containing Si to enhance the high-temperature performance, the distribution of silicide particles is difficult to control using traditional dual-phase region thermo-mechanical processing. Wang et al. [103] prepared TiBw/TA15-Si composite and controlled the material microstructure by hot rolling at 1000 °C with a height reduction of 60%. The microstructure of the as-rolled composite consisted of coarse α lamellae aligned parallel to the rolling direction, and fine equiaxed α grains with similar distribution to those shown in Fig. 2.8 (a). Additionally, large

silicide precipitates with a size of approximately 1 μm were observed near the α/β interfaces. Compared to the as-sintered composite, the distribution of silicide particles did not change significantly, but their size increased, coarsening of the silicide particles were coarsened during the hot rolling in dual-phase region. Wang et al. attributed the growth of silicide particles to the high temperature and strain energy introduced during hot deformation.

Multidirectional forging introduces significant amount of plastic deformation into TMCs, enabling effective refinement of the microstructure while avoiding the anisotropy induced by unidirectional deformation. Fig. 2.8 (b) illustrates the microstructure obtained by Zhang et al. [99] through multidirectional forging at 1000 °C with a total true strain of 1.44. Following multidirectional forging, the TiBw reinforcements in the TMCs maintained network distribution, while the matrix exhibited a typical bimodal microstructure with an average grain size of ~10 μm. Observing Fig. 2.8 (b2), it is evident that most of the grains in the composites became equiaxed and exhibited a uniform size distribution after thermo-mechanical processing, resulting in a tensile strength of 1100 MPa and an elongation of 9.2% at room temperature. However, compared to the same multidirectional forging process applied to the TA15 alloy (with an average grain size of 2 μm, tensile strength of 1077 MPa, and elongation of 20%) [104], the TiBw/TA15 composites required higher deformation temperatures and more forging pass, resulting in an insufficient grain refinement and reduced strengthening efficiency compared to TA15 alloy.

The TMCs investigated in the aforementioned studies achieved refined microstructures and improved mechanical properties after thermo-mechanical processing in dual-phase region. However, due to the processing parameters were limited by the reinforcements, it was challenging to achieve grain sizes below 10 μm and obtain uniform microstructures. This indicates low efficiency in microstructural refinement for TMCs. Nevertheless, Liu et al. [100] achieved a uniform fine-grained microstructure in (TiBw/La2O3)/Ti composite with an average grain size of ~3 μm through solution treatment prior to hot deformation. The resultant microstructure is shown in Fig. 2.8 (c). Liu et al. suggested that the solution treatment contributed to the refinement of the α/β lamellae prior to thermo-

mechanical processing, providing extra recrystallization nucleation sites in the material. Moreover, the crosspoints of the lamellar structures were prone to decomposition, facilitating the formation of uniform equiaxed α grains. Although Si were not added to the composite, this method also holds the potential to modify the size and distribution of silicide particles through dissolution and dynamic precipitation.

2.2.4 Optimization of thermo-mechanical processing parameters

To avoid the production of defects in composites by undesirable thermal processing parameters, which can lead to a decrease in performance or even cracking and failure during component forming, hot compression tests are often conducted to investigate the hot deformation behavior of the material. By observing the macroscopic morphology and microstructure of the material after deformation under different temperatures, strain rates, and deformation degree, the evolution of the microstructure under different thermal processing parameters can be revealed, which helps the optimization of processing parameters. Additionally, the stress-strain curves obtained from hot compression tests can be used to establish the constitutive equations for hot deformation and construct processing maps, providing guidance for thermal processing and numerical simulations.

Thermal processing maps, constructed on the basis of dynamic materials modeling (DMM) proposed by Prasad et al. [105] in 1984, are commonly used as a guidance tool for thermal processing of metallic materials. In recent years, DMM has also been applied to guide the thermal processing of metal matrix composites. DMM assumes that power inputted during the thermal processing is dissipated in two forms: dissipated to the surroundings in the form of heat, or stored as elastic energy or interfacial energy within the material, which are referred to as power dissipation content and power dissipation co-content, respectively. The ratio of measured power dissipation co-content to the theoretical maximum is defined as the dissipation efficiency. Higher ratio of power dissipation co-content indicate that the material stores more energy through microstructure changing, indicating significant microstructural refinement. By processing with the parameters corresponding to highest dissipation efficiency, optimal microstructural refinement can be achieved. Ziegler et al. [106] suggest that, in addition to dissipation efficiency, it is crucial to

assess the "safety" of energy dissipation paths during thermal processing to avoid the formation of undesirable microstructures such as cracks, shear bands, and abnormally coarsened grains. Based on the principle of maximum entropy production rate, Ziegler et al. proposed instability criteria for material plastic deformation. Thermal processing maps can be obtained by combining the dissipative efficiency map with the instability map. It is generally considered suitable for thermal processing to have higher dissipative efficiency outside the instability range. Both dissipative efficiency and material instability can be calculated using the material's strain rate sensitivity index, which provides simple testing methods with good agreement with engineering practices. Therefore, despite the controversy surrounding the ambiguous physical meaning of DMM theory, thermal processing maps are still widely adopted to guide the determination of thermo-mechanical processing parameters for metal materials [107].

The microstructural refinement mechanisms of matrices in TMCs are different in the single-phase and dual-phase regions. Therefore, the distributions of thermal dissipation efficiency and instability of TMCs shows significant difference above and below the β transformation temperature. The typical processing map of TMCs and the corresponding deformation microstructures are shown in Fig. 2.9 [108]. In the dual-phase region, the peak thermal dissipation efficiency typically occurs at 50 °C to 150 °C below the β transformation temperature, at strain rates of 0.001 s^{-1} to 0.1 s^{-1}. Large number of equiaxed recrystallized grains sizes 5 μm to 10 μm can be observed in the deformation microstructure under these conditions. In the single-phase region, the peak power dissipation efficiency usually occurs at 50 °C to 100 °C above the β transformation temperature, at strain rates of 0.1 s^{-1} to 1 s^{-1}. Under these conditions, lamellar microstructure formed by the β→α transformation of recrystallized β grains is commonly observed, with the typical size of prior β grains ranging from 20 μm to 40 μm [37, 108–112]. The instability zone below β transformation temperature is commonly observed at low temperatures and high strain rates. Cao et al. [110] found that the size of the instability zone increases with the increased reinforcement content. The fracture and debonding of the reinforcements are the main reasons of instability in composites at low temperatures and high strain rates, this conclusion is also supported by other studies [108, 112, 113]. In addition to reinforcement content, the composition of the matrix also

significantly affects the dissipation efficiency of the composites. Lin et al. [114] found that hydrogenation can shift the thermal processing window of TMCs in the dual-phase region towards higher strain rates and lower deformation temperatures, improving their deformability. Meanwhile, a higher content of β-stabilizers changes the ideal processing conditions towards lower strain rates [115, 116]. Zhang et al. [117, 118] found that the initial microstructure of titanium alloys also affects the hot deformation behaviors of composites. Composites with fine initial microstructures have fine deformation microstructures, but in the meanwhile exhibiting deformation resistance and larger instability zone on the processing map. Therefore, processing parameters of materials with different initial microstructures should be separately optimized.

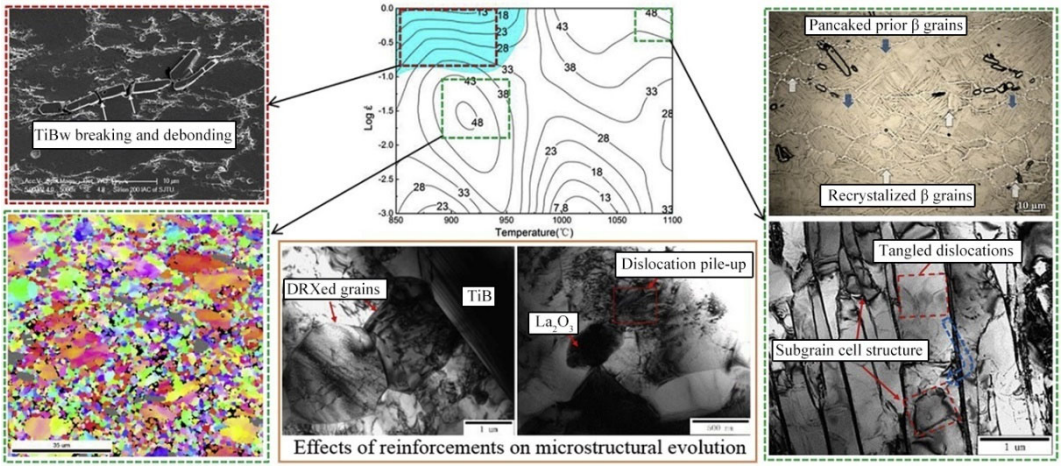

Fig. 2.9The typical processing map and microstructures obtained at different deformation conditions [108]

2.2.5 Heat treatment manipulation of microstructure and mechanical property

Thermal treatment can effectively control the microstructure of titanium alloy matrices, thereby influencing the mechanical properties of TMCs. However, for TMCs using near-α titanium alloys as the matrix, it is hard to improve the strength through the precipitation of dispersive second phase. Moreover, the reinforcements generated through in-situ reactions exhibit good thermal stability, making them difficult to be tailored by heat treatment. Therefore, the mechanical properties of TMCs with near α-Ti matrix is typically hard to regulate through thermal treatment. For instance, Guo et al. [119] performed heat treatment on (TiBw+La_2O_3)/Ti composite with as-cast microstructure at 10 °C – 30 °C above the β transformation

temperature. They found that the morphologies of both TiBw and La_2O_3 reinforcements remained unchanged after the heat treatment, only the grain growth in the titanium alloy matrix was observed. Since the as-cast composites have coarse initial microstructure, the room temperature and high temperature tensile properties of the composites did not exhibit significant change.

Zhang et al. [120] fabricated (TiBw+La_2O_3) composites with two different compositions using casting and thermo-mechanical processing in the single-phase region, then investigated the evolution of microstructure and mechanical properties of the composites after heat treatment above the β transformation temperature. It was revealed that the size of lamellar clusters increased significantly after heat treatment, and the tensile strength and elongation of the composites decreased simultaneously. Wang et al. [121] conducted heat treatment on (TiBw+La2O3)/7715D composites with three different compositions in the single-phase region. After the heat treatment, the tensile strength of the composites decreased with different degrees and the elongation increased slightly. However, due to the small magnitude of performance changing and excessive strength reduction in some composites, the heat treatment possesses only limited meaning.

Huang et al. [122] investigated the response of TiBw/TC4 composite obtained with single-phase region hot extrusion to heat treatment. It was found that the strength of the as-extruded composite increased from 1230 MPa to 1388 MPa after a 900 °C soak followed by quenching and a subsequent 6-hour aging at 530 °C. However, the elongation decreased from 6% to 1%, making it unsuitable for industrial applications. Additionally, annealing the as-extruded composites at 1200 °C for 1 h, both the strength and elongation were decreased. Huang et al. attributed this to the stress concentration on reinforcements caused by grain coarsening. Taking a different approach, Wang et al. [123] compared the microstructure and mechanical properties of TiBw/TA15-Ti network-laminated composites subjected to hot rolling in dual-phase region and heat treatments at different temperatures. The results showed that as the heat treatment temperature increased, the strength of the material gradually decreased. However, due to the back-stress strengthening induced by the heterogeneous microstructure, the composite exhibited excellent work hardening capability, leading to a significant increase in elongation after heat treatment at

700 °C – 800 °C. However, when the temperature reached 900 °C, the Ti layer underwent β transformation, resulting in the elimination of the heterogeneous microstructure and the back-stress strengthening, which lead to a simultaneous decrease in strength and ductility.

Based on the aforementioned studies, it can be concluded that TMCs with near α-Ti matrix that processed in single-phase region exhibit limited ability for microstructure and performance tailoring by heat treatment. This limitation is primarily attributed to two reasons. Firstly, the as-prepared TMCs or TMCs processed in single-phase region have coarse microstructures and poor plasticity, resulting in limited space for strength-ductility trade-off. Secondly, it is difficult to obtain large amount of dispersive second phase in composites adopting near α-Ti or low-alloy α+β Ti as matrix through hot treatment, and the lamellar microstructure is hard to be changed, making the composites insensitive to heat treatment. On the other hand, for TMCs processed in dual-phase region, there is a high degree of strain energy storage, offering the potential for further microstructural tailoring through static recrystallization. Additionally, the refined grain size provides larger space for microstructure tailoring, hence the mechanical properties of TMCs processed in dual-phase region can be effectively modified through heat treatment.

2.3 Research gap

Based on the above analysis, it can be concluded that TiBw reinforced near α-Ti composites exhibit excellent high-temperature performance and good room-temperature strength and ductility. The composites have favorable deformability in the single-phase region, making them suitable for hot forming. However, the resultant coarse lamellar microstructure limits the potential of microstructure and performance tailoring by heat treatment. Although thermo-mechanical processing in the dual-phase region yields refined grains, the brittle TiBw reinforcements may limits the processing parameters, making it difficult to achieve sufficient grain refinement. Moreover, the size and distribution of silicide particles can hardly be controlled by hot deformation in dual-phase region, posing negative influences on the mechanical performance of the composites. Solid solution treatment prior to thermo-mechanical processing can promote dynamic recrystallization, leading to refined microstructure even at lower deformation degree. Additionally, solution

treatment can facilitate the redistribution of silicide particles, offering the potential to control their distribution and morphology. However, the deformation behavior of materials after solid solution treatment differs significantly from that of the as-prepared materials, making the investigation of deformation behaviors necessary. Furthermore, the refined microstructure obtained with thermo-mechanical processing can be vastly tailored by heat treatment. Investigating the heat treatment response of the material can help to reveal the ideal heat treatment parameters for different service purposes, as well as elucidating the strengthening and deformation mechanisms of materials with different microstructures.

2.4 Hypothesis, research objectives, and structure of thesis

Hypothesis:

In the present research, we propose that:

(1) Solid solution treatment in single-phase region prior to thermo-mechanical processing can significantly refine the grain size and redistribute the silicide particles in TiBw/TA15(Si) composite.

(2) The plastic strain induced into the composite during thermo-mechanical processing can be revealed by the orientation distribution of TiBw reinforcements, thereby reconstructing the strain distribution.

(3) The room temperature and high temperature properties as well as the deformation mechanisms of TiBw/TA15(Si) composites after thermo-mechanical processing can be significantly tailored with heat treatment.

Research objectives

This study takes TiBw/TA15(Si) composites with network architecture as an example, aiming to achieve microstructural refinement and microstructure and mechanical properties regulation through thermal processing and heat treatment. The major objectives of the present study are as follows:

(1) Design and fabricate TiBw/TA15(Si) composites with different compositions,

optimizing the composition based on room-temperature mechanical properties and the dissolution temperature of silicide particles, thereby obtaining a composite suitable for dual-phase microstructure control.

(2) Investigate the high-temperature compression behavior of the composites in the dual-phase region after refining the initial microstructure through solid solution treatment, revealing the microstructural evolution mechanisms during hot deformation and determine the optimized processing parameters.

(3) Investigate the evolution of orientation distribution of TiBw reinforcements during hot deformation, establish a quantitative relationship between reinforcement orientation and plastic deformation of the composites, elucidate the strain distribution in hot compression specimens.

(4) Achieve dual refinement of the microstructure in TiBw/TA15(Si) composite through thermo-mechanical processing, reveal the mechanism of microstructure dual refinement, and subject the composite to different heat treatments conditions to investigate the evolution of microstructure and mechanical behaviors.

The structure of thesis

Chapter 1 introduces the background of this thesis. The application of DRTMCs is briefly introduced, the challenges of microstructure and mechanical properties controlling are discussed, and research plan is presented. Chapter 2 reviewed the literatures concerning the preparation, the thermo-mechanical processing, and the heat-treatment microstructure manipulation of DRTMCs, discusses the research gap, and proposes the research objectives. Chapter 3 presents the research, materials preparation, and analysis methodologies used in this thesis. In Chapter 4, the influence of composition on room-temperature tensile properties and the solid solution temperature of silicide particles in TiBw/TA15(Si) is investigated to select materials that exhibit both excellent room-temperature strength-ductility synergy and suitability for dual-phase region thermal processing and microstructure regulation through heat treatment. In Chapter 5, the evolution of matrix microstructure and reinforcement orientation during thermo-mechanical processing is studied, and the optimized thermal processing parameters are obtained. In

Chapter 6, fine-grained TiBw/TA15(Si) composite are prepared through solid solution treatment and isothermal hot pressing, and the microstructure and room-temperature/high-temperature tensile deformation behaviors under different heat treatment conditions are investigated. The structure of the present thesis is schematically illustrated in Fig. 2.10.

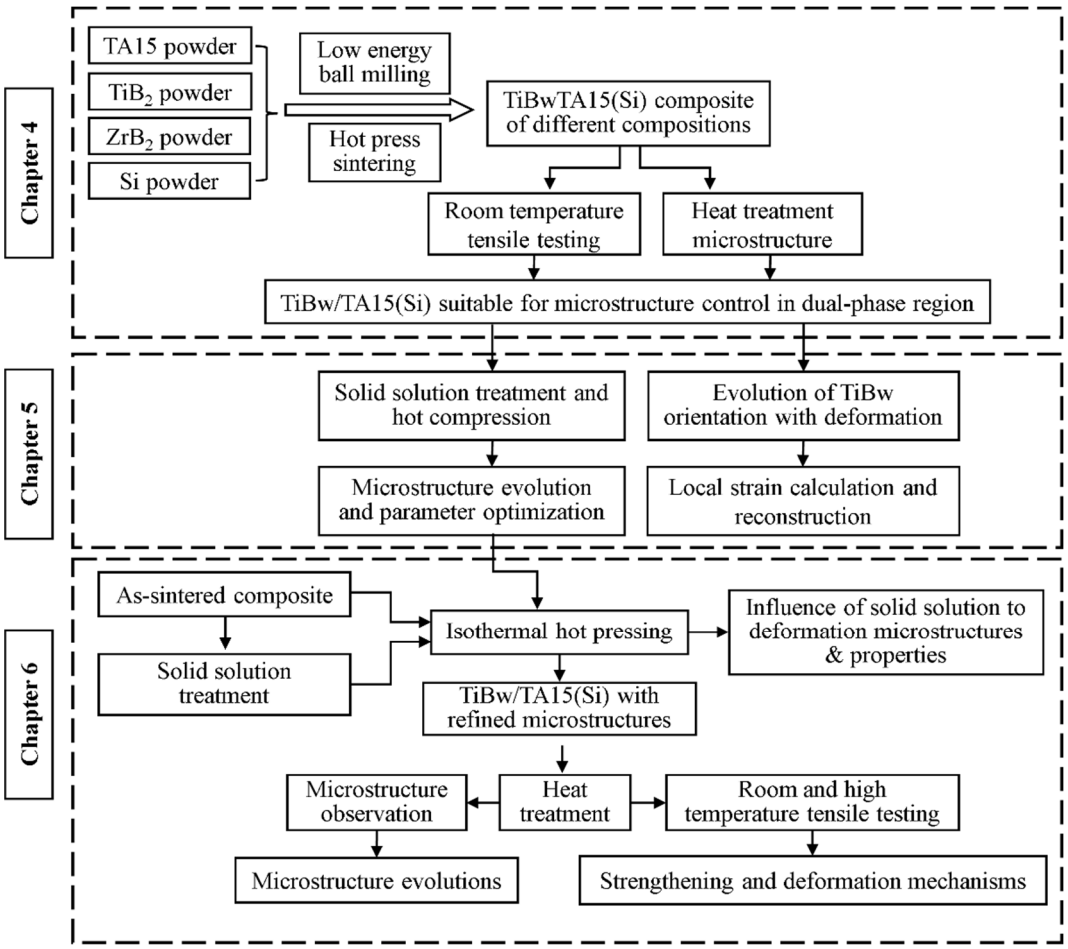

Fig. 2.10 Schematic diagram of the structure of the present thesis

Chapter 3 Methodology and experimental materials

3.1 Research methodology

The methodology to achieve the objectives of this study are as follows:

(1) Preparation of TiBw/TA15(Si) composites with network architecture. TiBw/TA15(Si) composites with 3.4 vol.% of TiBw reinforcements and different Si and Zr contents were designed based on thermodynamic calculations. The TA15, TiB_2, ZrB_2, and Si powders were mixed using low-energy ball milling under Ar protection, with a milling speed of 180 rpm, a ball-to-powder ratio of 3:1, and a milling time of 5 hours. The mixed powders were placed in a graphite mold and sintered to achieve densification in a vacuum hot-press sintering furnace. Firstly, the furnace chamber was evacuated to a vacuum pressure below 1×10^{-2} Pa, then heated at a rate of 10 °C/min to 1300 °C and held for 1.5 h. After reaching the desired temperature, a pressure of 20 MPa was applied to the powder by hydraulic press. After the holding period, the pressure was released at 800 °C and the material was cooled to room temperature before removal from the furnace.

(2) Composition optimization of TiBw/TA15(Si) composites. The mechanical properties of TiBw/TA15(Si) composites with different compositions were evaluated through room-temperature tensile tests. The materials were subjected to a 30-minute heat treatment at temperatures ranging from 960 °C to 1040 °C, followed by quenching, to observe the dissolution behavior of silicide particles at different temperatures in the various compositions. Composite with a favorable combination of room-temperature strength and ductility, and complete silicide solid solution below the β transformation temperature, was selected for further investigation.

(3) Investigating the high-temperature compression behaviors and optimizing the thermo-mechanical processing parameters. The materials were first subjected to a solid solution at 1050 °C for 30 minutes then cooled to room temperature, to obtain a refined lamellar microstructure and dissolve the silicide particles. Using the Gleeble 1500D thermal-physical simulation platform, hot compression tests were conducted on the pre-treated composites at deformation

temperatures of 870 °C, 890 °C, 910 °C, 930 °C, and 950 °C, and strain rates of 1 s^{-1}, 0.1 s^{-1}, 0.01 s^{-1}, and 0.001 s^{-1}. The evolution of microstructure during hot compression was observed to investigate the mechanisms of deformation and microstructure refinement, a processing map was constructed to obtain optimized processing parameters.

(4) Investigating the evolution of TiBw orientation distribution during high-temperature plastic deformation. The rotational of TiBw reinforcements during high-temperature plastic deformation was analyzed to establish a quantitative correlation between reinforcement rotation and material plastic deformation, along with a method to calculate the local plastic deformation based on reinforcement orientations. The accuracy of the method was validated using computer simulations. The strain distribution in hot compression sample of TiBw/TA15(Si) composites was reconstructed, and the accuracy of the reconstruction was verified by comparing the calculated value with the deformation of the network structure.

(5) Refining the microstructure of TiBw/TA15(Si) composites and revealing the influence of solid-solution treatment to the post-deformation composites. The composites were subjected to isothermal hot pressing individually and a combined process of solid solution followed by isothermal hot pressing. Prior to isothermal hot pressing, the composite were processed into Φ 40 mm × 40 mm cylinders with a reverse radius of R=2 mm to reduce stress concentration. Tungsten carbide plates (Φ 100 mm × 30 mm, with edge reverse radius of R=4 mm) were used to isolate the composite billets and graphite molds. During the isothermal hot pressing, the furnace chamber was first evacuated to a vacuum pressure below 1×10^{-2} Pa, then heated to 920 °C with a rate of 10 °C/min. The temperature was held for 20 minutes, before the composite billets were compressed to 25% of its original height at a strain rate of 0.003 s^{-1} (both temperature and strain rate were determined based on the processing map). Upon finishing, the pressure was lifted, and the deformed billets were cooled in furnace to room temperature. Composite subjected to both solid solution pre-treatment and isothermal hot pressing and that without pre-treatment were compared to investigate the effects of solid solution on the microstructure and mechanical properties.

(6) Heat treatment manipulation of microstructures of TiBw/TA15(Si) with

refined microstructure and mechanical properties investigation. Four different heat treatment processes were employed to TiBw/TA15(Si) treated with solid solution and isothermal hot pressing: 980 °C / 30 min / air-cooling, 1010 °C / 30 min / air-cooling, 1050 °C / 30 min / air-cooling, and 1010 °C / 30 min / water-quenching. A comparison was made between the microstructure, room temperature tensile properties, and deformation behaviors of materials in different heat treatment conditions to study the strengthening mechanisms and room temperature plastic deformation mechanisms of composites with different microstructures. The high-temperature tensile properties and deformation microstructure of the composites were investigated at deformation temperatures of 700 °C, 750 °C, and 800 °C, and strain rates of 0.003 s^{-1}, 0.001 s^{-1}, and 0.0003 s^{-1}, to reveal the high-temperature plastic deformation mechanisms of composites with different microstructures and different deformation conditions.

In the aforementioned process, the heat treatment of materials was conducted in a tube furnace. Initially, the tube furnace was evacuated to low vacuum and then filled with high-purity (>99.99%) argon gas, which was repeated three times to clean the furnace. Subsequently, the tube furnace was heated to the desired temperature at a rate of 10 °C/min, and the materials to be treated were loaded into the chamber. Upon loading, the furnace was cleaned three times with high-purity argon gas, and the timer started after the temperature was stabilized. After the soaking period, the materials were removed and either air-cooled or water-quenched to room temperature.

3.2 Raw materials

Spherical TA15 near α titanium powder supplied from Xian Sailong Ltd. (China) with a nominal composition of Ti-6.5Al-1Mo-1V-2Zr in weight percentage was adopted as the raw material for titanium alloy matrix, the interstitial element contents are listed in Table 3.1. The diameter of TA15 powder ranges from 75 μm – 150 μm, with an average of 100 μm. TiB_2 powder and ZrB_2 powder supplied from Forsman Ltd. (China) were adopted as reactants for TiB reinforcements, the purities of the supplied powders are 99.5%. Si powder supplied from Beijing Xingrongyuan Ltd. was adopted to modify the high temperature properties of TA15 alloy matrix, the purity of the powder is 99.8%.

Table 3.1 Interstitial element contents in TA15 spherical powder (wt.%)

Element	H	C	O	N
Content	0.005	0.01	0.09	0.008

3.3 Analysis methodology

3.3.1 Phase analysis

The material was analyzed for phase identification using a PANalytical Empyrean X-Ray Diffractometer (XRD). The instrument utilized Cu K_α radiation with a wavelength of 0.15406 nm. The measurements were conducted with a 40 kV accelerating voltage and 40 mA current. The scanning range spanned from $2\theta=20°$ to 90° at a continuous scanning rate of 6°/min.

3.3.2 Microstructrue characterization

Helios NanoLab 600i scanning electron microscope (SEM) manufactured by FEI was used to examine the microstructure, surface morphology, and tensile fracture surfaces of the samples. Surface morphology was observed in secondary electron (SE) mode at an operating voltage of 20 kV and an operating current of 0.69 nA. Backscattered electron (BSE) mode was used for qualitative observation of element distribution and crystal orientation on the sample surfaces, with an operating voltage of 5 kV and an operating current of 5 nA. The element distribution in the material was characterized using the energy-dispersive X-ray spectroscopy (EDS) system integrated with the SEM.

Crystal orientations in the materials were collected using a SUPRA 55 SAPPHIRE scanning electron microscope manufactured by Carl Zeiss, along with an Electron Backscatter Diffraction (EBSD) analyzer. The collected crystal orientation data was subsequently analyzed using the MTEX toolbox in the MATLAB software environment provided by MathWorks.

The samples used for SEM observation and EBSD analysis were obtained through Wire Electrical Discharge Machining (WEDM). Subsequently, the observation surface was ground using sandpaper from low to high grits up to 4000# to eliminate WEDM machining marks and residual stress from previous grinding. After grinding, coarse polishing was performed using a 0.5 μm diamond polishing agent to remove

grinding marks, followed by fine polishing using a 0.05 μm colloidal SiO_2 agent to eliminate diamond scratches and residual stress from coarse polishing. Finally, a 0.2 vol.% hydrofluoric acid (HF) aqueous solution was used to etch the sample for 4 seconds to obtain a stress-free surface.

The Talos F200x transmission electron microscope (TEM) was used to analyze the microstructure, phases, element distribution, and crystal orientation in the material. For TEM analysis, a 300 μm thick slice was first obtained using the WEDM. The slice was then ground using sandpaper up to 2000# grit to remove WEDM marks. Subsequently, the sample was continuously ground with sandpaper of 2000# grit until the thickness was less than 50 μm. After grinding, a Φ3 mm disc was punched from the sample, and the central area of the disc was processed using the GATAN 695 ion milling system to create a thin region suitable for TEM observation.

3.4 Mechanical properties measurement

3.4.1 Room temperature tensile test

Room temperature tensile testing was performed using an Instron-5569 universal testing machine. The sample dimensions and testing method were determined according to the GB/T228-2002 standard for room temperature tensile testing of metallic materials. The dimensions of the plate-shaped sample adopted for the testing are shown in Fig. 3.1. The displacement rate was set at 0.5 mm/min, which corresponds to a strain rate of approximately 5.6×10^{-4} s^{-1}. The deformation of the tested sample was accurately measured using an electronic extensometer with a gauge length of 10 mm.

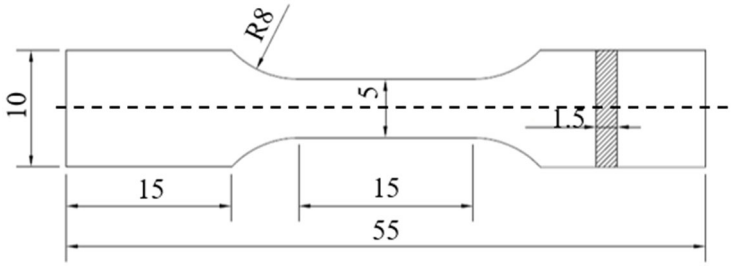

Fig. 3.1 Sample dimensions for room temperature tensile testing (unit: mm)

The true stress and true strain are calculated as follows:

$$\sigma_T = \sigma(1+\varepsilon) \tag{2-1}$$

$$\varepsilon_T = \ln(1+\varepsilon) \tag{2-2}$$

In which σ_T is the true stress, ε_T is the true strain, σ is the engineering stress, and ε is the engineering strain.

The work hardening rate of the material is calculated by taking the derivative of true stress with respect to true strain. The starting point of the non-uniform plastic deformation stage is determined by the intersection of the true stress-true strain curve and the work hardening rate curve. Alternatively, it can be obtained by identifying the highest point on the engineering stress-strain curve. The results obtained from both methods are the same.

The room temperature tensile test specimens were first machined from the material using WEDM. Subsequently, the specimens were polished with sandpaper up to 800# grit to remove WEDM marks. Surfaces of the specimens for slip trace analysis were treated the same as the specimens used for SEM observation. Digital Image Correlation (DIC) technique was used to analyze the strain distribution on the specimen's surface. Prior to the DIC analysis, speckle patterns were sprayed onto the specimen surface using pigments and a spray gun. During the test, a Hikvision industrial camera with a resolution of 3072×2078 pixels and a capture rate of 2 fps is used to record the displacement of the speckle patterns on the specimen surface. After the experiment, GOM software was utilized to analyze the displacement of the speckle patterns and obtain the strain distribution on the specimen's surface.

3.4.2 High temperature tensile test

The high-temperature tensile test was conducted on an AG-X Plus universal testing machine equipped with a furnace. The sample dimensions are shown in Fig. 3.2. During the experiment, the clamp was heated to the specified temperature along with the furnace. Subsequently, the sample was loaded and allowed to achieve equilibrium. After the temperature stabilization, the sample was subjected to a 3-

minute thermal soaking, and loading was applied after the soaking period. After fracture, the sample was water-cooled to room temperature to preserve its microstructure. The machining and grinding methods for the high-temperature tensile samples were consistent with those used for room temperature tensile samples.

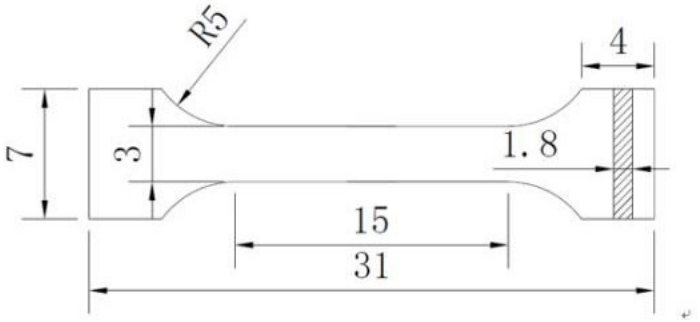

Fig. 3.2 Sample dimensions for high temperature tensile testing (unit: mm)

3.4.3 Hot compression test

The hot compression test was performed using the Gleeble 1500D thermo-physical simulation platform. Cylindrical specimens with dimensions of Φ8 mm × 12 mm were used for testing. Prior to the test, a PtRh-Pt thermocouple was welded onto the sample for temperature control. During the test, the sample was clamped using a pre-load of 500 N. Graphite sheets were used for lubrication between the sample and the clamps. Subsequently, the sample chamber was evacuated to low vacuum, and the sample was heated to the desired temperature at a rate of 10 °C/s and held for 2 min. The load was applied after the holding period. Once the desired strain was reached, the load was removed, and the sample was immediately water-cooled to room temperature to preserve the microstructure for subsequent observation.

Chapter 4 Preparation and composition optimization of TiBw/TA15(Si) composites

4.1 Introduction

TiBw/TA15(Si) composites with network architectures utilizes near-α high-temperature TA15 titanium alloy as the matrix. In-situ reaction is employed to generate TiBw reinforcements with network distribution to enhance the high-temperature performance while retaining ductility. Si is a common alloying element in high-temperature titanium alloys. The addition of Si not only produce silicide precipitates to hinder dislocation movements and improve room temperature strength, but also enhances high-temperature performance and creep resistance through dynamic aging. In this study, Si element is added to TA15 to form (Ti, Zr)$_x$Si$_y$ particles to enhance both the room temperature and the high temperature strength. Additionally, Zr element is added to balance the loss of Zr by silicide precipitation. By investigating the microstructure and room temperature mechanical properties of the composites, and the high-temperature microstructure evolution with varying amounts of Si and Zr elements, the composition of TiBw/TA15(Si) composites is optimized to achieve both good comprehensive performance and controllable microstructure in dual-phase region.

4.2 Composition design and preparation of TiBw/TA15(Si) composites

4.2.1 Composition design of TiBw/TA15(Si) composites

Previous research has shown that the TiBw/TA15(Si) composite exhibits excellent room temperature strength and ductility, as well as good high-temperature strength and durability. The material achieves optimal comprehensive performance with a reinforcement content of 3.4 vol.%. The present study focuses on refining the microstructure of TiBw/Ta15(Si) composites with a reinforcement content of 3.4 vol.% through hot deformation in dual-phase region. Subsequent heat treatments are employed to further regulate the microstructure and mechanical properties of the composites. In order to control the distribution of silicide particles while avoiding the elimination of the deformation microstructure, the temperature for

silicide dissolution should be kept below β transformation temperature. Additionally, Zr element is added to the alloy to maintain the stability of the matrix composition after silicide precipitation. By adjusting the content of Si and Zr elements in the material, it is aimed to achieve both excellent performance and controllable microstructures by heat treatment in dual-phase region.

The alloying elements Mo, V, Al, and Zr in TA15 can potentially affect the β transformation temperature. Additionally, the silicide are precipitated in the form of $(Ti,Zr)_xSi_y$ ternary compounds, making it challenging to determine the β transformation temperature and silicide dissolution temperature based on binary phase diagrams for compositional design. To estimate the phase transformation temperature and silicide dissolution temperature, JMatPro software was utilized in this study to calculate the phase composition of the material. Based on the chemical composition of TA15 (Ti-6.5Al-1Mo-1V-2Zr, in weight percent), the phase compositions of the matrix under different temperatures with varying Si and Zr element contents were calculated. The material compositions used for calculations and their denotations are listed in Table 4.1, the calculation was carried out assuming there are only α-Ti, β-Ti, and $(Ti,Zr)_xSi_y$ silicide in TA15 alloy matrix.

Table 4.1 The compositions for phase calculations in JMatPro

Denotation	Composition / wt.%
Si0.3Zr2.0	6.5Al-1Mo-1V-2Zr-0.3Si-Balanced Ti
Si0.3Zr3.0	6.5Al-1Mo-1V-3Zr-0.3Si-Balanced Ti
Si0.3Zr4.0	6.5Al-1Mo-1V-4Zr-0.3Si-Balanced Ti
Si0.6Zr2.0	6.5Al-1Mo-1V-2Zr-0.6Si-Balanced Ti
Si1.0Zr2.0	6.5Al-1Mo-1V-2Zr-1Si-Balanced Ti

The phase compositions of matrix with different Si and Zr contents are shown in Fig. 4.1. It can be observed in Fig. 4.1 (a)-(e) that at high temperatures, the TA15(Si) matrix consists solely of β phase, the α phase and silicide appear as the temperature decreases. During the cooling process, the weight fraction of α phase increases rapidly and the weight fraction of silicide increases slowly near the β transformation temperature. Upon reaching 800 °C, the content of each phase no longer significantly changes, with the mass fraction of silicide being significantly influenced by the Si content and less affected by the Zr content. As shown in Fig.

4.1 (f), the addition of Si element slightly increases the β transformation temperature and significantly raises the dissolution temperature of the silicide. When the content of Si exceeds 0.6 wt.%, the silicide can only dissolve above the β transformation temperature. The addition of Zr element slightly decreases the β transformation temperature of the matrix while moderately increasing the dissolution temperature of the silicide. The increase in silicide dissolution temperature indicates that Zr element contributes to the high-temperature stability of the silicide. When the content of Zr exceeds 3 wt.%, the dissolution temperature of the silicide surpasses the β transformation temperature of the matrix.

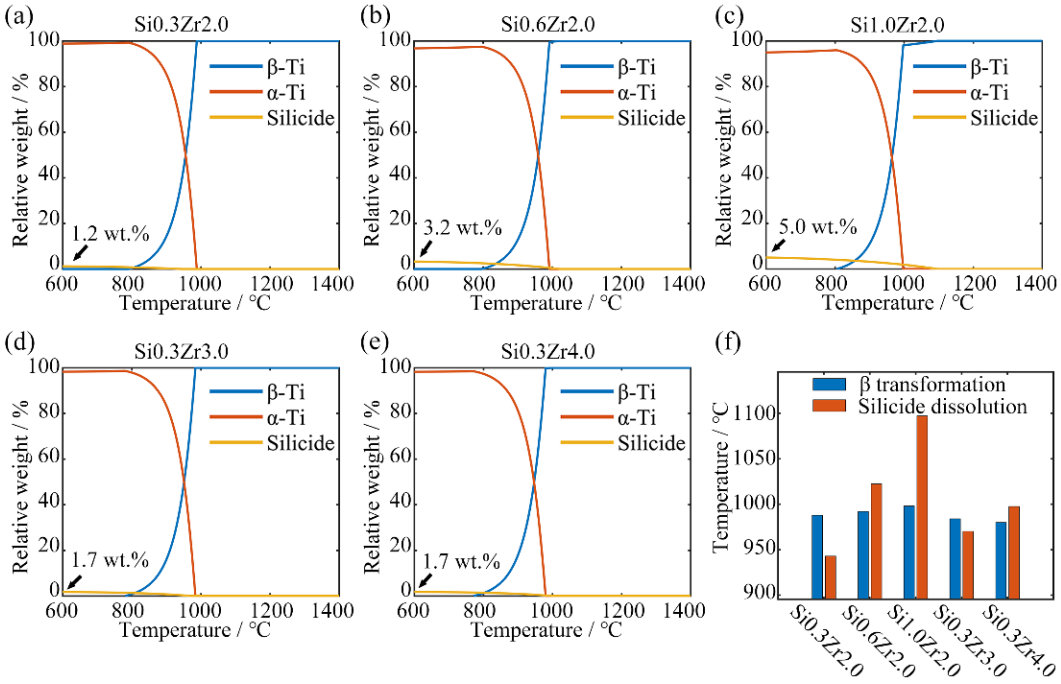

Fig. 4.1 Phase fraction of TiBw/TA15(Si) with the change of element composition, (a)-(e) phase compositions of composites at different temperatures with varying chemical compositions, (f) β transformation temperatures and silicide dissolution temperatures of composites with different chemical compositions

The calculation results indicate that a Si content below 0.3 wt.% and Zr content below 3 wt.% yields silicide dissolution temperatures that lower than β transformation temperature of the matrix. Increasing the Si or Zr content in the matrix raises the dissolution temperature of the silicide relative to the β transformation temperature. Since the presence of interstitial elements such as O and N can increase the β transformation temperature thereby reducing the silicide dissolution temperature relative to the phase transformation, the contents of Si and Zr in composites for composition optimization is determined to be ~0.5 wt.% and

~3 wt.%, respectively. The compositions and denotations of the TiBw/TA15(Si) composites for experimental composition optimization are listed in Table 4.2.

Table 4.2 The compositions and denotations of prepared composites

Denotation	Matrix composition / wt.%	TiBw fraction / vol.%
Si0.3Zr2.3	6.5Al-1Mo-1V-2.3Zr-0.3Si-Balanced Ti	3.4
Si0.3Zr3.0	6.5Al-1Mo-1V-3Zr-0.3Si-Balanced Ti	
Si0.3Zr4.0	6.5Al-1Mo-1V-4Zr-0.3Si-Balanced Ti	
Si0.5Zr2.3	6.5Al-1Mo-1V-2.3Zr-0.5Si-Balanced Ti	
Si0.5Zr3.0	6.5Al-1Mo-1V-3Zr-0.5Si-Balanced Ti	
Si0.5Zr3.6	6.5Al-1Mo-1V-3.6Zr-0.5Si-Balanced Ti	
Si0.75Zr3.6	6.5Al-1Mo-1V-3.6Zr-0.75Si-Balanced Ti	
Si1.0Zr2.3	6.5Al-1Mo-1V-2.3Zr-1Si-Balanced Ti	

4.2.2 Sintering procedure design and materials preparation of TiBw/TA15(Si) composites

Powder metallurgy was employed to prepare the TiBw/TA15(Si) composites with network architecture. Spherical TA15 pre-alloyed powder was used as the matrix, and TiB_2 and ZrB_2 powders were adopted as the reactants to form in-situ TiBw reinforcements. The contents of Si and ZrB_2 powders were adjusted to control the content of Si and Zr in the matrix. The raw powders were mixed through low-energy ball milling, and the morphologies of the powders before and after mixing, as well as the low-energy ball milling process, are shown in Fig. 4.2. As shown in Fig. 4.2 (a), the TA15 particles exhibit a spherical shape with a diameter of approximately 100 μm and a smooth surface, while TiB_2, ZrB_2, and Si powders are amorphous particles with diameters ranging from 1 μm to 5 μm. Fig. 4.2 (b) shows that the shape of TA15 powder remains unchanged after ball milling. Ceramic powders are uniformly attached to the surface of TA15 particles, with only a few ceramic powders scattered around. In the high magnification image shown in Fig. 4.2 (c), the surface of TA15 particles after ball milling appears rough, onto which the ceramic powders are tightly embedded.

The sintering process of the composites is schematically shown in Fig. 4.3. The powder mixture was first heated to the desired temperature, since β-Ti has better deformability and diffusivity than α-Ti, the consolidation temperature for TMCs is usually above β transformation temperature. During heating, TiBw reinforcements

are generated via in-situ reactions as follows:

$$TiB_2+Ti=2TiB \quad (4\text{-}1)$$

$$ZrB_2+2Ti=2TiB+Zr \quad (4\text{-}2)$$

Thermodynamic calculations show that above reactions have negative Gibbs free energies above 600 °C, indicating the spontaneous occurrence during the sintering process. Liberated Zr produced by Eq. 4-2 will dissolve into the titanium alloy matrix and diffuse inward from the surface to the core of TA15 particle, together with dissolved Si.

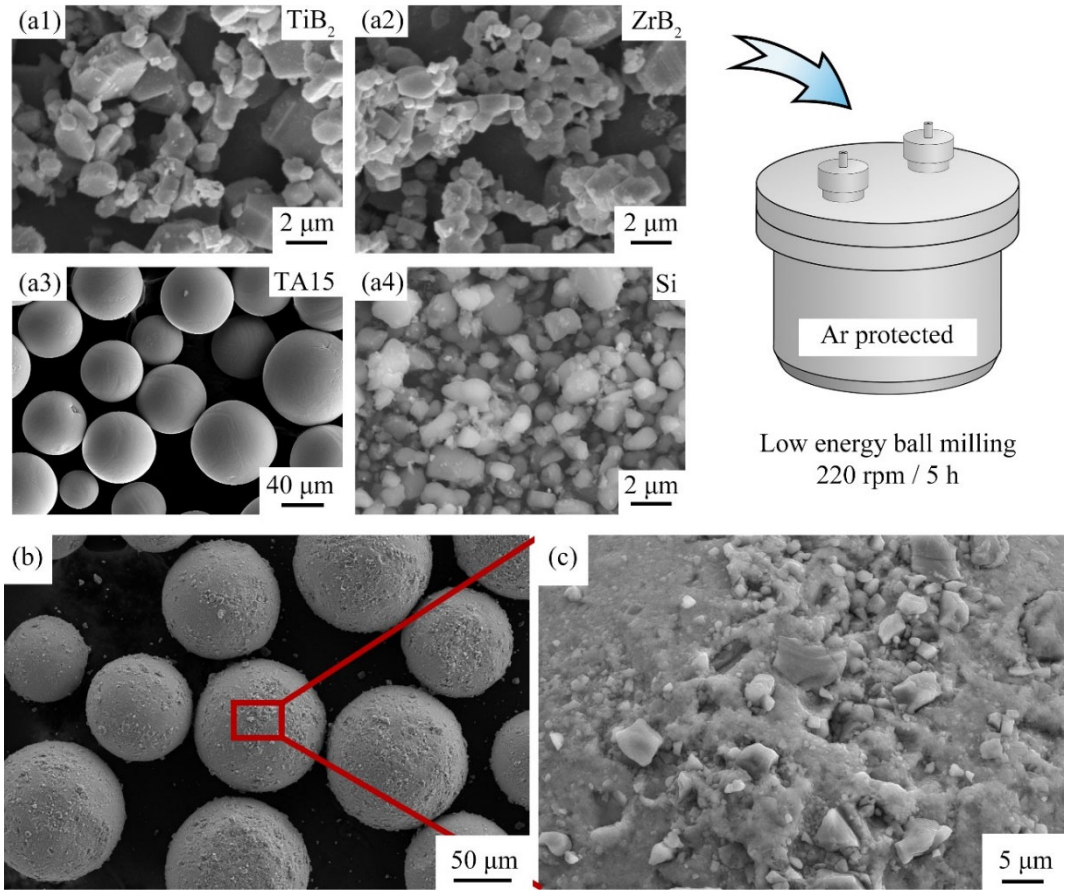

Fig. 4.2 Preparation method and morphologies of powder mixture by low-energy ball milling, (a) raw materials and ball milling process, (b) mixture powders in low magnification, (c) surface morphology of the mixed powder

Upon reaching the specified temperature, the composites were compacted by applying pressure using a hydraulic press, as shown in Fig. 4.3 (c). During the densification process, the spherical TA15 powders came into contact with each other, forming polygonal interfaces. The TiBw reinforcements generated by in-situ

reaction were distributed on these contact interfaces, forming network structures. During the holding stage, TiBw reinforcements in the composites grew under the Ostwald ripening, while the β grains continue to grow until constrained by TiBw reinforcements distributed in network manner. Therefore, the size of the β grains in the network structured TiBw/TA15(Si) composites was determined by the size of the TA15 powders. After the holding stage, the composites were cooled to room temperature in the furnace, as shown in Fig. 4.3 (d). When the composites were cooled below the β transformation temperature, lamellar α precipitated within the β phase following the BOR, forming laminated microstructure. Additionally, when the material were cooled below the silicide dissolution temperature, silicide particles also precipitated within the matrix.

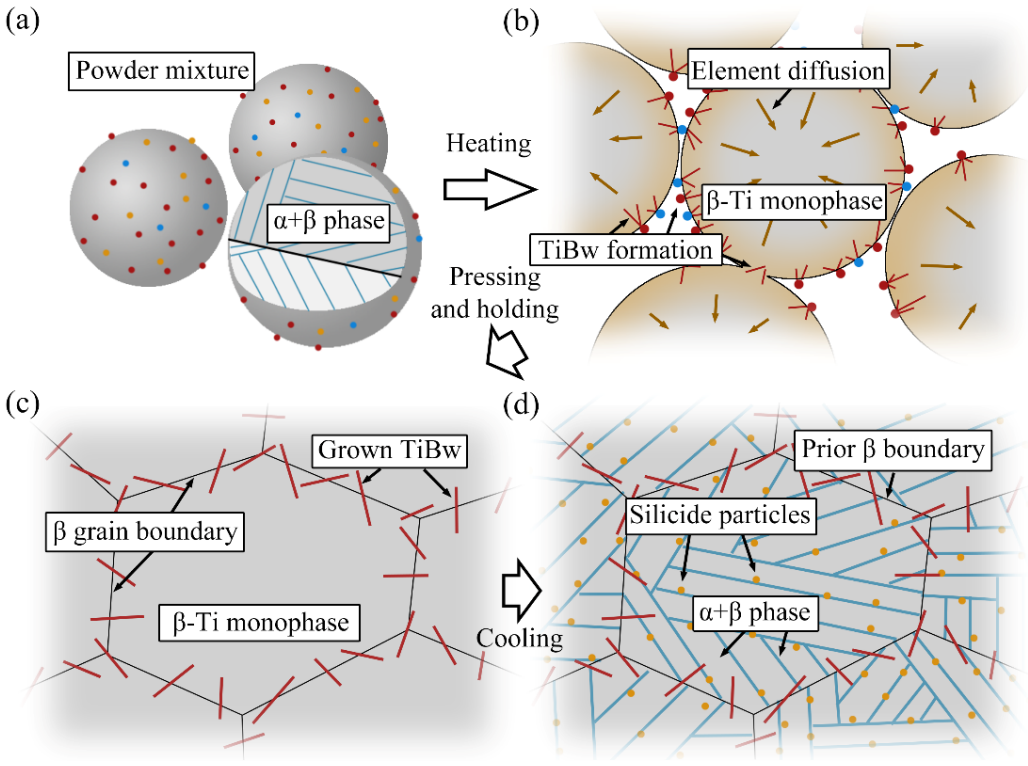

Fig. 4.3 Schematic diagrams of the consolidation process of TiBw/TA15(Si) composites
(a) powder mixture，(b) in-situ reaction and element diffusion after heating, (c) densification after applying load, (d) formation of room-temperature microstructure after cooling

The target of composites sintering is not only achieving full densification, but also ensuring the uniform diffusion of alloying elements within the matrix. To this end, Fick's second law is used to estimate the diffusion process of externally added Si and liberated Zr from the surface to the core of the TA15 powder after ball milling:

$$\frac{\partial \phi}{\partial t} = D\frac{\partial^2 \phi}{\partial x^2} \tag{4-3}$$

In which φ is the concentration of the diffusion element, t is the diffusion period, x is the diffusion distance, and D is the diffusion coefficient. Approximating the process with 1-dimensional diffusion and solve Eq. 4-3, the relationship between the concentration of diffusion element with the of diffusion period and diffusion distance can be obtained:

$$\phi(x,t) = (\phi_1 - \phi_0)\left(1 - \mathrm{erf}\left(\frac{x}{2\sqrt{Dt}}\right)\right) + \phi_0 \tag{4-4}$$

In which φ_1 is the concentration of the element at equilibrium, φ_0 is the initial concentration of the diffusion element, x is the distance to the diffusion source, and t is the time passed since the diffusion begins. The diffusion coefficient of an element in β phase can be calculated with the equation proposed by Kohler and Herzig [124]:

$$D = D_0 \exp\left(-\frac{Q}{RT}\right)\exp\left(\Omega\frac{{T_M}^2}{T^2}\right) \tag{4-5}$$

In which D is the diffusion coefficient, D_0 is the frequency coefficient that determined by diffusion element, Q is the activation energy determined by diffusion element, and R is the ideal gas constant, which is 8.314 J/(mol·K), T_M is the melting point of titanium, which is 1941 K, T is the temperature for diffusion, Ω is a constant determine by the diffusion element.

For the diffusion of Zr and Si elements in β-Ti, the values of D_0, Q, and Ω are 1.59×10^{-4}, 316 kJ/mol, 4.34[125] and 4.22×10^{-5}, 259 kJ/mol, 2.52[126], respectively. Taking the average radius of TA15 powder, 50 μm, as the diffusion distance, the diffusion of elements at different temperatures and sintering times can be calculated using Eqs. 3-4 and 3-5. The diffusion degree of an element can be evaluated by comparing the change in concentration at the core of TA15 particle, φ-φ_0, with the difference between the equilibrium concentration and the initial concentration, φ_1-φ_0. The relationship between the diffusion degree of Zr and Si

with sintering time and temperature is shown in Fig. 4.4.

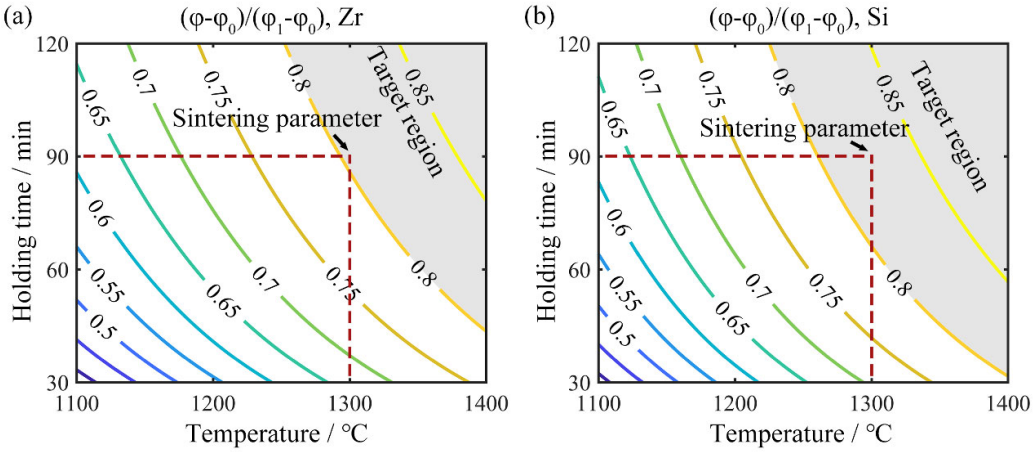

Fig. 4.4 The diffusion degree of different elements in TA15 powder during consolidation, (a) Zr element, (b) Si element

From Fig. 4.4, it can be observed that lower sintering temperatures require longer holding times for the center of powder to reach the same diffusion degree. Due to the higher diffusion coefficient, Si requires a shorter time and lower temperature than Zr to achieve the same diffusion degree. Since the diffusion of Zr is slower than Si, the sintering process should be designed based on the diffusion degree of Zr. Consider the diffusion degree of 0.8 as a sufficient diffusion, it requires a holding time of 120 minutes at 1250 °C, 90 minutes at 1300 °C, or 45 minutes at 1400 °C to achieve the sufficient diffusion of Zr. Taking the equipment capabilities and time costs into account, the sintering temperature is determined to be 1300 °C and the holding time is determined to be 90 min.

The microstructure and elemental distribution of the as-sintered composites under BSE contrast are shown in Fig. 4.5. In BSE contrast, elements with higher atomic numbers appear brighter. The TiBw reinforcements, enriched with B, exhibit a dark contrast, while α-Ti appears as a darker gray contrast. β-Ti is enriched with elements with high atomic numbers such as Mo and V, is in a light-gray contrast. The silicide particles, enriched with Zr, exhibit the brightest contrast. The low-magnification micrograph of the composite is shown in Fig. 4.5 (a), revealing the short rod-shaped morphology of the TiBw reinforcements that distributed in a network manner. The TA15 matrix consists of α-Ti lamellae and β-Ti, with the lamellar width of approximately 10 μm. No continuous grain boundary α phase was formed in the

matrix due to the presence of TiBw.

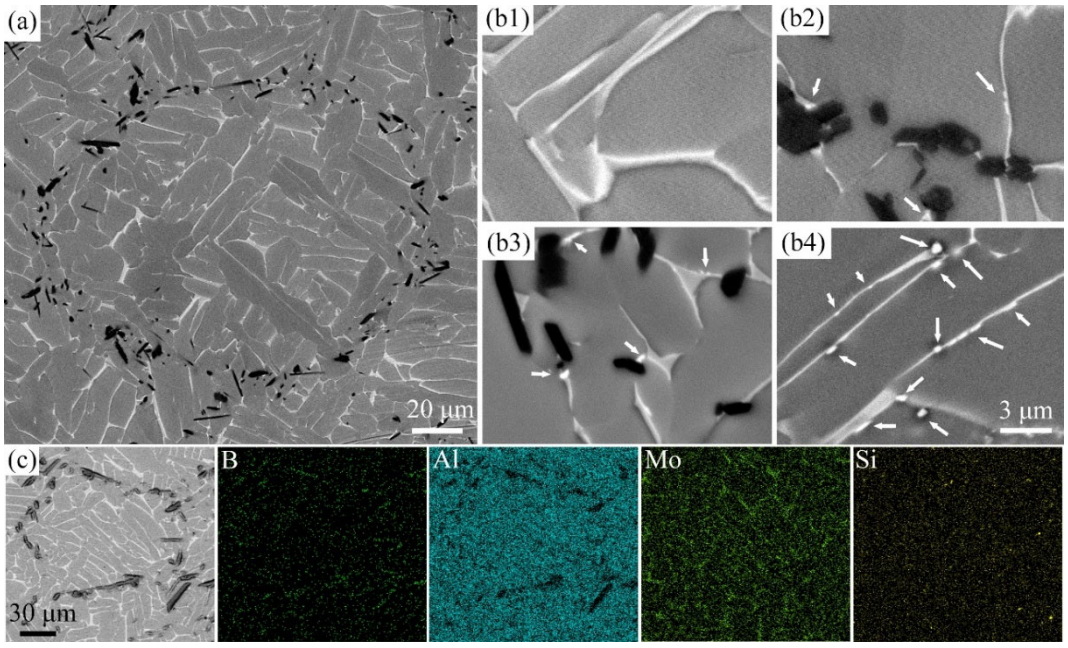

Fig. 4.5 Microstructures and element distributions of as-sintered TiBw/TA15(Si) composites, (a) Microstructure of as-sintered TiBw/TA15(Si) composites at low magnification, (b) precipitation of silicide in composites with different compositions: (b1) Si0.3Zr2.3, (b2) Si0.3Zr3.0, (b3) Si0.3Zr4.0, (b4) Si1.0Zr2.3, (c) element distribution in the as-sintered composite

The distribution of silicide particles in the matrix is shown in Fig. 4.5 (b). Silicide particles are likely to precipitate at the α/β phase boundaries and around the TiBw reinforcements, with the sizes of hundreds of nanometers. The quantity of precipitated silicide varies with the chemical compositions of composites. In the Si0.3Zr2.3 composite shown in Fig. 4.5 (b1), silicide particles can hardly be observed. However, as the Zr content increases, the amount of silicide precipitations gradually increases, as seen in Si0.3Zr3.0 and Si0.3Zr4.0 in Fig. 4.5 (b2) and (b3), respectively. Keeping the Zr content constant, increasing the Si content significantly raise the amount of silicide precipitation, as shown in Fig. 4.5 (b4). Comparing with Fig. 4.1, it is evident that the variation in the amount of silicide precipitations with the chemical compositions of composites is consistent with the calculated results. Fig. 4.5 (c) depicts the elemental distribution in the material, demonstrating that B is mainly distributed in the TiBw reinforcements, Al is primarily present in the α phase, Mo is enriched in the β phase, and Si is dispersively distributed throughout the material.

To further analyze the morphology, distribution, and crystal structure of silicide

particles in the composites, TEM was employed for characterization, and the results are presented in Fig. 4.6. Observing Fig. 4.6 (a) and (d), silicide particles are predominantly distributed around α/β interfaces, with sizes ranging from tens of nanometers to several micrometers. Due to the significantly higher solubility of Si in β-Ti compared to α-Ti, Si tend to enrich in the β phase while cooling after sintering. As the α phase grows, the concentration of Si in β-Ti gradually increases, eventually reaching the solid solubility limit and resulting in the observed distribution of silicide particles surrounding or within β-Ti.

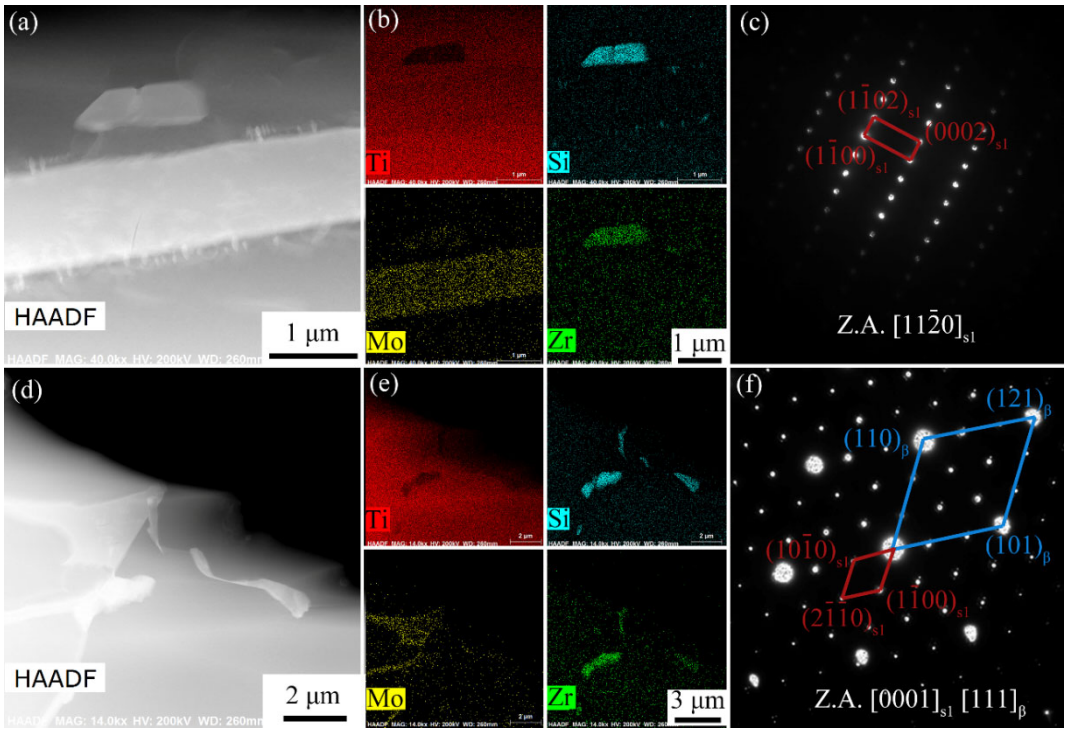

Fig. 4.6 TEM micrographs of silicide particles in as-sintered TiBw/TA15(Si) composites
(a), (d) High-Angle Annular Dark Field (HAADF) imaging, (b), (e) element distribution in silicide particles, (c), (f) Selected Area Electron Diffraction (SAED) patterns of silicide particles

In Fig. 4.6 (b) and (e), the enrichment of Si and Zr within the silicide suggests the precipitation of a ternary $(Ti,Zr)_xSi_y$. Previous studies on zirconium-containing titanium alloys have identified two main types of precipitated silicides, namely $(Ti,Zr)_5Si_3$ and $(Ti,Zr)_6Si_3$, referred to as s1 type and s2 type silicides, respectively [127]. Both types of silicides belong to the hexagonal crystal structure but exhibit different lattice parameters. The lattice parameters for s1 type silicide are a=b=0.78 nm and c=0.54 nm, while for s2 type silicide, the lattice parameters are a=b=0.70 nm and c=0.37 nm [127]. Differentiating between these two types of silicides can

be achieved through SAED patterns, as shown in Fig. 4.6 (c) and (f). Based on the interplanar spacings, the observed silicide particles in Fig. 4.6 are identified as s1 type. The silicide particle in Fig. 4.6 (d) exhibits an orientation relationship of $[0001]_{s1} \parallel [111]_{\beta}$ and $(1\text{-}100)_{s1} \parallel (110)_{\beta}$ with β-Ti, while those in Fig. 4.6 (a) show no significant orientation relationship with the surrounding matrix, which may be attributed to lattice structure or crystal orientation changes during the growth.

4.3 Room temperature tensile tests of TiBw/TA15(Si) composites

The room temperature mechanical properties of TiBw/TA15(Si) composites were evaluated using tensile testing, and the macroscopic morphology of the tested specimens and typical stress-strain curves are shown in Fig. 4.7. As observed in Fig. 4.7 (a), the tensile specimens of TiBw/TA15(Si) with different compositions exhibit normal fracture without significant necking, indicating a same macroscopic fracture mode. Fig. 4.7 (b) demonstrates that the stress-strain curves of TiBw/TA15(Si) composites with different compositions exhibit similar features, transitioning from the linear elastic stage to the plastic deformation stage without distinct yield. The ultimate tensile strength and elongation of the composites with different compositions are presented in Table 4.3 and Table 4.4, respectively.

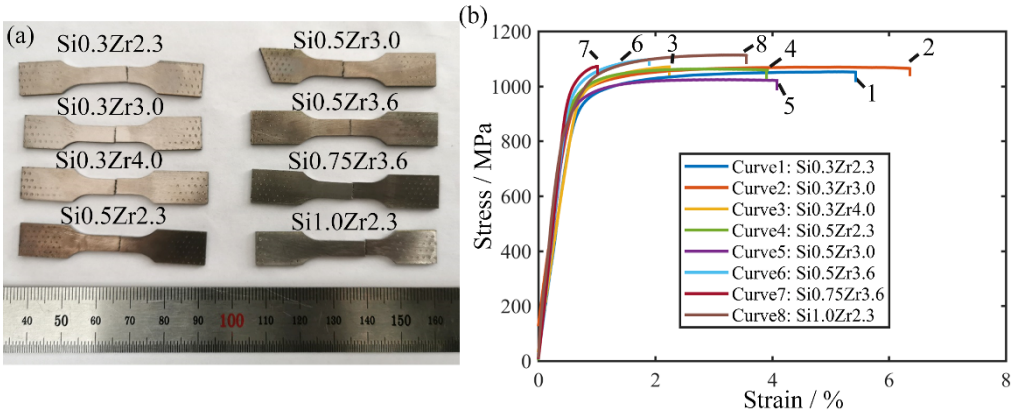

Fig. 4.7 Fractured tensile samples and typical tensile stress-strain curves of TiBw/TA15(Si) (a) macroscopic morphologies of fractured specimens with different compositions, (b) typical stress-strain curves of composites with different compositions

As shown in the table, increasing the Si content and Zr content both enhance the tensile strength of the material while reducing its elongation, demonstrating a typical strength-ductility trade-off. When the additions of Zr and Si elements are below 3 wt.% and 0.5 wt.% respectively, their influence on the material's strength

and ductility is relatively small, with the tensile strength keep around 1050 MPa and the elongation keeps around 5%. The strength of the material slightly increases with an increase in Zr content in the matrix. However, when the Zr content exceeds 3 wt.%, the elongation significantly decreases to below 2%, indicating pronounced brittleness. The addition of Si elements effectively improves the material's strength with relatively minor loss in ductility. When the Si content reaches 1 wt.%, the tensile strength can exceed 1100 MPa. Four composites, namely Si0.3Zr2.3, Si0.3Zr3.0, Si0.5Zr2.3, and Si1.0Zr2.3, exhibit good comprehensive room temperature mechanical properties.

Table 4.3 Tensile strengths of TiBw/TA15(Si) with different Zr and Si contents

Zr content / wt.%	2.3	3.0	3.6	4
Si content / wt.%	Tensile strength / MPa			
0.3	1049±23	1060±25	—	1086±40
0.5	1054±21	1012±17	1076±34	—
0.75	—	—	1091±37	—
1.0	1120±26	—	—	—

Table 4.4 Tensile elongations of TiBw/TA15(Si) with different Zr and Si contents

Zr content / wt.%	2.3	3.0	3.6	4
Si content / wt.%	Elongation / %			
0.3	5.7±1.3	6.7±2.1	—	1.5±0.3
0.5	6.6±2.4	3.9±0.5	1.7±0.4	—
0.75	—	—	1.2±0.3	—
1.0	3.1±1.2	—	—	—

The tensile fracture surfaces of TiBw/TA15(Si) composites with different compositions were observed using SEM, and the results are shown in Fig. 4.8. Low-magnification micrographs of the fracture surfaces of Si0.3Zr3.0 and Si0.75Zr3.6 are presented in Fig. 4.8 (a) and (b) respectively. Despite significant differences in elongation between the two materials, both fracture surfaces exhibit rough, granular morphologies, indicating that the fracture mode of TiBw/TA15(Si) composites is not significantly influenced by the chemical compositions and mechanical properties, which is consistent with the observations in Fig. 4.7 (a). The size of the granular structure at the fracture surface is approximately 100 μm, which is consistent with the size of the TiBw networks. Higher magnification morphology

of the fracture surface is shown in Fig. 4.8 (c), revealing a large number of TiBw reinforcements and tearing edges formed by the TA15 matrix near the reinforcements, indicating a microscopic ductile fracture. Fig. 4.8 (d) displays a low-magnification side view of the fractured tensile sample of TiBw/TA15(Si) composite, revealing that the primary crack propagates along the TiBw network, with several secondary crack branches observed around the primary crack. Fig. 4.8 (e) provides a high-magnification micrograph near the main crack, showing numerous cracks within the TiBw reinforcements. These cracks can propagate along the long axis of the TiBw, causing the reinforcement to split, or perpendicular to the long axis of the TiBw, resulting in fracture of the reinforcements.

Based on the crack propagation in the as-sintered TiBw/TA15(Si) composites, it can be concluded that the matrix composition does not significantly affect the crack initiation and propagation. During tensile loading, stress concentration occurs within the reinforcements due to their higher elastic modulus compared to the matrix. Additionally, the strain mismatch between the reinforcements and the matrix caused by the plastic deformation of the matrix further intensifies it. TiBw reinforcements fracture when the stress within the reinforcements exceeds their strength, releasing stress and accommodating strain. Since the (100) planes of TiBw reinforcements have the closest packing and the largest interplanar spacing (0.612 nm), cracks are prone to initiate and propagate along the (100) planes, which is corresponding to the long axis of the reinforcements. Besides, the TiBw reinforcements mainly experience normal stress along their long axis, which may lead to fracture perpendicular to the long axis.

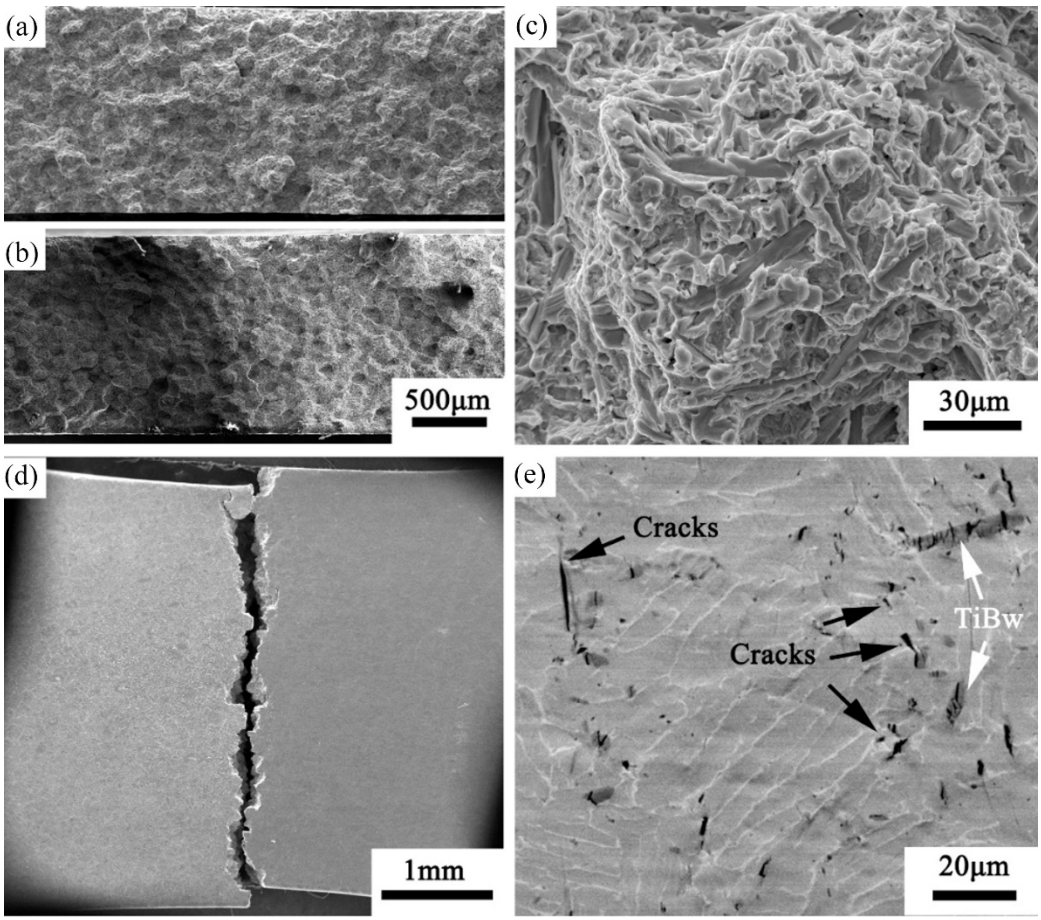

Fig. 4.8 SEM micrographs of fracture surfaces and side-faces of TiBwTA15(Si) composites, (a), (b) Si0.5Zr2.3 and Si0.3Zr3 fracture surfaces in low magnifications, (c) Si0.5Zr2.3 fracture surface in high magnification, (d) Si0.5Zr2.3 fracture side face in low magnification, (e) Si0.5Zr2.3 fracture side face in high magnification

Once initiated, cracks in the reinforcements propagates by connecting with each other. Due to the difficulty of crack propagation through the ductile TA15 matrix, the cracks primarily extend along the network distributed TiBw reinforcements, which effectively prolongs the crack propagation path. Additionally, since the TiBw reinforcements are not interconnected, the cracks must also traverse the ductile TA15 matrix in order to connect, resulting in the formation of tearing edges observed in Fig. 4.8 (c). The longer crack propagation path and the plastic tearing of the matrix significantly increase the energy absorption during the fracture, endowing the composites with good ductility.

4.4 Microstructure evolution of TiBw/TA15(Si) at high temperatures

In order make the composites suitable for microstructure regulations in the dual-phase region and prevent the elimination of hot deformation microstructures in this

process, it is necessary to keep the dissolution temperature of silicide below the β transformation temperature. To determine the dissolution temperatures of silicides in composites with different compositions, the composites were quenched after being held at different temperatures for 30 minutes, and the resultant microstructures were observed. Fig. 4.9 shows the quenched microstructures of composites with different Si content when the Zr content is 2.3 wt.%.

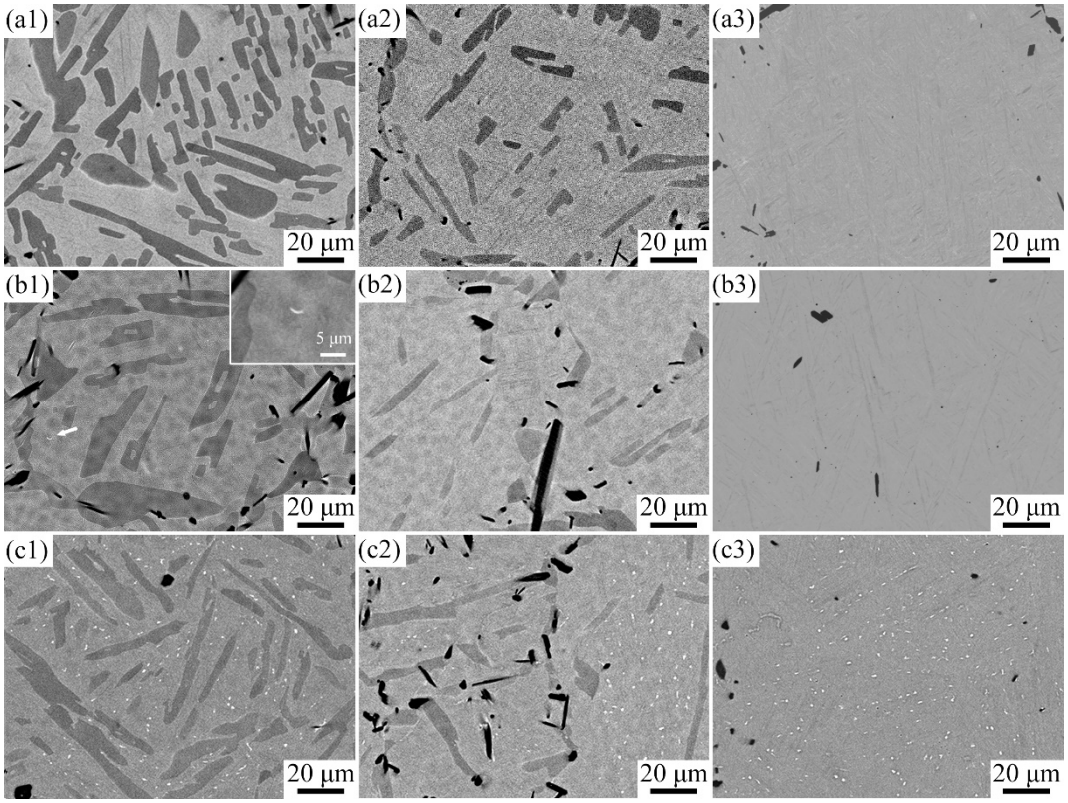

Fig. 4.9 TiBw/TA15(Si) with different Si contents after quenched from temperatures (a) Si0.3Zr2.3, (b) Si0.5Zr2.3, (c) Si1.0Zr2.3, subfigures 1 – 3 are obtained at 980 °C，1020 °C and 1040 °C, respectively

It can be observed from Fig. 4.9 that the microstructures of the TiBw/TA15(Si) composites underwent significant changes after holding and quenching. At high temperature, α phase dissolved and the volume fractions decreased, while the proportion of β phase significantly increased, which then formed transformed β phase (β_T) upon quenching. As the holding temperature increased, the proportion of the α phase in the matrix gradually decreased, while the proportion of β_T increased. The variations in the proportion of β_T with material compositions and holding temperatures, obtained through digital image analysis, are shown in Table 4.5. It is evident that the β transformation temperature of the material is between 1020 °C and 1040 °C, which is higher than the calculated result in Fig. 4.1. With an increase

in Si content, the proportion of β_T in the material at the same temperature slightly increased but remained at a similar level.

Table 4.5 Volume fraction of β_T in composites with different Si contents

Denotations	Holding temperature / °C		
	980	1020	1040
Si0.3Zr2,3	65.4%	83.3%	100%
Si0.5Zr2.3	67.3%	86.0%	100%
Si1.0Zr2.3	70.1%	86.3%	100%

After a 30-minute holding at 980 °C, the silicide in the Si0.3Zr2.3 composite completely dissolved, while residual silicide particles were still present in Si0.5Zr2.3 and Si1.0Zr2.3. Only a small amount of residual silicide particles was observed in Si0.5Zr2.3, whereas a significant amount of silicide residue remained in Si1.0Zr2.3. After a 30-minute holding at 1000 °C, the remaining silicide particles in Si0.5Zr2.3 also dissolved completely, but those in Si1.0Zr2.3 did not significantly dissolve. It can be concluded from Fig. 4.9 that the dissolution temperatures of silicides in the TiBw/TA15(Si) composites increase with an increased Si content. When the Zr content is 2.3 wt.%, keeping the Si content below 0.5 wt.% allows complete dissolution of silicide at the dual-phase region. The microstructures of composites with 0.3 wt.% Si content and different Zr contents after holding at different temperatures and quenching is shown in Fig. 4.10.

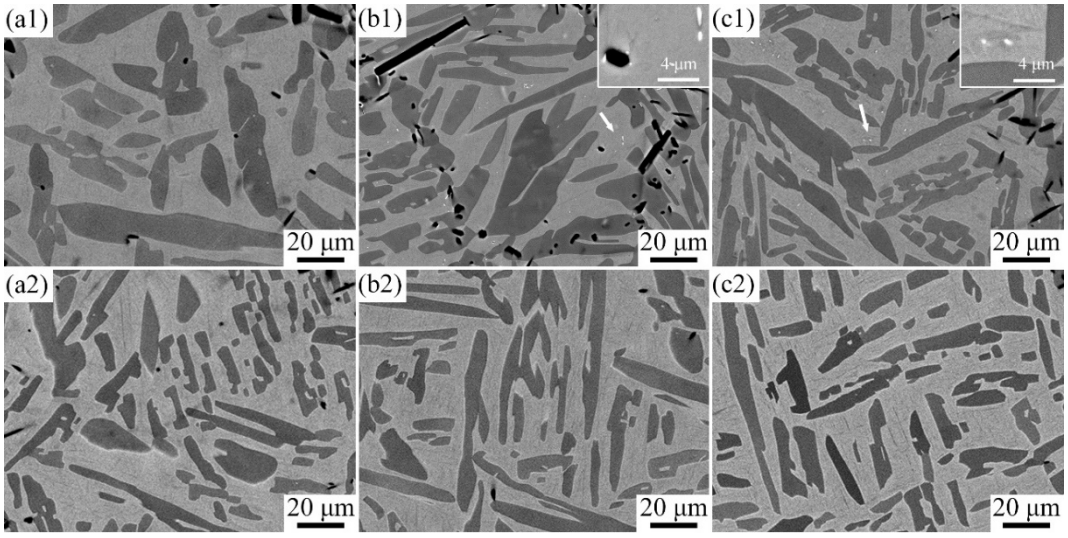

Fig. 4.10 TiBw/TA15(Si) with different Zr contents after quenched from temperatures,
(a) Si0.3Zr2.3, (b) Si0.3Zr3.0, (c) Si0.3Zr4.0, subfigures 1 and 2 are 960 °C and

980 °C, respectively

According to the digital image analysis of the microstructures shown in Fig. 4.10, the proportion of β_T remains approximately 48% for materials with different Zr contents at 960 °C and around 55% at 980 °C, showing no significant variation. At 960 °C, the silicide particles were completely dissolved in the Si0.3Zr2.3, while residual silicides were still present in Si0.3Zr3.0 and Si0.3Zr4.0 composites, with slightly higher silicide content in Si0.3Zr4.0 compared to Si0.3Zr3.0, confirming the stabilizing effect of Zr on silicide. When the holding temperature increased to 980 °C, the silicides in all three materials were completely dissolved, indicating that materials with Si content of 0.3 wt.% and Zr content of 4 wt.% or below can achieve complete silicide dissolution in the dual-phase region. Considering both the room temperature mechanical properties and the dissolution temperature of silicide, the Si0.3Zr3.0 composite is chosen for subsequent experiments.

4.5 Summary

This chapter presents the design of TiBw/TA15(Si) composites suitable for thermo-mechanical processing and heat treatment in the dual-phase region, based on thermodynamic calculations and diffusion models. Composites with different compositions were prepared, and their tensile properties at room temperature and microstructures at high temperatures were investigated for material selection. The substantial results are summarized below:

(1) Thermodynamic calculations indicate that the β transformation temperature of the TiBw/TA15(Si) composites is approximately 980 °C. It increases with an increased Si content and decreased Zr content. The silicide dissolution temperature rapidly increases with an increased Si content and slightly increases with an increased Zr content. When the Si content is below 0.3 wt.% and the Zr content is below 3 wt.%, the silicide in the material can completely dissolve below the β transformation temperature. Based on this, TiBw/TA15(Si) composites with different compositions are designed for optimization. Estimated using Fick's second law, the sintering temperature was determined to be 1300 °C and the holding period was determined to be 90 min.

(2) TiBw/TA15(Si) composites with different compositions were prepared using

low-energy ball milling and hot-press sintering. Microscopic analysis revealed a defect-free microstructure, with TiBw reinforcements distributed in a network manner with a grid size of approximately 100 μm. Silicide particles primarily precipitated along the α/βinterfaces, and the precipitation quantity increased with the Si and Zr content. TEM analysis showed that the silicides were ternary $(Ti,Zr)_xSi_y$, with s1 type $(Ti,Zr)_5Si_3$ being predominate. The silicides exhibited an orientation relationship of $[0001]_{s1} \parallel [111]_\beta$ and $(1\text{-}101)_{s1} \parallel (110)_\beta$ with the β phase in the matrix.

(3) The room temperature tensile properties of TiBw/TA15(Si) composites with different compositions were tested, showing strengths ranging from 1020 MPa to 1100 MPa and elongations ranging from 1.5% to 6.7%. The addition of Si and Zr elements increased the strength of the materials but decreased the elongation. When the Si content was below 1.0 wt.% and the Zr content was below 3 wt.%, the materials exhibited good room temperature strength and ductility. The fracture mode of different TiBw/TA15(Si) composites was identical, with cracks initiating and propagating within the network distributed TiBw reinforcements, leading to an interconnection and fracture.

(4) The β transformation temperature of TiBw/TA15(Si) composites is between 1020 °C and 1040 °C. The solid-solution temperature of silicide particles increased significantly with increased Si content and increased slightly with an increased Zr content. Silicide particles can dissolve completely below the β transformation temperature when the Zr content is below 4 wt.% and the Si content is below 0.5 wt.%. Considering the mechanical properties and high-temperature microstructure, the composite with the composition 3.4 vol.% TiBw/Ti-6.5 wt.%Al-1 wt.%Mo-1 wt.%V-3 wt.%Zr-0.3 wt.% Si is selected for further investigation.

Chapter 5 Hot deformation constitutive equations and strain distributions of TiBw/TA15(Si) composites

5.1 Introduction

In the previous chapter, the compositions and sintering parameters for TiBw/TA15(Si) composites were designed based on thermal dynamic calculations and element diffusion. Composites with a series of chemical compositions were fabricated, and the composition was optimized to achieve good comprehensive mechanical properties and silicide that controllable by heat treatment in dual-phase region. In this chapter, the microstructure evolutions in the matrix and realignment of TiBw reinforcements during the hot deformation of TiBw/TA15(Si) composite will be investigated. To achieve a refined deformation microstructure, solid-solution treatment is applied to obtain a refined initial microstructure and dissolve the silicide particles. Subsequently, high-temperature compression tests are conducted to investigate the effects of deformation temperature, strain rate, and deformation degree on the microstructure. Afterwards, the hot deformation constitutive equation of TiBw/TA15(Si) composite is established, and a thermal processing map is constructed to optimize the thermo-mechanical processing parameters. To determine the relationship between the orientation distribution of TiBw and the deformation degree of the composite, the rotation of TiBw reinforcements during hot deformation is first analyzed. Subsequently, the influences of principal direction and principal strain of the plastic deformation to the orientation distribution of TiBw reinforcements are revealed. Finally, a method quantitatively calculate the local plastic deformation of the composites based on the orientation distribution of TiBw reinforcement is established, and error analysis is conducted using computer simulations. The method is then applied to analyze the strain distribution in hot deformed samples of TiBw/TA15(Si) composites, the validation of which is then performed by comparing the results with both the macroscopic deformation of the sample and the microscopic deformation of TiBw network structures.

5.2 Solid-solution treatment prior to hot deformation

The study by Liu et al. [100] demonstrated that the initial microstructure of TMCs

poses significant influence toward their hot deformation behaviors. By refining the initial microstructure with solid-solution treatment followed by water quenching prior to hot deformation in dual-phase region, the microstructure of TMCs can be significantly refined, resulting from the introduction of additional nucleation sites for recrystallization. Inspired by this, in the present study, solid-solution treatment is performed on TiBw/TA15 (Si) composites prior hot compression to better efficiency for grain refinement. Additionally, solid-solution treatment dissolves silicide particles, making them reprecipitate during hot deformation, which prevents the growth of silicide particles by Oswald ripening. To ensure a uniform microstructure, the solid-solution temperature is chosen above the β transformation temperature. To achieve a fine initial microstructure and low internal stresses, air cooling (AC) is adopted after heat treatment. Ultimately, the heat treatment parameter prior to the hot compression is determined as soaking at1050 °C for 30 minutes followed by AC. The material before solid-solution treatment is denoted as S-Ti (Sintered), while that after solid-solution treatment is denoted as ST-Ti (Solution-Treated).

The microstructures and element distributions of the composites before and after heat treatment are shown in Fig. 5.1, indicating a significant refinement of the microstructure after heat treatment. S-Ti exhibits coarse lamellar microstructure with an α lath width of approximately 10 μm - 15 μm. Silicide precipitations are observed at the α/β interfaces. Element mapping reveals the enrichment of Ti and Mo in the α and β phases, respectively, while Si is concentrated in the silicides. The microstructures and element distributions of ST-Ti after heat treatment are shown in Fig. 5.1 (b), demonstrating a significant refinement of the lamellar width from 10 μm to 2 μm in the matrix. Element mapping shows that although Ti and Mo elements are still enriched in the α and β phases of ST-Ti, respectively, the narrower spacing between α laths leads to a more uniform element distribution compared to S-Ti. Meanwhile, Si exhibits a uniform distribution in the ST-Ti with no silicide precipitation observed, indicating a complete solid solution. Due to the rapid cooling rate of the material, silicide do not have sufficient time to nucleate and precipitate, resulting in silicon being supersaturated in the matrix. The solid solution of Si prevents the silicides from further growth through Oswald ripening during thermal processing, which is beneficial for silicide refinement after hot deformation.

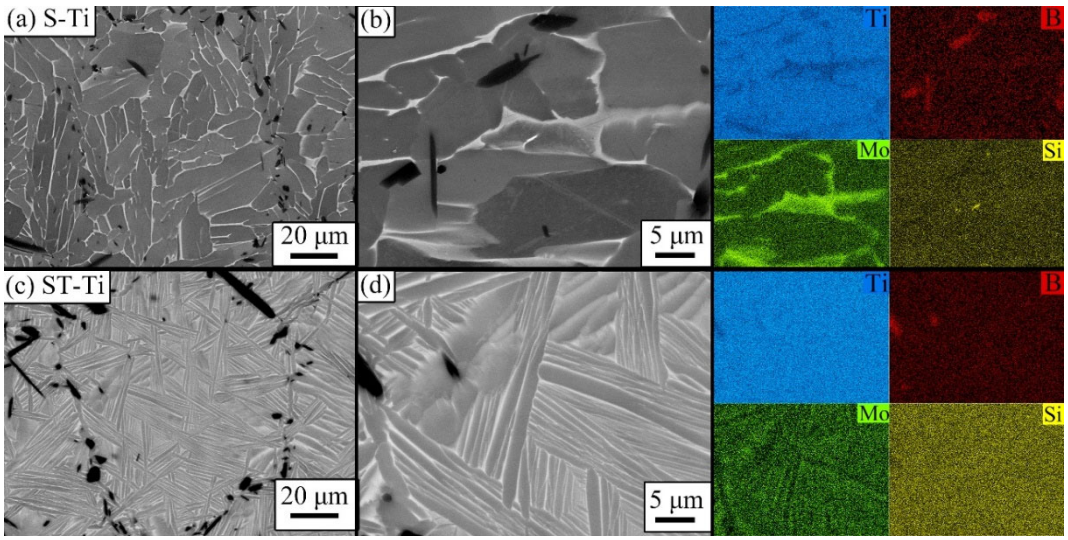

Fig. 5.1 Microstructures and element distribution maps of TiBw/TA15(Si) composites before and after solution treatment, (a), (b): S-Ti, (c), (d): ST-Ti

To investigate the grain growth during the heat treatment in the single-phase region and the orientation of TiBw reinforcements before and after heat treatment, EBSD analysis was performed, and the orientations of the original β grains were reconstructed based on the orientation of α phases using BOR. The results are shown in Fig. 5.2. From Fig. 5.2 (a), it can be observed that the α phase in S-Ti exhibits random orientation. The crystal orientation in each α lath is the same, and α laths with a same crystal orientation can form a cluster with the size of ~40 μm. Observing Fig. 5.2 (c), it can be seen that the α phase still shows random orientation after the heat treatment, but the sizes of the α laths are significantly reduced. Meanwhile, the size of clusters does not show significant changes. Based on BOR, the orientation of the original β grains in S-Ti and ST-Ti was reconstructed, which exhibit similar morphologies, as shown in Fig. 5.2 (b) and (e). The original β grains in the matrix before and after heat treatment are both equiaxed with a diameter of approximately 100 μm, with grain boundaries consistent with the TiBw distribution of networks. This indicates that the TiBw reinforcements is capable of restricting grain boundary migration and preventing the growth of the original β grains during both the sintering and heat treatment process by pinning effect. Fig. 5.2 (c) and (f) show the distributions of the [010] directions of TiBw reinforcements in S-Ti and ST-Ti. Since the long axis of TiBw is the same as its [010] direction, Fig. 5.2 (c) and (f) also represent the geometrical orientations of TiB whiskers. It can be observed that the orientations of TiBw reinforcements in both S-Ti and ST-Ti are completely random, indicating that heat treatment does not affect the orientations

of TiBw reinforcements.

In summary, it can be observed that the 1050 °C / 30 min / AC solid-solution treatment of can significantly refine the microstructure, dissolve the silicide particles, and obtain a more uniform element distribution in the as-sintered TiBw/TA15(Si) composite. Meanwhile, the heat treatment did not change the orientation distribution of the matrix and reinforcements, and the original β grains did not undergo growth due to the constraint of TiBw reinforcements.

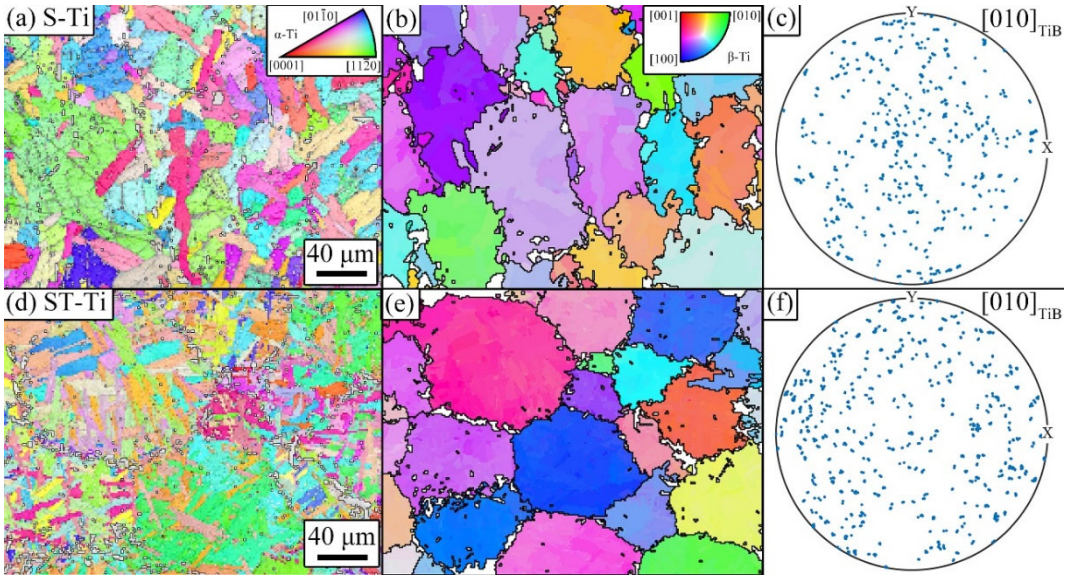

Fig. 5.2 Crystal orientations in TiBw/TA15(Si) before and after solid-solution treatment
(a) orientation map of α phase in S-Ti, (b) prior β grains reconstructed from (a), (c) orientation distribution of TiBw in S-Ti, (d) orientation map of α phase in ST-Ti, (e) prior β grains reconstructed from (d), (f) orientation distribution of TiBw in ST-Ti

5.3 Microstructure evolution during hot compression tests

High-temperature compression tests were conducted on TiBw/TA15(Si) composites after solid-solution treatment at different temperatures and strain rates to investigate the deformation behaviors in the dual-phase region and optimize the thermo-mechanical processing parameters. The hot compression tests were performed using the Gleeble 1500D thermal-physical simulation platform. The test temperatures ranged from 870 °C to 950 °C with intervals of 20 °C, and the strain rates were set at 1 s^{-1}, 0.1 s^{-1}, 0.01 s^{-1}, and 0.001 s^{-1}. The schematic diagram of the test procedure and the results are shown in Figure 4.3.

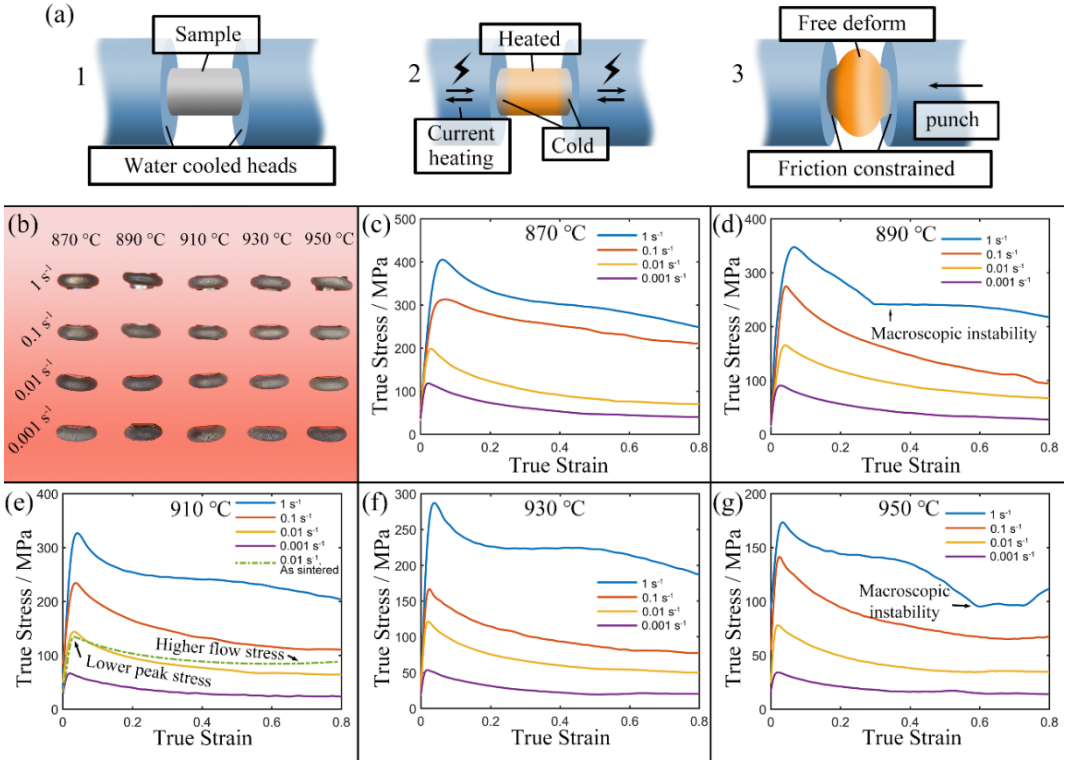

Fig. 5.3 Results of high-temperature compression tests of TiBw/TA15(Si) composites (a) schematic diagram of the hot compression procedure, (b) macroscopic morphologies of samples after hot compression, (c) – (g) true stress-true strain curves obtained at different conditions: (c) 870 °C, (d) 890 °C, (e) 910 °C, (f) 930 °C, (g) 950 °C

Fig. 5.3 (a) is the schematic diagram of the hot compression test procedure. During the test, the compression sample was clamped onto the die and subsequently heated by high-frequency current. Upon reaching the desired temperature, the specimen was soaked for a certain duration to ensure temperature uniformity and promote complete microstructural transformation. Then, the specimen was compressed to 60% height reduction (corresponding to a true strain of 0.92) at the given strain rates. After deformation, the specimen was quenched to preserve microstructure. The dies are facilitated by circulating water, causing lower temperatures at the ends of the specimen due to heat conduction, resulting in poor deformability. Additionally, the ends of the specimen were constrained by friction. The poor deformability at the ends of the sample resulted in the barrel-like morphology after compression. The macroscopic morphologies of the samples after hot compression tests are shown in Fig. 5.3 (b), indicating uniform deformation for all specimens except those tested under the conditions of 890 °C / 1 s^{-1} and 950 °C / 1 s^{-1}, which showed macroscopic instability. The hot compression true stress-true strain curves of the composites are presented in Fig. 5.3 (c)–(g), demonstrating a decrease in

stress with the increasing of deformation temperature and the decreasing of strain rate. Except for the specimens that exhibited macroscopic instability, similar features are observed in all stress-strain curves. The stress-strain curves can be roughly divided into three stages: work hardening before reaching the peak stress, flow softening after reaching the peak stress, and steady-state flow where stress no longer significantly changes with strain. Such stress-strain curves are commonly observed in metals undergoing dynamic recrystallization and are referred to as dynamic recrystallization type curves.

The high-temperature stress-strain relationship in metallic materials is the result of the competing mechanisms of strain hardening and softening. In the early stages of plastic deformation, dislocations are activated and multiply through interactions with second phases and other dislocations, leading to an increase in dislocation density and work hardening. When the dislocation density reaches a certain threshold, dynamic recrystallization is triggered, and a large number of dislocations are consumed to form defect-free grains. The softening mechanism dominates in this stage, resulting in a rapid decrease in compressive stress with strain. When the hardening due to dislocation accumulation and the softening due to dislocation consumption reach a balance, the stress-strain curve reaches the steady-state flow stage, where the stress and microstructure no longer significantly changes with strain.

To investigate the evolution of material microstructure during hot deformation, the central parts of the deformed specimens were observed using SEM. BSE imaging was utilized to qualitatively observe the substructures and recrystallization induced by plastic deformation, based on the electron channeling contrast produced in α phase. The microstructures of ST-Ti after deformation at different temperatures and a strain rate of 1 s^{-1} are shown in Fig. 5.4. It can be observed that severely deformed lamellae that perpendicular to the compression direction occurred in composites deformed at 870 °C / 1 s^{-1} and 910 °C / 1 s^{-1}. The TiBw reinforcements also rotated to the direction that perpendicular to the compression direction, in which cracks are observed. Furthermore, Fig. 5.4 (c) shows that the specimen deformed at 950 °C / 1 s^{-1} exhibited a fully laminated microstructure with randomly oriented lamellae and continuous grain boundary α phases. The original β grains in the material

appeared equiaxed with a size of approximately 40 μm, as determined by the grain boundary α phases. No cracks were observed within the TiBw reinforcements under this condition. The significant differences in the microstructure indicate the β transformation temperature was exceeded during the compression at 950 °C / 1 s^{-1}. This is attributed to the heat produced by the compression and the poor heat dissipation at high strain rates overheated the compressed sample. The overheating at 950 °C / 1 s^{-1} may also be the reasons for the macroscopic instability observed in Fig. 5.4 (a) and the bended stress-strain curve in Fig. 5.4 (g). High-magnification microstructures shown in Fig. 5.4 (d) and (e) reveal that dynamic recrystallization occurred in the composites deformed at 870 °C / 1 s^{-1} and 910 °C / 1 s^{-1}, which is consistent with the feature of the stress-strain curves. Significant electron channeling contrast was observed within the residual α laths, indicating the accumulation of dislocations and substructures. Comparing the microstructures in Fig. 5.4 (d) and (e), it can be observed that the size of recrystallized grains increased from approximately 200 nm to around 500 nm with the increase of deformation temperature. Besides, the volume fraction of recrystallized grains also increased with the increased temperature. This indicates that increasing the deformation temperature is beneficial for sufficient dynamic recrystallization at a strain rate of 1 s^{-1}.

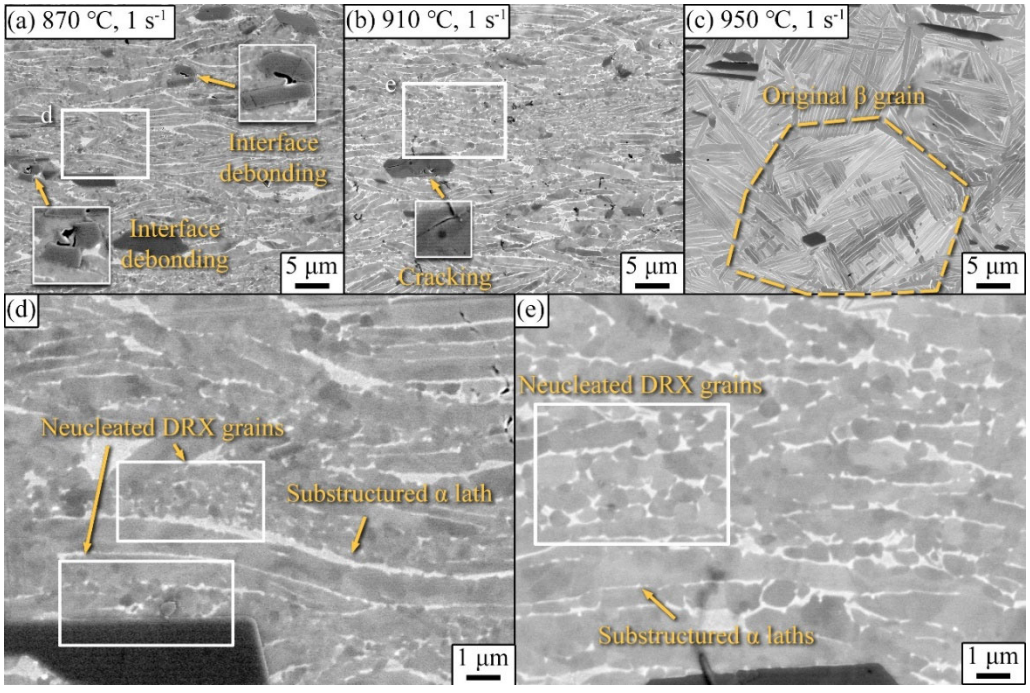

Fig. 5.4 Microstructures of ST-Ti deformed under different temperatures, at a rate of 1 s^{-1}

(a) 870 °C in low magnification, (b) 910 °C in low magnification, (c) 950 °C in low magnification, (d) 870 °C in high magnification, (e) 910 °C in high magnification

Fig. 5.5 presents the microstructures of compressed specimens after deformation at a strain rate of 0.1 s^{-1} and different temperatures. It can be observed that when the strain rate is 0.1 s^{-1}, the matrix exhibits a microstructure consisting of equiaxed recrystallized grains and residual α laths within 870 °C to 950 °C, indicating a good heat dissipation at the strain rate of 0.1 s^{-1}. Comparing Fig. 5.5 (a)-(c), it is evident that with the increasing of deformation temperature, the microstructures coarsen and the volume fraction of recrystallized grains first increases and then decreases, with a highest proportion observed at 910 °C. Additionally, in composites deformed at both 870 °C / 0.1 s^{-1} and 910 °C / 0.1 s^{-1}, fractured TiBw reinforcements are observed, while no fracture is observed in the composite deformed at 950 °C / 1 s^{-1}. Microstructures shown in Fig. 5.5 (d)-(f) reveal the precipitation of silicide particles can occur within α phase, at α/β phase interfaces, or at the interfaces between the matrix and TiBw. At 870 °C, silicide precipitates are refined but in large number, while at 910 °C, fewer but coarser silicide particles are observed. In the deformation microstructure at 950 °C / 0.1 s^{-1}, silicide particles are scarcely observed, indicating that the amount of silicide precipitation is determined by the solubility of Si and the number of precipitated silicide particles is determined by the nucleation rate at the deformation temperature.

It is noteworthy that in Fig. 5.5 (f), sudden change of electron channeling contrast is observed within the continuous residual α laths, indicating the presence of grain boundaries or subgrain boundaries. Furthermore, it is observed that the β phase tends to grow towards the boundaries in α phase. This can be attributed to two factors: firstly, the α/β interfaces and the grain boundaries within the residual α laths forms triple points with intersection angles of 90°. The growth of β phase into the boundaries within α laths helps to form intersection angles of 120° and reduce the total length the interfaces, thereby stabilize the triple points. Secondly, due to the disordered atomic arrangement near the grain boundaries, the diffusion coefficient near the grain boundaries is higher than that inside of grains, which facilitates the diffusion of β stabilizers towards the boundaries within α laths. The growth of the β phase towards the α grain boundaries leads to the spheroidization of the α laths, transforming the microstructure from laminated to equiaxed.

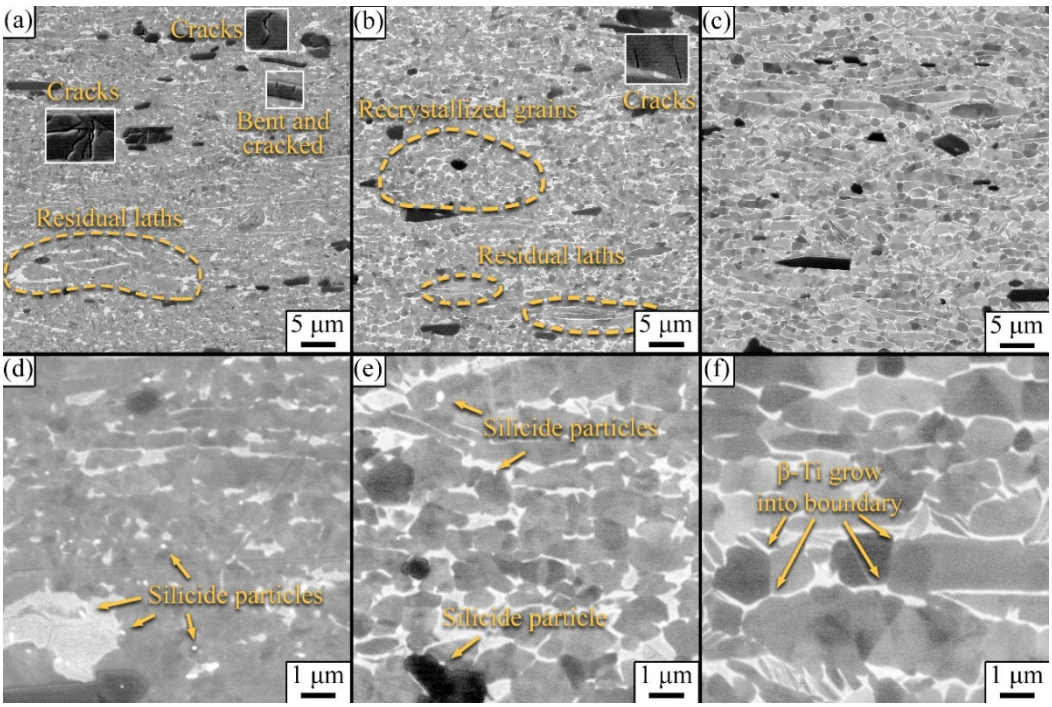

Fig. 5.5 Microstructures of ST-Ti deformed under different temperatures, at a rate of 0.1 s^{-1}, (a), (d) 870 °C, low and high magnifications, (b), (e) 910 °C, low and high magnifications, (c), (f) 950 °C low and high magnifications

Fig. 5.6 exhibits the microstructures of ST-Ti after hot compression at 870 °C – 950 °C and the strain rates of 0.01 s^{-1} and 0.001 s^{-1}. The microstructure of S-Ti deformed at 910 °C / 1 s^{-1} is also included for comparison. It can be observed that all of the deformation microstructures of ST-Ti are consisting of residual α laths and equiaxed recrystallized grains. With increasing deformation temperature and decreasing strain rate, both the width of residual laths and the sizes of recrystallized grain gradually increase. The volume fraction of recrystallized grains varies with temperature. At 910 °C, the volume fraction of recrystallized grains is higher at 0.01 s^{-1} than 0.001 s^{-1}, while at 870 °C, the material exhibits the most extensive recrystallization at 0.001 s^{-1}. This suggests that the dominant factor influencing the volume fraction of recrystallized grains varies at different temperatures.

At low temperatures, the dynamic recovery rate is low, leading to rapid dislocation accumulation. However, due to the slower grain growth and element diffusion, the recrystallized grains are unable to grow sufficiently at low temperatures. Therefore, reducing the strain rate at low temperatures helps increase the volume fraction of recrystallized grains. As the deformation temperature increases, both grain growth and element diffusion rates increase. However, the dynamic recovery rate also increases accordingly. At low strain rates, the dislocation density is consumed by

rapid dynamic recovery, leading to incomplete recrystallization. As the result, the strain rate corresponding to sufficient dynamic recrystallization gradually increases with the increasing temperature. Fig. 5.6 (a)-(e) reveals the fractured TiBw reinforcements in the samples deformed at 870 °C and 910 °C, while no fracture is observed in the sample deformed at 950 °C. Additionally, a significant precipitation of coarse silicide particles is observed in the material deformed at 870 °C / 0.001 s^{-1}, while only a small amount of is observed at 910 °C / 0.001 s^{-1}. This suggesting that reducing the strain rate simultaneously increases the size and quantity of precipitated silicide particles at low temperatures.

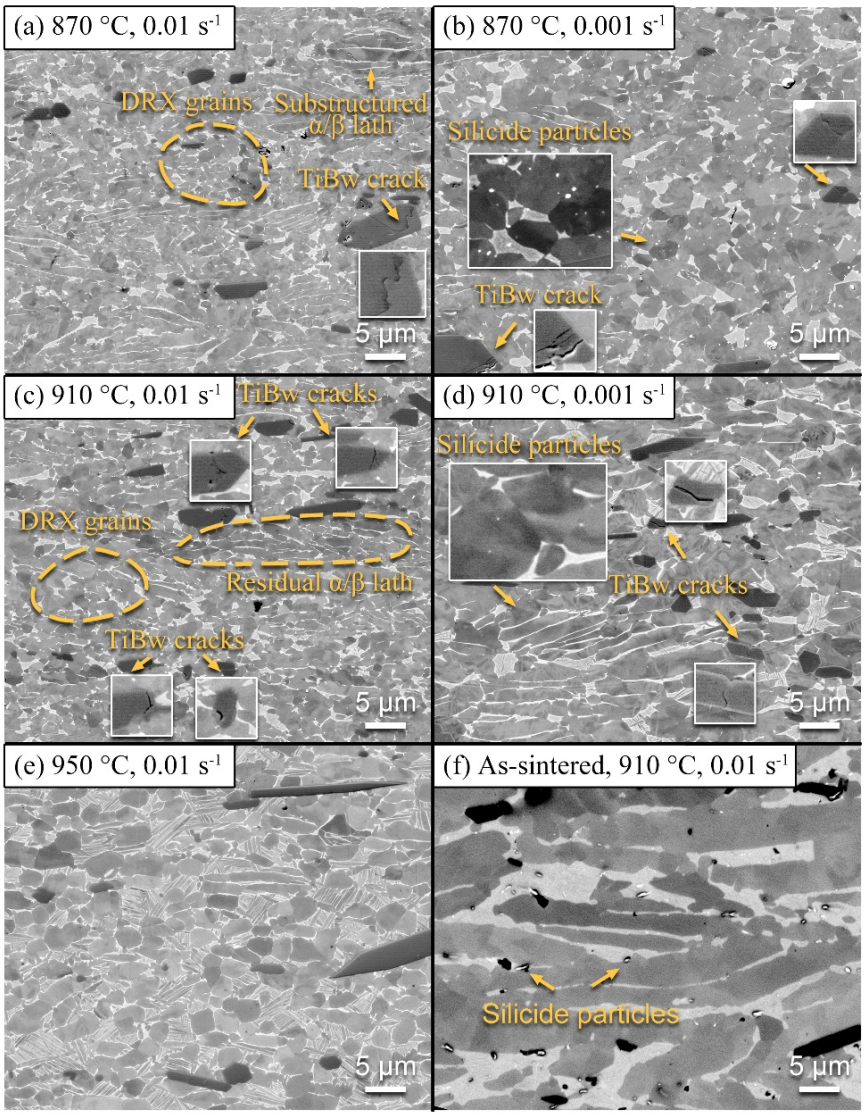

Fig. 5.6 Microstructures of S-Ti and ST-Ti deformed under different temperatures, at the rates of 0.01 s^{-1} and 0.001 s^{-1}, (a) – (e) microstructures of ST-Ti after deformation at different conditions, (f) microstructure of S-Ti after deformed at 910 °C / 0.01 s^{-1}

Fig. 5.6 (f) presents the microstructure of S-Ti obtained at 910 °C / 0.01 s^{-1}. Compared to the ST-Ti deformed under the same condition in Fig. 5.6 (c), S-Ti exhibits a significantly coarser microstructure, with almost no equiaxed α grains observable in the matrix. Furthermore, a large number of coarse silicide particles are observed at the α/β phase interfaces in S-Ti, indicating silicide growth during the hot deformation process. Significant contrast variations are observed within the α phase of S-Ti, indicating the presence of dislocations and substructures. The coarse α and β phases, along with the high dislocation density, contribute to the higher flow stress of S-Ti in Fig. 5.3 (e) compared to ST-Ti. The deformation microstructures of S-Ti and ST-Ti under 910 °C / 0.01 s^{-1} demonstrates that the solid solution treatment significantly refines the deformation microstructure, enhances dynamic recrystallization, and refines the silicide particles in the material.

To investigate the microstructure evolution at different deformation degrees, compression samples of ST-Ti were subjected to hot compressions at 910 °C / 0.1 s^{-1} with engineering strains of 2.5%, 5%, 10%, 20%, and 40%. The resulting microstructures are shown in Fig. 5.7. Fig. 5.7 (g)-(i) are microstructures of the ST-Ti deformed with 10%, 20%, and 40% engineering strain, respectively, at low magnifications. The gradual compression of the network structure formed by TiBw reinforcements with increasing strain can be observed. Additionally, the orientations of the TiBw reinforcements transitions gradually from a random distribution to a distribution that perpendicular to the compression direction with increased strain. Fig. 5.7 (b)-(f) display the microstructures of ST-Ti at high magnifications after compression with 2.5%, 5%, 10%, 20%, and 40% engineering strain, respectively. The composite has not yet yielded at ε=2.5%, therefore no significant deformation is observed. At ε=5%, the compressive stress reaches its peak, and macroscopic plastic deformation occurs, but the low deformation degree brings no significant change in microstructure. It is worth noting that a small amount of silicide precipitation can already be observed at this stage. Except for α/β interfaces and the internal of β phase, silicide particles can also be observed inside of α laths, which is resulted from the oversaturation of Si in α-phase by solid solution treatment. At ε=10%, the material enters the strain-softening stage, where distorted lamellae and continuous contrast variations within the α laths indicate the formation of substructures.

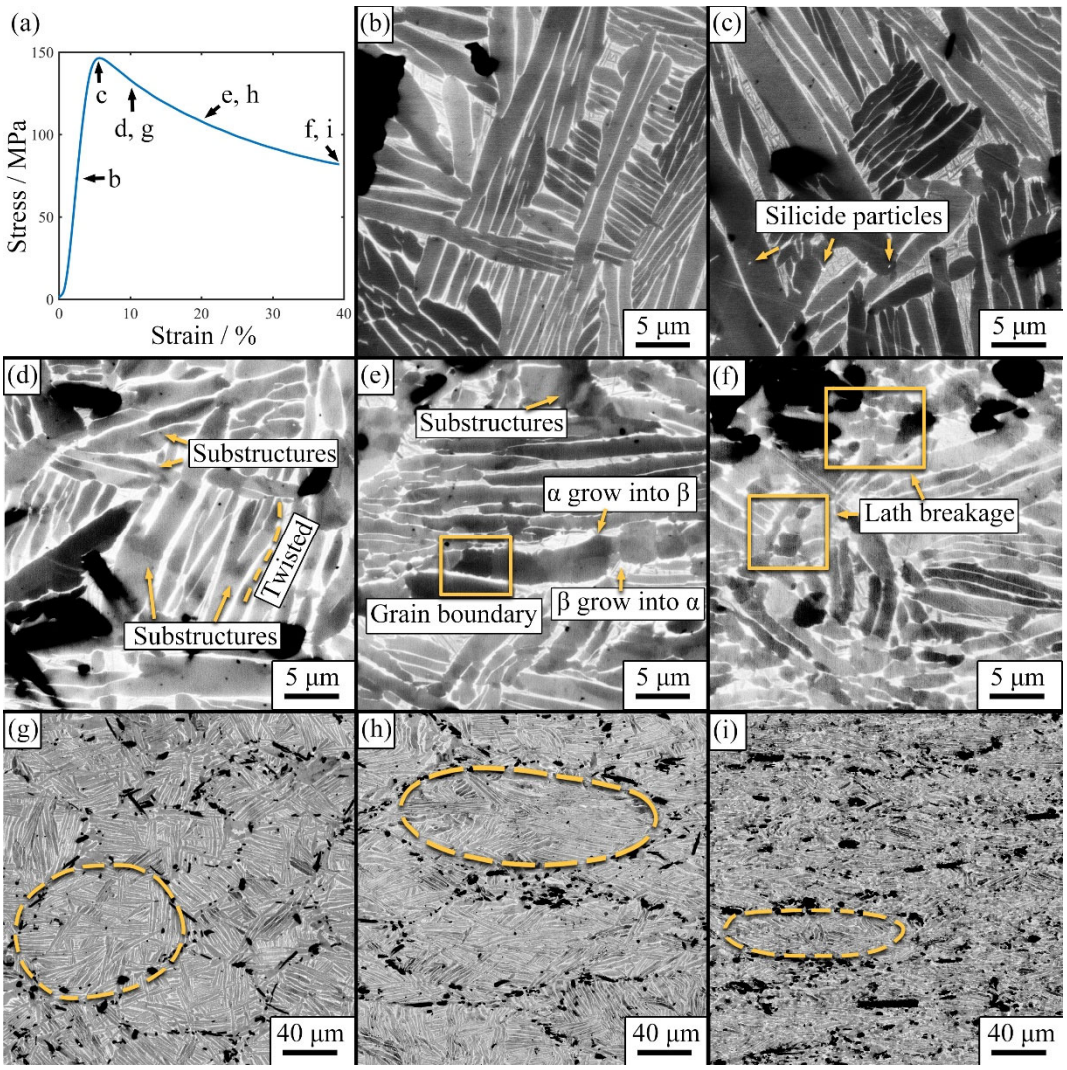

Fig. 5.7 Microstructures of ST-Ti deformed at 910 °C / 0.1 s^{-1}, with varying deformation degrees, (a) deformation degree of different samples, (b) ε=2.5%, (c) ε=5%, (d), (g) ε=10%, (e), (h) ε=20%, (f), (i) ε=40%

At 20% strain, sudden change of the electron channeling contrast can be observed withinα lamellae, indicating the formation of new grain boundaries or subgrain boundaries through dynamic recrystallization. Additionally, the α/β interfaces near the newly formed grain boundaries are observed to migrate into the grain boundaries to reduce the curvature, which creates a chemical potential gradient facilitating diffusion and interface migration. The migration of lamellar terminations suggests the instability of the lamellar microstructure, which prompts the microstructure spheroidization [87]. At ε=40%, the lamellae in the matrix undergo severe distortion, resulting in the generation of numerous equiaxed grains through spheroidization. Moreover, the spheroidization near the network structures is more pronounced, as the presence of larger strain gradients around the reinforcements leads to higher dislocation density and thereby more pronounced

recrystallization. At ε=60%, the microstructure of the material evolves into a highly equiaxed microstructure shown in Fig. 5.5 (e). It is worth noticing that, only minimum amount of silicide particles was observed precipitating inside of α phase during the hot compression at 910 °C / 0.01 s^{-1}. Although silicide particles may impede dislocations and encourage the nucleation of recrystallization grains, its slow precipitation rate and low volume fraction made its contribution to grain refinement limited. The microstructural evolution during high-temperature compression of the TiBw/TA15(Si) composites with network architecture is schematically depicted in Fig. 5.8.

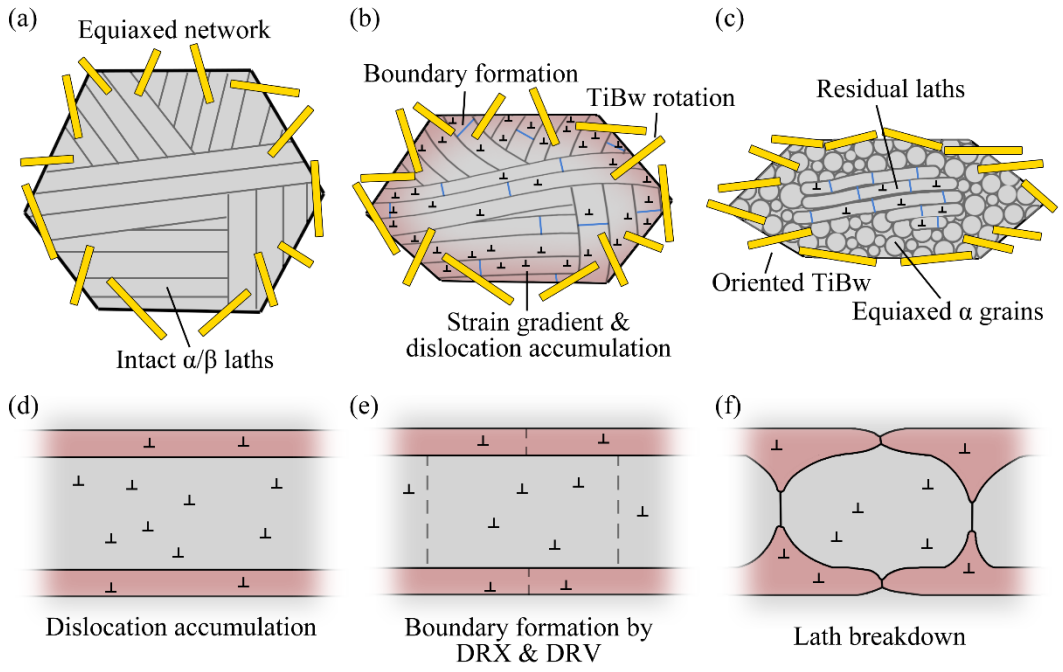

Fig. 5.8 Schematic diagram of microstructure evolution of TiBw/TA15(Si) composites during hot deformation, (a) – (c) microstructure evolution during hot deformation, (d) – (f) the decomposition of lamellar microstructure

Prior to hot deformation, TiBw in the material exhibited a random orientation with a network distribution, while the matrix consisted of lamellar α and β phases. During plastic deformation, as depicted in Fig. 5.8 (b), the network structure is gradually compressed, and TiBw reinforcements rotated toward the direction that perpendicular to compression axis. The lamellae in the matrix underwent distortion due to deformation, accumulating a significant amount of dislocations. Through dynamic recovery and recrystallization, new grain boundaries or subgrain boundaries formed within the lamellae, facilitating spheroidization. Higher strain gradients and dislocation densities were present near the TiBw reinforcements. As

shown in Fig. 5.8 (c), with continued deformation, the TiBw network structure is further compressed, resulting in strongly orientated TiBw. Lamellar microstructures with high strain energy storage decompose and spheroidize to form equiaxed α grains, while those with insufficient strain energy remain as residual. The process of lamellar decomposition is illustrated in Fig. 5.8 (d)-(f). During plastic deformation of the lamellar microstructure, the dislocation density initially increased rapidly. As deformation progressed, high-density dislocations caused dynamic recrystallization, leading to defect-free equiaxed grains within the lamellae, while dynamic recovery forms subgrain boundaries through the ordered arrangement of dislocations. Both mechanisms contributed to the formation of new interfaces within the material. Eventually, the newly formed interfaces within the lamellae, due to the high curvature at the lamellae terminations, facilitated element diffusion, leading to termination migration and ultimately the decomposition and spheroidization, forming equiaxed grains.

5.4 Constitutive equations and processing maps of TiBw/TA15(Si) composites

5.4.1 Constructing the constitutive equations

To quantitatively describe the hot deformation behaviors of the TiBw/TA15(Si) composites and elucidate its softening mechanism, the Arrhenius equation is employed to establish the constitutive equation for hot deformation. The Arrhenius equation is commonly used to describe the temperature-dependent behaviors of thermal activated processes. During hot compression, the relationship between the peak stress, the deformation temperature and the strain rate can be expressed as:

$$\dot{\varepsilon} = AF\left(\sigma_p\right)\exp\left(-Q / RT\right) \tag{5-1}$$

In which $\dot{\varepsilon}$ is the strain rate, σ_p is the compressive peak stress, T is the deformation temperature, Q is the activation energy, R is the ideal gas constant which equals 8.314 J/(mol·K), A is structure factor, which is a materials constant that obtainable with fitting. The specific form of Eq. 5-1 is determined by the function $F(\sigma_p)$:

$$F(\sigma_p)=\begin{cases}\sigma_p^{\,n_1} & \text{Power law, } \alpha\sigma_p < 0.8\\ \exp(\beta\sigma_p) & \text{Expotential law, } \alpha\sigma_p > 1.2\\ \left[\sinh(\alpha\sigma_p)\right]^{n_2} & \text{Hyperbolic-sine law, other conditions}\end{cases} \tag{5-2}$$

In which n_1, n_2, α and β are materials constants that obtainable by fitting. It can be observed that Eq. 4.1 can take three forms: power law, exponential law, and hyperbolic-sine law, depending on the peak stress. At low stress levels, the Arrhenius equation follows power law, while at high stress levels, it follows exponential law. When the stress levels are distributed over a wide range, the hyperbolic-sine law provides the best fit. To determine the appropriate form of Eq. 4.1, n_1 and β should first be obtained through fitting. The peak stresses used for calculation are listed in Table 5.1. By substituting the temperatures, strain rates, and stresses into Eq. 4.1 and 4.2, and taking Eq. 4.2 in the form of power law, n_1 can be calculated as 4.54. When taking Eq. 4.2 in the form of exponential law, β can be calculated as 0.03, resulting in α=0.0067. Based on peak stresses shown in Table 5.1, the minimum value of $\alpha\sigma_p$ is 0.24, and the maximum value is 2.71. This indicates that the constitutive relationships between peak stress, deformation temperature, and strain rate cannot be described by neither power law nor exponential law. Therefore, Eq. 4.1 is determined to obey the hyperbolic-sine law.

Table 5.1 Peak stresses of ST-Ti deformed at different conditions (MPa)

Strain rate / s^{-1}	Temperature / K				
	1143	1163	1183	1203	1223
1	405	348	327	284	179
0.1	318	277	238	166	143
0.01	199	165	145	119	79
0.001	118	91	70	53	35

The constitutive equation of hyperbolic-sine law is as follows:

$$\dot{\varepsilon} = A\left[\sinh(\alpha\sigma_p)\right]^{n_2}\exp(-Q/RT) \tag{5-3}$$

By substituting the stresses from Table 5.1 into Eq. 4.3 and performing linear fitting, the material constants required for the constitutive equation can be obtained. The

fitting results are listed in Table 5.2. It can be observed from Table 5.2 that the stress exponent n_2 in the hot deformation constitutive equation of ST-Ti is 3.3, indicating that the deformation is dominated by dislocation climbing [128]. The activation energy is 623 kJ/mol, which is relatively high compared to other TMCs (360 kJ/mol - 620 kJ/mol) [34, 129, 130], indicating that ST-Ti exhibits strong resistance to hot deformation. Our previous study indicated that S-Ti has a stress exponent of 3.2 and an activation energy for hot deformation of 593 kJ/mol [34]. Research of Li et al. [131] on the deformation behaviors of TA15 alloy with lamellar structure (lamellar width ~10 μm, similar to S-Ti) in the dual-phase region showed a stress exponent of 3.5 and an activation energy for hot deformation of 584 kJ/mol. It can be found that S-Ti, ST-Ti, and TA15 alloy all exhibit similar stress exponents, while ST-Ti shows a significantly higher activation energy for hot deformation compared to S-Ti and TA15 alloy. This indicates that the addition of TiBw reinforcements and the solid solution pretreatment do not alter the hot deformation mechanism of the materials, which is primarily governed by dislocation climb. Also, low volume fraction of reinforcement does not significantly affect the material's deformation resistance and flow softening mechanism. Therefore, S-Ti exhibits a similar activation energy for hot deformation as TA15 alloy. However, the abundant α/β interfaces generated by solid-solution treatment significantly impeded dislocation movement and shift the flow softening mechanism towards dynamic recrystallization, resulting in a notable increase in the activation energy.

Table 5.2 Materials constants of the constitutive equation

Materials constants	Fitted values
A	3.46×10^{25} s^{-1}
α	0.0067 MPa^{-1}
n_2	3.30
Q	623 kJ/mol

The Zener-Hollomon parameter (referred to as the Z parameter) is a temperature-dependent strain rate factor proposed by Zener and Hollomon [132] in 1944. It is defined as follows:

$$Z = \dot{\varepsilon} \exp\left(\frac{Q}{RT}\right) \tag{5-4}$$

Z parameter and the hyperbolic-sine stress factor sinh($\alpha\sigma_p$) in Eq. 4.3 exhibits linearity on the logarithmic coordinates, therefore Z parameter can be used to assess the goodness of the fitted hot deformation constitutive equation. The stress factors obtained from experimental measurements and those calculated from the constitutive equation are used to obtain Z parameters and compared on logarithmic coordinates. The results are shown in Fig. 5.9.

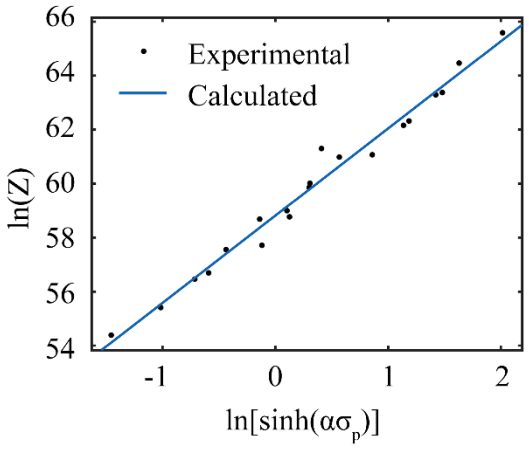

Fig. 5.9 The calculated and experimental values of Z parameters in logarithm coordinate

A good linearity is observed between the experimental values and the calculated ones exhibit a good. The fitting goodness is determined to be R_2=0.982, indicating the hot compression behaviors of ST-Ti well obeys the constitutive equation of hyperbolic law.

5.4.2 Constructing the processing map

In the present study, processing map is constructed to determine the optimal hot deformation parameters for the composites. The processing map is obtained by overlapping the dissipation efficiency map and the instability map, which shows the variation of dissipation efficiency and the instability of the material with respect of deformation temperature and strain rate, respectively. High dissipation efficiency indicates significant changes in the microstructure, which implies desirable deformation parameters, while instability region indicates deformation parameters with undesirable power dissipation route, which should be avoided. According to Prasad et al. [105], the power inputted by thermo-mechanical processing to the material can be expressed as follows:

$$P = \sigma\dot{\varepsilon} = \int_0^{\dot{\varepsilon}} \sigma \, \mathrm{d}\, \dot{\varepsilon} + \int_0^{\sigma} \dot{\varepsilon} \, \mathrm{d}\, \sigma = G + J \tag{5-5}$$

In which P is the power inputted by the processing equipment to the material, σ is the flow stress of the processed material, $\dot{\varepsilon}$ is the strain rate, G is the power dissipation content which indicates the power dissipated into ambient, while J is the power dissipation co-content which indicates the power stored in materials in the form of microstructure changes. Dissipation efficiency η is defined as the ratio between the actual dissipation co-content J and the theoretical maximum of the dissipation co-content J_{max}:

$$\eta = \frac{J}{J_{\max}} = \frac{\int_0^{\sigma} \dot{\varepsilon} \, \mathrm{d}\, \sigma}{\left(\sigma\dot{\varepsilon}\right)/2} \tag{5-6}$$

Since the experimental measurements of flow stress σ are discrete with respect of strain rate, the integration in Eq. 4.6 is not directly obtainable. In our previous research, a method for calculating the dissipation efficiency using cubic spline interpolation was proposed as follows [34]:

$$\eta(\dot{\varepsilon}) = 2 - \frac{2\left(\frac{\dot{\varepsilon}_{low}{}^{M+1}}{M+1}\left(\exp\frac{A}{M}\right)^{M} + \int_{\dot{\varepsilon}_{low}}^{\dot{\varepsilon}} \mathrm{S}(\dot{\varepsilon}) \, \mathrm{d}\, \dot{\varepsilon}\right)}{\mathrm{S}\left(\dot{\varepsilon}\right) \cdot \dot{\varepsilon}} \tag{5-7}$$

In which M is the strain rate sensitivity that obtained with linear regression, A is a material constant obtainable with linear regression, $\dot{\varepsilon}_{low}$ is the lowest strain rate in experiments, and $\mathrm{S}(\dot{\varepsilon})$ is a cubic spline function of flow stress with respect to the strain rate. The parameters M and A are calculated from the linear regression of flow stress to strain rate under logarithm coordinate, the linear regression is as follows:

$$\ln\sigma = A + M\ln\dot{\varepsilon} \tag{5-8}$$

Calculating the dissipation efficiencies under different deformation temperatures and strain rates, the dissipation efficiency map can be obtained. The instability map is given by the instability criterion that proposed by Ziegler et al. [106]:

$$\frac{\partial \ln J}{\partial \ln \dot{\varepsilon}} < 1 \tag{5-9}$$

In which J is the dissipation co-content, and $\dot{\varepsilon}$ is the strain rate. The processing map was constructed by substituting the flow stress of ST-Ti at a true strain of 0.4 into Eqs. 4.7 and 4.9. The stresses used for the calculation are shown in Table 5.3, the obtained processing map is shown in Fig. 5.10. It can be observed that the material exhibits the highest dissipation efficiency in the temperature range of 900 °C – 950 °C and the strain rate range of 0.01 s^{-1} – 0.001 s^{-1}. Combined with microstructural observations, it is evident the deformation parameters corresponding to high dissipation efficiencies yielded refined microstructures with high proportion of recrystallization grains, which validates the accuracy of the processing map. The peak value of dissipation efficiency covers a wide range of temperature and strain rate, indicating that ST-Ti has good tolerance to temperature decrease, which is desirable for industrial production environments. Additionally, there is also a dissipation efficiency peak near 930 °C / 1 s^{-1}. However, since this peak is close to the deformation parameters that lead to overheated microstructures and macroscopic instability, thermo-mechanical processing within this range should be avoided. Deformation instability can be observed at 870 °C – 880 °C and 0.1 s^{-1} – 1 s^{-1}, which is likely caused by the excessive fragmentation TiBw reinforcements, as inferred from the microstructure.

Table 5.3 Flow stresses of ST-Ti under different conditions at true strain=0.4

Strain rate / s^{-1}	Temperature / K				
	1143	1163	1183	1203	1223
1	302	241	241	224	135
0.1	252	147	133	93	77
0.01	91	90	77	60	38
0.001	53	40	29	22	16

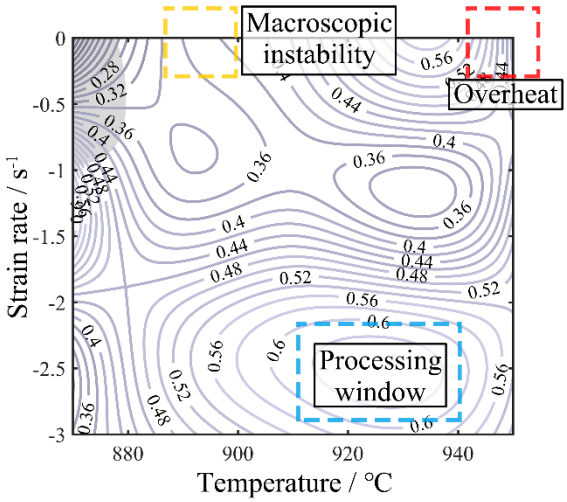

Fig. 5.10 Processing map of ST-Ti in the range of 870 °C – 950 °C, 1 s^{-1} – 0.001 s^{-1}

Combining the microstructure observations and the processing map, the ideal deformation parameters for TiBw/TA15(Si) composites after solid solution treatment is determined to be in the range of 900 °C – 950 °C and 0.01 s^{-1} – 0.001 s^{-1}. Compared to the composite without the solid solution treatment [34], the peak value of dissipation efficiency is shifted towards higher temperatures and lower strain rates in the present study. This may attribute to the increase of deformation temperature and decrease of strain rate can help to overcome the deformation resistance that raised by the solid solution treatment. Based on microstructural observations, it is evident that the material underwent significant grain refinement after hot deformation with the ideal processing parameters, resulting in a higher volume fraction of equiaxed α grains. This indicates that the peak values in the processing map accurately reflects the significant microstructural evolution of the material.

5.5 Influence of hot deformation to orientations of TiBw

5.5.1 Influence of hot deformation to the orientation of a single TiBw

During hot deformation of TMCs, TiBw reinforcements rotate with the flow of the metallic matrix, resulting in changes in the orientation distribution. To analyze the relationship between reinforcement orientation distribution and plastic deformation, it is necessary to first investigate the rotation of a single TiBw reinforcements during plastic deformation. The orientation of TiBw reinforcement is defined as shown in Fig. 5.11.

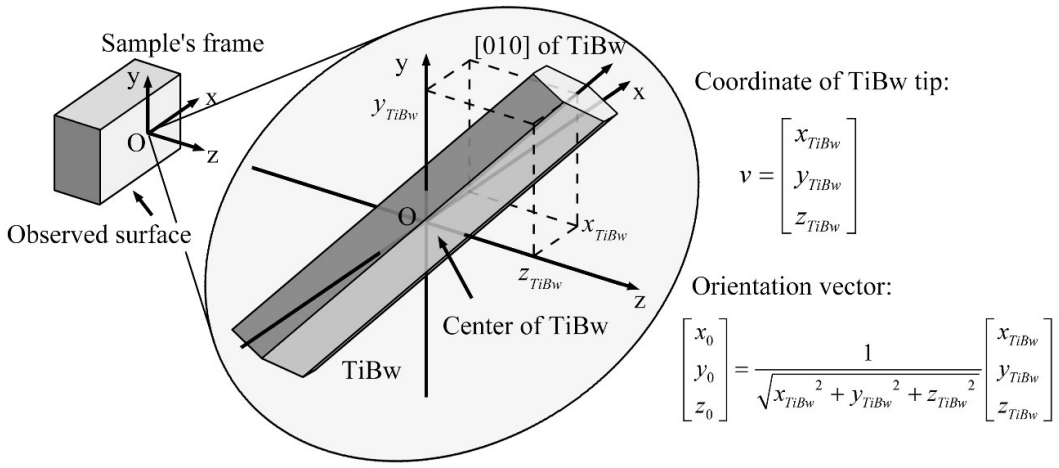

Fig. 5.11 The definition of orientation vectors

As shown in Fig. 5.11, for a composite specimen, a spatial Cartesian coordinate system (referred to as the sample frame) is established for the convenience of observation. For any TiBw reinforcement within the specimen, a vector is constructed from its centroid to its endpoint, denoted as [x_{TiBw} y_{TiBw} z_{TiBw}]. This vector represents the orientation of the TiBw reinforcement and has a length equal to half of the reinforcement's length. Since the orientation of the reinforcement is independent of its length, the length of the vector can be normalized to obtain the orientation vector of the reinforcement, denoted as [x_0 y_0 z_0]. The normalization is as follows:

$$\begin{bmatrix} x_0 \\ y_0 \\ z_0 \end{bmatrix} = \frac{1}{\sqrt{x_{TiBw}^2 + y_{TiBw}^2 + z_{TiBw}^2}} \begin{bmatrix} x_{TiBw} \\ y_{TiBw} \\ z_{TiBw} \end{bmatrix} \tag{5-10}$$

The uniform plastic deformation (tension, compression, and shearing) can be described with a second-order tensor with 6 independent components, called strain tensor:

$$\mathbf{E} = \begin{bmatrix} \varepsilon_{xx} & \varepsilon_{xy} & \varepsilon_{xz} \\ \varepsilon_{xy} & \varepsilon_{yy} & \varepsilon_{yz} \\ \varepsilon_{xz} & \varepsilon_{yz} & \varepsilon_{zz} \end{bmatrix} \tag{5-11}$$

In which ε_{xx}, ε_{yy}, and ε_{zz} are the normal strain components along x, y and z directions,

respectively, ε_{xy}, ε_{yz}, and ε_{zx} are the shear strain components along xy, yz and zx directions, respectively.

Then for any given point in the matrix near the short fiber, the coordinates before and after the deformation can be expressed as:

$$\begin{bmatrix} x_{fin} \\ y_{fin} \\ z_{fin} \end{bmatrix} = \begin{bmatrix} x_{in} \\ y_{in} \\ z_{in} \end{bmatrix} + \mathbf{E} \begin{bmatrix} x_{in} \\ y_{in} \\ z_{in} \end{bmatrix} \tag{5-12}$$

In which [x_{in}, y_{in}, z_{in},] and [x_{fin}, y_{fin}, z_{fin}] are the initial and the final coordinates of the given point, respectively. According to the model proposed by Guo et. al [91], short fibers in composites are reoriented similarly as shown in Eq. 5-12, only without changing their lengths. The orientation of the fiber after the deformation is given by:

$$\begin{bmatrix} x_0' \\ y_0' \\ z_0' \end{bmatrix} = \begin{bmatrix} x_0 \\ y_0 \\ z_0 \end{bmatrix} + \begin{bmatrix} \varepsilon_{xx} & \varepsilon_{xy} & \varepsilon_{xz} \\ \varepsilon_{xy} & \varepsilon_{yy} & \varepsilon_{yz} \\ \varepsilon_{xz} & \varepsilon_{yz} & \varepsilon_{zz} \end{bmatrix} \begin{bmatrix} x_0 \\ y_0 \\ z_0 \end{bmatrix} = \begin{bmatrix} 1+\varepsilon_{xx}x_0 + \varepsilon_{xy}y_0 + \varepsilon_{xz}z_0 \\ 1+\varepsilon_{yy}y_0 + \varepsilon_{xy}x_0 + \varepsilon_{yz}z_0 \\ 1+\varepsilon_{zz}z_0 + \varepsilon_{yz}y_0 + \varepsilon_{xz}z_0 \end{bmatrix} \tag{5-13}$$

$$\begin{bmatrix} x_1 \\ y_1 \\ z_1 \end{bmatrix} = \frac{1}{\sqrt{x_0'^2 + y_0'^2 + z_0'^2}} \begin{bmatrix} x_0' \\ y_0' \\ z_0' \end{bmatrix} \tag{5-14}$$

In which [x_0', y_0', z_0'] expresses the orientation of the redirected fiber before normalization, and [x_1, y_1, z_1] is the normalized orientation vector of the fiber, which has the same direction as [x_0', y_0', z_0'] and the length of 1. To determine any single component of the vector [x_0', y_0', z_0'] in the Eq. 14, all three components in [x_0, y_0, z_0] along with three out of six unique components in the strain tensor **E** must be used. However, by using the technique of coordinate transformation, this problem can be significantly simplified. The strain tensor **E** can be written as:

$$\mathbf{E}=\begin{bmatrix}\varepsilon_{xx} & \varepsilon_{xy} & \varepsilon_{xz}\\ \varepsilon_{xy} & \varepsilon_{yy} & \varepsilon_{yz}\\ \varepsilon_{xz} & \varepsilon_{yz} & \varepsilon_{zz}\end{bmatrix}=\begin{bmatrix}\mathbf{e_1} & \mathbf{e_2} & \mathbf{e_3}\end{bmatrix}\begin{bmatrix}\varepsilon_1 & 0 & 0\\ 0 & \varepsilon_2 & 0\\ 0 & 0 & \varepsilon_3\end{bmatrix}\begin{bmatrix}\mathbf{e_1} & \mathbf{e_2} & \mathbf{e_3}\end{bmatrix}^T \quad (5\text{-}15)$$

In which ε_1, ε_2, and ε_3 are the principal strains (or the eigenvalues) of the strain tensor, $\boldsymbol{e_1}$, $\boldsymbol{e_2}$, and $\boldsymbol{e_3}$ are the principal axes (or the eigenvectors) of the strain tensor. Since $\boldsymbol{e_1}$, $\boldsymbol{e_2}$, and $\boldsymbol{e_3}$ are all unit vectors that are perpendicular to each other, the 3×3 matrix $[\boldsymbol{e_1}\ \boldsymbol{e_2}\ \boldsymbol{e_3}]$ is a rotation matrix, which gives $[\boldsymbol{e_1}\ \boldsymbol{e_2}\ \boldsymbol{e_3}]^T=[\boldsymbol{e_1}\ \boldsymbol{e_2}\ \boldsymbol{e_3}]^{-1}$. Denoting the matrix $[\boldsymbol{e_1}\ \boldsymbol{e_2}\ \boldsymbol{e_3}]$ as **R**, Eq. 13 can be written as:

$$\begin{bmatrix}x_0'\\ y_0'\\ z_0'\end{bmatrix}=\begin{bmatrix}x_0\\ y_0\\ z_0\end{bmatrix}+\mathbf{R}\begin{bmatrix}\varepsilon_1 & 0 & 0\\ 0 & \varepsilon_2 & 0\\ 0 & 0 & \varepsilon_3\end{bmatrix}\mathbf{R}^{-1}\begin{bmatrix}x_0\\ y_0\\ z_0\end{bmatrix} \quad (5\text{-}16)$$

By left multiplying a vector in the sample frame with $\mathbf{R}^{-1}$, the vector is transformed into a new frame that is built by the principal axes of the strain tensor **E** (called the principal frame hereafter), under which the strain tensor has only 3 normal components, which gives:

$$\mathbf{R}^{-1}\begin{bmatrix}x_0'\\ y_0'\\ z_0'\end{bmatrix}=\mathbf{R}^{-1}\begin{bmatrix}x_0\\ y_0\\ z_0\end{bmatrix}+\begin{bmatrix}\varepsilon_1 & 0 & 0\\ 0 & \varepsilon_2 & 0\\ 0 & 0 & \varepsilon_3\end{bmatrix}\mathbf{R}^{-1}\begin{bmatrix}x_0\\ y_0\\ z_0\end{bmatrix} \quad (5\text{-}17)$$

Denoting the vectors $[x_{R0}, y_{R0}, z_{R0}]$ and $[x_{R0}', y_{R0}', z_{R0}']$ as the vectors $[x_0, y_0, z_0]$ and $[x_0', y_0', z_0']$ that being transformed into the principal frame, Eq 17 becomes:

$$\begin{bmatrix}x_{R0}'\\ y_{R0}'\\ z_{R0}'\end{bmatrix}=\begin{bmatrix}x_{R0}\\ y_{R0}\\ z_{R0}\end{bmatrix}+\begin{bmatrix}\varepsilon_1 & 0 & 0\\ 0 & \varepsilon_2 & 0\\ 0 & 0 & \varepsilon_3\end{bmatrix}\begin{bmatrix}x_{R0}\\ y_{R0}\\ z_{R0}\end{bmatrix}=\begin{bmatrix}(1+\varepsilon_1)x_{R0}\\ (1+\varepsilon_2)y_{R0}\\ (1+\varepsilon_3)z_{R0}\end{bmatrix} \quad (5\text{-}18)$$

And its normalized form:

$$\begin{bmatrix} x_{R1} \\ y_{R1} \\ z_{R1} \end{bmatrix} = \frac{1}{\sqrt{(1+\varepsilon_1)^2 x_{R0}{}^2 + (1+\varepsilon_2)^2 y_{R0}{}^2 + (1+\varepsilon_3)^2 z_{R0}{}^2}} \begin{bmatrix} (1+\varepsilon_1) x_{R0} \\ (1+\varepsilon_2) y_{R0} \\ (1+\varepsilon_3) z_{R0} \end{bmatrix} \quad (5\text{-}19)$$

In which [x_{R1}, y_{R1}, z_{R1}] is the orientation vector of the short fiber after the deformation that being transformed into the principal frame. Comparing Eq.18 with Eq. 13, two major changes are noticeable: Firstly, the number of unique components in the strain tensor is reduced from 6 to 3, and secondly, it takes only one component from [x_{R0}, y_{R0}, z_{R0}] and one component from the strain tensor to determine any single component in [x_{R0}', y_{R0}', z_{R0}']. In the following sections, the influence of principal directions and principal strain to the orientation distributions of reinforcements will be separately discussed.

5.5.2 Influence of principal directions of strain to orientations of TiBw

Imagine a bulk composite in which the short fiber reinforcements are isotropically oriented. Draw the orientation vectors of all fibers in the composites from the same starting point, and a sphere will be formed by the ends of orientation vectors, as shown in Fig. 5.12. This sphere is called the orientation sphere hereafter. Applying a uniform plastic strain onto the composite, the fiber reinforcements will rotate with the deformation of the composite, and their orientation vectors will be redirected as given in Eq. 13 and Eq. 14.

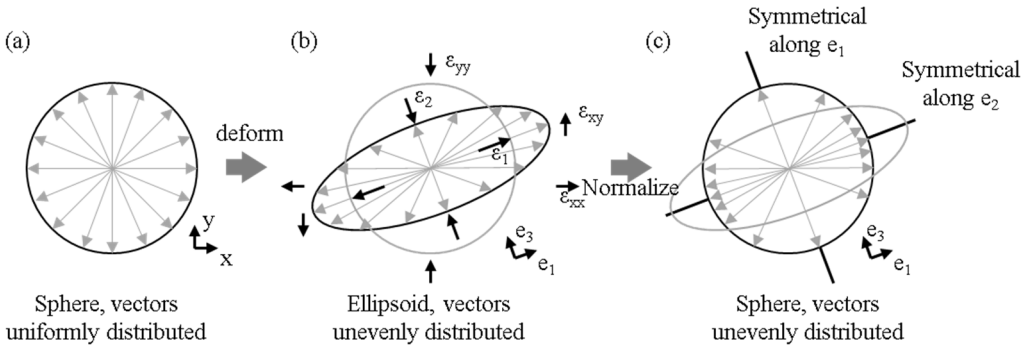

Fig. 5.12 The changing of orientation distribution of TiBw during deformation (a) Initial state, orientation vectors uniformly distributed, (b) orientation vectors after deformation but before normalization, (c) orientation vectors after normalization

In general conditions, a uniform strain has an ellipsoidal symmetry that is characterized by three two-fold rotational axes that perpendicular to each other.

Each rotational axe is one of the three principal axes of the strain. When the orientation sphere in Fig. 5.12 (a) is deformed following Eq. 13, the symmetry of the strain is transferred to the sphere, resulting in an ellipsoid shown in Fig. 5.12 (b). Normalizing the orientation vectors into unit vectors following Eq. 14, the ellipsoid becomes a new orientation sphere that has high density along the tension direction and low density along the compressive direction of the strain, as shown in Fig. 5.12 (c). Since the operation in Eq. 14 does not change the rotational symmetry, the ellipsoidal symmetry of the strain is preserved.

This inheritance of symmetry from the strain to the orientation sphere makes it possible to find the principal axes of strain. Assuming distribution of vectors in Fig. 5.12 (c) obeys a probability density function $p(x,y,z)$, then the symmetry the distribution of the vectors can be reflected by the covariance matrix of $p(x,y,z)$. It can be proven that the covariance matrix of $p(x,y,z)$ has a same set of principal directions as the strain.

Assuming the principal directions of the orientation sphere in Fig. 5.12 (c) are the same as the directions of the x, y, and z axes, the probability density of orientation vectors on the sphere is shown as Fig. 5.13 (a). Projecting the probability density function onto the xy plane gives a 2-dimensional distribution as shown in Fig. 5.12 (b), which can be written as a 2-dimensional probability density function $p_z(x,y)$:

$$p_z(x,y) = \int_{-1}^{1} p(x,y,z)\,dz \tag{5-20}$$

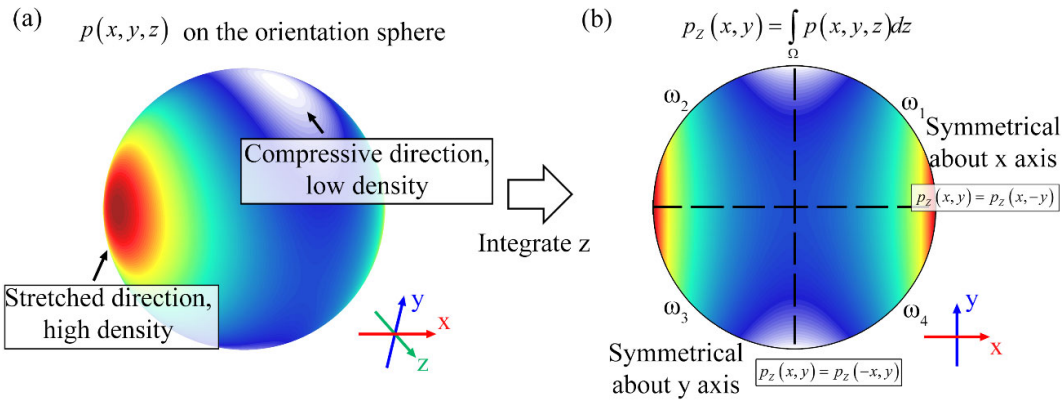

Fig. 5.13 The 3-dimensional distribution of TiBw probability density, (a) probability density distribution of orientation vectors on the orientation sphere, (b) the probability density after projected to the xy plane

A uniform deformation has mirror symmetry along its principal directions. Therefore, for composites with randomly oriented reinforcements, the orientations of reinforcements also exhibit mirror symmetry along the principal directions of the strain after the plastic deformation, which can be described as:

$$p_z(x,y) = -p_z(-x,y) \tag{5-21}$$

And:

$$p_z(x,y) = -p_z(x,-y) \tag{5-22}$$

It can be seen that, $p_z(x,y)$ can be divided into four symmetrical regions, ω_1, ω_2, ω_3, and ω_4, as shown in Fig. 5.13 (b). For a random vector $[x\ y\ z]$ that obeys the probability density function $p(x,y,z)$, its covariance matrix can be written as:

$$\begin{aligned}\mathrm{var}\left(\begin{bmatrix}x & y & z\end{bmatrix}\right) &= \mathrm{E}\begin{bmatrix} z^2+y^2 & -xy & -xz \\ -xy & x^2+z^2 & -yz \\ -xz & -yz & x^2+y^2 \end{bmatrix} \\ &= \iiint_{\Omega} p(x,y,z)\begin{bmatrix} z^2+y^2 & -xy & -xz \\ -xy & x^2+z^2 & -yz \\ -xz & -yz & x^2+y^2 \end{bmatrix} dxdydz\end{aligned} \tag{5-23}$$

Assuming the principal directions of the strain are the same as those of the covariance matrix, then the non-diagonal components of the covariance matrix should be all zeroes. Take the covariance between the element x and element y as an example, the non-diagonal components of the covariance matrix can be calculated as follows:

$$\begin{aligned}\mathrm{cov}(x,y) &= \iiint_{\Omega} p(x,y,z)(-xy)dxdydz \\ &= \iint_{\Omega} p_z(x,y)(-xy)dxdy = \sum_{i=1}^{4}\iint_{\omega_i} p_z(x,y)(-xy)dxdy \\ &= \iint_{\omega_1}\left[(xy)\left(p_z(-x,y)+p_z(x,-y)-p_z(x,y)-p_z(-x,-y)\right)\right]dxdy \\ &= 0\end{aligned}$$

(5-24)

Eq. 5-24 shows that under the principal axes, the covariant of element x and y is zero. With a similar method, it can be revealed that all non-diagonal components in the covariance matrix are zeroes. Therefore, the covariance matrix of the probability density function $p(x,y,z)$ of the reinforcements orientations shares a same set of principal directions with the strain. Therefore, it can be concluded that the principal directions of the orientation distribution of the reinforcements are determined by the principal directions of the plastic strain.

5.5.3 Influence of principal strains to orientations of TiBw

Based on previous discussions, it is revealed that the relationship between plastic deformation and orientation distributions of reinforcements is the simplest under the principal frame, therefore the discussion in the present section is based on the principal frame.

the analytical description of the 3-dimensional relationship between the principal strains and the orientational distribution of short fibers is not seen in the literature yet, however, the 2-dimensional relationship has been sufficiently researched in recent decades [91- 96]. Therefore, it will be most convenient to start the attempt by projecting the fiber orientations onto 2-dimensional planes. Regretfully, projecting the probability density function $p(x,y,z)$ directly onto the xy-plane, yz-plane or zx-plane produces singularity on the boundary. Therefore, the fiber orientations are described with the tilting angle instead of rectangular coordinate to avoid the singularity.

The definition of the tilting angles α, β, and γ is schematically shown in Fig. 5.14. In the principal frame, take an arbitrary orientation vector (x,y,z) and project the vector onto the xy, yz, and zx-planes, three projected 2-dimensional vectors, (x,y), (y,z) and (x,z) can be obtained.

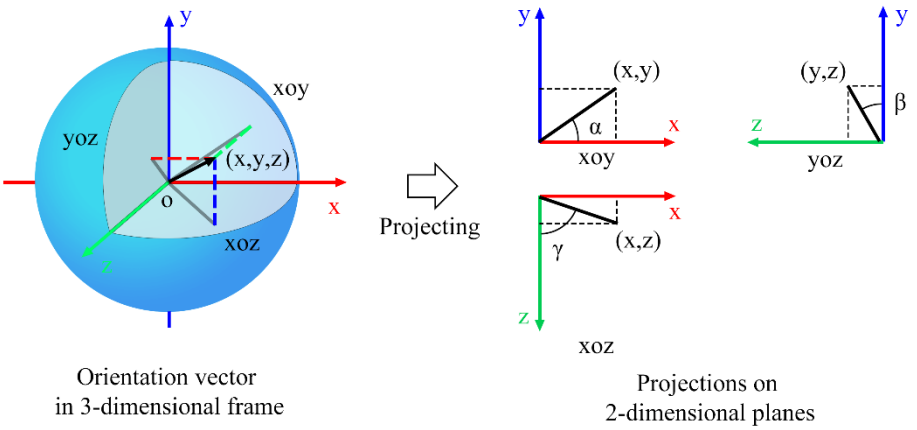

Fig. 5.14 Definition of tilting angles of TiBw

The tilting angles α, β and γ of this vector are then defined in a similar manner that used in the 2-dimensional analysis [91]: The angle between the x-axis and vector (x,y) on the xy-plane is defined as α, the angle between the y-axis and vector (y,z) on the yz-plane is defined as β, and the angle between the z-axis and vector (x,z) on the zx-plane is defined as γ. The relationships between x, y, z and α, β, γ are expressed as:

$$\begin{cases} \alpha = \arctan\left(y/x\right) \\ \beta = \arctan\left(z/y\right) \\ \gamma = \arctan\left(x/z\right) \end{cases} \tag{5-25}$$

Substituting Eq. 5-19 into Eq. 5-25, the relationship between the tilting angles of the orientation vector before and after straining can be obtained:

$$\begin{cases} \tan\alpha_1 = \dfrac{y_1}{x_1} = \dfrac{\left(1+\varepsilon_2\right)y_0}{\left(1+\varepsilon_1\right)x_0} = \dfrac{\left(1+\varepsilon_2\right)}{\left(1+\varepsilon_1\right)}\tan\alpha_0 \\ \tan\beta_1 = \dfrac{z_1}{y_1} = \dfrac{\left(1+\varepsilon_3\right)z_0}{\left(1+\varepsilon_2\right)y_0} = \dfrac{\left(1+\varepsilon_3\right)}{\left(1+\varepsilon_2\right)}\tan\beta_0 \\ \tan\gamma_1 = \dfrac{x_1}{z_1} = \dfrac{\left(1+\varepsilon_1\right)x_0}{\left(1+\varepsilon_3\right)z_0} = \dfrac{\left(1+\varepsilon_1\right)}{\left(1+\varepsilon_3\right)}\tan\gamma_0 \end{cases} \tag{5-26}$$

In which α_0, β_0, γ_0 and α_1, β_1, γ_1 are the tilting angles of the orientation vectors before and after straining, respectively. If the short fibers in a bulk composite are oriented in a uniformly random manner prior to straining, the probability of its pointing toward any direction should be equal. The probability density functions of its tilting

angles are:

$$f_0(\alpha_0) = g_0(\beta_0) = h_0(\gamma_0) = 1/\pi \tag{5-27}$$

In which f_0, g_0, and h_0 are the probability density functions that describe the distribution of the tilting angles prior to straining: α_0, β_0, and γ_0, respectively. Combining Eq. 5-26 with the relationship given in Eq. 5-27, the probability density functions of the tilting angles after straining can be obtained:

$$\begin{cases} f_1(\alpha_1) = \dfrac{d\alpha_0}{d\alpha_1} f_0(\alpha_0) = \dfrac{1}{\pi} \cdot \left(\dfrac{(1+\varepsilon_2)}{(1+\varepsilon_1)} \cos^2 \alpha_1 + \dfrac{(1+\varepsilon_1)}{(1+\varepsilon_2)} \sin^2 \alpha_1 \right)^{-1} \\ g_1(\beta_1) = \dfrac{d\beta_0}{d\beta_1} f_0(\beta_0) = \dfrac{1}{\pi} \cdot \left(\dfrac{(1+\varepsilon_3)}{(1+\varepsilon_2)} \cos^2 \beta_1 + \dfrac{(1+\varepsilon_2)}{(1+\varepsilon_3)} \sin^2 \beta_1 \right)^{-1} \\ h_1(\gamma_1) = \dfrac{d\gamma_0}{d\gamma_1} h_0(\gamma_0) = \dfrac{1}{\pi} \cdot \left(\dfrac{(1+\varepsilon_1)}{(1+\varepsilon_3)} \cos^2 \gamma_1 + \dfrac{(1+\varepsilon_3)}{(1+\varepsilon_1)} \sin^2 \gamma_1 \right)^{-1} \end{cases} \tag{5-28}$$

In which f_1, g_1, and h_1 are the probability density functions that describe the distribution of the tilting angles after straining: α_1, β_1, and γ_1, respectively. To simplify the calculation, take $a=(1+\varepsilon_2)/(1+\varepsilon_1)$, $b=(1+\varepsilon_3)/(1+\varepsilon_2)$, $c=(1+\varepsilon_1)/(1+\varepsilon_3)$, and consider the constraint induced by volume invariant: $(1+\varepsilon_1)\times(1+\varepsilon_2)\times(1+\varepsilon_3)=1$, Eq. 5-28 becomes:

$$\begin{cases} f_1(\alpha_1) = \dfrac{1}{\pi} \cdot \left(a \cos^2 \alpha_1 + a^{-1} \sin^2 \alpha_1 \right)^{-1} \\ g_1(\beta_1) = \dfrac{1}{\pi} \cdot \left(b \cos^2 \beta_1 + b^{-1} \sin^2 \beta_1 \right)^{-1} \\ h_1(\gamma_1) = \dfrac{1}{\pi} \cdot \left(c \cos^2 \gamma_1 + c^{-1} \sin^2 \gamma_1 \right)^{-1} \end{cases} \tag{5-29}$$

The relationship between the principal strains and the distribution of fiber orientations is then constructed. Eq. 5-29 demonstrates that the principal strain determines the parameters a, b, and c in the probability density function of the reinforcement orientation.

5.5.4 Calculating local strain tensor with orientations of TiBw

As discussed above, the orientation distribution of TiBw reinforcements in TMCs can be influenced by hot deformation. The principal direction of strain determines the principal direction of the covariance matrix of the probability density function of TiBw orientation distribution, while the principal strain determines the parameters in the probability density function. However, in practical situations, it is challenging to directly measure plastic strain inside of materials, while the orientation of TiBw can be easily determined with EBSD technique. Utilizing the quantitative relationships between the reinforcement orientation distribution and the plastic strain that obtained in the previous sections, it is possible to calculate the plastic strain in the hot deformed composites with the orientation distributions of TiBw.

Assuming a set of TiBw orientations with the total number of i, $[x^O_1\ y^O_1\ z^O_1]$, …… ,$[x^O_n\ y^O_n\ z^O_n]$, are measured in the sample frame, then the principal directions can be obtained by calculating the covariance matrix of the reinforcement orientation distribution. Since the probability density function corresponding to the orientation distribution of TiBw is unknown, the triple integration in Eq. 5-23 cannot be directly obtained. However, it can be approximated by mathematical expectation. We have:

$$\begin{aligned}\operatorname{cov}\left(\begin{bmatrix}x & y & z\end{bmatrix}\right) &= E\left(\begin{bmatrix} z^2+y^2 & -xy & -xz \\ -xy & x^2+z^2 & -yz \\ -xz & -yz & x^2+y^2 \end{bmatrix}\right) \\ &\approx \frac{1}{n}\sum_{i=1}^{n}\left(\begin{bmatrix} {z^O}_i^2+{y^O}_i^2 & -{x^O}_i{y^O}_i & -{x^O}_i{z^O}_i \\ -{x^O}_i{y^O}_i & {x^O}_i^2+{z^O}_i^2 & -{y^O}_i{z^O}_i \\ -{x^O}_i{z^O}_i & -{y^O}_i{z^O}_i & {x^O}_i^2+{y^O}_i^2 \end{bmatrix}\right)\end{aligned} \tag{5-30}$$

In which cov([x y z]) is the covariance matrix of the orientation vectors of TiBw reinforcements. By calculating the eigenvectors of the covariance matrix, its principal directions are obtainable:

$$\left(\operatorname{cov}\left(\begin{bmatrix}x & y & z\end{bmatrix}\right)-\lambda\right)\mathbf{e}=0 \tag{5-31}$$

In which λ is the eigenvalue and **e** is the eigenvector of the covariance matrix. By solving Eq. 5-31, three independent eigenvectors can be obtained (normalized and neglecting sign), which are the principal directions of the covariance matrix, as well as the principal directions of the strain. The principal frame can be built using the eigenvectors as the axes. Transforming the orientation vectors from the sample frame into the principal frame, the principal strain can be easily analyzed. The coordinate is carried out with:

$$\begin{bmatrix} x^P{}_i \\ y^P{}_i \\ z^P{}_i \end{bmatrix} = \begin{bmatrix} \mathbf{e_1} & \mathbf{e_2} & \mathbf{e_3} \end{bmatrix}^{-1} \begin{bmatrix} x^O{}_i \\ y^O{}_i \\ z^O{}_i \end{bmatrix} \tag{5-32}$$

In which $\mathbf{e_1}$, $\mathbf{e_2}$, and $\mathbf{e_3}$ are the principal directions of strain, which are calculated from the covariance matrix. $[x^O{}_i\, y^O{}_i\, z^O{}_i]$ is the i^{th} orientation vector under the sample frame, and $[x^P{}_i\, y^P{}_i\, z^P{}_i]$ is the i^{th} orientation vector under the principal frame.

Tilting angles of each reinforcement can be calculated with Eq. 5-25. By applying parameter estimation to the parameters, a, b, and c in Eq. 5-29, the principal strains are obtainable. The present study takes the Maximum Likelihood Estimation (MLE) as the approach for parameter estimation. MLE takes all the reinforcement orientations obtained with experiment as a sample taken from the population. The parameters are estimated by maximizing the likelihood of producing the sample from the population. The likelihood functions for each tilting angles are:

$$\begin{cases} L_\alpha\left(a\middle|\alpha_1,...,\alpha_n\right) = \prod_{i=1}^{n} f_a\left(\alpha_i\right) = \dfrac{1}{\pi^n}\prod_{i=1}^{n}\left(a\cos^2\alpha_i + \dfrac{1}{a}\sin^2\alpha_i\right)^{-1} \\ L_\beta\left(b\middle|\beta_1,...,\beta_n\right) = \prod_{i=1}^{n} g_b\left(\beta_i\right) = \dfrac{1}{\pi^n}\prod_{i=1}^{n}\left(b\cos^2\beta_i + \dfrac{1}{b}\sin^2\beta_i\right)^{-1} \\ L_\gamma\left(c\middle|\gamma_1,...,\gamma_n\right) = \prod_{i=1}^{n} H_c\left(\gamma_i\right) = \dfrac{1}{\pi^n}\prod_{i=1}^{n}\left(c\cos^2\gamma_i + \dfrac{1}{c}\sin^2\gamma_i\right)^{-1} \end{cases} \tag{5-33}$$

In which α_i, β_i, and γ_i are the tilting angles calculated from the i^{th} orientation vector. Multiplying the likelihood functions in Eq. 5-33, taking the logarithm and ignoring the constant produced, the comprehensive likelihood function is obtainable:

$$L'\left(a,b,c\middle|\alpha_1,\beta_1,\gamma_1,...,\alpha_n,\beta_n,\gamma_n\right)=-\sum_{i=1}^{n}\ln\left(a\cos^2\alpha_i+\frac{1}{a}\sin^2\alpha_i\right)$$
$$-\sum_{i=1}^{n}\ln\left(b\cos^2\beta_i+\frac{1}{b}\sin^2\beta_i\right)-\sum_{i=1}^{n}\ln\left(c\cos^2\gamma_i+\frac{1}{c}\sin^2\gamma_i\right) \quad (5\text{-}34)$$

Substituting all the tilting angles into Eq. 5-34, and searching for the *a*, *b*, and *c* that maximize Eq. 5-34, the maximum likelihood estimations of each parameter are obtained. Utilizing the volume constancy during plastic deformation, which gives $(1+\varepsilon_1)\times(1+\varepsilon_2)\times(1+\varepsilon_3)=1$, the principal strains can be calculated from *a*, *b*, and *c*:

$$\begin{cases}\varepsilon_1=\left(c/a\right)^{1/3}-1\\ \varepsilon_2=\left(a/b\right)^{1/3}-1\\ \varepsilon_3=\left(b/c\right)^{1/3}-1\end{cases} \quad (5\text{-}35)$$

Substituting the principal strains and principal axes back into Eq. 5-15, the strain tensor in the sample frame can be obtained, thus giving the local strain in the hot deformed composites by the orientation distributions of TiBw reinforcements.

5.5.5 Error analysis by simulations

Simulative approach was taken to examine the performance of the present method under different conditions. The procedure is illustrated in Fig. 5.15:

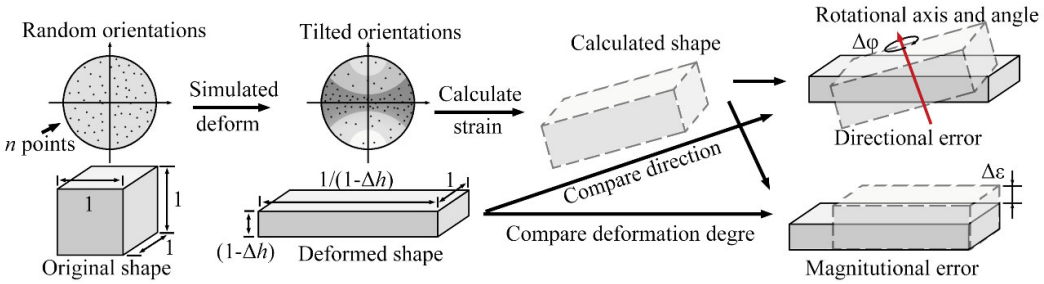

Fig. 5.15 The procedure for simulated error analysis

Firstly, a set of *n* randomly distributed orientation vectors is generated, to simulate the orientation distribution of reinforcements in the composites before plastic deformation. It is assumed that the material is initially a 1×1×1 cubic. Then, the material is subjected to a simulated rolling, resulting in a reduction in height by Δh, the length becomes $1/(1-\Delta h)$, and the width remains unchanged. Based on this, the

initial orientation vectors are rotated according to Eq. 4.13 and 4.14. The rotated orientation vectors are used to calculate the principal axes and the principal strains. The angular difference $\Delta\varphi$ between the calculated principal direction and the set deformation direction is taken as the directional error, and the difference $\Delta\varepsilon$ between the calculated height reduction and the set height reduction is taken as the error of strain magnitude. $\Delta\varphi$ and $\Delta\varepsilon$ are calculated for n = 50, 100, 200, 400, 800, and Δh = 0, 0.1, 0.2, 0.3, 0.4, 0.5, 0.6, 0.7, 0.8, 0.9, 0.95. For each n and Δh, simulations are performed on 500 different sets of randomly generated orientation vectors for statistical analysis. The results are shown in Fig. 5.16.

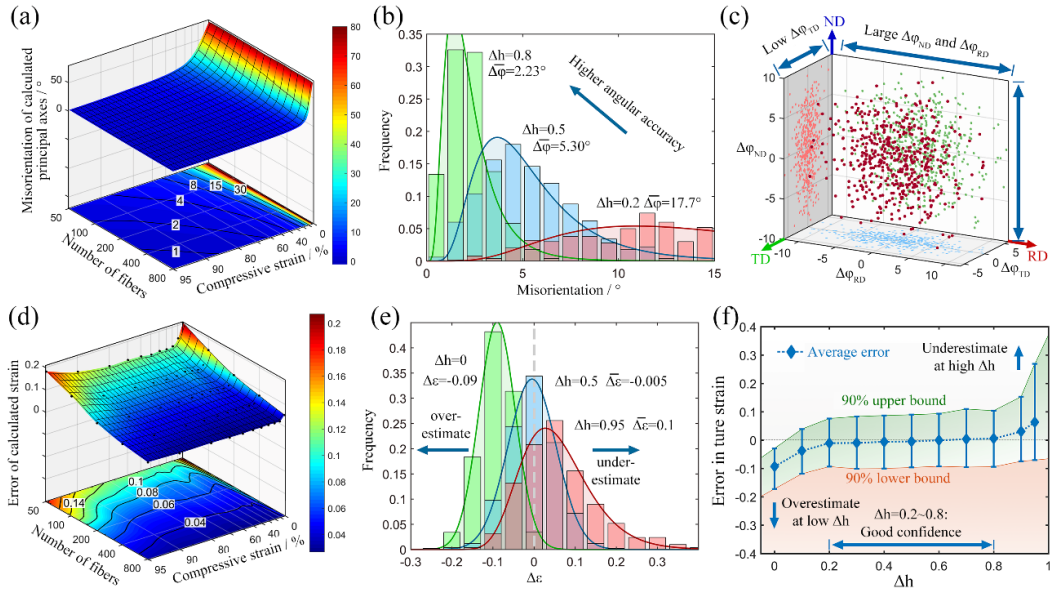

Fig. 5.16 Results of the simulated error analysis. (a)-(c): The misorientations between the principal axes of calculated and the exerted strain, (a) average misorientation at different conditions; (b) misorientation distribution at different Δh when n=200; (c) misorientation scatterplot in axis-angle space when Δh=0.8 and n=200; (d)-(f) The error between the magnifications of calculated strains and exerted strains: (d) Average error at different conditions, (e) error distribution at different Δh when n=200, (f) interval with good confidence when n=200

As shown in Fig. 5.16 (a), the calculated strain has significant misorientation between the pre-set strain at low Δh or n. With the increase of Δh or n, the directional error decreases drastically, an average misorientation lower than 15° is obtainable when n>200 and Δh>0.4. The directional error of calculated strain obeys log-normal distribution, as shown in Fig. 5.16 (b). The increase of Δh results in both higher accuracy and lower error dispersion. Fig. 5.16 (c) shows the scatter plot of misorientations at n=200 and Δh=0.8 in the axis-angle space. Each point in Fig. 5.16 (c) represents the misorientation of a calculated strain, the line connecting the

origin and the point represents the rotation axis, and the distance between the point and the line represents the misorientation angle. It is revealed that the misorientation is higher about the RD and ND, and lower about the TD.

The directional error reflects the difference between the principal directions of the covariance matrix of the orientation vectors and the principal directions of the strain, as the principal directions of the strain are determined by the covariance matrix of the orientation vectors. Theoretically, the covariance matrix calculated from Eq. 4.23 have the same principal directions as the plastic strain, without any error. However, since the measured number of reinforcements is finite, the continuous probability density function can be only estimated with discrete measurements, leading to directional errors.

Considering the measured orientation of reinforcement as a sample drawn from a population following a certain probability density function, on one hand, a smaller sample size makes the samples harder to accurately reflect the population, resulting in poorer accuracy. On the other hand, the discrete reinforcement orientations include not only the anisotropy caused by plastic deformation, but also that from the sampling randomness. At low deformation degree, the anisotropy caused by plastic deformation is weaker compared to that caused by sampling randomness. Hence, there is a significant difference between the principal directions of the covariance matrix and the plastic strain. As the deformation increases, the anisotropy caused by plastic deformation becomes more prominent, whereas the influence of sampling randomness decreases. Consequently, with larger deformation, the computed principal directions of strain become more accurate. The variations of errors at different directions observed in Figure 4.16 (c) are also caused by the varying intensity of anisotropy caused by plastic deformation in different directions. The anisotropy of the reinforcement orientation resulting from strain is strongest in the RD and ND. Therefore, the computed principal directions are less likely to tilting away from the RD and ND, resulting in higher accuracy about TD.

The error of strain magnitude exhibits a different distribution compared to that of the direction, as shown in Fig. 5.16 (d). While the average error of strain magnitude decreases monotonously with n, increased error is observed at both low Δh and high Δh. As displayed in Fig. 5.16 (e), the error of strain magnitude obeys normal

distribution. Contradicting to that of the directional error, the error of strain magnitude shows narrower distribution at low Δh. Meanwhile, the peak of the error distribution drifts away from $\Delta\varepsilon$=0 when Δh is too high or too low, implying the algorithm has the tendency to over-estimate the strain at low Δh and under-estimate the strain at high Δh.

The calculated deformation direction reflects the orientationality of the reinforcement distribution, while the calculated strain magnitude reflects the degree of anisotropy in the reinforcement orientation distribution. At low Δh, the anisotropy caused by deformation is weak compared to the that caused by sampling randomness. Consequently, the calculated strain magnitude primarily reflects the anisotropy induced by sampling randomness, which leads to an overestimation. Conversely, when Δh is too high, the anisotropy caused by deformation becomes pronounced. In such cases, if the number of reinforcements is limited, the sampled quantity cannot adequately represent the strong anisotropy in the population, resulting in an underestimation of the strain magnitude. In both scenarios, increasing the number of reinforcements used for calculation can enhance the accuracy of the results.

Fig. 5.16 (f) shows the variation of the error distribution with Δh when n=200. The center, the 10th percentile, and the 90th percentile of the error distribution is marked in the plot. With the increase of Δh, the error distribution becomes broader, and the center of the error moves first from negative to 0, then from 0 to positive, which is consistent with the trend seen in Fig. 5.16 (e). Noticeably, the width of error distribution and the locations of center are nearly constant between the interval $0.2 \leq \Delta h \leq 0.8$. Meanwhile, errors in this interval distribute symmetrically about 0, with 80% of the results fall within ±10% of the preset strain, indicating a favorable accuracy. It is worth noting that achieving such accuracy requires only 200 reinforcements. For the TiBw/TA15(Si) composites in the present study, more than 200 TiBw reinforcements can be obtained within an area of 200 μm × 200 μm. Therefore, this method enables the calculation of plastic strain distribution in the material in a mesoscopic resolution. Expanding the measurement area improves the accuracy of the calculation but reduces spatial resolution. Conversely, reducing the measurement area increases spatial resolution at the expense of accuracy.

5.6 Quantitative analysis of strain in TiBw/TA15(Si) composites

5.6.1 Plastic strain in hot rolled TiBw/TA15(Si) composites

To preliminarily examine the feasibility of the proposed approach, the plastic strain in the as-rolled TiBw/TA15(Si) composite, in which the distribution of plastic strain is relatively uniform, was first calculated from the orientation distribution of TiBw reinforcements. The composite was hot rolled at 950 °C with a 60% height reduction to introduce an unequal amount of strain in different directions. The microstructure of the composites before and after hot rolling is shown in Fig. 5.17.

The TiBw/TA15(Si) composite was rolled from a Φ60 mm × 20 mm cylindrical billet into a 127 mm × 68 mm × 8.7 mm ellipsoidal plate, the basal plane of the cylinder is parallel with the normal direction (ND) of the rolled plate. Judged by the change in billet dimensions, the magnitude of deformations is determined to be 112%, 13%, and -56% along the rolling direction (RD), the transverse direction (TD), and the ND, respectively. The microstructures of TiBw/TA15(Si) composite before and after rolling are shown in Fig. 5.17 (a) and Fig. 5.17 (b), TiBw reinforcements are in black contrast. Initially, the reinforcements were distributed in an equiaxed network-manner without orientation preference. After the composite was hot rolled, the network structure was elongated and the TiBw reinforcements were tilted toward the rolling direction. The orientation distribution of TiBw is revealed by $(010)_{TiB}$ pole figures shown in Fig. 5.17 (c) and Fig. 5.17 (d). The intensity of $(010)_{TiB}$ pole was evenly distributed in all directions initially but then intensified near RD and lowered near ND after rolling, indicating the rolling deformation tends to orient TiBw toward RD and away from ND.

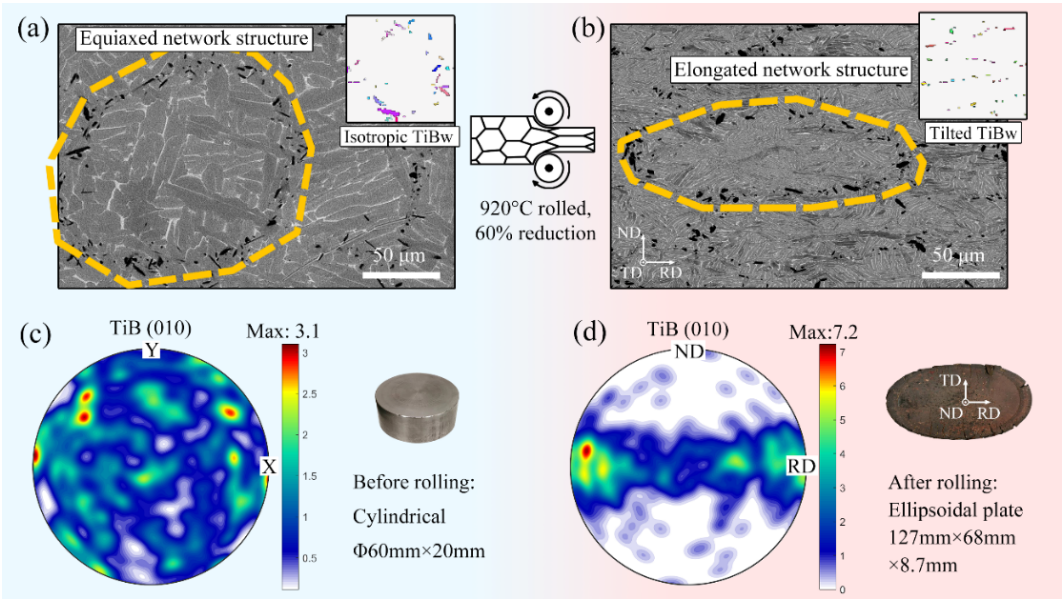

Fig. 5.17 The microstructures of TiBw/Ti composites (a) before and (b) after the hot-rolling, and the pole figures of the (010) surface of TiB (c) before and (d) after the hot-rolling

The process for calculation is illustrated in Fig. 5.18. Firstly, the orientations of TiB short fibers were extracted as orientation vectors using EBSD technique. Secondly, the principal axes of the strain were determined by calculating the rotational inertia of the orientation sphere. The orientation vectors were then converted into the principal frame. Thirdly, the principal strains were calculated by estimating the parameters in the probability density function. And finally, the strain was obtained by rotating the principal strains back into the sample frame.

When recording the orientations of TiB, the RD, ND, and TD of the rolled plate were taken as the x-axis, y-axis, and z-axis to build the observer's frame, as given in Fig. 5.18 (a). Indexed TiBw with a size smaller than 3 pixels were discarded for noise reduction, and the orientations of both [010] and [0-10] directions of the remaining TiB short fibers were recorded in the form of orientation vectors for the subsequent calculations. In the present case, a total of 227 effective measurements were obtained and 454 orientation vectors were recorded. According to the previous analysis, a good accuracy can be expected with the number of measurements over 200 and the height reduction about 60%.

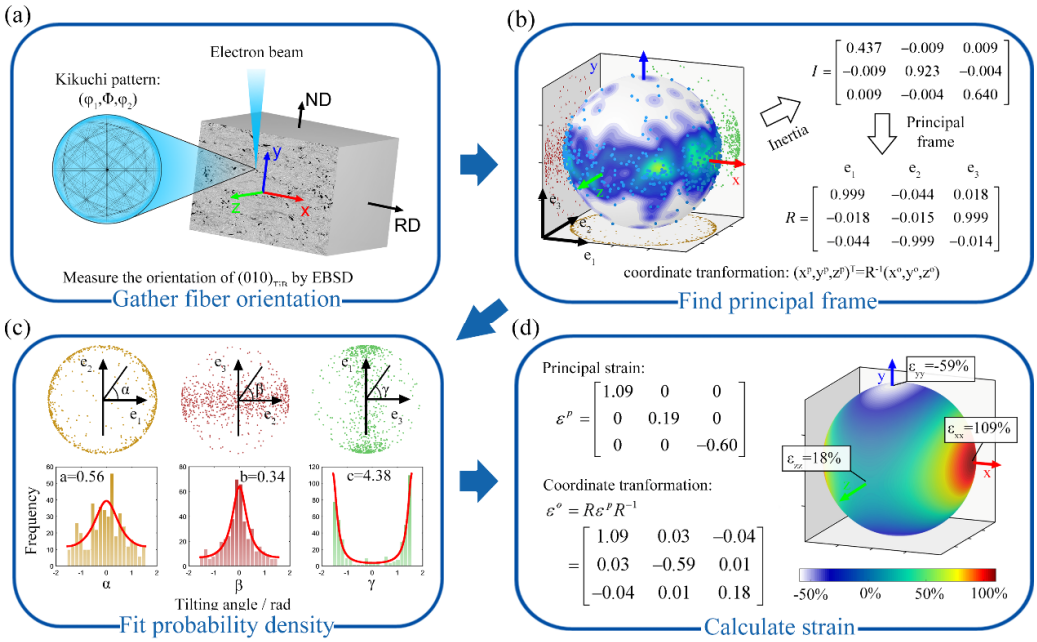

Fig. 5.18 Process of calculating the deformation status of TiBw/TA15(Si) after hot rolling,
(a) gather the fiber orientations, (b) calculate the principal directions, (c) calculate the principal strains, (d) calculate the strain tensor in the sample frame

Plotting the endpoints of the orientation vectors in the observer's frame gives the blue dots shown in Fig. 5.18 (b). the density distribution of these orientation vectors is reflected on the orientation sphere in the figure. The principal axes of the plastic deformation are derivable from the rotational inertia of the orientation vectors, by first calculating the covariance matrix as in Eq. 5-30, then solve Eq. 5-31 to obtain the eigenvectors of the matrix. The values of calculated inertia tensor **I** and eigenvectors $\mathbf{e}_1$, $\mathbf{e}_2$, and $\mathbf{e}_3$ are given in Fig. 6b. Define the rotation matrix as $\mathbf{R}=[\mathbf{e}_1, \mathbf{e}_2, \mathbf{e}_3]$, the orientation vectors can be transformed into the principal frame with Eq. 5-31.

Projecting the orientation vectors onto the planes formed by $\mathbf{e}_1\mathbf{e}_2$, $\mathbf{e}_2\mathbf{e}_3$, and $\mathbf{e}_3\mathbf{e}_1$, and calculating the tilting angles of the projected vectors by Eq. 5-25, the angular form of the orientation vectors, α_i, β_i, and γ_i are obtainable. The endpoints of the projected vectors and the distribution of α, β, and γ are shown in Fig. 5.18 (c). The distribution of the tilting angle shows good symmetry about 0°, implying the principal axes of strain were calculated correctly. The principal strains of the composites can be calculated through Eq. 5-26 by MLE. The calculated values of a, b, and c and the resultant fitting curves show are in good agreement with the distributions of orientation vectors, indicating Eq. 5-26 is suitable to describe the 3-dimensional

distribution of fiber orientations. The principal strains are then calculated from Eq. 8 to be ε_1=109%, ε_2=19%, and ε_3=-60%.

Finally, the strain tensor is obtainable by substituting the calculated principal strains and the principal axes into Eq. 5-15, which rotates the principal strains back into the observer's frame. The results are shown in Fig. 5.18 (d). The normal strains along the x-axis (RD), y-axis (ND), and z-axis (TD) are calculated to be 109%, -59%, and 18%, respectively. Notice that the normal strains along RD, ND, and TD are close to the principal strains, and the shear strains are all close to 0, because the RD, ND, and TD are close to the principal axes. The result matches well with the macroscopic deformation of the composites billet, which is 112% along RD, -56% along ND, and 13% along TD, indicating the present method can reveal the plastic deformation of TiB/TA15(Si) composite with good accuracy.

5.6.2 Strain distribution in hot compressed TiBw/TA15(Si) composites

It is already known that during the hot compression tests on Gleeble 1500D, the temperature gradients and frictional constraints significantly reduce the deformability at the ends of compression sample. To quantitatively investigate the strain distribution in the compression sample, strain tensors in different positions of the sample was calculated with the orientations of TiBw. The cross-section of the sample and the collected EBSD data are shown in Fig. 5.19. A cylindrical TiBw/TA15(Si) composite with an initial size of Φ8 mm × 12 mm was subjected to hot compression on a Gleeble 1500D platform under the conditions of 910 °C / 0.01 s^{-1} and a nominal strain of 40%. Prior to hot compression, the material underwent a solution treatment of 1050 °C / 30 min / AC. As shown in Fig. 5.19 (a), the compressed sample exhibits a barrel-like shape with a noticeable bulge at the center compared to the ends. EBSD data was gathered in a rectangular area of 11 mm × 2 mm near the center of the specimen, with a step size of 1 μm. Due to the large area collection area, the EBSD data was collected in multiple sub-regions and merged automatically. Fig. 5.19 (b)-(d) show the orientation maps of TiBw in the marked regions in Fig. 5.19 (a). It can be observed that TiBw reinforcements in region b retains a network distribution, while the region c exhibits a significant rotation of the reinforcements perpendicular to the compression direction, along with severely deformed network structures. Region d is located in the bulging region of the

sample, where the network structure formed by TiBw reinforcements is slightly compressed. Fig. 5.19 (e) presents the full data gathering area, showing that the gathering range covers one side of the specimen's edge.

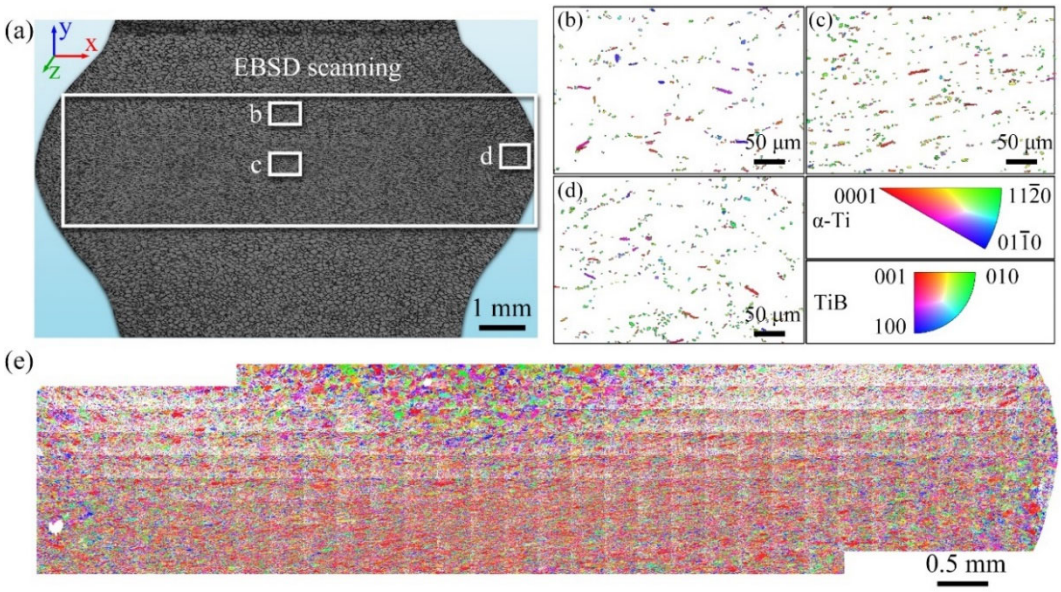

Fig. 5.19 Area for EBSD data collection of the compressive sample, (a) cross-section of the sample, (b) – (d) TiBw orientations in different regions of the sample, (e) orientations of α phase in the data collection area

The steps to construct the strain map is shown in Fig. 5.20. The raw EBSD data was first divided into several sections. In the present case, the size of each section is 200 μm × 200 μm, obtaining 39 × 11 sections in total. Secondly, the local strain tensor in each section was calculated separately following the process that discussed in the previous section. Finally, the local strains calculated in each section was merged to form the strain map. Since each strain tensor contains 6 independent components, a total of 6 strain maps presenting were given. In the present case, cubic interpolation was performed to obtain smooth results.

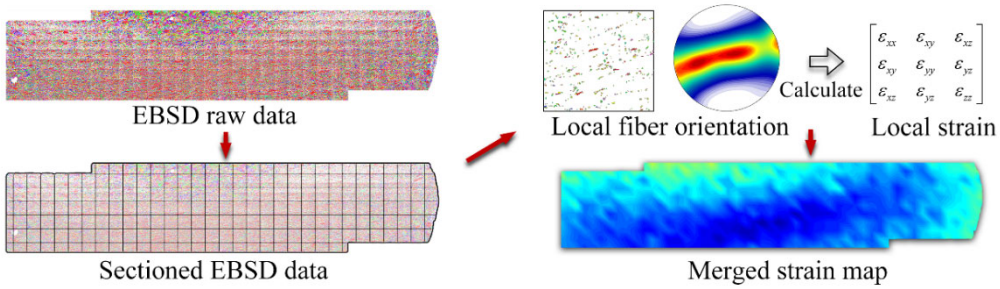

Fig. 5.20 Approach for strain distribution reconstruction in compressive sample

The strain distribution near the center of the sample calculated from the fiber orientations was shown in Fig. 5.21, each component of the strain tensor is shown separately. The distribution of the von-Mises equivalent (VME) strain calculated from the strain components via Eq. 5-36 is shown in Fig. 5.21 (b). The values of the normal strain along the x-axis, y-axis, and z-axis (ε_{xx}, ε_{yy}, and ε_{zz} in Fig. 5.21 (a)) are positive, negative, and positive, respectively, indicating that the sample was stretched along the x-axis and z-axis, and was compressed along the y-axis, a result that can be expected from the compression test.

$$\begin{aligned}\varepsilon_{VME} &= \frac{1}{3}\sqrt{2\left[\left(\varepsilon_1-\varepsilon_2\right)^2+\left(\varepsilon_2-\varepsilon_3\right)^2+\left(\varepsilon_3-\varepsilon_1\right)^2\right]} \\ &= \frac{1}{3}\sqrt{2\left[\left(\varepsilon_{xx}-\varepsilon_{yy}\right)^2+\left(\varepsilon_{yy}-\varepsilon_{zz}\right)^2+\left(\varepsilon_{zz}-\varepsilon_{xx}\right)^2\right]+6\left(\varepsilon_{xy}{}^2+\varepsilon_{yz}{}^2+\varepsilon_{xz}{}^2\right)}\end{aligned}$$

(5-36)

Most noticeably, the compressive strain is the highest at the center of the sample, reaching a maximum of -1.5 true strain, which is equivalent to ~75% height reduction. The region with high compressive strain covers a wide range along the radius direction of the sample, but a small range in the compressive direction. The region characterized by the intensive compression along the y-axis is denoted as region I. Looking upward from region I, ε_{yy} decreases rapidly from -1.5 to about -0.3, indicating the deformation was severely constrained. The region characterized by the constrained compressive strain is denoted as region II. An interesting distribution of shear strain in the xy-plane, ε_{xy}, can be observed at the "shoulder" of the sample, which is denoted as region III. Observing the bulged part of the sample, slightly negative strains along both the x-axis and y-axis are noticeable, meanwhile, the normal strain along the z-axis is significantly positive. This region is denoted as region IV.

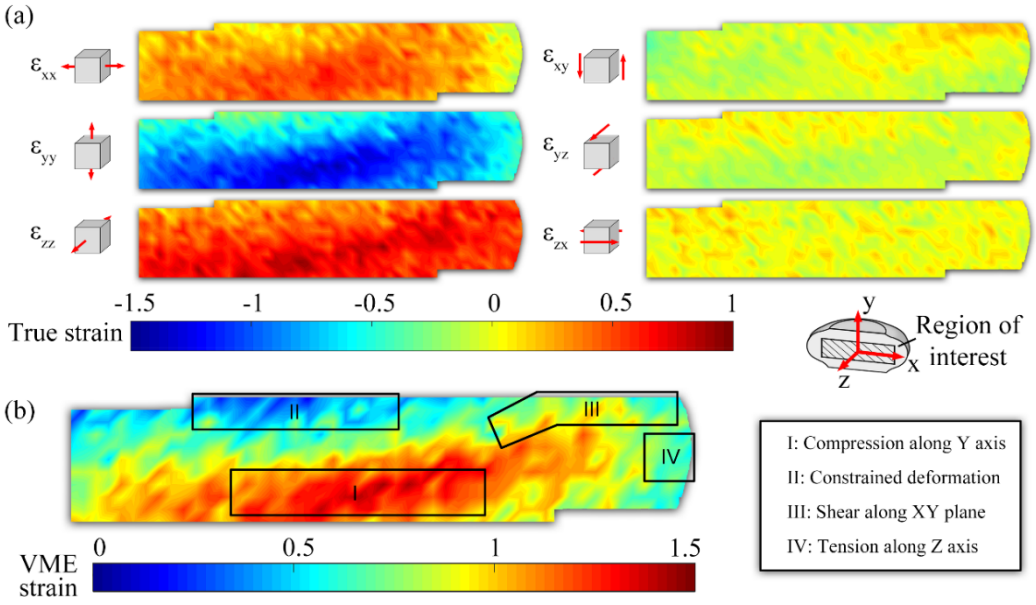

Fig. 5.21 Strain distribution near the center of hot compressive sample, (a) the distribution of different strain components, (b) the distribution of VME strain

Through the strain states of different regions, the formation of the strain distribution in the hot-compressed sample can be inferred. The center of the sample was far away from the water-cooled compression heads, therefore the temperature there was the highest throughout the sample, making it most vulnerable to plastic deformation. During the hot compressing, the center of the sample was compressed along the y-axis and expanded along the radius direction of the sample, the region I was thereby formed. The ends of the sample were cold and constrained by friction, which made it nearly impossible to be deformed. As the result, the compressive strain exerted to the sample was mostly accommodated by region I, making the compressive strain in the region I far higher than the nominal one (40%). While the region I was expanded significantly along the radius direction of the sample, region II was hardly deformed. The difference between the displacements of these two regions created a shear strain, which was then accommodated by the conjunction of them, resulting in the high ε_{xy} in the region III. The expansion of the region I lead to the bulging at the middle of the sample, which created the region IV. As the region IV moved gradually away from the compression axis, the compressive stress exerted on this region grew low. Consequently, region IV was not submitted to sever compressive strain. Instead, the constant expansion of the region I pushed the region IV to expand in its radius, resulting in the tensile-like strain state. The absence of compressive stress and the domination of tension stress in the region IV can also be evidenced by the formation of vacancies and the debonding of reinforcement

interfaces.

Fig. 5.20 (b) displays the significant variation of VME strain that ranging from 0.3 to 1.5. Hot compression tests have been adopted as an important method to reveal the microstructure evolution of materials during thermo-mechanical processing. However, the result of the present work shows that the area suitable for microstructure observations (the region I in Fig. 5.20 (b)) is less than 15% of the sample's sectioned surface. A slight deviation from the suitable area can lead to a significant change in the deformation degree, therefore a completely different microstructure. Meanwhile, the strain corresponding to the observed microstructure can be far higher than the exerted strain, and designing the manufacturing procedures based on the height reduction of compressive samples without further check can be misleading. However, utilizing the technique proposed in the present work, the relationship between the microstructure and deformation degree is easily obtainable with good accuracy, and the result can serve as strong evidence for the process design.

5.6.3 Validation of calculated strain by the deformation of TiBw networks

Since the strain state in the compressive sample shows great variety, it can be used to examine the validity of the calculation. To this end, 10 points at different locations of the compressive sample was picked out and the strain was calculated with EBSD data. The ratio of ε_{yy} and ε_{xx} was compared with the height-to-width ratios of the deformed network structure to examine the accuracy, the results are shown in Fig. 5.22. The locations of the measured points are marked in Fig. 5.22. Points 1 to 8 are located along the compressive axis of the sample. These points were submitted to uniaxial compressive strain. Point 9 is located at the bulged part of the sample and point 10 is located at the "shoulder" part of the sample.

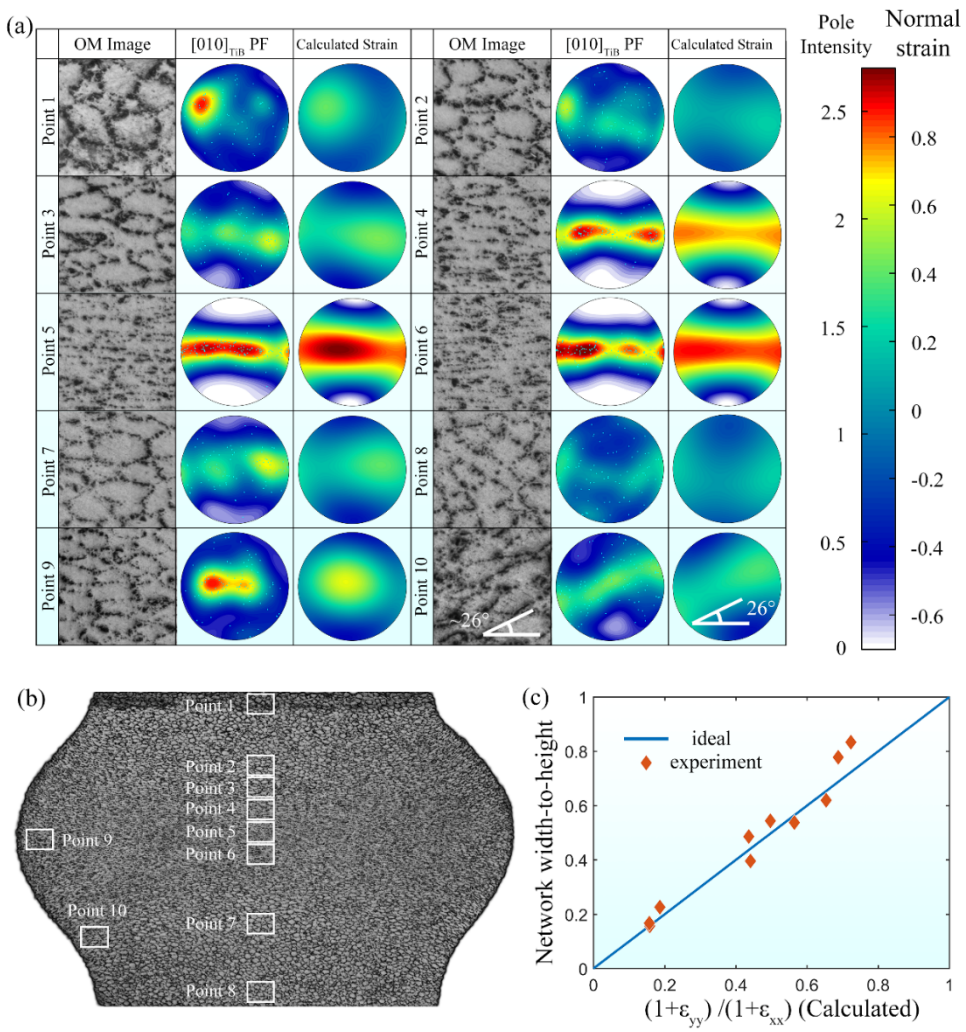

Fig. 5.22 Comparison of calculated strains the network deformations in different regions of compressive sample, (a) The morphologies of deformed network structures, the corresponding $[010]_{TiB}$ pole figures, and the calculated strain at different points on the compressive sample. (b) The locations of the selected points on the sample. (c) The comparison of ε_{yy} / ε_{xx} measured from the deformed network structures and calculated with fiber orientations, error bars reveal the standard deviations of the measured values

Observing the micrographs shown in Fig. 5.22 (a), the network structures that locate near the center of the sample were subjected to high degree of compressive deformation, which is consistent with the calculated strains. Point 9 shows a tensile strain along the z-axis, however, this strain cannot be reflected by the deformation of network structures in the xy-plane. Network structures in the point 10 were stretched by the shearing strain to form an angle with the compressive direction, which is correctly embodied by the calculated strain.

The calculated values of $(1+\varepsilon_{yy})/(1+\varepsilon_{xx})$ are compared with the height-to-width ratio of the network structures, and the results are shown in Fig. 8c. The blueline denotes

an ideal accuracy, points closer to the ideal line indicates better accuracy in the calculated strain. Most of the scattered points are distributed near the ideal line, only the points with high $(1+\varepsilon_{yy})/(1+\varepsilon_{xx})$ values shows mild discrepancy. High $(1+\varepsilon_{yy})/(1+\varepsilon_{xx})$ value implies low deformation degree, which can lead to an overestimation as analyzed in the previous section. As the result, the calculated deformation are higher than the measured ones when the measured height-to-width ratio is close to 1. Overall, the deformation of the network structures is in good agreement with the calculated value, which indicates the strain calculated from the EBSD data has good validity under various deformation status.

5.7 Summary

In this chapter, the initial microstructure of TiBw/TA15(Si) composite was refined through the solid-solution treatment, and hot compression test was conducted to the as-treated composites to investigate the hot deformation behaviors in dual-phase region. The hot deformation constitutive equation was established, and the evolution of the matrix microstructures as well as the orientation distribution of TiBw reinforcements was studied. The distribution of plastic deformation in the material after hot deformation was analyzed. The substantial results are summarized as follows:

(1) After the 1050 °C / 30 min / AC solid-solution treatment, the lamellae width in TiBw/TA15(Si) composite was refined from 10 μm to 2 μm, and the silicide particles in the matrix were completely dissolved. Hot compression tests were conducted on the solution-treated material at temperatures ranging from 870 °C to 950 °C and strain rates ranging from 1 s^{-1} to 0.001 s^{-1}. The compression stress-strain curves of the material exhibited dynamic recrystallization behavior, with the compression stress decreasing with increasing compression temperature and decreasing strain rate. Comparing with the untreated material, it was found that the solution treatment increased the peak stress during high-temperature compression and reduced the steady-state flow stress of the material.

(2) At 950 °C / 1 s^{-1}, the material forms a fully lamellar microstructure due to overheating, while under other deformation conditions, a mixed microstructure composed of equiaxed α grains and residual α/β lamellae is formed. A high content

of equiaxed α grains is obtainable at deformation temperatures and low strain rates, or at high deformation temperature and high strain rate. Silicide particles are likely to precipitate at low deformation temperatures and low strain rates. The spheroidization of lamellar microstructure is achieved through the terminal migration at the newly formed interfaces within the lamellae. The solid-solution treatment significantly refines the grains and silicide particles in the material after deformation.

(3) After the solid-solution treatment, the variation of peak stress with temperature and strain rate during hot compression can be described by Arrhenius equation of hyperbolic-sine law. The apparent activation energy for hot deformation is 623 kJ/mol, which is 30 kJ/mol higher than that of the as-sintered material, indicating that refinement of the lamellar microstructure enhances the hot deformation resistance. The processing map reveals the processing window for the solution-treated material is in the range of 900 °C to 950 °C, and 0.01 s^{-1} to 0.001 s^{-1}. The instability region is observed near 870 °C / 1 s^{-1}.

(4) The principal directions of strain in TiBw/TA15(Si) composites can be calculated using the covariance matrix of reinforcement orientations. By estimating the parameters in the probability density function of reinforcements orientation, the principal strains can be determined. Combined, the plastic strain tensor in the TiBw/TA15(Si) composite after hot deformation can be obtained. This method exhibits good accuracy within the range of compression strain from 20% to 80%. The main sources of computational error are the randomness in the initial distribution of particles and insufficient number of reinforcements to adequately estimate the probability density function.

(5) The strain distribution in hot compression samples obtained using Gleeble 1500D exhibits significant inhomogeneity. The central region of the sample experiences predominantly compressive strain, with plastic deformation reaching three times the average of the specimen. The shoulder region primarily undergoes shear strain to accommodate the deformation difference between the center and the ends. The bulging region experiences tensile strain normal to the cross-section, resulting from the expansion of the central portion of the specimen. The ends of the specimen show minimal deformation. The accuracy of the algorithm was verified

by comparing the calculated strain with the deformation of network structures in different regions in the compression specimens, and with the macroscopic deformation of as-rolled samples, which yields satisfying consistence.

Chapter 6 Microstructure and mechanical properties regulation of TiBw/TA15(Si) composites by thermo-mechanical processing and heat treatment

6.1 Introduction

In the previous chapter, the evolution of the matrix microstructure and reinforcements orientation during the hot deformation of TiBw/TA15(Si) composites in the dual-phase region were investigated. It was revealed that the solid-solution treatment effectively refines the hot deformation microstructure of TiBw/TA15(Si) composites. The ideal parameters for hot deformation were obtained from the processing map. Additionally, the strain distribution in the hot compression sample was reconstructed using TiBw reinforcements orientation, which revealed that the deformation in the center of the specimens was significantly higher than the average deformation, suggesting that higher deformation degree is required in engineering practice to achieve the same microstructure as in hot compression samples.

Based on these results, this chapter aims to prepare TiBw/TA15(Si) composites with refined microstructures using the combined technique of solid-solution treatment and isothermal hot pressing in the dual-phase region. A comparison will be made with the material obtained solely through isothermal hot pressing to analyze the influence of the solution treatment on the post-deformation microstructures and properties of the material. Subsequently, the material with refined microstructure will be subjected to heat treatment for microstructure regulation. The mechanical properties of the materials treated with parameters will be characterized through room temperature tensile tests, and the macroscopic plastic deformation behavior during the tensile process will be studied using digital image correlation (DIC) method. Upon investigating the slip system activation and dislocation configuration, the plastic deformation mechanisms of the heat-treated composites will be revealed. Furthermore, the high-temperature tensile behaviors of TiBw/TA15(Si) composites in different heat treatment states will be investigated at temperatures ranging from 700 °C to 800 °C, to reveal the hot deformability of TiBw/TA15(Si) composites

after grain refinement, and the evolution of the deformation mechanisms at different temperatures and strain rates.

6.2 Microstructure refinement of TiBw/TA15(Si) composites by isothermal hot-pressing

6.2.1 Microstructure evolution of TiBw/TA15(Si) composites after isothermal hot-pressing

Large billets before and after solid solution treatment were isothermally pressed using the ideal processing parameters obtained with the processing map, and compared for the microstructures and mechanical properties, in order to reveal the influence of solid solution to the microstructure evolution and the strengthening effects of the deformed composites. The procedure for the isothermal hot pressing is schematically illustrated in Fig. 6.1. The isothermal hot pressing was conducted within a vacuum hot-pressing furnace. A cylindrical ST-Ti billet sized Φ40×40 mm was first loaded into the furnace, and the furnace was then pumped to a vacuum of ≤ 0.01 Pa, after that, the billet was heated to 920 °C and held for 20 min, followed by compressing with a hydraulic press to 25% of its original height. The compress deformation was finished within 7 min so that the strain rate was estimated to be 0.003 s^{-1}. Once the deformation is completed, the heating and pressing were immediately terminated, the deformed composite billet was then cooled within the furnace to room temperature. The deformed ST-Ti billet is denoted as STP-Ti. For comparison purpose, a S-Ti billet was also treated with the same route, the deformed S-Ti billet is denoted as SP-Ti.

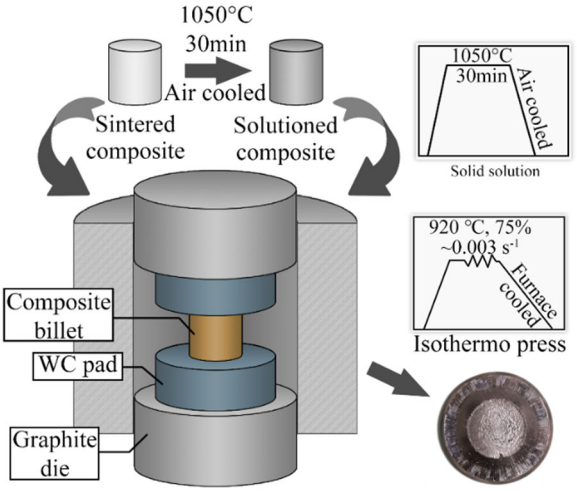

Fig. 6.1 Schematic diagram of isothermal hot pressing of TiBw/TA15(Si) composite

The microstructures of the material after isothermal hot pressing are shown in Fig. 6.2. Fig. 6.2 (a) and (c) show the microstructures of the untreated material after isothermal hot pressing, revealing a compressed network structure with residual lamellar structures in the matrix, which are oriented perpendicular to the compression direction. At higher magnification, partial decomposition of the β phase is observed, and the α lamellae retains coarse morphology. Besides, significant silicide precipitates around the α/β interfaces are seen. Sudden change of the electron channeling contrast are observable within the α lamellae, indicating the presence of multiple α grains.

Fig. 6.2 (b), (d), and (e) show the microstructures of the material after heat treatment and subsequent isothermal hot pressing. Similar to SP-Ti, the network structure in STP-Ti is compressed during deformation, but STP-Ti exhibits a finer matrix microstructure. It can be observed at high magnification that the matrix of STP-Ti consists of numerous equiaxed α grains with the size of ~2 μm. The laminated β phase are mostly decomposed, with only a small amount preserved. Due to the slow cooling rate after hot pressing, a significant amount of silicide particles are precipitated in the matrix. No significant difference is observed between the microstructures of STP-Ti at the center and the edge of the billet, indicating good uniformity. Compared to the microstructures obtained from hot compression tests, the proportion of equiaxed α grains is higher after isothermal hot pressing, with a higher amount of silicide particles precipitated in coarser size, which is attributed to the slow cooling rate after isothermal hot pressing. The prolonged cooling

allowed for the sufficient element diffusion and static recrystallization in the titanium alloy matrix, which promoted a more completed spheroidization. Additionally, the slower cooling rate provided sufficient time for silicide particles to precipitate and grow. It is noticed that there are quite a few silicide particles distributing at α-grain boundaries. Considering the silicide particles mainly located inside of α phase and α/β boundaries after hot compression test, this phenomenon may imply the migration of α-grain boundaries is impeded by silicide particles, slowing the grain growth of α-grains during the prolonged cooling stage.

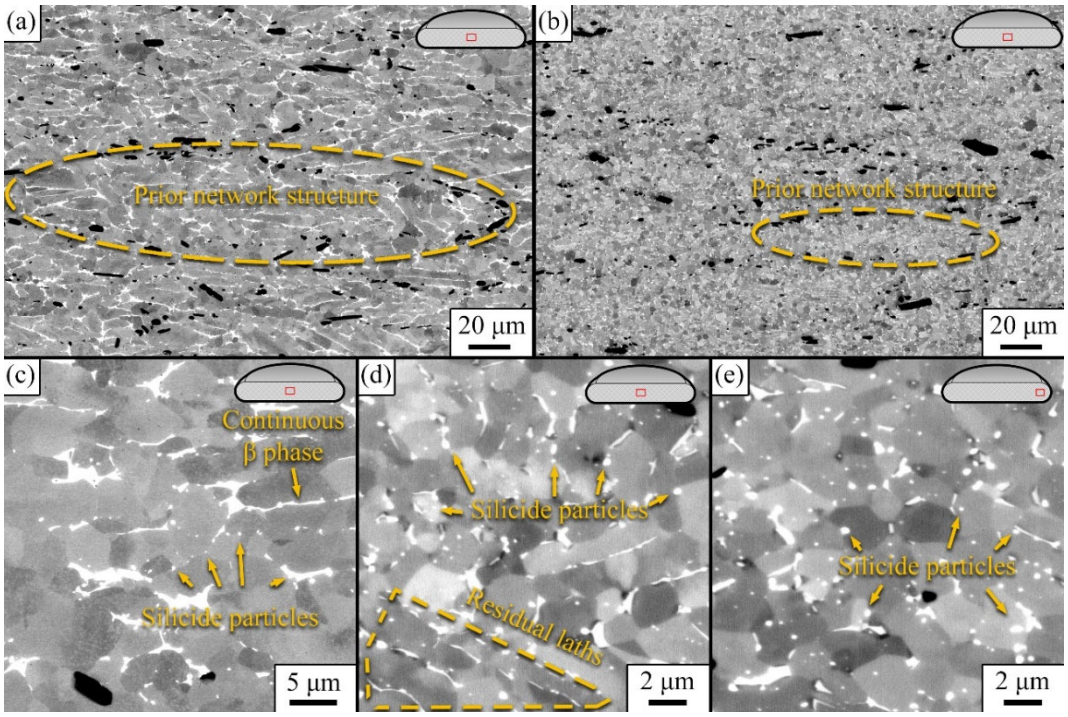

Fig. 6.2 Microstructures in TiBw/TA15(Si) composites after isothermal hot pressing, (a) center of SP-Ti billet in low magnification, (b) center of STP-Ti billet in low magnification, (c) center of SP-Ti billet in high magnification, (d) center of STP-Ti billet in high magnification, (e), edge of STP-Ti billet in high magnification

The TEM images showing the morphology and the distribution of silicide particles before and after isothermal hot press are shown in Fig. 6.3. It can be seen from Fig. 6.3 that the silicide particles have no fixed shape. They tend to precipitate at α/β boundaries in S-Ti and SP-Ti. While in STP-Ti, the silicide particles are observed both inside of α grains and at grain boundaries. The enrichment of Zr is seen in the silicide, which implies the silicide can be either $(Ti,Zr)_5Si_3$ (s_1 type) or $(Ti,Zr)_6Si_3$ (s_2 type). Both types of silicides are hexagonal structure, but their lattice constants are different.

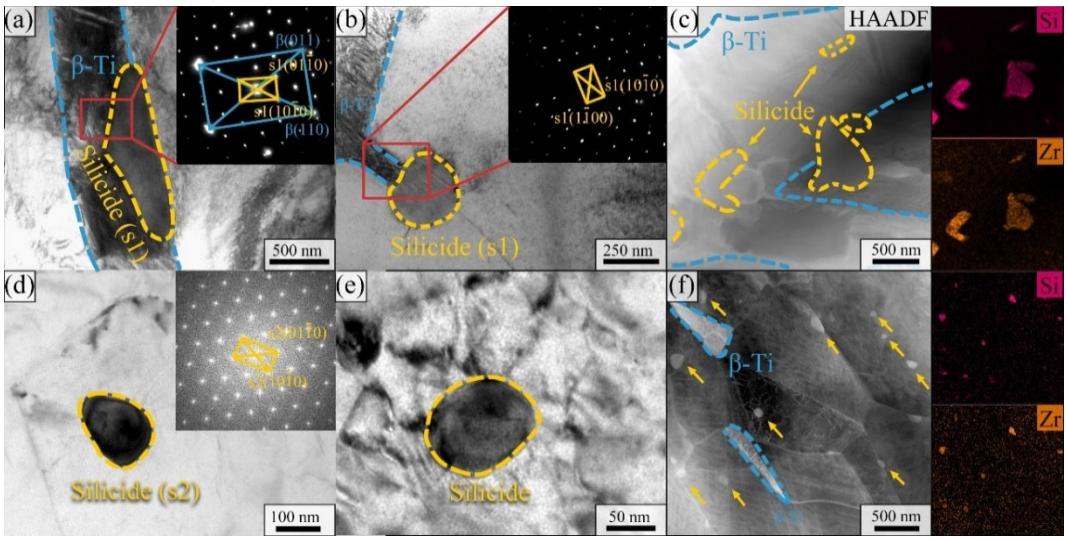

Fig. 6.3 TEM analysis of silicide particles in the composite after isothermal hot pressing, (a) – (c) silicide particles in β-phase of SP-Ti, (d) – (f) silicide particles in STP-Ti

Through select area electron diffraction (SAED), both silicide particles of s_1 type and s_2 type are identified in S-Ti, orientation relationships: $\{110\}_\beta//\{11\text{-}20\}_{s2}$, $<111>_\beta//<1\text{-}100>_{s2}$ and $\{110\}_\beta//\{1\text{-}100\}_{s2}$, $<111>_\beta//<0001>_{s2}$ are found between β-Ti and the adjacent silicide particles, implying the silicide particles are nucleated inside of β-Ti. Silicide particles seen in SP-Ti are mainly s_1 type, however, the orientation relationship between silicide and β-Ti is not necessarily preserved. Silicide particles seen in STP-Ti is significantly finer than those seen in S-Ti and SP-Ti, with the average size smaller than 100 nm. No obvious orientational relationship is observed between the silicide particles and α grains in STP-Ti, indicating the orientation relationship might be lost during the nucleation and the growth of α grains.

EBSD technique was employed to investigate the crystal orientations in SP-Ti and STP-Ti, the results are shown in Fig. 6.4. Numerous equiaxed α grains in both SP-Ti and STP-Ti that exhibit relatively random orientations are observable Fig. 6.4. Adjacent grains with similar orientations can be seen in both materials, indicating microtexture developed during the isothermal hot pressing. Statistical analysis shows that the average grain size in SP-Ti is 3.6 μm, whereas that in STP-Ti is 1.6 μm, indicating the significant improvement in grain refinement efficiency resulted from solid-solution treatment. Fig. 6.4 (c) and (d) show weak textures of $(11\text{-}20)_\alpha$ parallel to the compression direction (CD) and $(0001)_\alpha$ parallel to the radial direction (RD) in both SP-Ti and STP-Ti, with slightly higher pole intensity is

observed in STP-Ti compared to SP-Ti.

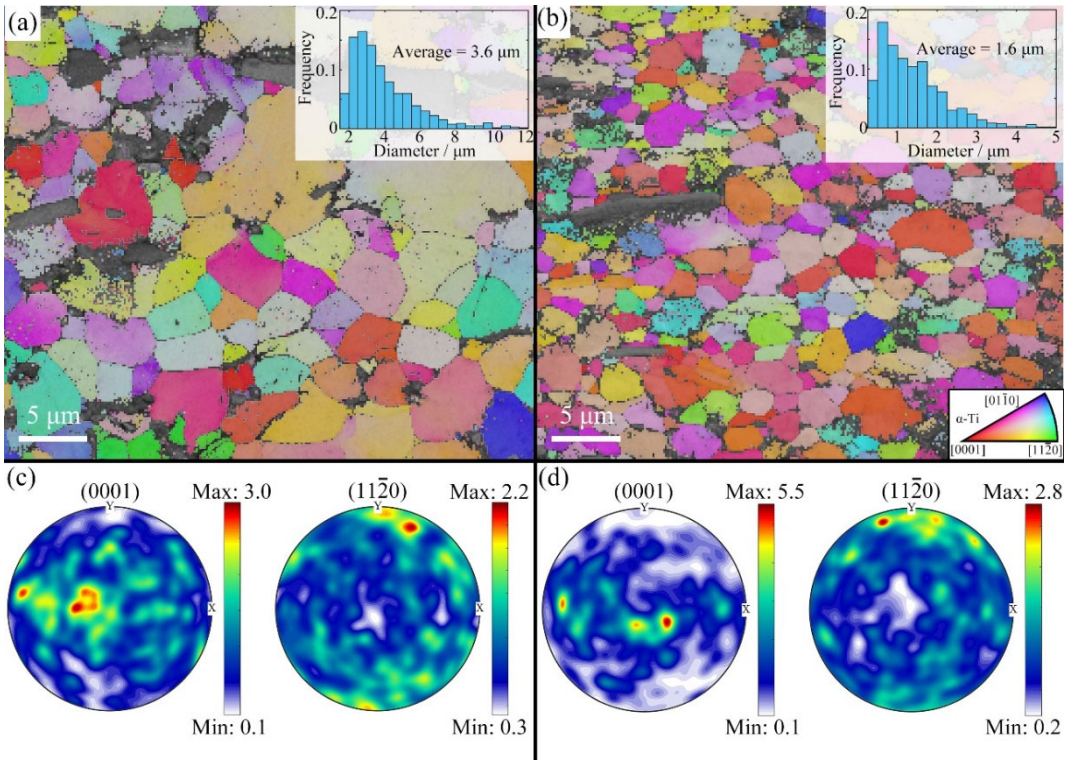

Fig. 6.4 Crystal orientations of α phase in composites after isothermal hot pressing (a) SP-Ti, orientation distribution map of α phase, (b) STP-Ti, orientation distribution map of α phase, (c) SP-Ti, pole figures of α phase, (d) STP-Ti, pole figures of α phase

The crystal orientation obtained from EBSD can be used to calculate the distribution of Geometrically Necessary Dislocations (GNDs) utilizing the lattice curvature. The degree of lattice curvature is related to the type of dislocations and their Burgers vectors. Pantleon proposed that the lattice curvature induced by each dislocation can be described by a curvature tensor [133]:

$$\kappa^{D} = |b|\left(e_b \otimes e_\xi - \frac{1}{2}\mathrm{trace}\left(e_b \otimes e_\xi\right)\right) \tag{6-1}$$

In which κ^{D} is the curvature tensor, b is the Burgers vector, e_b is the unit vector with a same direction as the Burgers vector, e_ξ is a unit vector with a same direction as the dislocation line.

The total lattice curvature is composed by the curvature resulted from each dislocation:

$$\kappa = \sum_{i=1}^{N} \rho^{D}{}_{i} \kappa^{D}{}_{i} \tag{6-2}$$

In which κ is the total lattice curvature tensor, $\rho^{D}{}_{i}$ is the density of the i^{th} type dislocation, $\kappa^{D}{}_{i}$ is the curvature lattice of the i^{th} type dislocation, N is the total number of dislocation types.

Eq. 5.2 indicates that the total lattice curvature tensor is a linear combination of the curvature tensors corresponding to each type of dislocation, where the coefficients represent the density of each dislocation type. However, due to the infinite possible combinations of dislocation tensors to form the total curvature tensor, Eq. 5.2 alone cannot determine the dislocation density in the material. Therefore, Pantleon further assumes that the dislocation configuration in the material tends to minimize the total energy of dislocations, which can be expressed by the following equation:

$$W = \sum_{i=1}^{N} \rho^{D}{}_{i} w^{D}{}_{i} \tag{6-3}$$

In which W is the total energy of dislocations, $w^{D}{}_{i}$ is the relative elastic strain energy of each type of dislocations.

By minimizing the energy in Eq. 5.3 while obeying Eq. 5.2, the density of each type of dislocation can be calculated. The dislocation types, and the Burgers vectors and relative elastic strain energy of each type of dislocation used for calculations are presented in Table 6.1, and the calculated dislocation density distributions in ST-Ti and STF-Ti are shown in Fig. 6.5.

In Fig. 6.5 (a), it can be observed that there are numerous interwoven structures with a dislocation density of approximately 10^{15} /m^2 in SP-Ti. Some line-like structures with dislocation densities of approximately 10^{16} /m^2 can also be observed, which may represent subgrain boundaries. It can be seen in Fig. 6.5 (b) that the dislocation density in STP-Ti is significantly lower than in SP-Ti, besides, grains with small sizes and equiaxed morphologies tend to exhibit low dislocation densities, while grains with large sizes and elongated morphologies typically exhibit high dislocation densities.

Table 6.1 Properties of dislocations of different slip systems in α-Ti

Type	Slip plane	Direction of Burgers vector	Magnitude of Burgers vector/ nm	Relative energy	Number of symmetries
Edge basal	{0001}	<11-20>	2.9	1	3
Edge prismatic	{1-100}	<11-20>	2.9	1	3
Edge pyramidal <a>	{1-101}	<11-20>	2.9	1	6
Edge pyramidal <c+a>	{1-101}	<11-23>	5.6	3.56	12
Screw <a>	—	<11-20>	2.9	0.68	3
Screw <c+a>	—	<11-23>	5.6	2.43	6

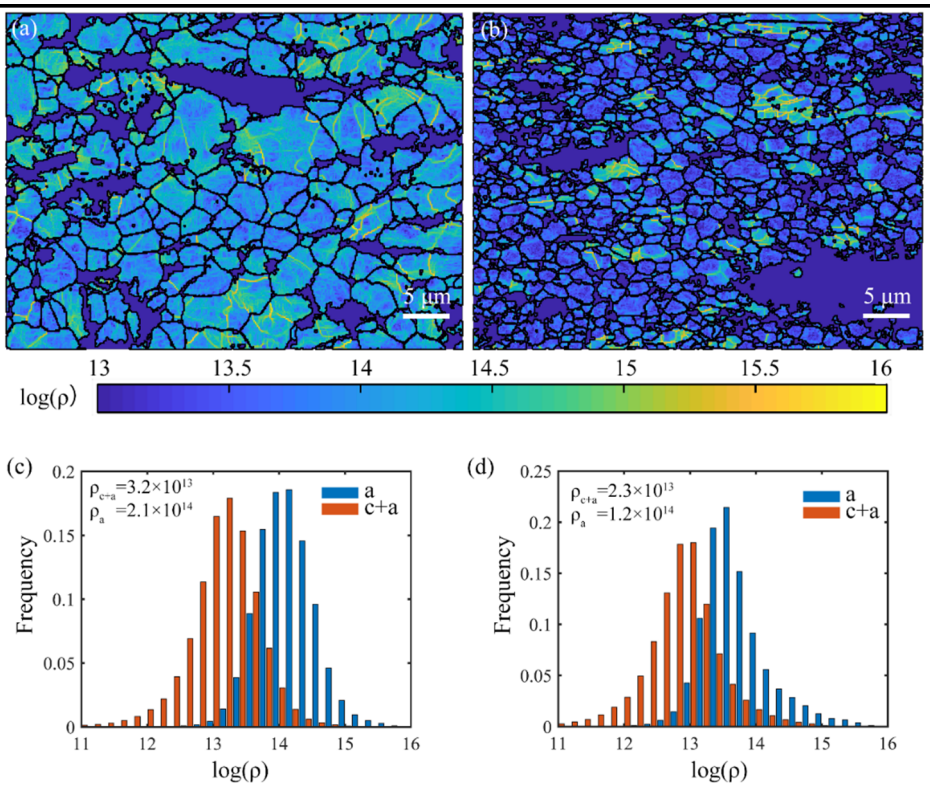

Fig. 6.5 Dislocation densities in SP-Ti and SPT-Ti, (a) dislocation density map in SP-Ti, (b) dislocation density map in STP-Ti, (c) dislocation density distribution in SP-Ti, (d) dislocation density distribution in STP-Ti

Fig. 6.5 (c) and (d) present the frequency distribution of dislocation density in the material, showing a roughly logarithm normal distribution. The density of <c+a> type dislocations is one order of magnitude lower than that of <a> type dislocations, primarily due to the high elastic strain energy and unfavorable activation. In SP-Ti, the density of <a> type dislocations is 2.1×10^{14} /m^2, the density of <c+a> type dislocations is 3.2×10^{13} /m^2, and the total dislocation density is 2.4×10^{14} /m^2. In STP-Ti, the density of <a> type dislocations is 1.2×10^{14} /m^2, the density of <c+a> type dislocations is 2.3×10^{13} /m^2, and the total dislocation density is 1.4×10^{14} /m^2.

It can be observed that the geometrically necessary dislocation density in STP-Ti is approximately 40% lower than in SP-Ti. This is attributed to the more completed recrystallization of STP-Ti during isothermal hot pressing, where newly formed grains engulf a significant number of dislocations while growing. Furthermore, the lower dislocation density also contributes to the lower steady-state flow stress exhibited by STP-Ti during hot compression.

Comparing Fig. 6.2 and Fig. 6.4, it is noticeable that although α laths in SP-Ti have already decomposed into equiaxed grains, the relative positions of α phase and β phase are scarcely changed, which results in a lamellar-like morphology. This can be explained by the diffusion of β stabilizers, as schematically illustrated in Fig. 6.6.

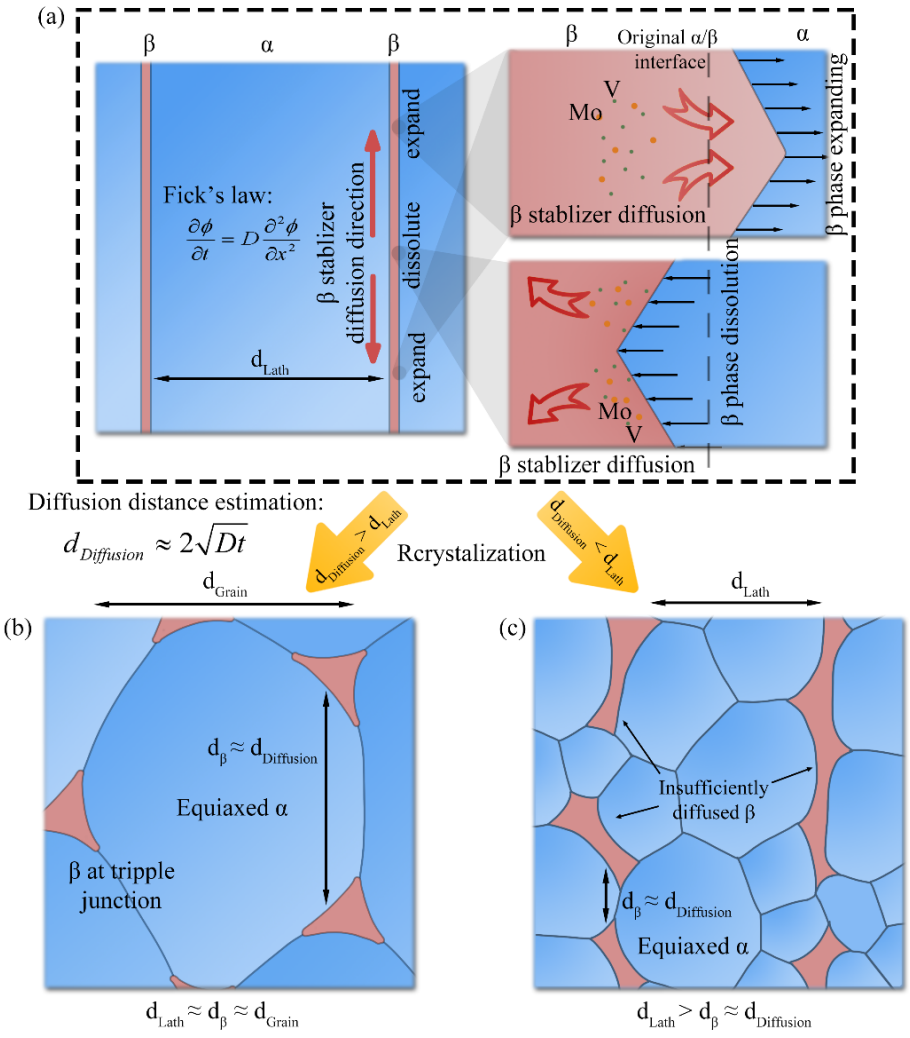

Fig. 6.6 Schematic diagram of element diffusion and lath breakdown during isothermal hot pressing, (a) The diffusion tendency of β stabilization elements in β phase, (b) and (c) the recrystallized microstructures at different conditions: (b) diffusion distance of β stabilizers greater than lath width, (c) diffusion distance of β stabilizers smaller than lath width

When new boundaries form within the lamellae and lamellae become unstable, the migration of β and α phases occurs due to chemical potential gradients, resulting in spheroidization of the lamellae. This phenomenon has been observed in this study in Fig. 5.5 and Fig. 5.7, and is schematically illustrated in Fig. 5.8. When the migration distance of the β phase, d_{β}, is greater than the interlamellar spacing, d_{Lath}, the β phase can uniformly distribute within the material after decomposition, giving the material an equiaxed morphology, as shown in Fig. 6.6 (b). However, the uniform distribution of β phase is unachievable when the migration distance is smaller than the lath width, resulting in the retained lamellar morphology, as in Fig. 6.6 (c).

During the migration of the β phase, the sites where β phase dissolves exhibit the highest concentration of β stabilizers, while the sites where β phase grows have the lowest concentration. Driven by concentration gradients, β stabilizers continuously diffuse from the dissolution sites to the growth sites to support the migration. Therefore, the migration distance of the β phase during hot deformation is controlled by the diffusion distance of β stabilizers within the β phase, which can be described by Fick's second law. The differential form of Fick's second law and its 2-D solution are given by Eq. 4-3 and Eq. 4-4. In such diffusion processes, the diffusion distance of an element can be estimated by the following the equation:

$$d_{Diffusion} = 2\sqrt{Dt} \tag{6-4}$$

In which $d_{Diffusion}$ is the diffusion distance, D is the diffusion coefficient, and t is the diffusion period.

The diffusion coefficients of β stabilizers, Mo and V, in the β phase can be calculated using Eq. 4-5. Based on parameters determined by Gibbs et al. [134] and Neumann et al. [135], the diffusion coefficients of Mo and V in β-Ti at 920 °C are 9.2×10^{-15} m^2/s and 2.9×10^{-15} m^2/s, respectively. Taking the diffusion period as t=420 s, which is the deformation time for isothermal hot pressing, the diffusion distances of Mo and V can be estimated as 3.9 μm and 7.0 μm, respectively. Comparing with the microstructure in Fig. 5.1, it is observed that the diffusion distances of Mo and V are both larger than the lamellar width of the as-treated material but smaller than

that of the as-sintered material. Consequently, STP-Ti exhibits a uniform equiaxed microstructure after isothermal hot pressing, while the untreated SP-Ti retains its lamellar microstructure.

6.2.2 Tensile properties of as-pressed TiBw/TA15(Si) composites

The tensile stress-strain curves and the strain hardening rates of the composites are shown in Fig. 6.7. The tensile properties are shown in Table 6.2. It can be seen from Fig. 6.7 (a) and Table 6.2 that, both the strength and the elongation of the composite are increased after isothermal hot pressing. Remarkably, a significant increase in the yield strength from 957MPa to 1100 MPa is obtained after the composite is processed by solid solution followed with isothermal hot press. Compared to SP-Ti, the solid solution treatment increases the yield strength of the hot-pressed composite by 8.4%, and the ultimate strength by 6.7%. However, the elongation is decreased from 11.3% to 7.7%.

Compared to the as-forged TA15 alloy [104], the tensile modulus of the composite has increased by approximately 10 GPa, which is close to the calculated value (11.2 GPa) based on the mixture rule (with a TiB volume fraction of 3.4 vol% and an elastic modulus of 440 GPa). This indicates that the improvement in tensile modulus of the composite is primarily attributed to the TiBw reinforcements. Due to the coarse grain size of S-Ti (34 μm), the strengthening effect from grain refinement is weak, resulting in significantly lower yield strength and tensile strength compared to the as-forged TA15 alloy. After isothermal hot-pressing, although the grain size of SP-Ti is still coarser than that of the as-forged TA15 alloy, both the yield ultimate strength have reached the level of the as-forged alloy. Additionally, the yield strength and tensile strength of STP-Ti are significantly higher than those of the TA15 alloy, indicating that the TiBw reinforcements and precipitated silicides have a good strengthening effect on the material. However, since the TiBw reinforcements are incapable of plastic deformation, they acted as crack initiators. As a result, the elongation of all composites is significantly reduced compared to the as-forged TA15 alloy.

As seen in Fig. 6.7 (b), S-Ti shows good strain hardening capability at the true strain of 0.02-0.03, but it drops quickly short before the fracture of the sample at

the true strain of 0.05. A special drop and regrowth of strain hardening rate is observed in STP-Ti at the true strain of 0.02, which is a unique phenomenon frequently seen in near-α Ti with equiaxed microstructure. The necking of STP-Ti is reached at the true strain of 0.06, the necking of SP-Ti occurs at the true strain of 0.08, which are both higher than that of STP-Ti, indicating the homogeneous deformation capability of TiBw/TA15(Si) composites can be enhanced by isothermal hot press.

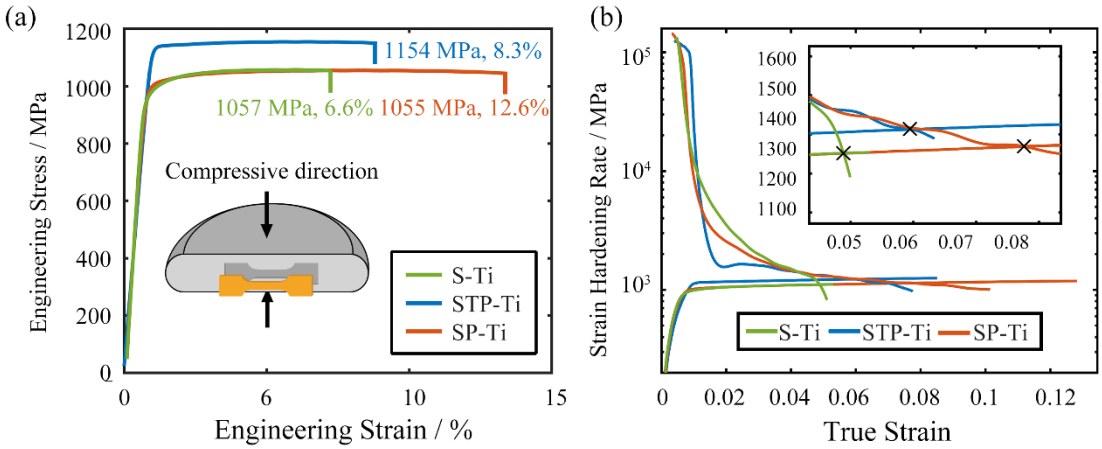

Fig. 6.7 Room temperature tensile properties of S-Ti, SP-Ti and STP-Ti, (a) typical stress-strain curves, (b) typical true stress-true strain curves and strain hardening rates

Table 6.2 Tensile properties of S-Ti, SP-Ti, STP-Ti and TA15 alloy [104]

Materials	Elastic modulus / GPa	Grain size / μm	$\sigma_{0.2}$ / MPa	Ultimate strength / MPa	Elongation %
TA15 [104]	110	2	1033	1077	19.8
S-Ti	124±7	34	957±8	1060±25	6.7±2
STP-Ti	120±12	1.6	1100±20	1136±12	7.7±1
SP-Ti	117±10	3.6	1015±6	1065±14	11.3±1

To reveal the origin of the extra strengthening effect brought about by solid-solution treatment, the contributions of different strengthening mechanisms to the yield strength of STP-Ti and SP-Ti are analyzed and compared. The theoretical strength of TiBw/near α-Ti σ_{th} is mainly contributed by the lattice friction $\sigma_{P\text{-}N}$, solid solution strengthening σ_{SS}, Grain boundary strengthening σ_{GB}, Orowan strengthening σ_{Orowan}, dislocation strengthening σ_{D}, and the strengthening of TiBw reinforcement by load transfer effect σ_{LT}. We have:

$$\sigma_{th} = \sigma_{P-N} + \sigma_{SS} + \sigma_{GB} + \sigma_{Orowan} + \sigma_{D} + \sigma_{LT} \quad (6\text{-}5)$$

The lattice friction and the solid solution in metallic materials are determined by the composition and the crystal structure of the metals. Since the composition of STP-Ti and SP-Ti are the same, the contributions of $\sigma_{P\text{-}N}$ and σ_{SS} to σ_{th} are identical. Orowan strengthening is the strengthening effect induced by the dislocations bowing around hard precipitations. In order to trigger Orowan strengthening, the hard precipitations must be present at the interiors of grains, rather than at grain boundaries [137]. Since the silicide particles that locate at grain interiors are only observed in STP-Ti, the contribution of Orowan mechanism to strength is only considered in STP-Ti and ignored in SP-Ti. Dislocation strengthening can be divided into two parts: the strengthening by geometrically necessary dislocation (GND) σ_{GND} , and the strengthening by statistically stored dislocation (SSD) σ_{SSD}. It is widely believed that the dislocation hardening is predominated by GND at the initial stage of plastic deformation [138-140]. The load-bearing effect of TiBw is depended by the volume fraction, the size, the aspect ratio and the spatial orientation of TiBw [92,141]. These features are nearly uninfluenced by hot treatment, only the aspect ratio and the orientation of TiBw can be changed by hot deformation. As the deformation conditions which determines the orientation distribution of TiBw in STP-Ti and SP-Ti are identical, the contributions of load-bearing effect to the theoretical strength are deemed to be same [94,141].

Based on the discussions above, the factors that may contribute to the extra strengthening of STP-Ti are determined as follows: the difference in grain boundary strengthening $\Delta\sigma_{GB}$, the extra Orowan strengthening of STP-Ti $\sigma_{Orowan,STP}$, and the difference in dislocation strengthening $\Delta\sigma_{D}$, which can be approximated by its GND part $\Delta\sigma_{GND}$. The difference between the theoretical strength of STP-Ti and SP-Ti is hence calculated by:

$$\Delta\sigma_{th} = \sigma_{th,STP} - \sigma_{th,SP} = \Delta\sigma_{GB} + \sigma_{Orowan,STP} + \Delta\sigma_{GND} \quad (6\text{-}6)$$

The difference in grain boundary strengthening can be calculated based on the Hall-Petch relationship [142]:

$$\Delta\sigma_{GB} = \sigma_{GB,STP} - \sigma_{GB,SP} = \frac{k_{H-P}}{\sqrt{d_{STP}}} - \frac{k_{H-P}}{\sqrt{d_{SP}}} \quad (6\text{-}7)$$

In which d_{STP} and d_{SP} are the grain size of STP-Ti and SP-Ti, respectively, k_{H-P} is the Hall-Petch constant, the value of which is 0.3 MPa·m$^{1/2}$ for titanium [137]. Take d_{STP}=1.6 μm and d_{SP}=3.6 μm, $\Delta\sigma_{GB}$ is calculated to be 74.8 MPa.

The contribution of Orowan strengthening in STP-Ti to its strength can be calculated by Orowan relationship that modified by Ashby [143]:

$$\sigma_{Orowan,STP} = \frac{0.81MGb}{2\pi(1-v)^{1/2}} \cdot \frac{\ln(d_p/b)}{\frac{1}{2}d_r\sqrt{3\pi/2f_p} - d_p} \quad (6\text{-}8)$$

In which M=2.9 is the Taylor factor [144,145], G=45 GPa is the shear modules of titanium, b=0.29 nm is the Burgers vector of type <a> dislocation in titanium, v=0.32 is the Poisson ratio of titanium, d_p=70 nm is the average diameter of silicide particles in STP-Ti (estimated from TEM images), and f_p=0.005 is the volume fraction of silicide particles in STP-Ti that locate at the grain interiors (estimated from SEM images). Substituting above parameters into Eq. 10, the contribution of Orowan strengthening to the theoretical strength of STP-Ti is determined to be 32.3 MPa.

The contribution of GND density to the difference of the theoretical strength between STP-Ti and SP-Ti can be calculated by Taylor relationship:

$$\Delta\sigma_{GND} = \sigma_{GND,STP} - \sigma_{GND,SP} = M\alpha Gb\sqrt{\rho_{GND,STP}} - M\alpha Gb\sqrt{\rho_{GND,SP}} \quad (6\text{-}9)$$

In which α is an empirical constant, the value of which is usually taken to be 0.15 for severely deformed titanium [146], $\rho_{GND,STP}$=1.4×10^{14} m^{-2} and $\rho_{GND,SP}$=2.4×10^{14} m^{-2} are the average GND density of STP-Ti and SP-Ti that previously obtained with EBSD data. The meanings and the values of M, α, G and b are the same as those in Eq. 6-8. The value of $\Delta\sigma_{GND}$ is calculated to be -20.8 MPa. Attributing to the lower recrystallization degree of SP-Ti, the GND density is higher in SP-Ti than that in STP-Ti, and the value of $\Delta\sigma_{GND}$ is therefore calculated to be negative, indicating

the dislocation strengthening in STP-Ti is less significant than that in SP-Ti.

Combining the results calculated from Eq. 6-6 to Eq. 6-9, the value of $\Delta\sigma_{th}$ is determined to be 86.3 MPa, which is close to the experimental value 85 MPa. The result shows the higher strength of STP-Ti compared to SP-Ti is originated from the refinement of α grains and the redistribution of silicide particles. Although the high recrystallization degree lowers the effect of dislocation strengthening in STP-Ti, the overall effects induced by solid solution treatment is beneficial to the strength of the hot-pressed composite.

6.2.3 Fractography of as-pressed TiBw/TA15(Si) composites

The side faces of the fractured tensile samples are shown in Fig. 6.8. It can be found in Fig. 6.8 (a) – (c) that, while the cracks of all three composites propagate perpendicular to the tensile direction, the crack of SP-Ti is frequently redirected toward the tensile direction.

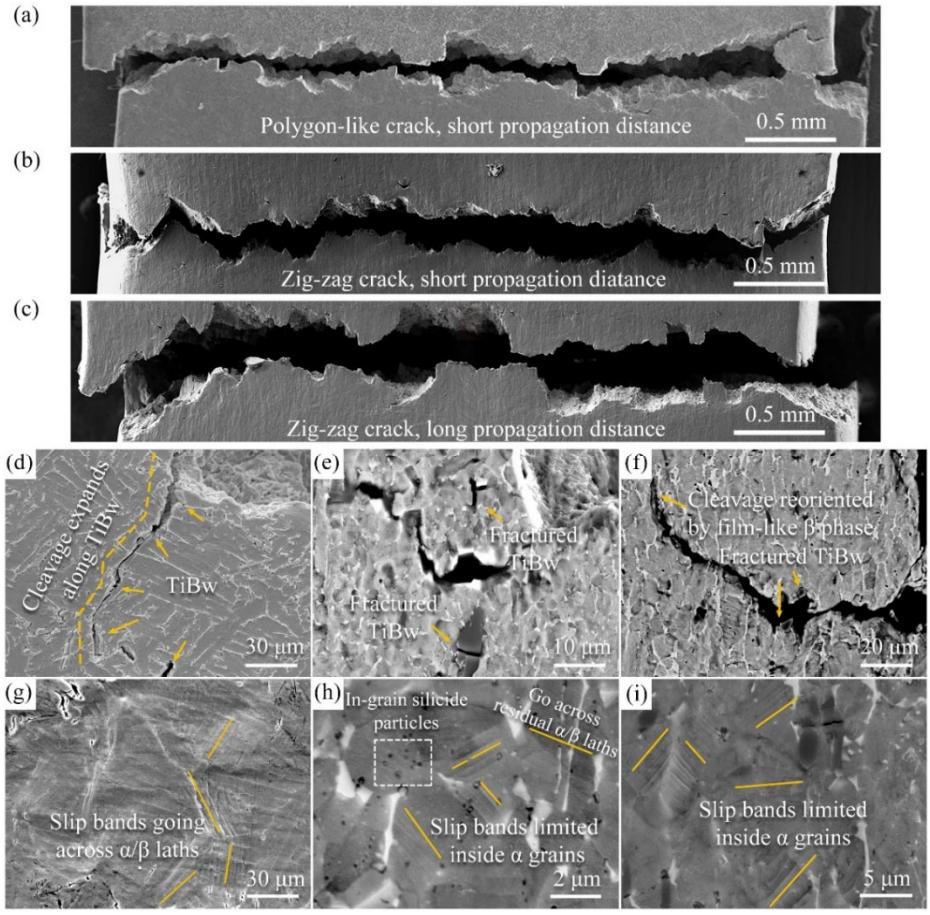

Fig. 6.8 Fracture side-faces of S-Ti, ST-Ti and STP-Ti: (a) and (d) S-Ti, (b) and (e) STP-Ti, (c) and (f) SP-Ti

At higher magnifications, cracks in S-Ti are observed to propagate along TiBw network, which create the polygon-like fracture seen in Fig. 6.8 (a). Since the strength and the elastic modules of TiBw are far higher than those of titanium matrix, there will be a high level of stress concentration in TiBw during the plastic deformation stage. As the result, cracks nucleate preferentially in TiBw reinforcements, which then link together and form the main crack, resulting in the polygon-like crack seen in S-Ti. For the same reason, cracks in STP-Ti and SP-Ti also tend to propagate along fractured TiBw.

However, since the cleavages in TiBw are preferably nucleate along the longitudinal direction of TiBw [147], the oriented TiBw by hot press can redirect the crack toward the tensile direction, leading to longer crack propagation distance and consequently, better energy absorption capability. Furthermore, oriented β laths in SP-Ti are also observed to be able to redirect the crack toward the tensile direction (Fig. 6.8 (e)), which further enhances the plasticity of SP-Ti. Intensive slipping traces are visible on the surface of S-Ti at a low magnification, as shown in Fig. 6.8 (g). The slipping traces on the surface of S-Ti are capable of going across α/β laths with identical orientations, consequently, the slipping traces can be up to 50 μm in length. The long slipping distance can lead to severe stress concentration on adjacent grains and TiBw reinforcements, causing the early yield and fracture of the tensile sample. Slipping traces observed on STP-Ti (Fig. 6.8 (h)) and SP-Ti (Fig. 6.8 (i)) are less pronounced than that on S-Ti, the length of the traces is about 2 μm for STP-Ti, and about 4 μm for SP-Ti, respectively. The slipping traces in STP-Ti are observed to go across residual α/β laths, implying the residual α/β laths may negatively influence the strength of the hot-pressed composite. Also, slipping traces are observed to going across silicide particles in STP-Ti, indicating the activation of Orowan mechanism.

The fracture surfaces of the tensile samples are shown in Fig. 6.9. A clear difference is seen between the fracture surface of S-Ti and those of the hot-pressed composites.

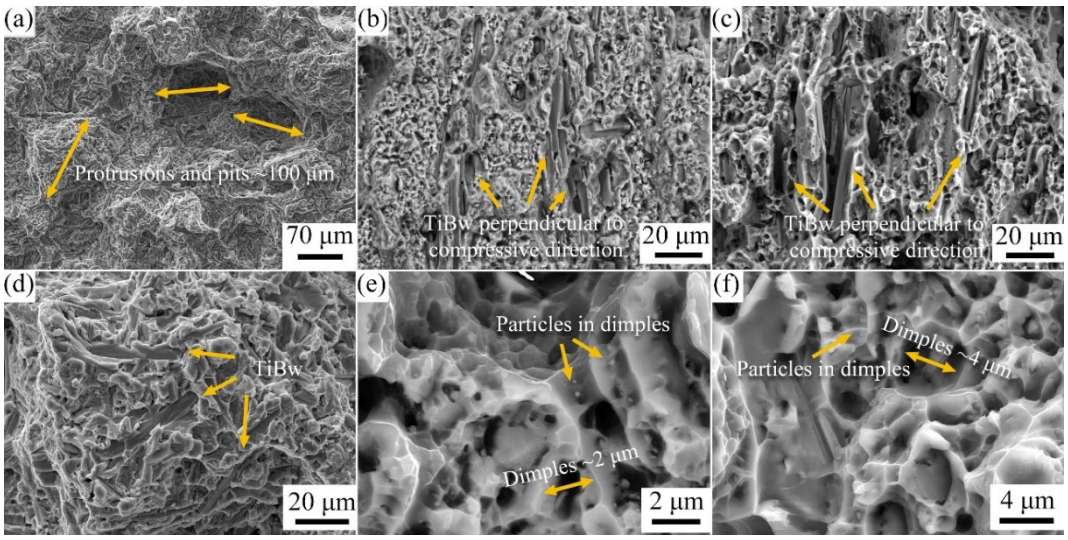

Fig. 6.9 Fracture surfaces of S-Ti, ST-Ti and STP-Ti, (a), (d) S-Ti, (b), (e) STP-Ti, (g), (f) SP-Ti

Most remarkably, protrudings and pits that mark the edge of TiBw networks in S-Ti are visible in Fig. 6.9. Although the main crack in S-Ti propagates by linking the fractured TiBw, the semi-continuous distribution of TiBw still forces the crack to go across ductile titanium matrix. As a result, numerous tearing ridges are seen in Fig. 6.9 (d) between the fractured TiBw. Fractography morphologies observed in STP-Ti and SP-Ti exhibit similar features, as shown in Fig. 6.9 (b) and (c). TiBw exposed on the fracture surfaces are aligned perpendicular to the compression direction. Unlike S-Ti, in which the crack propagates only along the TiBw-rich region, the cracks in STP-Ti and SP-Ti have to go across titanium matrix. As a result, large number of dimples that mark the ductile fracture are observed. The size of dimples is about 2 μm in STP-Ti and about 4 μm in SP-Ti, similar to the size of equiaxed α grains in each composite. Particles with the size of ~100 nm are occasionally observed in the dimples, implying the silicide particles may provide nucleation sites for cracks.

6.3 Influence of heat treatment to microstructure of TiBw/TA15(Si) composites

In order to further control the material microstructure, improve the strength-ductility synergy, and reveal the influence of microstructure on material properties, heat treatments with different conditions were performed on STP-Ti. To prevent the coarsening of silicide particles, the heat treatment temperatures were set above the dissolution temperature of the silicide. To obtain materials with different contents

of lamellar microstructure, heat treatments were conducted at 980 °C and 1010 °C in the dual-phase region, and at 1050 °C in the single-phase region. To avoid silicide precipitation during the cooling process and achieve a stable microstructure, the materials were air-cooled to room temperature after the completion of heat treatment. Additionally, to examine the influence of lamellar morphology on material properties, one sample was water-quenched to room temperature after heat treatment at 1010 °C. The heat treatment conditions and corresponding denotations of materials are shown in Table 6.3 and Figure Fig. 6.10.

Table 6.3 Denotations and corresponding heat treatment procedures

Denotation	Temperature / °C	Duration / min	Cooling condition
STP-Ti	—	—	—
STP-980AC	980	30	Air cooling
STP-1010AC	1010	30	Air cooling
STP-1050AC	1050	30	Air cooling
STP-1010WQ	1010	30	Water cooling

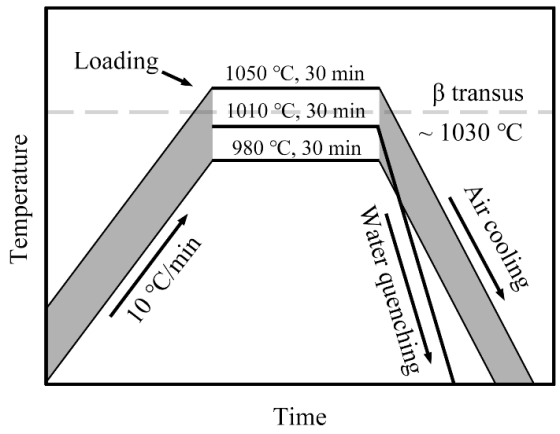

Fig. 6.10 Schematic diagram of heat-treatment procedures

The microstructures of the STP-980AC, STP-1010AC, and STP-1050AC after heat treatment are shown in Fig. 6.11. It can be observed that the matrix of the materials treated in the two-phase region consists of equiaxed α grains and lamellar microstructure, with the colonies of the lamellae exhibiting equiaxed morphology. According to digital image analysis, the lamellar microstructure takes up approximately 50% in the STP-980AC and approximately 70% in the STP-1010AC, indicating the content of lamellar microstructure increase with heat treatment temperature.

From Fig. 6.11 (a) and (b), it can be observed that the equiaxed α grain size obtained after 980 °C / 30 min / AC heat treatment is approximately 4 μm, and the size of each colony is approximately 5 μm. From Fig. 6.11 (c) and (d), it can be seen that as the heat treatment temperature increases to 1010 °C, the content of equiaxed α grains significantly decreases. Meanwhile, the size of equiaxed α grains slightly increases to 5 μm - 7 μm, and the size of colonies significantly increases to approximately 10 μm. Besides, the equiaxed α grains are mainly distributed surrounding the colonies.

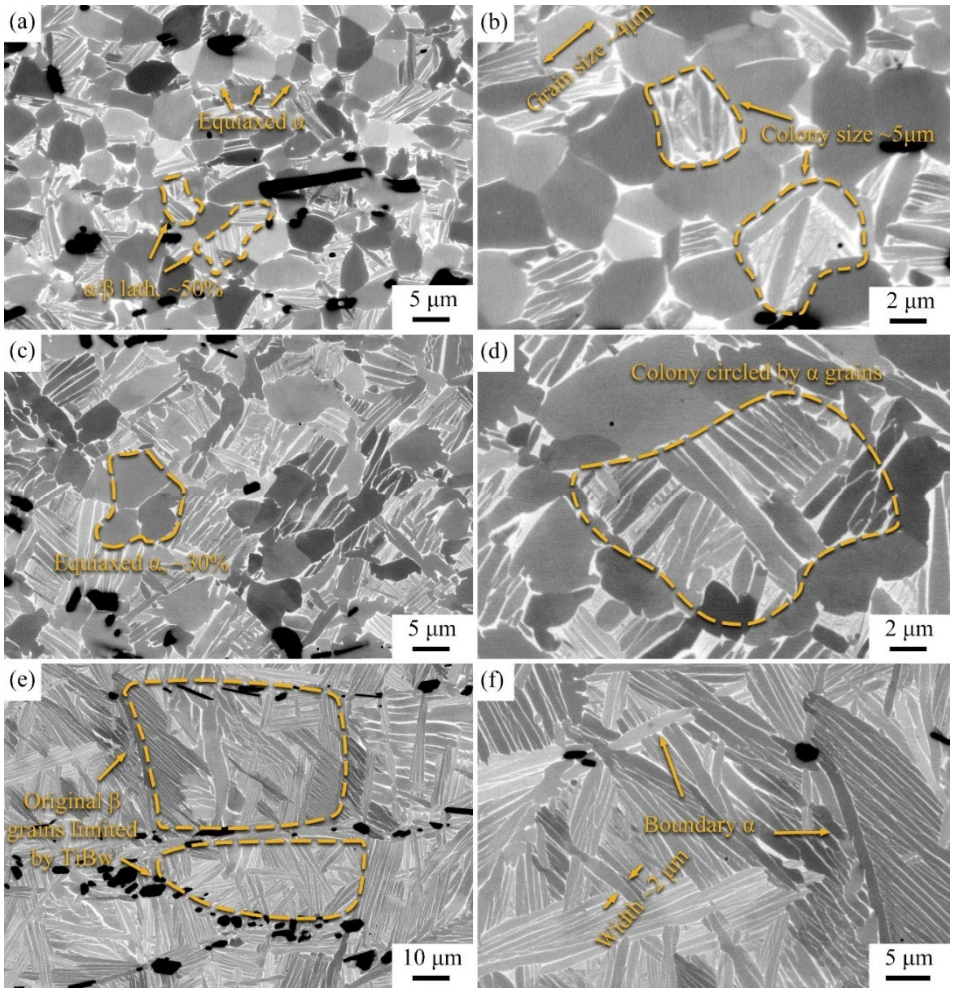

Fig. 6.11 Microstructures of STP-Ti underwent heat-treatment and air-cooling, (a), (b) 980 °C / 30 min / AC, (c), (d) 1010 °C / 30 min / AC, (e), (f) 1050 °C / 30 min / AC

From Fig. 6.11 (e) and (f), it can be observed that after heat treatment at 1050 °C, the matrix exhibits a fully lamellar microstructure, with lamellae aligned in a basket-weave manner and with the thickness of 1 μm - 2 μm. Continuous grain boundary α phases can be observed surrounding the lamellae, which can be used to distinguish the shape and size of the original β grains. The grain boundary α phase

are typically interrupted at the TiBw networks, indicating that the TiBw networks restricts excessive growth of β grains during the heat treatment. It can be inferred from the grain boundary α phase that the size of the original β grains in STP-1050AC is approximately 50 μm, which is significantly larger than that in STP-980AC and STP-1010AC. This suggests that the residual α phase can reduce the growth of the original β grains during heat treatment.

The microstructure of STP-1010WQ is shown in Fig. 6.12. It can be observed that the matrix is primarily composed of near equiaxed α grains and transformed β phase containing numerous lamellae. Due to the rapid cooling rate, the β stabilizers are supersaturated in the transformed β phase, resulting in a brighter contrast under BSE mode. According to digital image analysis, the content of transformed β phase is approximately 70%, which is the same as the content of lamellar microstructure in STP-1010AC. The equiaxed α grains in the matrix of STP-1010WQ are distributed around the transformed β phase, and have a size of approximately 5 μm - 7 μm, while the size of the each transformed β colony is approximately 10 μm. The size and distribution of equiaxed and lamellar microstructures are similar to those in STP-1010AC, with the only difference being the morphology of the lamellar microstructure. This indicates that the heat treatment temperature primarily determines the content, size, and distribution of equiaxed α grains and lamellar microstructures, while the cooling rate determines the morphology of the lamellar microstructure. At shown in Fig. 6.12 (b), it can be observed that the transformed β phase contains numerous fine needle-like α' phase and a small amount of coarse primary α lamellae, with the width of the needle-like α' phases being about tens of nanometers and the size of the primary α lamellae being about hundreds of nanometers.

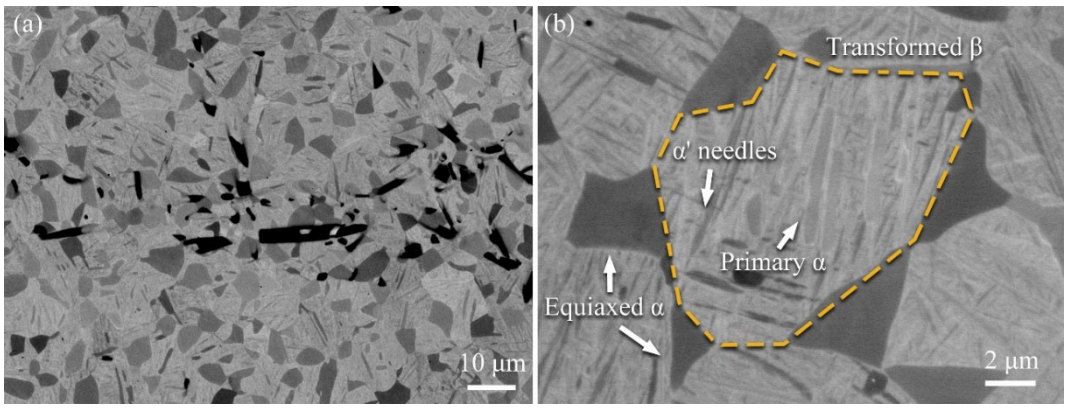

Fig. 6.12 Microstructures of STP-Ti after 1010 °C / 30 min treatment and water quenching, (a) low magnification, (b) high magnification

To investigate the microstructures obtained under different cooling rates, TEM observations were conducted on both STP-1010AC and STP-1010WQ, and the results are shown in Fig. 6.13. The field of view in Fig. 6.13 (a) includes the lamellar microstructure (indicated by the dashed line on the left) and the equiaxed α grains (indicated by the dashed line on the right). Evenly distributed dislocations at the α/β interfaces are observed in Fig. 6.13 (b). Since the α/β interfaces in the lamellar microstructure are semi-coherent, the interplanar spacings are slightly different on two sides of the interfaces. Therefore, the misfit dislocations are evenly spaced on the interfaces to reduce the lattice distortion [148].

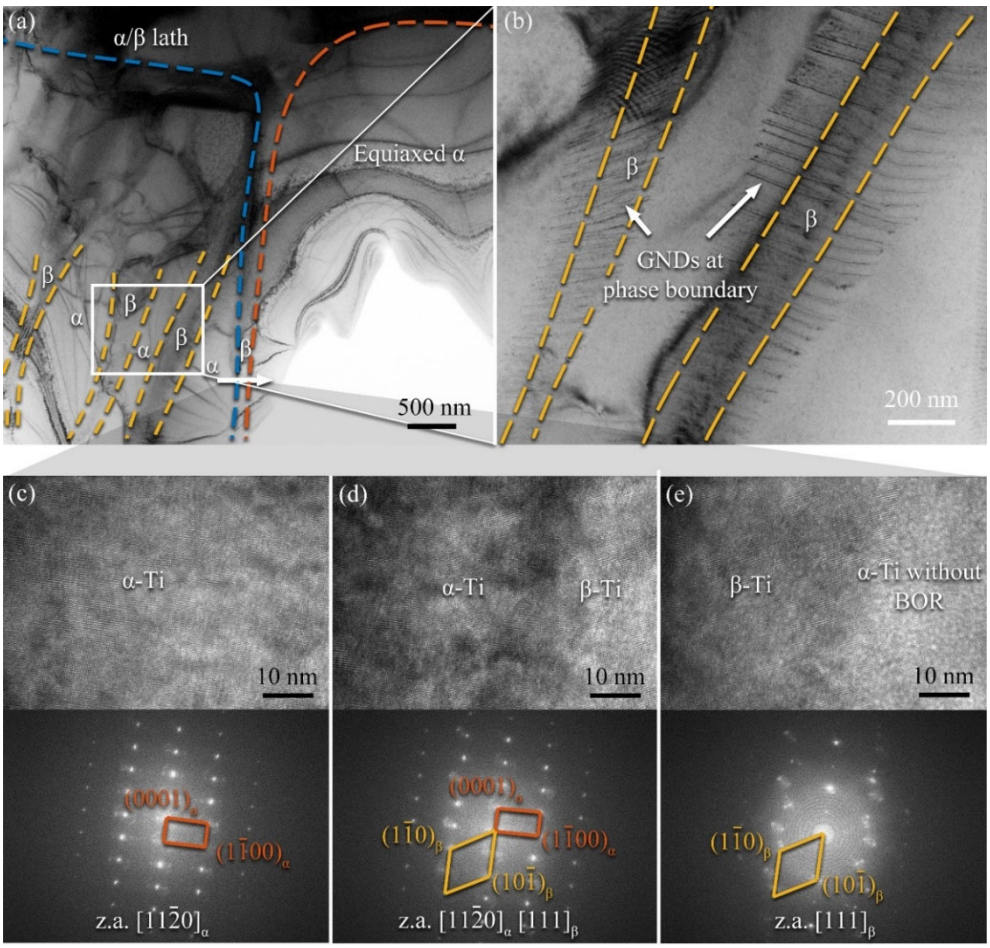

Fig. 6.13 TEM analysis of STP-1010AC, (a) equiaxed α grains and lamellar microstructures, bright field imaging, (b) α/β interfaces, bright field imaging, (c) – (e) HRTEM images and FFT patterns of interfaces between β phase, α laths and equiaxed α grains

High Resolution TEM (HRTEM) images were photographed along the arrow in Fig. 6.13 (a) and processed with Fast Fourier Transformation (FFT), to show the orientation relationships betweenβ phase and α phase with different morphologies, the results are shown in Fig. 6.13 (c) – (e). It can be observed that when both the lamellar α phase and the β phase are present in the field of view (as in Fig. 6.13 (d)), the FFT simultaneously reveals patterns corresponding to the $[11\text{-}20]_{\alpha}$ zone axis and the $[111]_{\beta}$ zone axis. Furthermore, the patterns corresponding to the $(0001)_{\alpha}$ plane are parallel to that of the $(1\text{-}10)_{\beta}$ plane, indicating a Burgers orientation relationship between the lamellar α phase and the β phase. However, when both the β phase and the equiaxed α phase are present in the field of view (as in Fig. 6.13 (e)), the FFT only reveals patterns corresponding to the $[111]_{\beta}$ zone axis, indicating the absence of a clear orientation relationship between the equiaxed α phase and the lamellar β phase.

The results of TEM analysis of STP-1010WQ are shown in Fig. 6.14. Fig. 6.14 (a) displays the equiaxed α grains and the transformed β phase, where the transformed β phase consists of numerous lamellae with widths of tens of nanometers. Elemental distribution analysis was conducted at low and high magnifications, as shown in Fig. 6.14 (b) and (c), respectively. It can be observed that the β stabilizer Mo is enriched in the transformed β phase, which shows a uniform distribution. This indicates that the βelements do not have sufficient diffusion time while cooling, leading to the formation of oversaturated α' lamellae through shearing.

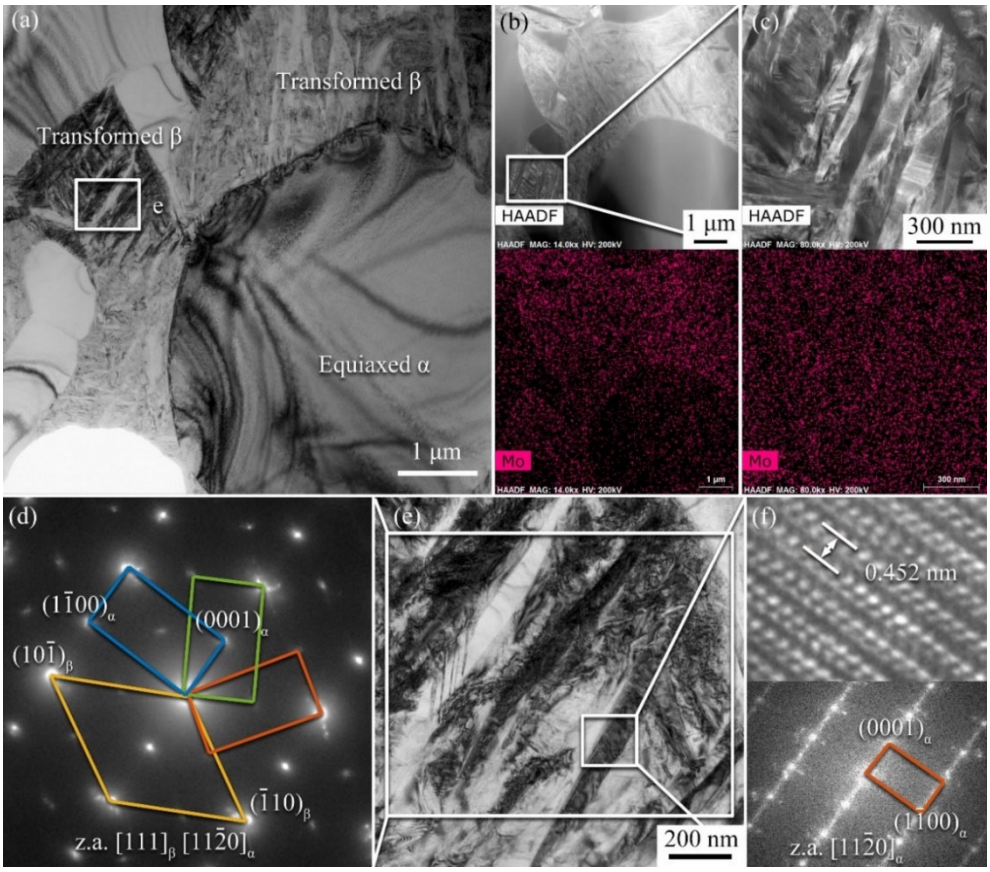

Fig. 6.14 TEM analysis of STP-1010WQ, (a) equiaxed α grains and nearby transformed β phase, bright field imaging, (b) distribution of Mo at low magnification, (c) distribution of Mo in transformed β phase, (d) SAED pattern in transformed β phase, (e) transformed β phase in bright field imaging, (f) α' phase in transformed β phase, HRTEM imaging and corresponding FFT pattern

SAED analysis was performed on the transformed β phase, and the obtained diffraction patterns are shown in Fig. 6.14 (d). Electron diffraction patterns corresponding to the $[111]_\beta$ zone axis as well as three different orientations of the $[11\text{-}20]_{\alpha'}$ zone axis can be observed, indicating that the transformed β phase consists of both α' phase and residual β phase. All the patterns of the α' phase exhibit the

$(0001)_{\alpha'} \parallel (110)_{\beta}$ and $[11\text{-}20]_{\alpha'} \parallel [111]_{\beta}$ orientation relationship with the residual β phase, indicating that the phase transformation from β to α' obeys Burgers relationship. Due to the presence of α' phase with different orientations in the transformed β phase, multiple sets of diffraction patterns corresponding to α' phase were obtained. Fig. 6.14 (e) shows a bright field image of the transformed β phase at high magnification, lens-shaped α' phase are observable. HRTEM imaging of an α' lamella is shown in Fig. 6.14 (f). It can be observed that the [0001] direction of the α' phase is aligned with the long axis of the lamella, and the interplanar spacing of the (0001) plane is approximately 0.452 nm, which is consistent with the interplanar spacing of the (0001) plane of α phase. FFT image reveals that the patterns of α' phase are elongated along the (0001) direction, which may be attributed to the introduction of numerous defects during the shear transformation. Additionally, similar to STP-1010AC, no significant orientation relationship was observed between the equiaxed α grains and the transformed β phase in STP-1010WQ.

X-ray diffraction (XRD) analysis was conducted on S-Ti, STP-Ti, STP-980AC, STP-1010AC, STP-1050AC, and STP-1010WQ, to investigate the influence of heat treatment on the crystal structure of the materials. The results are shown in Fig. 6.15. It can be observed that diffraction peaks corresponding to α-Ti, β-Ti, and TiB are present in all materials. The (110) peaks of β-Ti in S-Ti and STP-Ti are locate at approximately 39.3°, While in STP-980AC, STP-1010AC, and STP-1050AC, the $(110)_{\beta}$ peak locate at approximately 39.2°, exhibiting a leftward shift. Noticeably, in STP-1010WQ, the $(110)_{\beta}$ peak shows a significant leftward shift, which locates at approximately 39.0°.

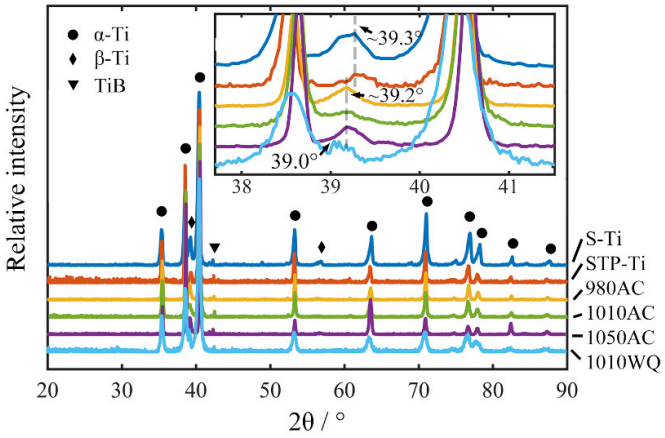

Fig. 6.15 XRD patterns of TiBw/TA15(Si) composites with different treatment

According to the Bragg's law of diffraction:

$$2d\sin\theta = k\lambda \tag{6-10}$$

In which d is the interplanar spacing, θ is the diffraction ancle, k is the order of diffraction, and λ is the wavelength of X-ray. It is indicated from Eq. 6-10 that, when the wavelength remains constant, a decrease in diffraction angle indicates an increase in the interplanar spacing. Hence, the leftward shifting of the $(110)_\beta$ peaks suggests that the lattice constant of the β phase increases after heat treatment. During the preparation, S-Ti and STP-Ti underwent furnace cooling to room temperature, allowing for extensive element diffusion. As a result, the β phase in S-Ti and STP-Ti contains a high concentration of β stabilizers and a low concentration of α stabilizers. On the other hand, STP-980AC, STP-1010AC, and STP-1050AC are cooled to room temperature through air cooling. Although the β→α transformation during air cooling is diffusion-controlled, the short diffusion time limits the enrichment of β stabilizers in β phase, and α stabilizers in α phase. Consequently, materials underwent air cooling have fewer β stabilizers and more α stabilizers in the β phase compared to those underwent furnace cooling. STP-1010WQ was water-cooled to room temperature, allowing minimal element diffusion during the phase transformation. Therefore, the residual β phase in STP-1010WQ contains the least amount of β stabilizers and the highest concentration of α stabilizers. In the TA15 alloy, the atomic radii of the β stabilizers Mo and V are smaller than that of Ti, while the atomic radius of the α stabilizer Al is larger than that of Ti. Consequently, as the concentration of β stabilizers decreases and the

concentration of α stabilizer increases, the lattice constant of the β phase increases, resulting in a leftward shift of the diffraction peaks.

To quantitatively analyze the influence of heat treatment temperature on the crystal orientations of materials, EBSD technique was employed to reveal the crystal orientations in STP-980AC, STP-1010AC, and STP-1050AC. Based on the Burgers orientation relationship, the original β grains were reconstructed to restore their morphologies and distributions at high temperatures. The sizes and orientations of the α phase before reconstruction, the residual α phase after reconstruction, and the original β grains were analyzed. The EBSD analysis results for STP-980AC are shown in Fig. 6.16.

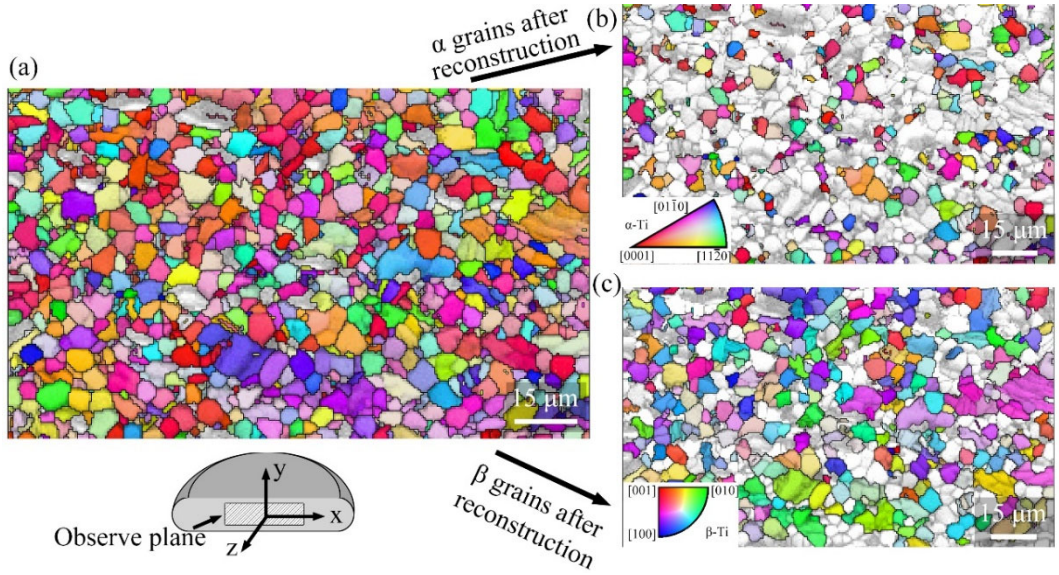

Fig. 6.16 EBSD analysis of STP-980AC, (a) orientation map of α-Ti, (b) residual α grains after reconstruction of original β grains, (c) orientation map of original β grains

From Fig. 6.16 (a), it can be observed that the α grains in STP-980AC mostly exhibit equiaxed morphology, with some regions showing a continuous distribution of grains with similar orientations. This indicates the existence of microtextures after the 980 °C heat treatment. Residual α grains that do not satisfy the BOR and reconstructed prior β grains are shown in Fig. 6.16 (b) and (c), respectively. It can be seen that the α grains that do not satisfy BOR exhibit equiaxed morphology, and are distributed around the prior β grains, which is consistent with the observations in Fig. 6.11 (a). It is worth noting that the content of residual α grains is significantly fewer than the reconstructed original β grains, which contradicts with the

observation in Fig. 6.11 (a), indicating some equiaxed α grains are included for the reconstruction of β grains because satisfying BOR.

Fig. 6.17 presents the pole figures of different crystal planes and grain size distributions for the α phase before reconstruction, residual α phase after reconstruction, and the original β phase in STP-980AC. It can be observed that the α phase in STP-980AC before reconstruction exhibits a weak compressive texture with (0001) || RD, (11-20) || CD, and (1-100) || CD, which is consistent with the texture observed in STP-Ti before heat treatment. The average grain size is approximately 5.8 μm, which is significantly larger than that of STP-Ti.

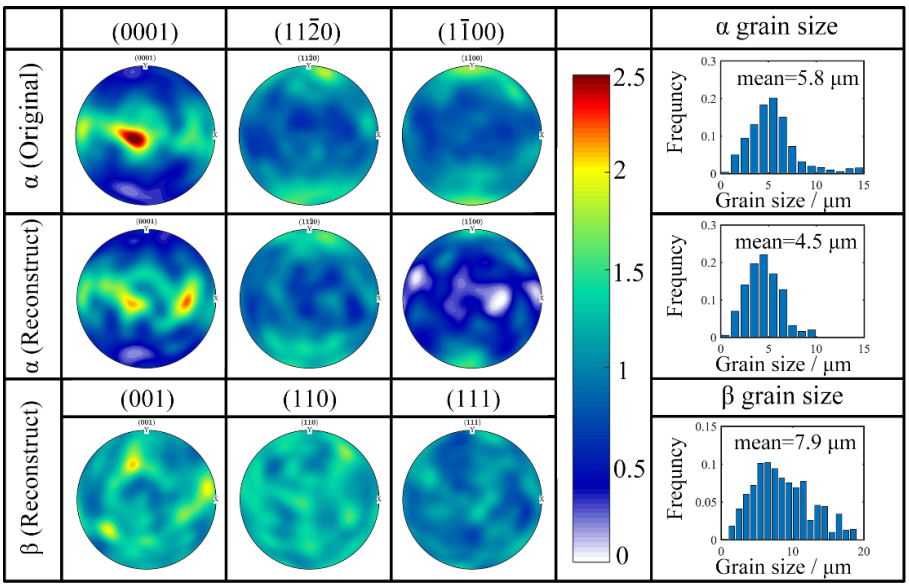

Fig. 6.17 Pole figures and grain size distribution of α phase, residual α phase after reconstruction, and prior β phase in STP-980AC

After the parent phase reconstruction, it was found that the residual α grains still exhibit a compressive texture, with (1-100) || CD being more pronounced compared to that before reconstruction. In contrast, the orientation distribution in the original β grains is nearly uniform, without any significant texture observed. This indicates that the texture in STP-Ti is eliminated during the α→β transformation and subsequent static recovery and recrystallization. Statistical analysis reveals an average size of 4.5 μm for the reconstructed residual α grains, consistent with the size of equiaxed α grains observed in Fig. 6.11 (a). The average size of the original β grains is 7.9 μm, which is larger than the size of lamellar colonies observed in Fig. 6.11 (a). This also suggests that the reconstruction of the original β grains includes

some equiaxed α grains that satisfy BOR.

The EBSD analysis results for STP-1010AC are shown in Fig. 6.18, revealing the presence of a significant amount of lamellar microstructure. After reconstructing the original β grains, the residual α grains that do not satisfy BOR exhibit equiaxed morphology, and their content is significantly reduced compared to that in STP-980AC, From Fig. 6.18 (c), it can be observed that the lamellar microstructure in STP-1010AC is reconstructed into the original β grains, and the equiaxed α grains are primarily distributed at the triple junctions of the original β grains. Compared to STP-980AC, the reconstructed original β grains after 1010 °C heat treatment show a significant increase in size.

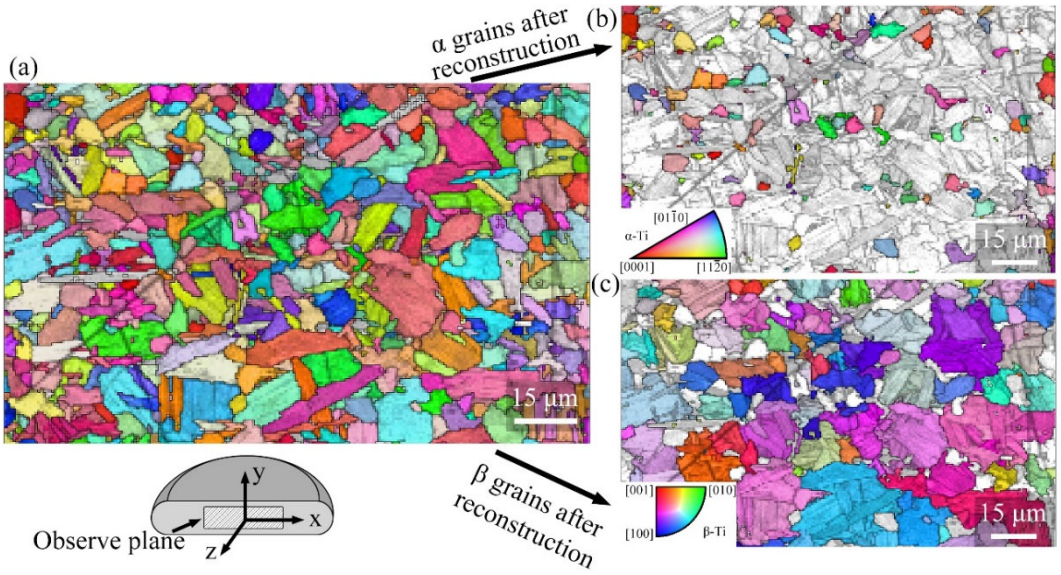

Fig. 6.18 EBSD analysis of STP-1010AC, (a) orientation map of α-Ti, (b) residual α grains after reconstruction of original β grains, (c) orientation map of original β grains

Fig. 6.19 illustrates the pole figures of the α phase and original β phase, as well as the grain size distribution, before and after parent phase reconstruction in STP-1010AC. Prior to reconstruction, the orientation distribution of the α phase appears random without any significant texture. After reconstruction, the residual α phase exhibits a slight decrease in pole density for the (0001) plane in the compression direction, and a slight increase in pole density for the (11-20) and (1-100) planes in the compression direction. However, the degree of texture is weaker compared to STP-980AC, indicating that increasing the annealing temperature weakens the texture intensity in the residual α grains. Similar to STP-980AC, no significant

texture is observed in the reconstructed original β phase. The average grain size of the α phase before reconstruction is 8.8 μm, while the size of the residual α grains after reconstruction is 5.8 μm, both are higher compared to those in STP-980AC, indicating an increased grain growth rate. The size of the reconstructed original β grains is 19.8 μm, which is significantly larger than the original β grain size in STP-980AC. This is not only due to the increased growth rate of β grains at high temperatures but also because the hindrance to the growth of original β grains is reduced due to the decreased content of α phase.

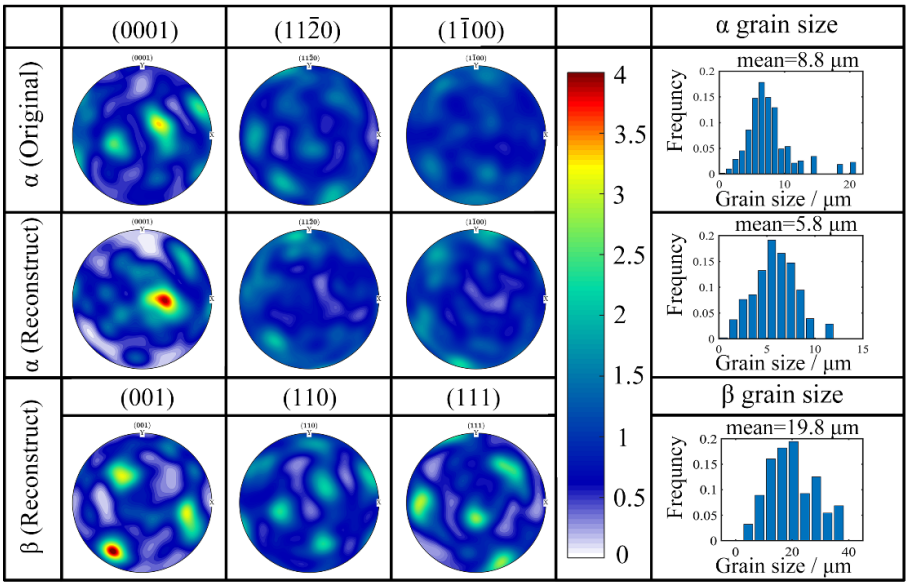

Fig. 6.19 Pole figures and grain size distribution of α phase, residual α phase after reconstruction, and prior β phase in STP-1010AC

Fig. 6.20 shows the EBSD analysis results for STP-1050AC. In Fig. 6.20 (a), it can be observed that all α phases a lamellar morphology. All the α phase were reconstructed into original β grains, indicating the α phase obeys BOR. The reconstructed original β grains exhibit an equiaxed shape with their grain boundaries aligning well with the compressed TiBw network, suggesting that the growth of β grains during heat treatment is primarily restricted by TiBw reinforcements. Fig. 6.20 (c) shows the pole figures of the α phase before the reconstruction and the original β phase after the reconstruction, as well as the grain size distribution. It can be observed that there is no significant texture exhibited by the material before and after reconstruction, indicating that the heat treatment in β phase region can eliminate the texture generated by isothermal hot pressing. The average grain size of the α phase in STP-1050AC is 27.8 μm. Since α lamellae in a

same colony are identified as a single grain, this grain size reflects the average size of the colony. After parent phase reconstruction, the average size of original β grains is 66.4 μm, which is slightly smaller than the size of the original β grains in the as-sintered composite. This indicates that the heat treatment in the single-phase region significantly reduces the effect of grain refinement brought by thermo-mechanical processing in dual-phase region.

Based on the results from Fig. 6.16 to Fig. 6.20, it can be concluded that as the heat treatment temperature increases, the content of equiaxed α phase in the material decreases while the grain size slightly increases, whereas the size of the original β grains rapidly increases. When heat treatment is conducted below the β transformation temperature, the residual equiaxed α grains in the matrix can restrict the growth of β grains, and this restriction weakens as the content of α phase decreases. When the heat treatment temperature rises above the β transformation temperature, the growth of β grains is only hindered by TiBw reinforcements. The overall texture intensity in the material decreases with increasing heat treatment temperature. When heat treatment is conducted below the β transformation temperature, the residual equiaxed α grains partially retain the texture formed during hot deformation in dual-phase region. However, in the lamellar microstructure where α→β transformation occurs, the texture is mostly eliminated during the processes such as phase transformation, static recovery, recrystallization, and β grain growth.

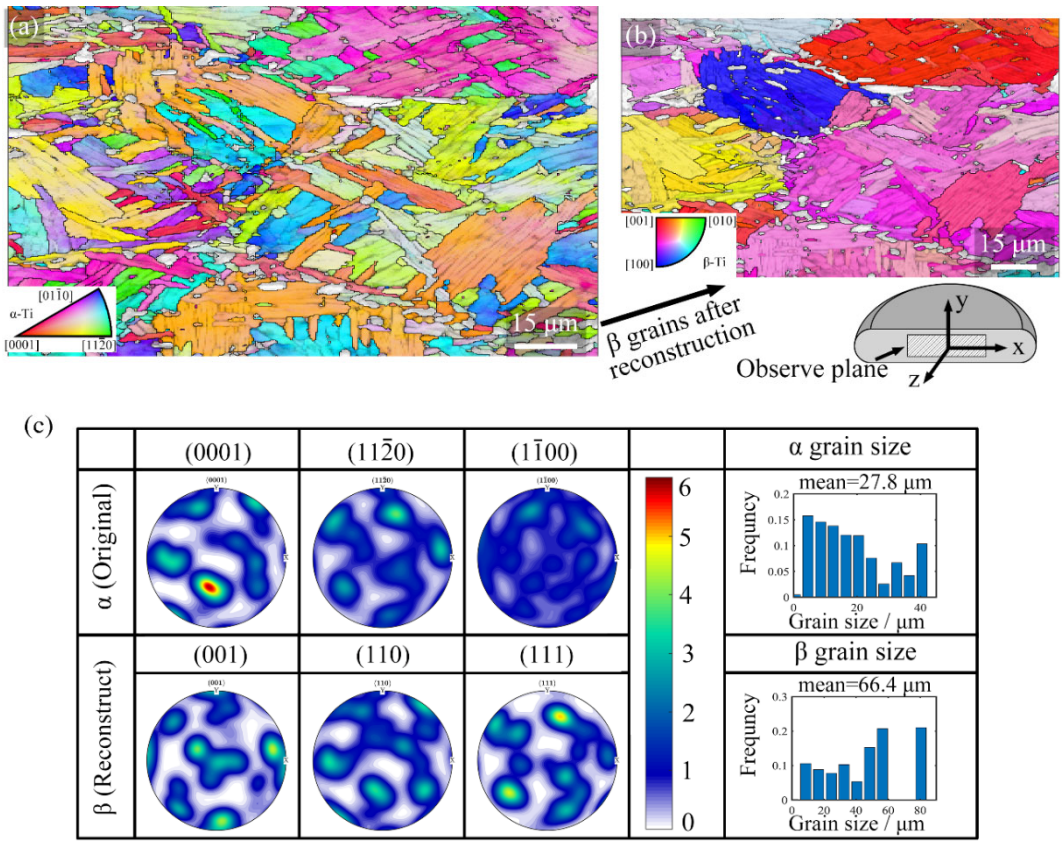

Fig. 6.20 EBSD analysis of STP-1050AC, (a) orientation map of α-Ti, (b) orientation map of original β grains, (c) Pole figures and grain size distribution of α phase and prior β phase in STP-1050AC

6.4 Influence of heat treatment to tensile behaviors of TiBw/TA15(Si) composites

6.4.1 Tensile properties of TiBw/TA15(Si) composites after heat treatment

Tensile tests were conducted to evaluate the room temperature mechanical properties of STP-980AC, STP-1010AC, STP-1050AC, and STP-1010WQ. The results are presented in Fig. 6.21 and Table 6.4. The room temperature tensile stress-strain curves and mechanical properties of S-Ti and STP-Ti are also included for comparison.

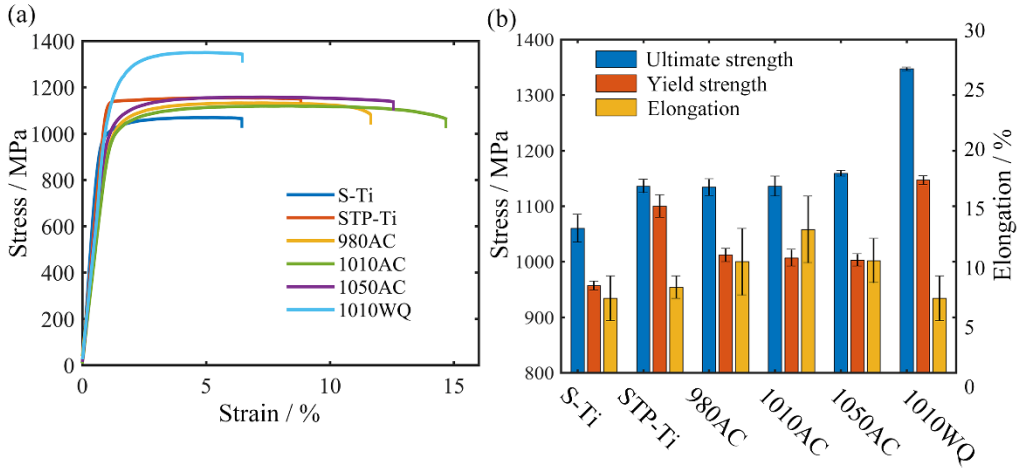

Fig. 6.21 Room temperature tensile properties of TiBw/TA15(Si) with different treatments, (a) typical stress-strain curves, (b) room temperature tensile properties

Table 6.4 Room temperature tensile properties of TiBw/TA15(Si) with different treatments

Material	$\sigma_{0.2}$ / MPa	Ultimate strength / MPa	Elongation %
S-Ti	957±8	1060±25	6.7±2
STP-Ti	1100±20	1136±12	7.7±1
STP-980AC	1012±12	1134±15	10.0±3
STP-1010AC	1007±15	1136±18	12.9±3
STP-1050AC	1003±11	1159±5	10.1±2
STP-1010WQ	1147±20	1347±3	6.7±2

As shown in Fig. 6.21, after thermo-mechanical processing in dual-phase region, all materials exhibit higher yield strength and tensile strength compared to S-Ti. Comparing STP-Ti with the heat-treated materials, it is observed that the yield strength of all air-cooled materials significantly decreases from 1100 MPa to approximately 1005 MPa. With increasing heat treatment temperature, the yield strengths of the materials slightly decreases while the tensile strengths are less affected by the heat treatment temperature. The tensile strength of STP-980AC and STP-1010AC remains close to 1135 MPa, which are similar to STP-Ti, while the tensile strength of STP-1050AC slightly increases to 1159 MPa. Moreover, the elongations of the materials subjected to heat treatment and air cooling are improved compared to STP-Ti. The elongations of STP-980AC and STP-1050AC increase from 7.7% to approximately 10%. The elongation of STP-1010AC shows a more significant increase to an average of 12.9%, which is approximately 65%

higher compared to that of STP-Ti. The water cooled STP-1010WQ exhibits the highest strength, with an average yield strength of 1147 MPa, which is approximately 5% higher than that of STP-Ti. The tensile strength is significantly increased to 1347 MPa, approximately 18% higher than that of STP-Ti. Meanwhile, the tensile elongation of STP-1010WQ decreases only slightly from 7.7% before heat treatment to 6.7%, remaining at the same level as the as-sintered material.

To investigate the effect of lamellar microstructure on the yield strength, the contributions of different strengthening mechanisms to the strength were analyzed for materials with different heat treatment conditions. The change of strength after heat treatment can be expressed as:

$$\Delta\sigma_{th} = \Delta\sigma_{P-N} + \Delta\sigma_{LT} + \Delta\sigma_{H-P} + \Delta\sigma_{Orowan} + \Delta\sigma_{GND} + \Delta\sigma_{lath} \qquad (6\text{-}11)$$

In which $\Delta\sigma_{th}$ is the changing in yield strength, $\Delta\sigma_{P\text{-}N}$ is the changing in lattice friction, $\Delta\sigma_{LT}$ is the changing in load transfer strengthening effect, $\Delta\sigma_{H\text{-}P}$ is the changing in fine grain strengthening effect, $\Delta\sigma_{Ororwan}$ is the changing in Orowan strengthening effect, $\Delta\sigma_{GND}$ is the changing in strengthening effect brought by dislocation density, and $\Delta\sigma_{lath}$ is the strengthening effect brought by lamellar microstructure.

As the heat-treatment doesn't change the chemical composition and reinforcement morphology in the material, hence the lattice friction and the effect of load transfer remained unchanged after heat treatment. The strengthening by grain refinement can be obtained with Eq. 6-7. Since the silicide particles were dissolved into the matrix after heat treatment, the Orowan strengthening effect was eliminated. The strengthening brought by the dislocation density can be calculated from Eq. 6-9, and the difference in the yield strength before and after heat treatment $\Delta\sigma_{th}$ was obtained by the tensile test. Therefore, the contribution of lamellar microstructure $\Delta\sigma_{lath}$ is obtainable with Eq. 6-11. The Strengthening effects in materials with different heat-treatment conditions are listed in Table 6.5.

Table 6.5 Strengthening effects in heat-treated and air-cooled materials

Materials	d_{Grain} / μm	ρ_{GND} 10^{14}/ m^2	f_{Lath} / %	$\Delta\sigma$ / Mpa	$\Delta\sigma_{H\text{-}P}$ / Mpa	$\Delta\sigma_{Orowan}$ / MPa	$\Delta\sigma_{GND}$ / MPa	$\Delta\sigma_{Lath}$ / MPa
STP-Ti	1.6	1.4	0	0	0	0	0	0
STP-980AC	5.8	1.3	50	-88	-113	-32	-2	59
STP-1010AC	8.8	1.1	70	-93	-136	-32	-8	83
STP-1050AC	27.8	1.1	100	-97	-180	-32	-8	123

From Table 6.5, it can be observed that compared to STP-Ti, the decrease in yield strength due to grain coarsening is 113 MPa, 136 MPa, and 180 MPa for STP-980AC, STP-1010AC, and STP-1050AC, respectively. The decrease in yield strength caused by the reduction in dislocation density due to heat treatment is 2 MPa, 8 MPa, and 8 MPa, respectively. The strength reduction due to the dissolution of silicides is 32 MPa for all materials. In total, the yield strengths are reduced by 143 MPa, 168 MPa, and 212 MPa for STP-980AC, STP-1010AC, and STP-1050AC, respectively. The experimentally obtained yield strength reductions are 83 MPa, 93 MPa, and 97 MPa, for STP-980AC, STP-1010AC, and STP-1050AC, respectively. Based on this, the strengthening contribution $\Delta\sigma_{lath}$ due to the lamellar microstructure in STP-980AC, STP-1010AC, and STP-1050AC can be calculated as 59 MPa, 83 MPa, and 123 MPa, respectively. The relationship between lamellar content and $\Delta\sigma_{lath}$ for different materials are plotted fitted with linear regression in Fig. 6.22.

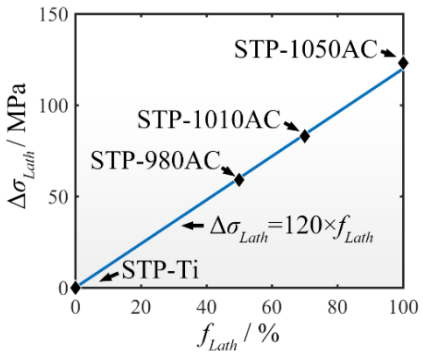

Fig. 6.22 Relationship between f_{Lath} and $\Delta\sigma_{Lath}$

Fig. 6.22 shows a clear linear relationship between the lamellae content in the

material and the strengthening effect caused by the lamellar microstructure. For every 1% increase in f_{lath}, $\Delta\sigma_{lath}$ increases by approximately 1.2 MPa. This result indicates that the lamellar microstructure provides higher strength compared to the pure α phase. The strengthening effect is primarily due to the different crystal structures of the α phase and β phase makes dislocations difficult to cross the α/β interfaces, thereby hindering the dislocation movements. The relationship between $\Delta\sigma_{lath}$ and f_{lath} suggests that the strength of the matrix approximately follows the rule of mixtures:

$$\begin{aligned}\sigma_{matrix} &= f_{Lath}\sigma_{Lath} + (1 - f_{Lath})\sigma_{\alpha} = \sigma_{Equiaxed} + f_{Lath}(\sigma_{Lath} - \sigma_{\alpha}) \\ &= \sigma_{\alpha} + \Delta\sigma_{Lath}\end{aligned} \quad (6\text{-}12)$$

In which σ_{matrix} is the yield strength of the matrix, σ_{lath} is the yield strength of lamellar microstructure, and σ_{α} is the yield strength of pure α phase. It is indicated by Eq. 6-12 that the change in yield strength caused by the lamellar microstructure is proportional to the lamellar content. Since each 1% increase in f_{lath} corresponds to approximately a 1.2 MPa increase in $\Delta\sigma_{lath}$, it can be concluded that the strength difference between the lamellar microstructure and the pure α phase in this study is approximately 120 MPa.

The true stress-strain curves, work hardening rates, and uniform elongations of the materials under different heat treatment conditions are shown in Fig. 6.23. It can be observed that the work hardening rates of materials after heat treatment significantly increase during the early stages of plastic deformation compared to STP-Ti. STP-1010WQ exhibits the highest work hardening rate in the early stage, but decreases rapidly as the strain increases, eventually entering the non-uniform stage at a true strain of 0.047 (equivalent to 4.8% engineering strain). The work hardening behaviors of STP-980AC, STP-1010AC, and STP-1010AC are similar, which decrease rapidly in the early stages but slow down as the strain increases. Consequently, the air-cooled materials enter the non-uniform deformation stage later than STP-1010WQ, at true strains of 0.066, 0.078, and 0.068 (equivalent to 6.8%, 8.1%, and 7.0% engineering strain), respectively.

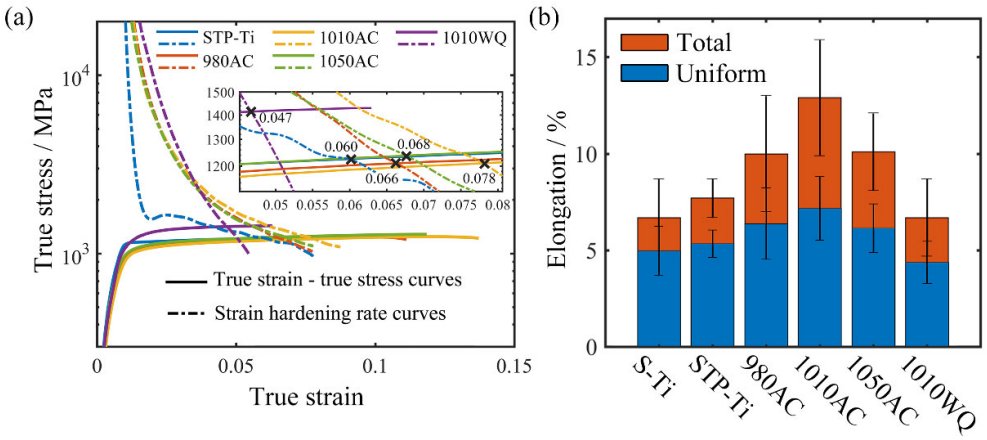

Fig. 6.23 Strain hardening and uniform deformation capabilities of TiBw/TA15(Si) after different treatments, (a) typical true stress-true strain curves, (b) comparison between total elongation and uniform elongation

From Fig. 6.23 (b), it can be observed that the uniform elongation of STP-Ti increases after heat treatment and air cooling but decreases after water cooling. Among them, STP-1010AC exhibits the best uniform deformability. It is worth noting that although the fracture elongation and uniform elongation of the materials show similar trends under different conditions, the proportion of uniform plastic deformation varies significantly among different materials. The uniform elongation of S-Ti takes up approximately 80% of its total elongation, indicating a limited necking before material fracture. In contrast, the proportion of uniform elongation for STP-1010WQ, which has similar total elongation as S-Ti, is approximately 65%, significantly lower than that of S-Ti. Meanwhile, the uniform elongation of STP-1010AC takes up about 55% of the total elongation, indicating that the material can endure a considerable amount of localized deformation before fracture.

6.4.2 Room temperature tensile behaviors of TiBw/TA15(Si) composites

In order to visually show the deformation localization in different materials during tensile test, the local strains in tensile samples of S-Ti, STP-Ti, STP-1010AC, and STP-1010WQ were measured using Digital Image Correlation (DIC) method. The results for S-Ti and STP-Ti are shown in Fig. 6.24.

In Fig. 6.24 (a), it can be observed that the strain is uniformly distributed in the S-Ti tensile specimen in the initial stage. When the tensile strain reached 2%, the strain

distribution started to exhibit higher values in the middle, and lower values at the ends of the specimen. The necking was determined to occur at a tensile strain of 5.0% according to the position of maximum engineering stress. After necking, plastic deformation was concentrated in a small region, and the specimen eventually fractured at a tensile strain of 5.3%, with uniform elongation takes up approximately 93% of the total elongation. Prior to fracture, the localized strain is distributed perpendicular to the tensile direction, which is consistent with the normal fracture mode observed in the as-sintered materials. No significant necking was observed near the strain localization region. Fig. 6.24 (b) shows the variations of the average strain and strain near the fracture point with time. It can be seen that until fracture, the plastic strain was distributed rather uniformly throughout the specimen, which was due to the inability of the material to withstand localized strain and the rapid fracture upon necking.

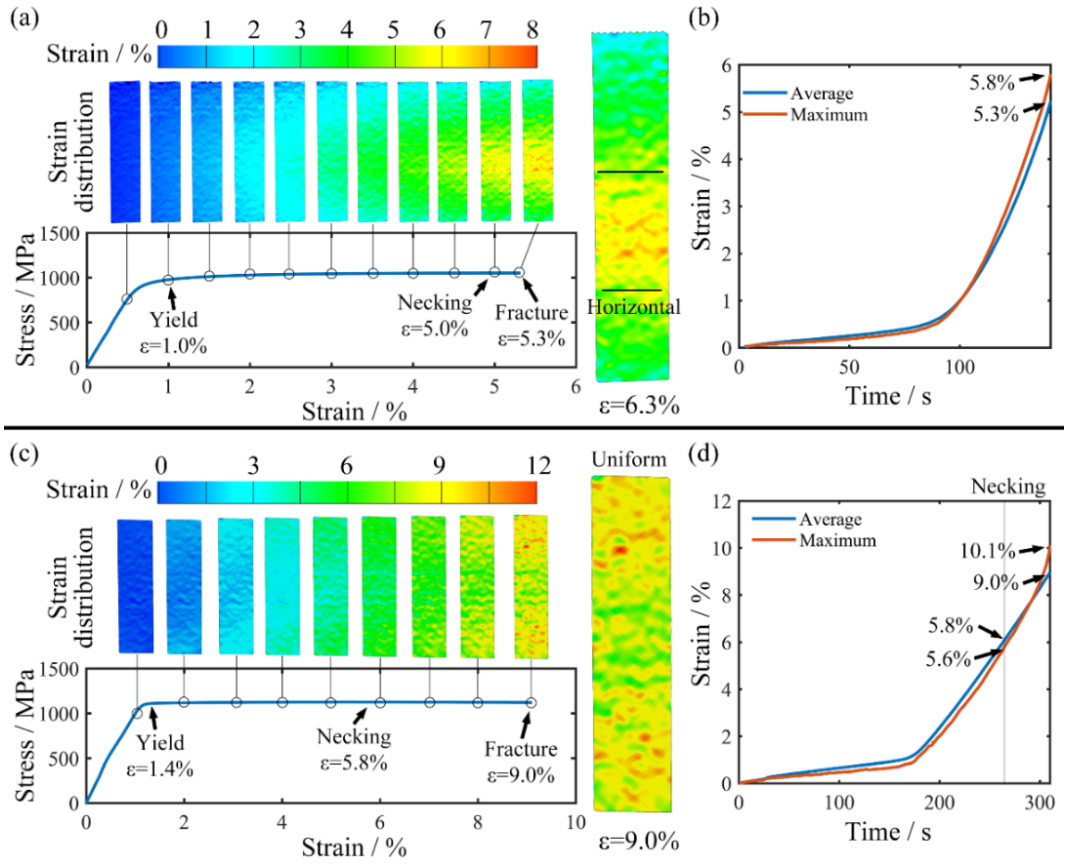

Fig. 6.24 DIC analysis of S-Ti and STP-Ti during room temperature tensile tests, (a) local strain distribution in S-Ti at different tensile strain, (b) average strain and strain near fracture point in S-Ti, (c) local strain distribution in STP-Ti at different tensile strain, (d) average strain and strain near fracture point in STP-Ti

In Fig. 6.24 (c), it can be observed that the strain distribution in the STP-Ti tensile

specimen exhibits slightly higher values at the ends and slightly lower values in the middle, which persists until fracture. Based on the position of the peak stress, necking is determined to occur at a tensile strain of 5.8%. Fracture took place at a tensile strain of 9.0%, with the uniform elongation takes up 60% of the total. However, the strain distribution reveals that there was no significant strain localization nor necking phenomenon in the specimen. This indicates that the necking judged from the stress-strain is not always reliable. In Fig. 6.24 (d), it can be seen that the strain near the fracture point of the STP-Ti specimen is only slightly higher than the overall deformation of the specimen. The strain difference is only 1%, indicating a significantly suppressed strain localization.

Fig. 6.25 presents the DIC observation results of STP-1010AC and STP-1010WQ tensile tests. In Fig. 6.25 (a), it can be observed that the strain in the STP-1010AC specimen extends from the middle towards the ends with the progression of tensile test. When the tensile strain reaches 4%, a strain localization region with an angle of ~45° to the horizontal direction begins to appear. Based on the stress-strain curve, necking occurs in the STP-1010AC tensile specimen at a strain of 5.8%, with the uniform elongation takes up only 43% of the overall elongation. Observing the strain distribution map, it can be seen that the deformation at the ends of the specimen no longer increases with increasing tensile strain after necking, indicating the intensive strain localization. Cross-shaped strain localization region is observed near the fracture point, indicating a shearing fracture mode, and a significant necking is observed near the fracture point, which is consistent with that indicated by the stress-strain curve. Comparing the strain near the fracture point and the average strain of the specimen in Fig. 6.25 (b), it is found that the strain near the fracture point is slightly higher than the overall strain in the initial stage of deformation, which then increases rapidly and far surpassing the average strain after necking. At the moment of fracture, the strain at the fracture point is 21.7%, which is significantly higher than the average strain, indicating that the STP-1010AC material can withstand a significant amount of localized strain.

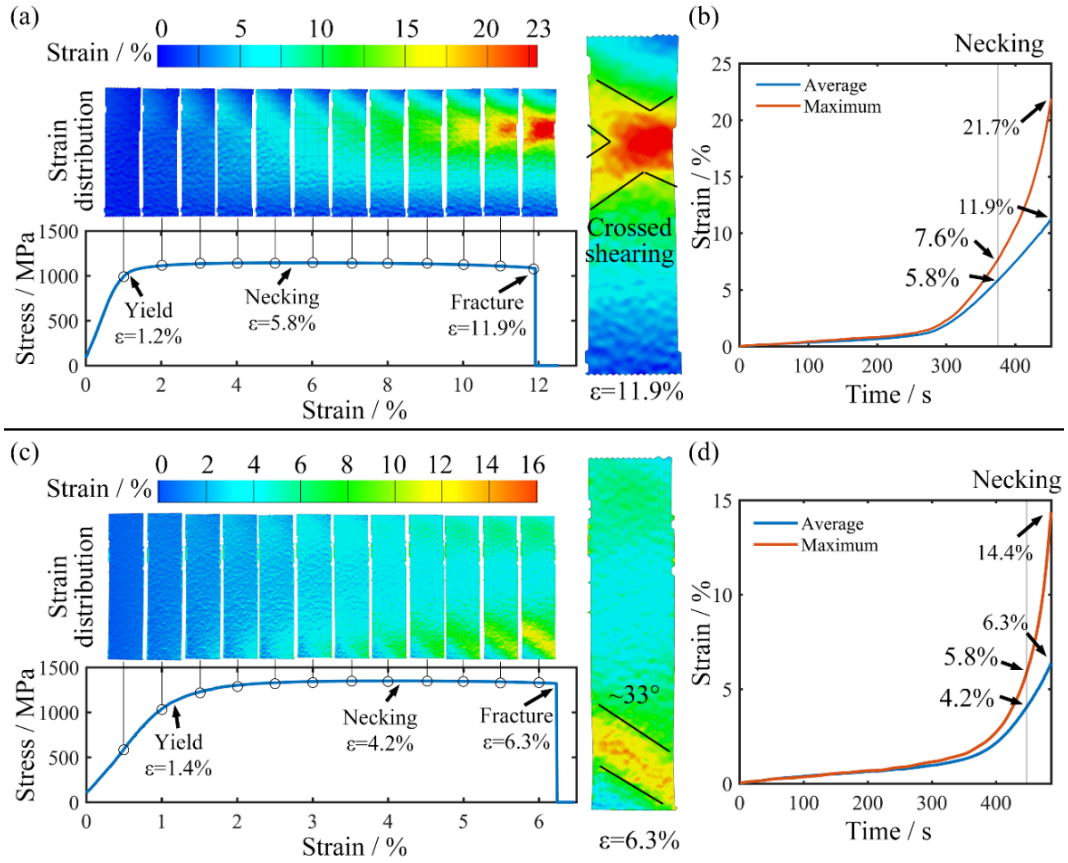

Fig. 6.25 DIC analysis of STP-1010AC and STP-1010WQ during room temperature tensile tests, (a) local strain distribution in STP-1010AC at different tensile strain, (b) average strain and strain near fracture point in STP-1010AC, (c) local strain distribution in STP-1010WQ at different tensile strain, (d) average strain and strain near fracture point in STP-1010WQ

Fig. 6.25 (c) depicts the strain distribution in the STP-1010WQ specimen during the tensile test. The specimen exhibits a uniform strain distribution when the tensile strain is less than 2%, which then evolves into a strain distribution that higher in the ends and lower in the middle. Based on the position of the peak in the stress-strain curve, necking occurs in the specimen at a tensile strain of 4.2%, with uniform elongation taking up 57% of the total elongation. Observing the strain distribution map, it can be seen that after necking, the strain mainly develops within a diagonal region. Necking is observed around the strain localization region before specimen fracture, indicating a shearing fracture mode. Compared to the cross-shaped strain localization region observed in STP-1010AC, only one shearing direction is observed in STP-1010WQ, indicating an inferior ability to resist the strain localization, which agrees well with the rapid declination in work hardening rate observed in Fig. 6.23. Comparing the strain near the fracture point and the average strain of the specimen, it is found that the fracture point of STP-1010WQ exhibits

a higher deformation degree in the early stage, which them accelerates after necking occurs. At the moment of specimen fracture, the strain at the fracture point reaches 14.4%, which is more than 200% of the average strain, demonstrating a better capacity to withstand localized plastic deformation than S-Ti and STP-Ti. This indicates that the poor tensile plasticity of STP-1010WQ is mainly attributed to its poor ability to resist strain localization.

Based on above analysis, it is revealed that the TiBw/TA15(Si) in it as-sintered state has coarse grain size and interconnected cracks, resulting in poor resistance to both localized strain and strain localization. However, after solid solution pretreatment and hot deformation in the dual-phase region, the composite exhibits significantly enhanced resistance to strain localization, although its ability to withstand localized strain remains weak. Nevertheless, due to the uniform distribution of strain throughout the specimen, the plasticity of the composite was significantly improved. After heat treatment of the hot-deformed composite, grain coarsening and increased dislocation slip distance occurred, leading to reduced resistance to strain localization. However, the complete dissolution of silicide particles resulted in a significantly improved tolerance to local deformation, which shifted the fracture mode of the composite from normal fracture to shearing, leading to the improved tensile plasticity. Notably, the composite obtained through water quenching after heat treatment exhibited high strength and improved local plastic deformation capability, thus demonstrating good combination of strength and ductility.

6.4.3 Slip trace of TiBw/TA15(Si) composites after room temperature tesnile testing

To investigate the mechanisms that lead to different deformation behaviors of materials in different states, the fracture side faces of the tensile specimens were examined. The fracture side faces of STP-980AC is shown in Fig. 6.26. As observed in Fig. 6.26 (a), the quantity and size of equiaxed α grains and lamellae colonies are similar in the STP-980AC material. Numerous slip traces can be observed both within the equiaxed α grains and the lamellae. Upon closer observation in Fig. 6.26 (b) and (c), multiple slip traces in different directions can be seen within the equiaxed α grains, indicating the activation of multiple slip systems. Continuous slip traces distributing in a single direction can be observed in lamellar

microstructures, indicating that the α/β interface cannot completely impede the penetration of dislocations. Fig. 6.26 (b) also shows the occurrence of continuous slip traces going across two adjacent equiaxed α grains, which may be attributed to the activation of the same slip system due to similar orientations. Fig. 6.26 (c) reveals the simultaneous presence of twins and slip lines in the equiaxed α grains. Since the critical resolved stress for twinning in near-α titanium alloys is much higher than that for slip, twinning may occur after slip is hindered in the material [136]. Fig. 6.26 (d) and (e) show the fracture side face after polishing. In Fig. 6.26 (d), lens-shaped twins can be observed in the equiaxed α grains, either traversing the entire grain or terminating at other twins. Fig. 6.26 (e) exhibits distorted lamellae and α grains with significant electron channeling contrast, indicating the accumulation of numerous dislocations in the material due to plastic deformation.

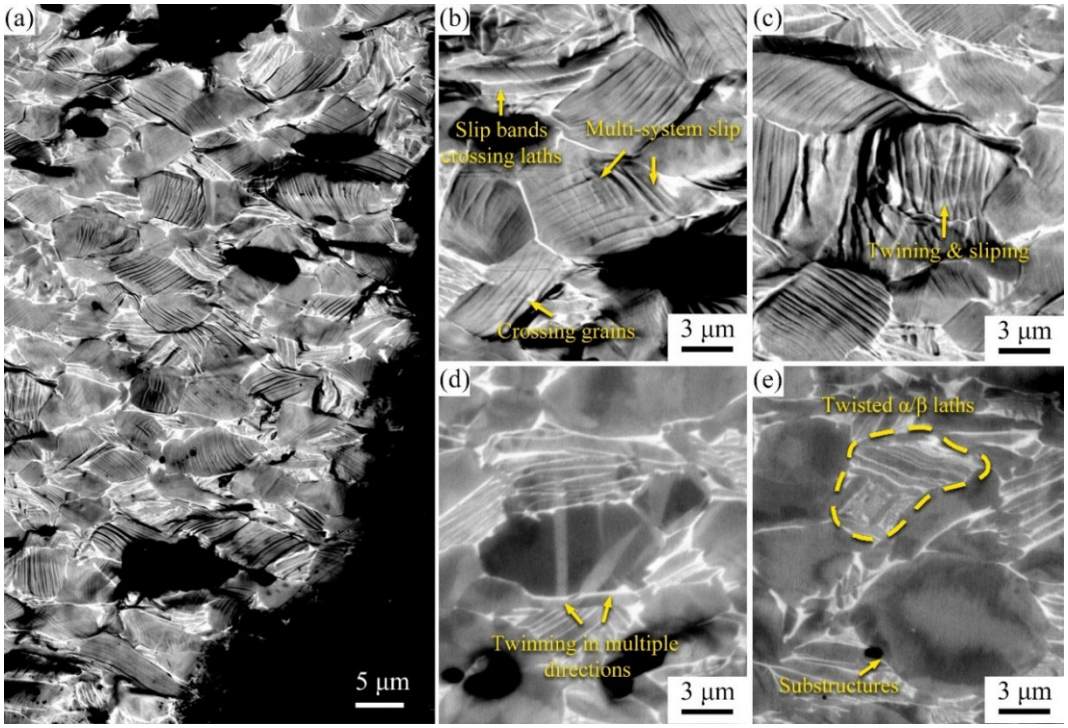

Fig. 6.26 BSE images of fracture side-faces of STP-980AC after room temperature tensile test, (a) low magnification morphology, (b), (c) slip traces, (d), (e) polished surface

Fig. 6.27 depicts the fracture side face of the STP-1010AC tensile specimen. Fig. 6.27 (a) reveals a significant increase in the content of lamellar microstructure compared to STP-980AC. Fractured TiBw reinforcements and numerous slip traces are observable on the fracture side face. In Fig. 6.27 (b), slip traces can be observed in both equiaxed α grains and lamellar microstructures. It is noticeable that, slip

traces are sparser but deeper in lamellar microstructures compared to those in equiaxed grains, indicating a high degree of strain localization [149]. Slip lines within the lamellae can propagate across the α/β interface into adjacent lamellae, and some slip traces exhibit different propagation directions within the α phase and β phases, suggesting different preferred slip directions. As shown in Fig. 6.27 (c), twins and slip lines coexist in some lamellae. Figure 5-27 (d) and (e) display the polished fracture side face, revealing significant orientation variations in the equiaxed α grains and the formation of twins within the lamellae. Twins in the lamellae can occur in multiple directions and extend continuously through the lamellae.

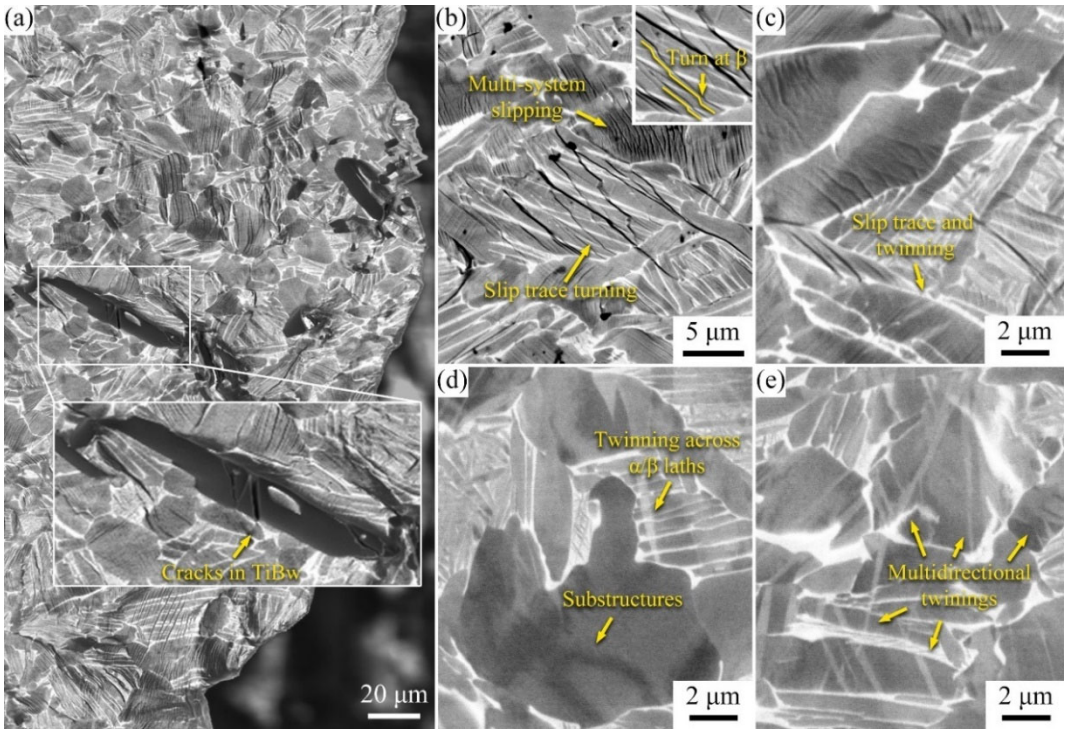

Fig. 6.27 BSE images of fracture side-faces of STP-1010AC after room temperature tensile test, (a) low magnification morphology, (b), (c) slip traces, (d), (e) polished surface

Fig. 6.28 presents the fracture side faces of the STP-1050AC.It can be seen from Fig. 6.28 (a) that the material consists of a fully lamellar microstructure, and a significant amount of reinforcements are fractured. In Fig. 6.28 (b) and (c), both slip traces and twins, which can penetrate the lamellae with same orientation, are observed within the lamellar microstructure. The slip traces in STP-1050AC are deep but have sparse distribution, which is similar to those in the lamellar microstructures of other materials. It is noteworthy that no slip lines parallel to the

lamellar direction are observed in STP-980AC, STP-1010AC, and STP-1050AC. In the laminated α phase, only the prismatic slips are parallel to the lamellar direction, therefore the absence of slip traces parallel to the α laths indicates the inhibition of prismatic slip in the α/β lamellae. Fig. 6.28 (d) exhibits lamellar microstructures that misaligned along the slip traces, indicating that slip can disrupt the integrity of the lamellar microstructure. it can be observed in Fig. 6.28 (e) that twins with different orientations can occur within lamellae with the same orientation, which either terminate at lamellae with different orientations or terminate at other twins.

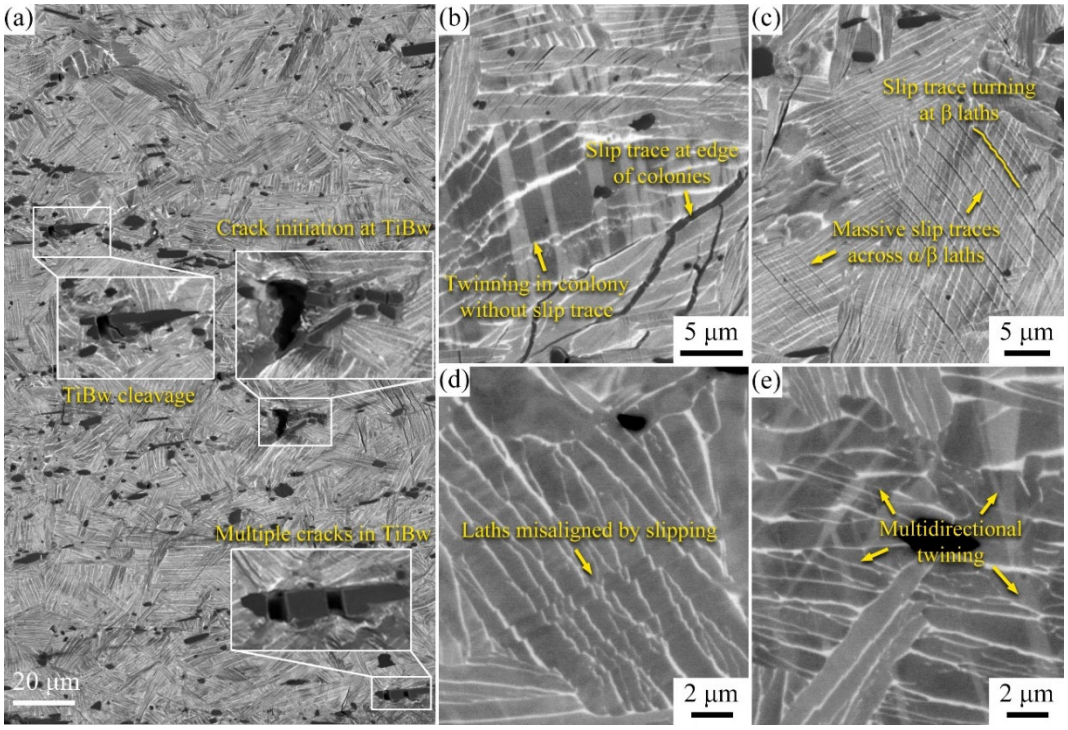

Fig. 6.28 BSE images of fracture side-faces of STP-1050AC after room temperature tensile test, (a) low magnification morphology, (b), (c) slip traces, (d), (e) polished surface

Fig. 6.29 illustrates the fracture side faces of STP-1010WQ. A significant number of fractured TiBw reinforcements can be observed in Fig. 6.29 (a). However, slip traces on the surface of the tensile specimen are difficult to observe at low magnification due to the limited plastic deformation before fracture. Upon closer examination in Fig. 6.29 (b) and (c), numerous intersecting slip traces are observed within the equiaxed α grains, indicating the activation of multi-system slip in α grains, which is similar to the behavior of equiaxed α grains in air-cooled materials. Due to the high strength of the transformed β phase, slip is less likely to activate,

resulting in less slip traces in the transformed β phase. Deep slip traces can be observed in the primary α laths in the transformed β phase, which is mostly parallel to the longitudinal direction of the laths, indicating the strain in transformed β phase is mainly accommodated by the internal primary α laths. Tan et al. [150] suggested that strain concentration within the primary α laths in water-quenched microstructures makes cracks more likely to initiate. In Fig. 6.29 (c), some slip lines can be observed crossing the primary α lamellae and the transformed β phase. The different propagation directions of slip traces in the two phases indicate different preferred slip directions. Observation of Fig. 6.29 (d) and (e) reveals the formation of twins in both equiaxed α phase and primary α laths. Unlike in the lamellae obtained with air-cooling, twins in the primary α laths cannot extend into adjacent lamellae through the transformed β phase.

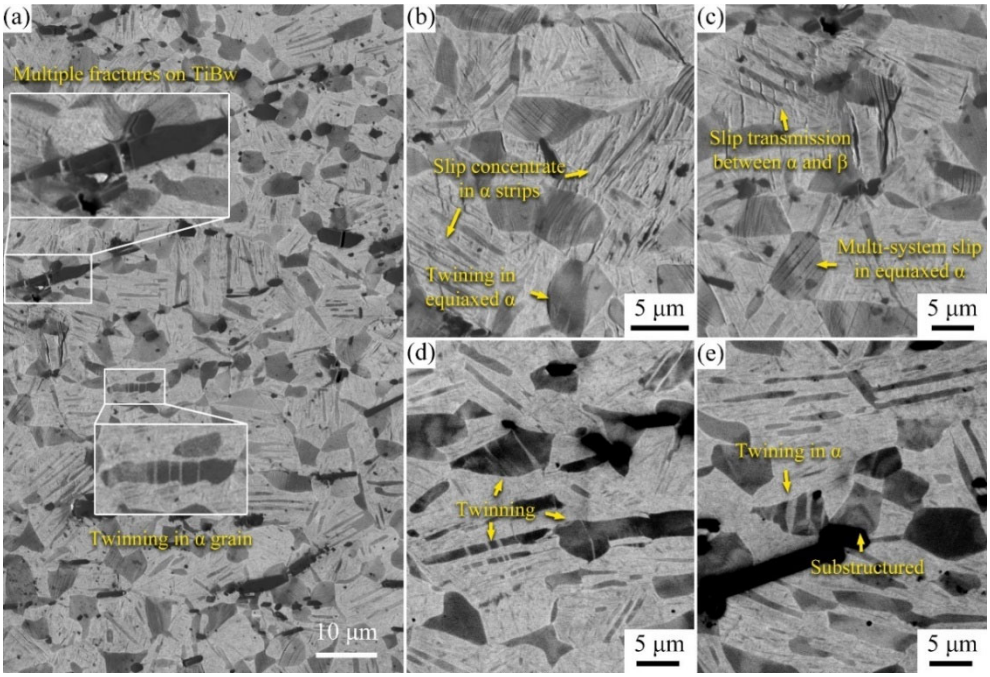

Fig. 6.29 BSE images of fracture side-faces of STP-1010WQ after room temperature tensile test, (a) low magnification morphology, (b), (c) slip traces, (d), (e) polished surface

In summary, the surface side faces STP-980AC, STP-1010AC, STP-1050AC, and STP-1010WQ tensile specimens indicate that the room temperature plastic deformation of TiBw/TA15(Si) composites is primarily achieved through slipping, twinning can help to accommodate the plastic strain when slip is hindered. The equiaxed α grains in the material are prone to multi-system slipping, and slip traces are mainly confined within individual α grains. The lamellar microstructures

obtained with air-cooling exhibits predominantly single-system slipping, with slip traces able to penetrate the α/β interfaces and induce the misalignment of lamellae, thereby compromising the integrity of the lamellar structures. Compared to equiaxed α grains, slip lines within the lamellar structure are sparser and more distinct, indicating a propensity for slip localization in the α/β lamellae. Besides, slip traces parallel to the lamellar direction are scarcely observed in the lamellar microstructure, suggesting the inhibition of prismatic slip within the lamellae. In water-quenched conditions, slip is significantly impeded by the transformed β phase, and deformation is primarily accommodated by coarse primary α lamellae.

The α/β phase boundaries can impede dislocation penetration, limiting the length of dislocation pile-ups within α lamellae [151], and accumulate a high density of dislocations internally [152], resulting in higher strength of the lamellar microstructure compared to monolithic α phase. However, dislocations traversing through the two-phase structure can induce the degradation of interface, reducing its ability to impede dislocations and resulting in the softening [153]. This also leads to the occurrence of strain localization. Based on this, Fig. 6.30 provides an illustrative depiction of the deformation behavior of lamellar microstructures in TiBw/TA15(Si) composites. As shown in Fig. 6.30 (a), before plastic deformation, the lamellar microstructure is intact, and the α/β interface provides significant resistance to dislocation movements. With the progress of plastic deformation, some dislocations penetrate the α/β interfaces and disrupt their integrity, which weakens the capability of interfaces to impede dislocations, allowing more dislocations to traverse the lamellae and further compromising the integrity of α/β interfaces. The interplay between dislocation traversal and interface weakening within the lamellae ultimately leads to severe misalignment of the lamellar microstructure, as shown in Fig. 6.28 (d). Since the dislocations penetrate the α/β interfaces along specific slip plane, the shear stress required for following penetrations are significantly lowered, resulting in one dominant slip direction within the lamellae. At the same time, the weakened α/β phase boundaries reduce the stress concentration within the lamellae, making the dislocations difficult to traverse the intact α/β interface. Therefore, slip is confined to a few weakened planes within the lamellae, leading to strain localization within the lamellar microstructures.

The mechanism for the suppression of prismatic slip within the lamellae can be explained by the configuration of slip systems illustrated in Fig. 6.30 (b). When the slip direction is <11-20>, which is the most common slip direction in α-Ti, there are three potential slip planes: basal, prismatic, and pyramidal. While in β-Ti, although both {110}<1-11> and {112}<11-1> slip systems are commonly activated at room temperature, the {112}<11-1> slip system has a higher critical resolved shear stress and is therefore more difficult to activate [154].

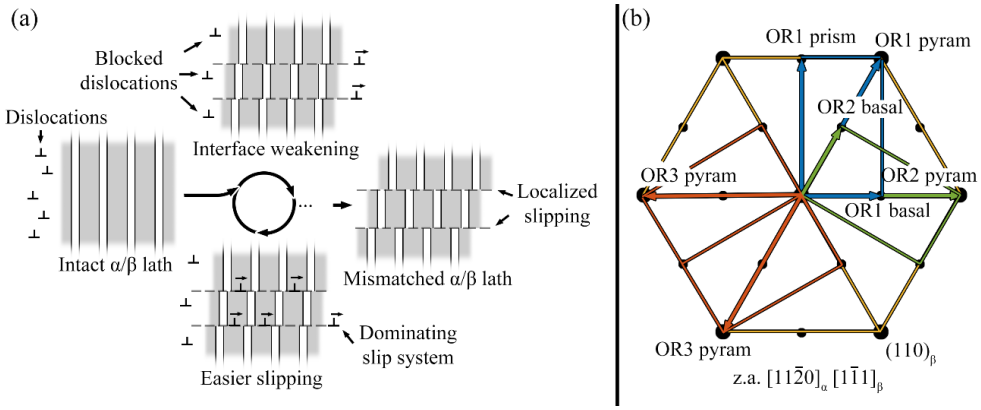

Fig. 6.30 Schematic diagrams of plastic deformation behaviors of lamellar microstructures, (a) softening mechanism of lamellae, (b) slip systems in lamellar microstructures

Due to the BOR between the α and β phases within lamellae, namely $(0001)_\alpha \parallel (110)_\beta$ and $[11\text{-}20]_\alpha \parallel [1\text{-}11]_\beta$, there exist a shared slip direction in two phases. Fig. 6.30 (b) depicts the electron diffraction patterns of the β phase and all α phase variants satisfying the BOR using this shared direction as the zone axis. It can be observed that under a single $[11\text{-}20]_\alpha \parallel [1\text{-}11]_\beta$ direction, there are three α variants that satisfy the BOR, denoting as OR1, OR2, and OR3. The basal plane of OR1 is parallel to the (110) plane of the β phase, while the pyramidal planes of OR2 and OR3 are parallel to the (110) plane of the β phase. Additionally, the basal plane of OR2 and OR3, and the pyramidal plane of OR1 are all parallel to each other. Therefore, lamellae with the OR1 orientation can always be compatible with the surrounding β phase and other α variants OR2 and OR3 when undergoing basal or pyramidal slip along the [11-20] direction. However, lamellae with the OR1 orientation are only compatible with the {112}<11-1> slip system of the β phase when undergoing slip along the prismatic plane, and are not directly compatible with α variants with OR2 and OR3 orientations. This leads to a greater constraint on the activation of prismatic slip compared to basal and pyramidal slip, resulting

in its suppression in the lamellar microstructure.

6.4.4 Slip activation of TiBw/TA15(Si) composites during room temperature tensile testing

In order to determine the activation of slip systems in materials under different state, the crystal orientations on the fracture side faces of the room temperature tensile specimens were analyzed using EBSD technique. The Taylor's plastic deformation model was employed to assess the most favorable slip systems, the actual activated slip system was determined by comparing the most favorable systems with the slip traces on the fracture side face. The Taylor's plastic deformation model assumes that in polycrystalline materials, the activation of slip systems in each grain is governed by both geometric and energetic conditions. The geometric condition postulates that the plastic deformation within each grain is consistent with the macroscopic plastic deformation of the material. This condition can be expressed mathematically as follows:

$$\varepsilon = \sum_{i=1}^{N} m_i \varepsilon^D{}_i \tag{6-13}$$

In which ε is the macroscopic deformation of the polycrystalline material, N is the total number of slip systems in a grain, m_i is the slip distance of the i^{th} system in the grain, and $\varepsilon^D{}_i$ is the slip direction of the i^{th} slip system in the grain, which is a second-order tensor.

For α-Ti, there are a total of 48 possible slip directions, including 6 on basal planes, 6 on prismatic planes, 12 <a> type on pyramidal planes, and 24 <c+a> type on pyramidal planes. However, the plastic deformation tensor has only 5 independent components, there are infinity number of possible ways to produce a strain tensor with 5 independent components by linearly combining 48 independent slip direction tensors. Therefore, Eq. 6-13 has infinity number of possible solutions, and additional constraints based on the energy condition are required to solve Eq. 6-13. The energy condition assumes that the slip systems within the grain will activate in a manner that minimizes the energy consumption. The work done for each slip system can be calculated by multiplying the slip distance and the critical resolved

shear stress required for activation. Thus, the work done during plastic deformation of a grain can be expressed as:

$$W = \sum_{i=1}^{N} m_i \tau^{C}{}_{i} \tag{6-14}$$

In which W is the work done on the grain to achieve plastic deformation, N is the total number of slip systems in the grain, m_i is the slip distance for the i^{th} system in the grain, $\tau^{C}{}_{i}$ is the critical resolved shear stress required to activate the i^{th} slip system in the grain.

By solving Eq. 6-13 under the constraint of minimizing Eq. 6-14, the slip distances m_i for each slip system can be determined, revealing the most favored slip systems for each grain. The relative critical resolved shear stresses for different slip systems used for calculations are shown in Table 6.6 [155]. Compared to Schmid's model, Taylor's model is capable of resolving the incompatibility between grains with different orientations in polycrystalline materials, providing higher accuracy when predicting the plastic deformation of polycrystalline materials. By plotting the most favorable slip directions for the four slip systems (basal, prismatic, <a> type pyramidal, and <c+a> type pyramidal) within each grain and comparing them with the directions of slip traces, the activation of slip systems within the grains can be determined. Statistical analysis of the activation of slip systems in TiBw/TA15((Si) composites of different states were conducted to investigate the influence of microstructure on slip system activation.

Table 6.6 Slip systems and corresponding relative CRSS in α-Ti [155]

Slip system	Slip plane	Slip direction	Relative CRSS
Basal	{0001}	<11-20>	1
Prismatic	{1-100}	<11-20>	1
Type <a> pyramidal	{1-101}	<11-20>	1
Type <c+a> pyramidal	{1-101}	<11-23>	4

The activation of slip systems in STP-Ti is illustrated in Fig. 6.31. In Fig. 6.31 (a), fine equiaxed grains are observed in STP-Ti, and microtextured regions where grains with similar crystal orientations that evolves from a same lamellae colony

are observable. A comparison between Fig. 6.31 (a) and the corresponding regions (Region I and Region II) in Fig. 6.31 (b) reveals that slip traces can directly propagate through the adjacent equiaxed α grains with similar orientations. In Region I, the most favorable slip planes (indicated by the green lines in Fig. 6.31 (a)) are almost in a same direction for all grains, resulting in nearly straight slip traces across Region I. In Region II, the slip traces exhibit bending due to the presence of slight orientation deviations between grains, which leads to non-parallel alignment of the most favorable slip planes and bent slip traces. In Region III shown in Fig. 6.31 (a), the grains exhibit significant orientation differences, hence the slip traces in Fig. 6.31 (b) are confined to a single grain. The activation frequencies of different slip systems in STP-Ti are depicted in Fig. 6.31 (c). It can be observed that prismatic slip has the highest activation frequency, accounting for approximately 51% of all slip traces, followed by basal slip with a frequency of around 30%. The occurrence of pyramidal slip is the lowest, with approximately 13% for <a> type and only 5% for <c+a> type.

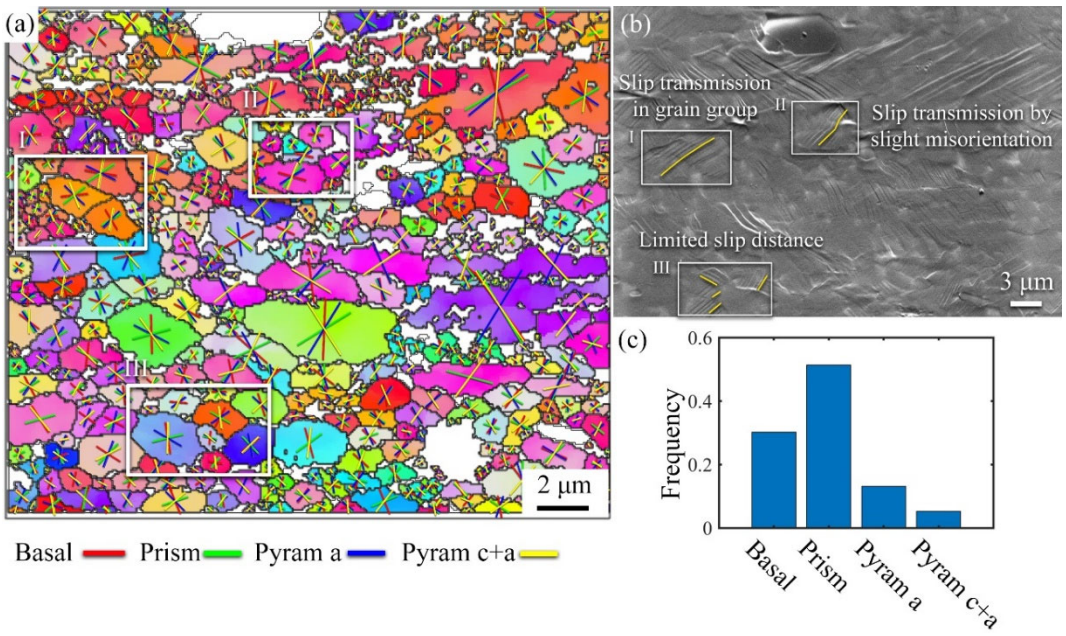

Fig. 6.31 Activation of slip systems in STP-Ti during room temperature tensile tests, (a) orientation map of α grains and the most favored slip direction for each system, (b) slip traces on the fracture side face, (c) the frequency of slip system activation

The activation of slip systems in STP-1010AC is illustrated in Fig. 6.32. It can be observed that STP-1010AC contains both equiaxed α phase and large-sized lamellar microstructures. The regions labeled as b and c in Fig. 6.32 (a) represent the lamellar microstructures in STP-1010AC. Due to the similar orientations of the α

phase within the lamellar microstructures, both regions b and c are identified as the same grain by EBSD. The morphologies of slip traces in regions b and c are shown in Fig. 6.32 (b) and (c), respectively.

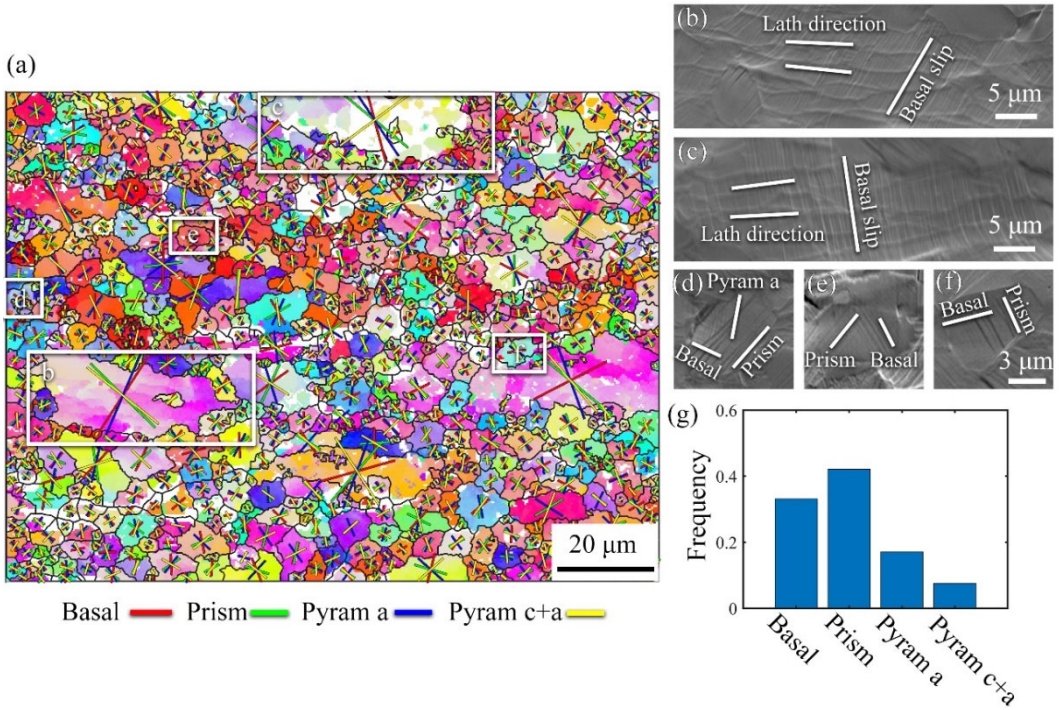

Fig. 6.32 Activation of slip systems in STP-1010AC during room temperature tensile tests, (a) orientation map of α grains and the most favored slip direction for each system, (b), (c), slip traces in the lamellar microstructures, (d) – (f) slip traces in equiaxed α grains, (g) the frequency of slip system activation

Consistent with the previous observations, the slip traces in regions b and c propagate through the lamellar structures, and only a single slip trace direction can be observed within the lamellar structures. Comparing with the most favorable slip directions for each slip system in Fig. 6.32 (a), it is found that the slip traces in Fig. 6.32 (b) and (c) belong to basal slip. Regions d-f in Fig. 6.32 (a) are the equiaxed α grains in the material. The morphologies of slip traces within these grains are shown in Fig. 6.32 (d)-(f), slip traces with multiple directions are observable within the equiaxed α grains. By comparing with the most favorable slip directions for each slip system, it is observed that the grains in Fig. 6.32 (d) activate basal, prismatic, and <a> type pyramidal slip, while the grains in Fig. 6.32 (e) and (f) activate basal and prismatic slip, respectively. The activation frequencies of different slip systems in STP-1010AC are depicted in Fig. 6.32 (g). Compared to STP-Ti, the frequency of prismatic slip in STP-1010AC significantly decreases from 51% to 42%, confirming the conclusion that the presence of lamellar microstructures suppresses

prismatic slip in the material. There is a slight increase in the activation frequencies of all other slip systems, with the activation frequency of basal slip increasing from 31% to 33%, <a> type pyramidal slip increasing from 13% to 17%, and <c+a> type pyramidal slip increasing from 5% to 7%.

The activation of slip systems in STP-1010WQ is shown in Fig. 6.33. Due to the fine structures and severe lattice distortion in the transformed β phase, the fraction of zero-solutions in STP-1010WQ is higher compared to other samples. The morphology of slip traces around the transformed β phase can be observed in Fig. 6.33 (b) – (d), with the corresponding locations marked in Fig. 6.33 (a).

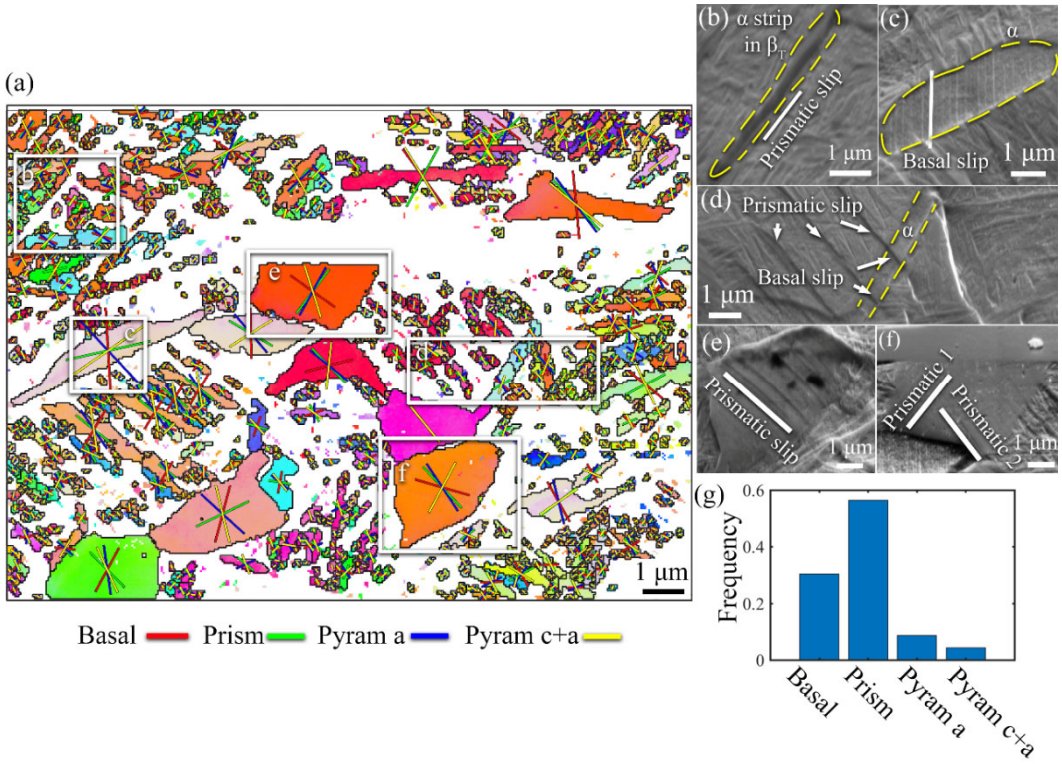

Fig. 6.33 Activation of slip systems in STP-1010WQ during room temperature tensile tests, (a) orientation map of α grains and the most favored slip direction for each system, (b) – (d), slip traces in the transformed β phase, (e), (f) slip traces in equiaxed α grains, (g) the frequency of slip system activation

It is observed that the slip traces in the transformed β phase are typically concentrated within the coarse primary α lamellae and oriented along the longitudinal direction of the lamellae. Comparing with the most favorable activation direction for each slip system, it is found that the primary α lamellae in Fig. 6.33 (b) and (d) activate prismatic slip. Although previous analysis has revealed that the activation of prismatic slip in laminated α phase is suppressed, the high

strength of the transformed β phase makes it difficult for slip traces to traverse, thus the slip traces are limited in the longitudinal direction of the primary α laths. Examining the primary α laths locating outside the transformed β phase in Fig. 6.33 (c) and (d), the activation of basal slip is observed. Slip traces in the equiaxed α grains are shown in Fig. 6.33 (e) and (f). It is determined that prismatic slip is activated in the grains shown in Fig. 6.33, while the grains in Fig. 6.33 (f) activate two distinct prismatic slip systems with different directions. It is worth noting that according to the Taylor's model, the second set of prismatic slip traces in Fig. 6.33 (f) is not the most favorable slip direction. However, their orientation is close to the slip traces in region (d), implying the slip might be activated to achieve intergranular strain compatibility. According to Fig. 6.33 (g), the frequency of prismatic slip in STP-1010WQ is 56%, which is significantly higher than those in STP-Ti and STP-1010AC. The frequency of basal slip is 30%, similar to the other two materials. The activation frequency of <a> type pyramidal slip is 8%, while that of <c+a> type pyramidal slip is 4%.

Based on the aforementioned analysis, in STP-Ti, prismatic and basal slip are the main activated slip systems. The distribution of slip traces in the material is influenced by microtexture region, in which slip traces can pass through multiple grains and extending the slip distance. In regions without microtexture, the slip distance is confined to the diameter of grains and the slip directions are more diverted, suppressing the strain localization. Ultimately, although STP-Ti exhibits a small amount of microtexture, the refined grain size and diverted grain orientations still provide excellent uniform deformability. After heat treatment and air cooling, a high proportion of prismatic slip in equiaxed α grains is maintained, but the presence of lamellar microstructures suppresses the activation of prismatic slip, leading to a significant decrease its activation frequency. Additionally, due to the limited slip direction and significant strain localization within the lamellar structures, the materials exhibit poorer uniform deformability after heat treatment and air cooling compared to STP-Ti. After heat treatment and water quenching, the activation of slip systems in equiaxed α grains remains similar to that in the air-cooled material. However, due to the difficulty of dislocations crossing the transformed β phase, plastic deformation in the transformed β phase is mainly accommodated by the activation of prismatic slip in the primary α laths, resulting

in severe deformation localization. This leads to a rapid decrease in work hardening rate and poor uniform plastic deformation capability of STP-1010WQ.

6.4.5 Dislocation configuration of TiBw/TA15(Si) composites after tensile testing

TEM was utilized to observe the dislocation configurations in STP-Ti, STP-1010AC, and STP-1010WQ after room temperature tensile deformation, to further investigate the influence of microstructures to the room temperature tensile behaviors. The TEM observations of STP-Ti after room temperature tensile deformation are presented in Fig. 6.34. In Fig. 6.34 (a), four adjacent equiaxed α grains are observable, numerous dislocations are present within the grains. The arrangement of dislocations varies among different grains, and no slip trace crossing the grain boundary is observed. Multiple equiaxed α grains can be seen in Fig. 6.34 (b). In each of the equiaxed α grains, dislocations arranged in different directions are present, indicating the activation of multi-system slip. Notably, continuous slip traces can be observed crossing both grain 1 and grain 2, suggesting a similar crystal orientation between the two grains, facilitating slip propagation across the grain boundaries. Fig. 6.34 (c) illustrates the distribution of dislocations near TiBw within α grains. When the dislocations are far from TiBw, they tend to align along the pyramidal plane (1-101) or basal plane (0001). However, when the dislocations are close to TiBw, they tend to align parallel to the TiBw/α-Ti interface, indicating that TiBw effectively impedes dislocation motion, which may lead to the strengthening of the composite but also the stress concentration in TiBw reinforcements. Dislocations are observed to pile up at the triple junctions of α grains in Fig. 6.34 (d). However, dislocations in the adjacent grains are not activated, indicating that the grain boundary effectively inhibits slip propagation across the grains. Fig. 6.34 (e) depicts the dislocation configurations near the silicide particle in STP-Ti, where numerous dislocations are entangled on the silicide, indicating its effective pinning effect on dislocations.

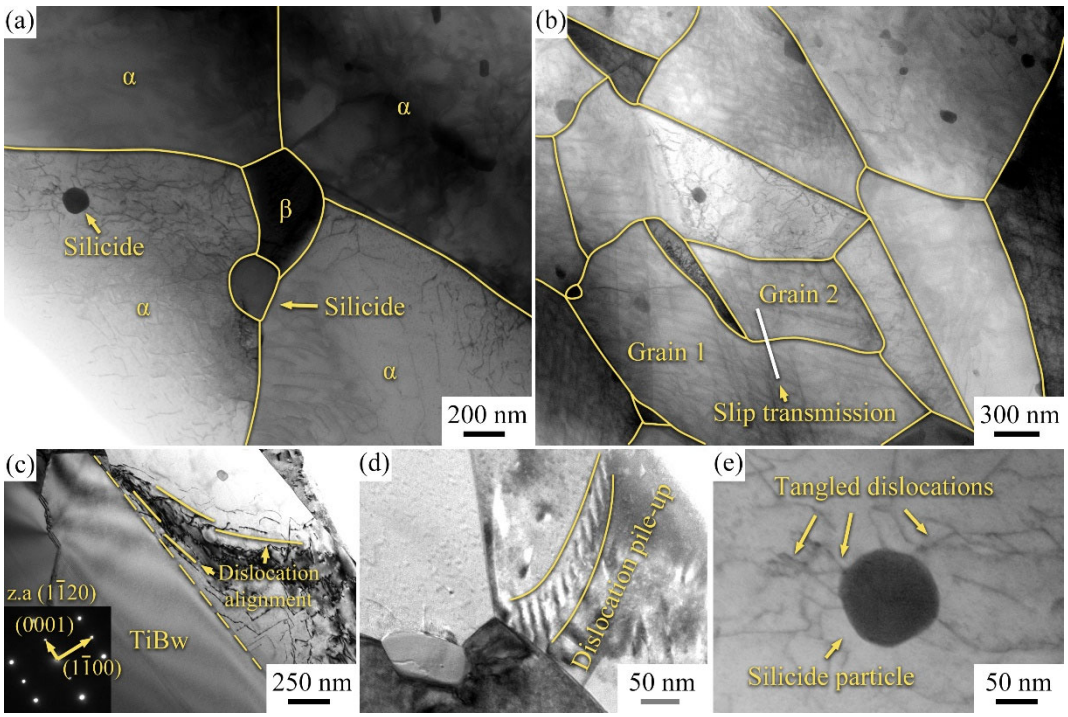

Fig. 6.34 TEM micrographs of STP-Ti after room temperature tensile test, (a), (b) α grains in different regions, (c) dislocations near TiBw, (d) dislocations hindered by grain boundary, (e) dislocations around the silicide particle

Fig. 6.35 illustrates the dislocation configurations in STP-1010AC. In Fig. 6.35 (a), a significant number of slip traces are observed in both equiaxed α grains and lamellar microstructure. Fig. 6.35 (b) presents the dislocations within grain 1, showing numerous slip traces parallel to the basal plane (0001) and a smaller amount that parallel to the pyramidal plane (1-101). Under the two-beam condition, when the operating vector **g**=[0001], the dislocations within the slip traces parallel to the basal plane are not visible, while a small number of dislocations are observed within the slip traces parallel to the pyramidal plane. Based on the criterion for dislocation invisibility, g·b=0, it can be concluded that the dislocations on the basal plane are of the <a> type, while the dislocations primarily distributed on the pyramidal plane are of the <c+a> type.

In Fig. 6.35 (c), the dislocation configurations within grain 2 are shown, revealing a significant amount of slip traces parallel to the (0001) plane. Small number of dislocations aligned along the (1-101) direction are also observed, indicating the coexistence of basal and prismatic slip in grain 2. Fig. 6.35 (d) displays the dislocations within the lamellar microstructure, where a large number of slip traces parallel to the (0001) plane can be observed traversing the lamellae. Misfit

dislocations are observed at the α/β interfaces, but no significant differences can be seen compared to that before room temperature tensile testing. Under the two-beam condition, when the operating vector **g**=[0001], a small number of <c+a> type dislocations are also visible within the lamellae aligning parallel to the (1-101) plane. However, no such dislocations are observed penetrating the α/β interfaces. Since the strain along the c-axis in α-Ti can only be accommodated by <c+a> type dislocations, despite the prevalence of basal slip in this lamellar microstructure, a small number of <c+a> type dislocations are still activated to accommodate the deformation along the c-axis. The dislocation configurations within grain 3 are illustrated in Fig. 6.35 (e), basal slip is predominated in this grain, while no significant activation of other slip systems is seen.

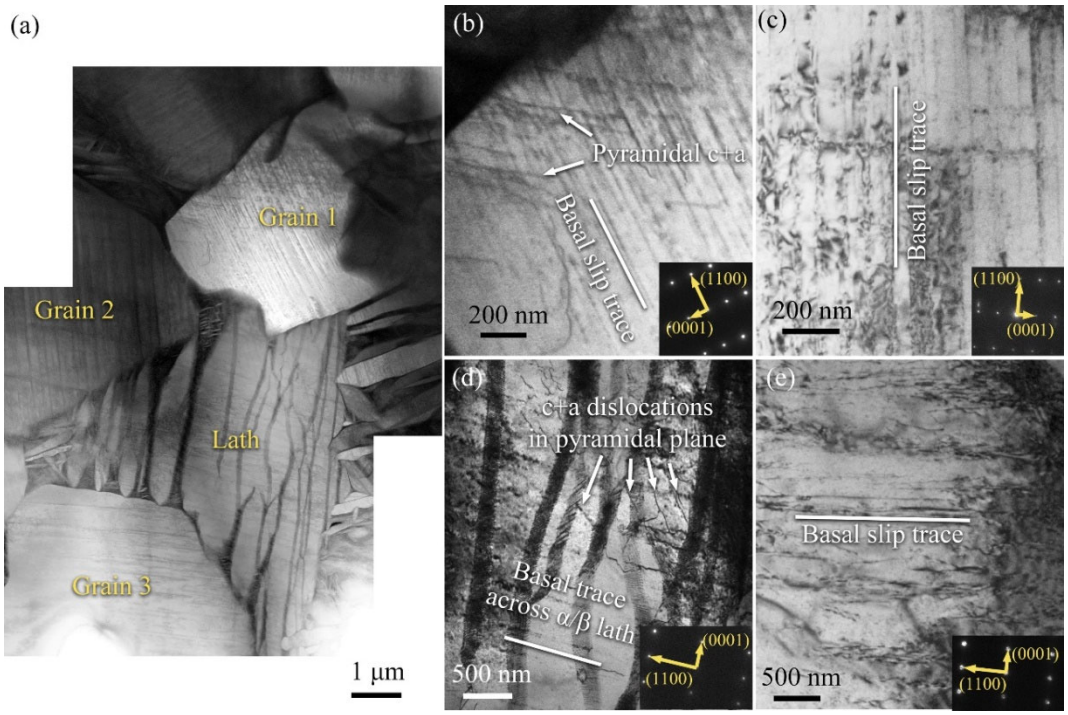

Fig. 6.35 TEM micrographs of STP-1010AC after room temperature tensile test, (a) bright field imaging at low magnification, (b) dislocations in grain 1, (c) dislocations in grain 2, (d) dislocations in lath structure, (e) dislocations in grain 3

The dislocation configurations in STP-1010WQ are shown in Fig. 6.36. In Fig. 6.36 (a), a nearly equiaxed α grain is located at the center, surrounded by transformed β phase. Within the equiaxed α grain, numerous slip traces are observable along two different directions. Determined by SAED, the slip traces are parallel to two distinct {1-101} planes, indicating pyramidal slip. Magnifying the equiaxed α grain in Fig. 6.36 (a) yields Fig. 6.36 (c), in which a large number of dislocations are seen

arranged along two intersecting slip traces.

Magnifying the transformed β phase in Fig. 6.36 (a) yields Fig. 6.36 (d), no apparent slip trace within the transformed β phase is observed, indicating the difficulty of dislocations activation, which is consistent with the SEM observation results. Rotating the α grain in Fig. 6.36 (a) to satisfy the two-beam condition with the operating vector **g**=[0001], the resulting dislocation configuration is shown in Fig. 6.36 (b), where most of the dislocations within the α grain are invisible, indicating the predominance of <a> type dislocations. Magnifying the marked region in Fig. 6.36 (b), Fig. 6.36 (e) reveals that despite the invisibility of <a> type dislocations, a small number of dislocations are still visible aligning within the slip traces, indicating the presence of <c+a> type dislocations. Hence, activation of both pyramidal <a> type slip and a small amount of pyramidal <c+a> type slip are activated in the grain.

The observations of dislocation configurations in STP-Ti, STP-1010AC, and STP-1010WQ collectively indicate the presence of significant multi-system slip within the equiaxed α grains, where basal, prismatic, or pyramidal planes can serve as slip planes. Although no prismatic slip is observed within the lamellae, the presence of a small number of <c+a> type dislocations within the lamellae suggests that, in addition to the predominant slip systems, a small amount of <c+a> type slip can be activated to accommodate strain along the c-axis. No slip traces are observed within the transformed β phase, indicating the difficulty of slip activation. Therefore, plastic deformation mainly occurs within the equiaxed α phase or other coarse lamellar α, confirming the earlier observations. Under the two-beam condition, a small number of <c+a> type dislocations are observed in most grains, indicating the significant role of <c+a> type dislocations in accommodating the deformation in α-Ti. However, due to the higher energy of <c+a> type dislocations and the large critical resolved shear stress required for the activation of <c+a> type slip, these dislocations cannot exist in large quantities within the material, which is consistent with the findings from the slip trace analysis.

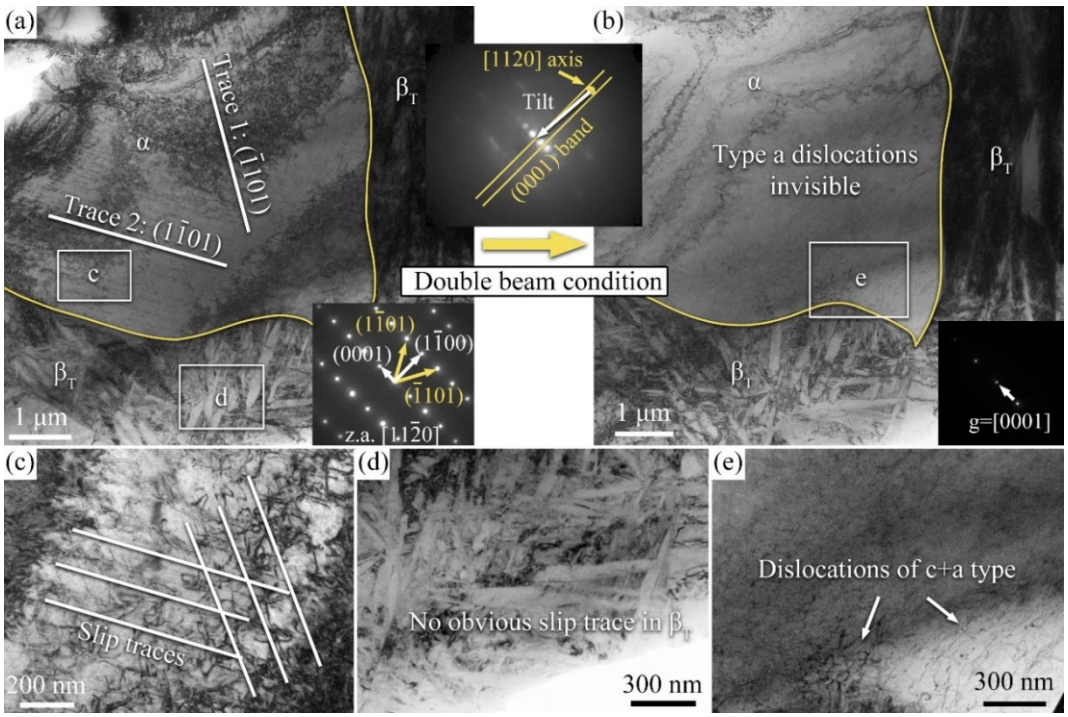

Fig. 6.36 TEM micrographs of STP-1010WQ after room temperature tensile test, (a) bright field imaging at low magnification, (b) two-beam condition with g=[0001], (c) slip traces in the equiaxed α grain, (d) transformed β phase in high magnification, (e) <c+a> type dislocations in equiaxed α grains under two-beam condition

6.5 High temperature tensile behaviors of TiBw/TA15(Si) composites

The high-temperature tensile deformation behavior of metallic materials is closely related to grain morphology. Typically, metal materials with small grain sizes and equiaxed morphologies can achieve a significant amount of uniform tensile deformation at suitable temperatures and strain rates, thus possessing the potential for forming complex components. In the previous section, TiBw/TA15(Si) composites with fine equiaxed grains were obtained through solid solution treatment and thermo-mechanical processing in dual-phase region, which are expected to exhibit favorable high temperature deformability. Therefore, in this section, the high temperature tensile test will be performed on TiBw/TA15(Si) composites under different conditions, and a comparison will be made with STP-Ti and STP-980AC to reveal the influence of material microstructure on high temperature tensile behavior. Finally, by microstructure observation of the materials after the tensile tests and kinetic analysis of the stress-strain curves under different conditions, the deformation mechanisms of the materials will be revealed.

6.5.1 High temperature tensile properties of TiBw/TA15(Si) composites

Fig. 6.37 and Fig. 6.38 show the macroscopic morphologies of the tensile specimens, and the tensile stress-strain curves of STF-Ti and STF-980AC at different temperatures and strain rates, respectively. For comparative purpose, the stress-strain curve of S-Ti at 800 °C/0.0003 s^{-1} is also included.

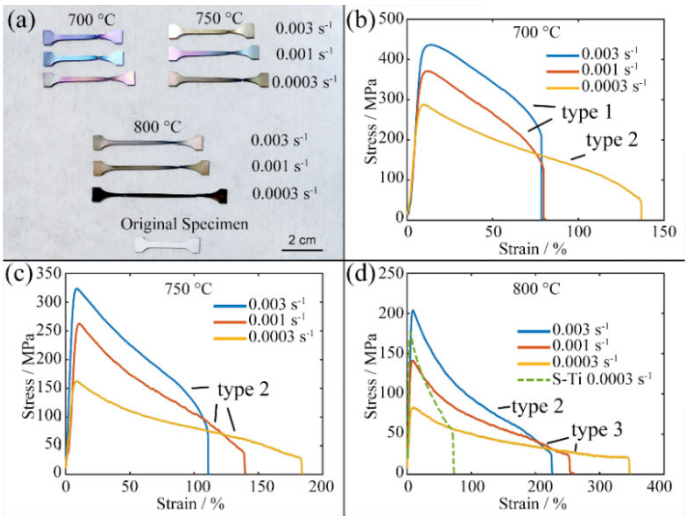

Fig. 6.37 Fractured samples and high temperature tensile stress-strain curves of STP-Ti, (a) tensile specimens after testing, (b) – (d) stress-strain curves at conditions, (b) 700 °C, (c) 750 °C, (d) 800 °C

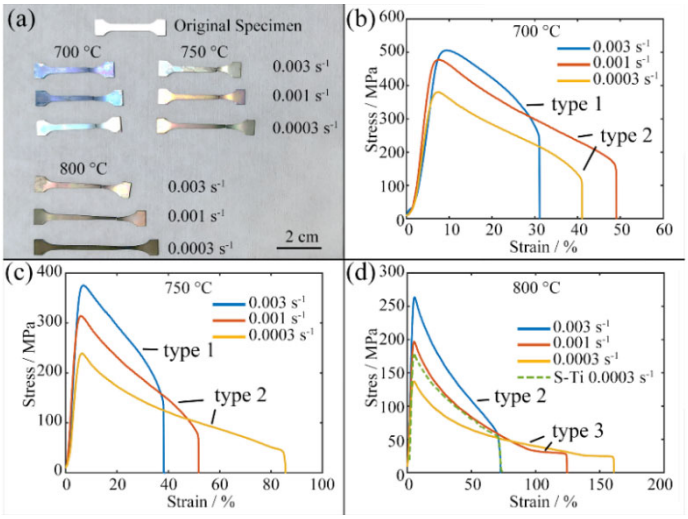

Fig. 6.38 Fractured samples and high temperature tensile stress-strain curves of STP-980AC, (a) tensile specimens after testing, (b) – (d) stress-strain curves at conditions, (b) 700 °C, (c) 750 °C, (d) 800 °C

From Fig. 6.37 (a), it can be observed that the STP-Ti exhibits uniform deformation throughout the specimen after high temperature tensile test, except near the fracture

point. Figures Fig. 6.37 (b) – (d) show that the stress-strain curves of STP-Ti exhibit a rapid increase in stress first, then reaching a peak value before gradually decreasing at different rates until fracture. The peak stresses during high temperature tensile decreases with increased deformation temperature and decreased strain rate, while the fracture elongations show the opposite tendency to that of the peak stresses. Fig. 6.38 (a) reveals that the macroscopic morphologies of the STP-980AC specimens are similar to those of STP-Ti, with deformation localization observed only near the fracture points. The stress-strain curves of STP-980AC exhibit similar characteristics to those of STP-Ti, and the changes of the peak stresses and elongations with respect to temperature and strain rate are consistent. The peak stresses and fracture elongations of different materials under different conditions are summarized in Table 6.7 and Table 6.8, respectively.

Table 6.7 High temperature tensile peak stresses of materials under different conditions / MPa

Materials	Temperature / °C	Strain rate / s^{-1}		
		0.003	0.001	0.0003
STP-Ti	700	436	371	287
	750	323	262	162
	800	204	141	83
STP-980AC	700	506	478	380
	750	376	314	239
	800	263	197	137
S-Ti	800	300	246	176

Compared to STP-Ti, STP-980AC exhibits higher peak stresses and lower elongations under the same conditions. STP-980AC achieves elongation exceeding 100% only at 800°C / 0.001 s^{-1} at 0.0003 s^{-1}, with a temperature increase of 100°C compared to STP-Ti to achieve the same deformability. This indicates that the grain growth and lamellar microstructure resulting from heat treatment harms the high temperature deformability of STP-980AC. Compared to S-Ti, both STP-Ti and STP-980AC exhibit higher elongation and lower peak stress at 800°C / 0.0003 s^{-1}. In comparison with other studies, STP-Ti in the present study achieves a temperature reduction of 50°C for achieving elongation exceeding 300% [129,130,156,157].

Table 6.8 High temperature tensile elongations of materials under different conditions / %

Materials	Temperature / °C	Strain rate / s^{-1}		
		0.003	0.001	0.0003
STP-Ti	700	79	81	136
	750	112	140	185
	800	227	260	348
STP-980AC	700	31	39	41
	750	39	52	86
	800	73	125	161
S-Ti	800	42	49	73

Based on the softening behaviors, the stress-strain curves can be qualitatively classified into three types. Type 1 stress-strain curves consist of work hardening, uniform softening, and accelerated softening stages. Type 2 stress-strain curves consist of work hardening, decelerated softening, and accelerated softening stages. Type 3 stress-strain curves consist of work hardening, decelerated softening, uniform softening, and steady-state stages. As the strain rate decreases and the deformation temperature increases, the stress-strain curves gradually transition from Type 1 to Type 2, and eventually to Type 3. In the following discussion, the microstructural features of the materials after high-temperature tensile test will be analyzed based on different types of stress-strain curves.

6.5.2 Hot tensile microstructure evolution of TiBw/TA15(Si) composites

Fig. 6.39 shows the typical macroscopic and microscopic morphology of specimens corresponding to type 1 stress-strain curves. The microstructure observation was carried out on three different locations: one at the fracture point (Fig. 6.39 (c)), one at the necking region (Fig. 6.39 (d)) and one at the uniformly deformed region (Fig. 6.39 (e)) to show a continuous evolution of the microstructure.

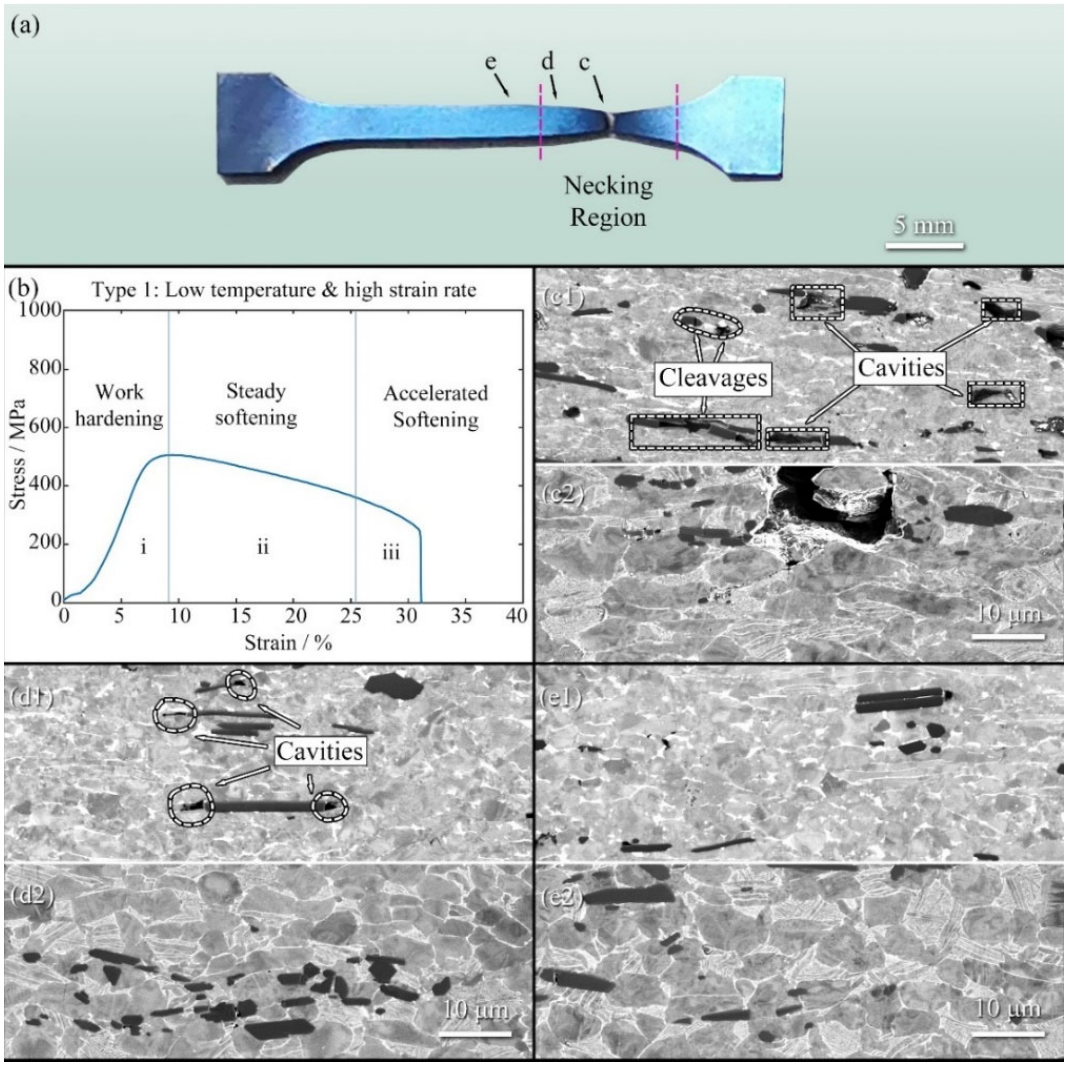

Fig. 6.39 Typical macroscopic and microscopic morphologies of samples with type 1 curves, (a) macroscopic morphology, (b) a typical type 1 stress-strain curve, (c) – (e) typical deformation microstructures at the positions marked in (a), subfigures 1 and 2 are corresponding STP-Ti and STP-980AC, respectively

Type 1 stress-strain curves feature a strain hardening stage, a steady softening stage and an accelerate softening stage. It is well known that the dynamic recrystallization (DRX) of metals is accompanied with the drastic decrease of dislocation density [158], the rapid softening after reaching the peak stress is therefore deemed as an important indicator of DRX [159]. Hence, the steady softening of the curves of type 1 implies the absence of DRX. Due to the low elongation, no significant stretch inside of the gauge length is observed in Fig. 6.39 (a), however, an obvious necking region can be seen near the fracture point, which is related to the accelerated softening stage in the stress-strain curve.

Observing the microstructure near the fracture point (Fig. 6.39 (c)), equiaxed grains

of STP-Ti and bimodal microstructure of STP-980AC are severely stretched along the tensile direction thanks to the strain localization. In the meanwhile, cloud-like contrast inside of α grains is observed, implying the accumulation of dislocations and substructures. From the fracture point to the evenly deformed region, the stretching in the microstructure becomes less obvious, whereas the cloud-like contrast still remains. As implied by the stress-strain curve, recrystallization grain is not observed throughout Fig. 6.39 (c) – (e), attributing to the low deformation temperature and the high strain rate. The low temperature and high strain rate also suppress the effectiveness of dynamic recovery, leading to the intensive accumulation of dislocations and the cloud-like contrast observed in the grains. Hence, the stress-strain curves of type 1 exhibit the highest flow stresses among all 3 types of curves. Aside from the stretching in the microstructure, the fracture of TiBw and cavities are also important features in Fig. 6.39 (c) – (e). From the necking region to the evenly deformed region, the number of fracture and cavities gradually decreases. It is also noticeable that cavities are highly likely to appear at the tips of TiBw. TiBw is very effective dislocation barrier, stress will concentrate on TiBw while TiBw hindering the movement of dislocations, eventually leading to the breakage of the whisker or the debonding of TiBw/Ti interface, creating nucleation site for cavity. The tips of TiBw bear the highest normal stress during plastic deformation, thereby having the highest probability of cavitation. The cavities release the stress from TiBw into the neighboring matrix, resulting in the localization of plastic strain which further prompts the formation of cavities. The cavitation and strain localization lead to the necking of the tensile specimens and the rapid decrease of tensile stress, the specimen will eventually fracture due to the expansion and connection of the cavities.

Fig. 6.40 Shows the typical morphology of the fractured specimens with type 2 stress-strain curves, and the corresponding microstructures. The homogeneously elongated region of type 2 specimen is obviously longer than that of type 1 specimens, showing a better tensile deformability. The tensile stress-strain curves of type 2 firstly show a strain hardening stage, after reaching the peak value, the stress drop first rapidly then gradually, forming a decelerated softening stage. This indicates the activation of dynamic recrystallization. After reaching a certain extent of elongation, an accelerated softening stage can be observed on the stress-strain

curve, resulting in the fracture of the specimen. A necking region corresponding to the accelerate softening stage can also be found on the specimen with type 2 curve.

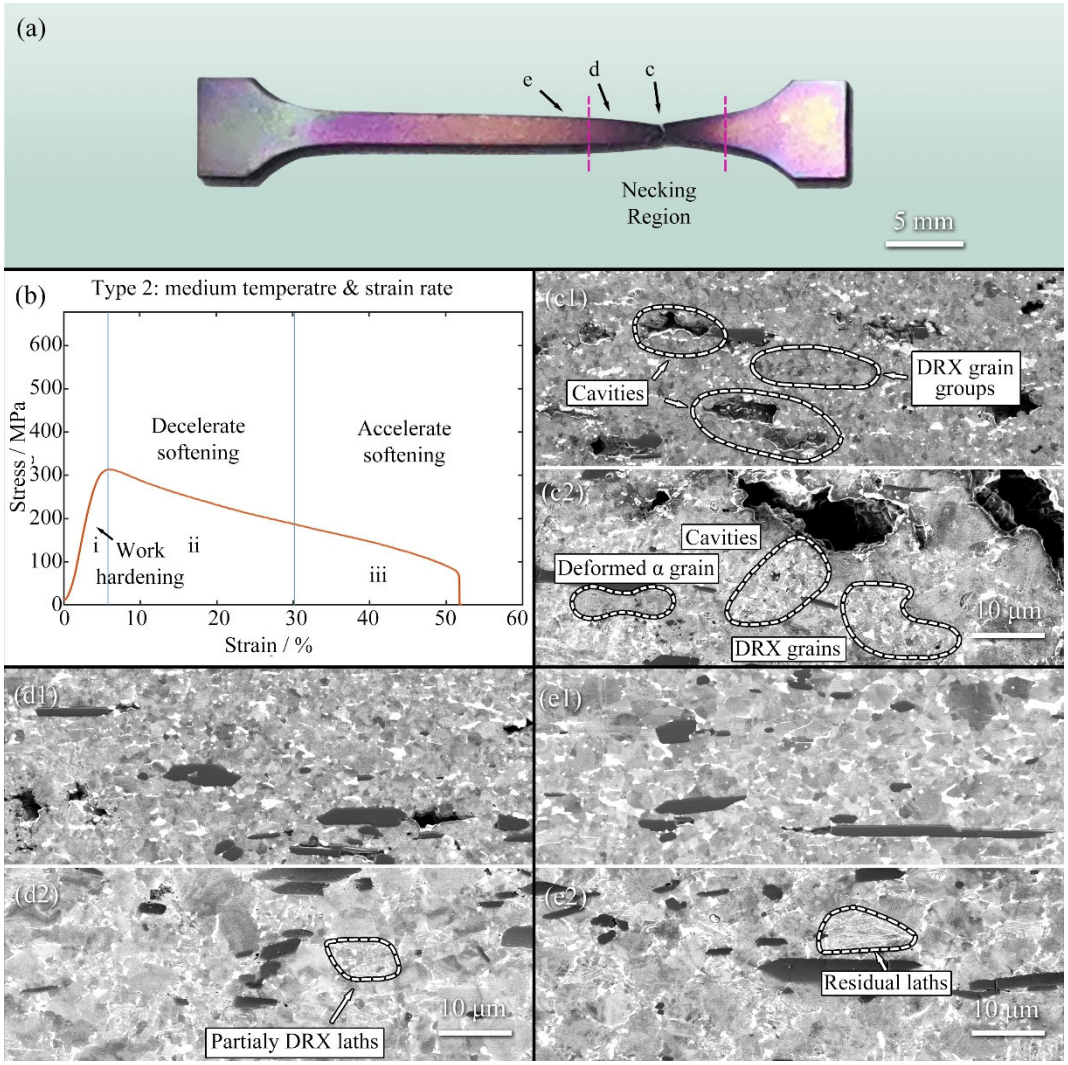

Fig. 6.40 Typical macroscopic and microscopic morphologies of samples with type 2 stress-strain curves, (a) macroscopic morphology, (b) a typical type 1 stress-strain curve, (c) – (e) typical deformation microstructures at the positions marked in (a), subfigures 1 and 2 are corresponding STP-Ti and STP-980AC, respectively

There are obvious differences between microstructures of type 1 and type 2. Most remarkably, a vast number of recrystallized grains are seen in Fig. 6.40 (c) – (e). In STP-Ti, recrystallization grains generate homogeneously inside the elongated original α grains, implying a continuous nucleation and growth of DRX grains. In STP-980AC, DRX grains mainly nucleate in α/β laths, leaving refined DRX α grains and broken β laths around the substructured original α grains. The degree of DRX weakens from the necking region to the evenly deformed region thanks to the gradually reduced deformation degree. As a result, the lamellar microstructures in

STP-980AC evolve from fully equiaxed (Fig. 6.40 (c2)) to partially recrystallized (Fig. 6.40 (d2)), and eventually to fully lath-like (Fig. 6.40 (e2)). DRX process consumes a vast number of dislocations and effectively relieves the stress concentration on TiBw, the fracture of TiBw is, therefore, less likely to be observed in Fig. 6.40 than in Fig. 6.39. However, cavities with large volume are still observable at TiBw/Ti interfaces, which is caused by the weakening of TiBw/Ti bonding with the elevating temperature, as proven by the works of other researchers [160,161]. Due to the higher flow stress of STP-980AC, the cavities observed in Fig. 6.40 (a2) are significantly larger than those of STP-Ti in Fig. 6.40 (a1), resulting in the early fracture of STP-980AC and consequently the reduced elongation.

The typical morphology of fractured specimen and the typical microstructures corresponding to type 3 curves are shown in Fig. 6.41. A significant extent of elongation of the fractured specimen is observable in Fig. 6.41 (a). Different from that observed in Fig. 6.39. And Fig. 6.40., the necking region in Fig. 6.41 (a) is longer but the extent of necking is less significant, implying a good capability of uniform deformation. Type 3 curves feature four stages, which started with a work hardening stage, followed by a decelerating softening stage and a steady softening stage, and end with a steady state flow stage. The steady state flow at the end of type 3 curves hints the dynamic grain coarsening according to the work of Mosleh et.al. [162], a special work hardening mechanism that activated under high strain, which is reflected on the prolonged necking region of the fractured specimens.

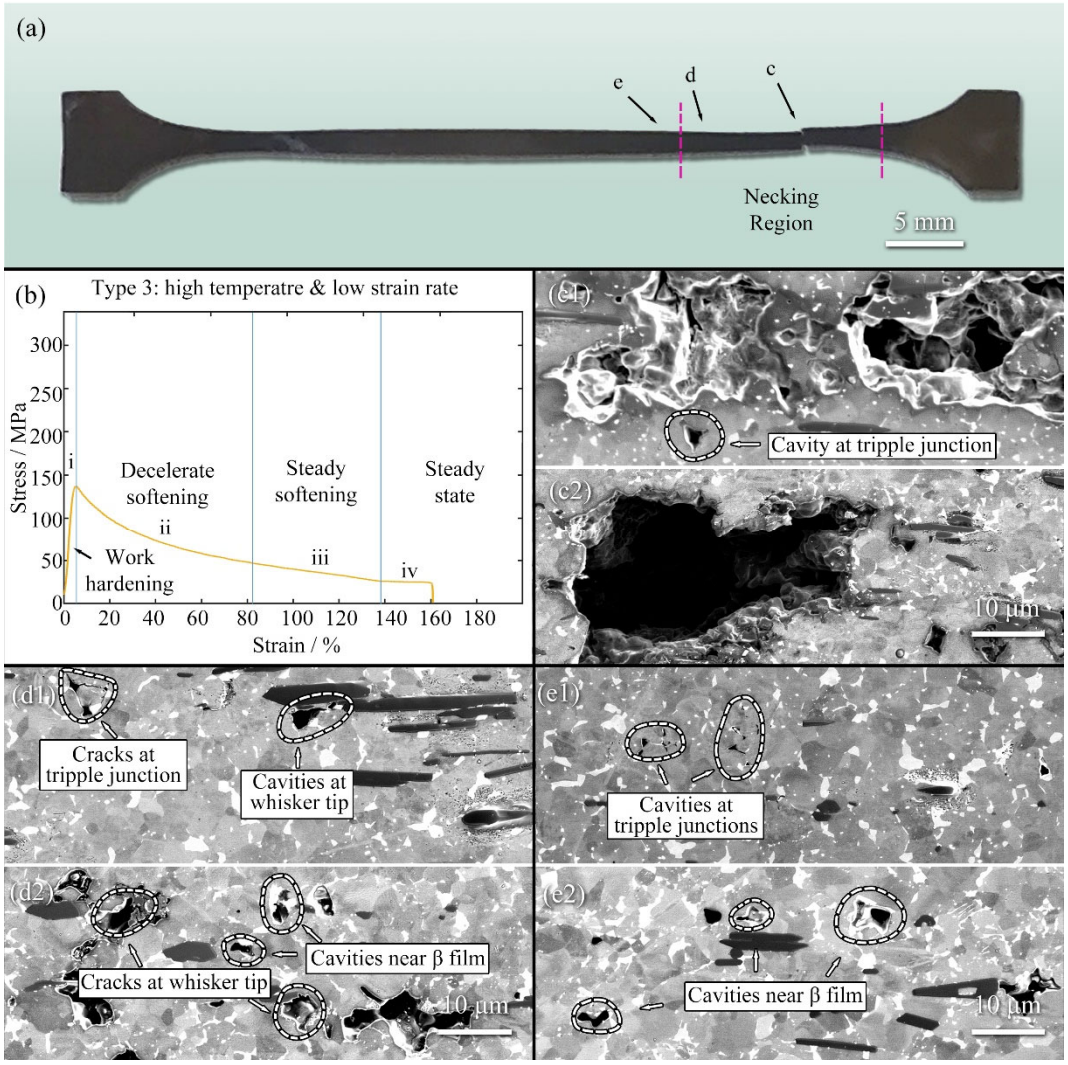

Fig. 6.41 Typical macroscopic and microscopic morphologies of samples with type 3 stress-strain curves, (a) macroscopic morphology, (b) a typical type 1 stress-strain curve, (c) – (e) typical deformation microstructures at the positions marked in (a), subfigures 1 and 2 are corresponding STP-Ti and STP-980AC, respectively

Vast volume of cavities can be observed in Fig. 6.41 (c). Most of the cavities nucleate at the TiBw-Ti interfaces, however, TiBw in the necking region remains intact. Besides, small cavities are observable at grain junctions in both STP-Ti and STP-980AC, a new cavitation location not seen in Fig. 6.39 nor Fig. 6.40, indicating a strong strain mismatch at grain boundaries and triple junctions. With the help of digital-optical method, the volume fraction of the cavities is estimated to be 12% - 17% at the fracture point of the specimens with type 3 stress-strain curves. By contrast, the volume fraction of the cavities is estimated to be ≤ 3% in specimens with type 1 curves, and 5% - 10% in specimens with type 2 curves, indicating the specimens with type 3 curves are more capable of resisting necking and tolerating damage. The α/β lath colonies in the STP-980AC composite dissolve completely,

evolving into β films distributing around α grains. Meanwhile, the microstructure of the STP-Ti is nearly unchanged after deformation. For both composites, neither α grains nor β phase is subjected to stretch after straining, also, the complex intragranular substructure observed in α grains in Fig. 6.39 and Fig. 6.40 is not observed in Fig. 6.41, implying the significant reduction in intragranular strain. These microstructure features, as pointed out by Alabort et.al. [163], are important indicators of grain boundary sliding (GBS), a grain boundary diffusion dominated mechanism commonly seen in the superplastic deforming of titanium alloys. In a plastic deformation process dominated by GBS, strain is mainly accommodated by the rotation and displacement of grains, the intragranular deformation is thereby minimized. It is worth noticing that, although the steady state stage is proven to be induced by dynamic grain coarsening [162], the grain size shows no obvious difference before and after deformation in the present study, probably due to the rapid fracture of the specimen following the steady state stage. Looking away from the fracture point, large cavities near TiBw disappear, leaving only small cavities at the tips of whiskers and grain boundaries (Fig. 6.41 (d)), and eventually only cavities at grain boundaries (Fig. 6.41 (e)). Despite of less stress concentration on TiBw due to the reduced intragranular dislocation accumulation, the ability of TiBw to cooperate with severe plastic deformation is quite limited. Hence, a strong strain mismatch exists between the matrix and TiBw reinforcements, which eventually lead to the cavitation at TiBw/Ti interface.

To further evidence the deformation mechanisms observed previously, EBSD analysis was carried out on the necking regions of the fractured samples. Samples of STP-Ti tested at 800 °C/0.0003 s^{-1}, STP-Ti tested at 750 °C/0.001 s^{-1} and STP-980AC tested at 750 °C/0.001 s^{-1} were selected for EBSD analysis. The geometrical necessary dislocation (GND) density maps are plotted to see the distribution of dislocations, the statistical distributions of GND density are also plotted. The results are shown in Fig. 6.42.

Two cavities can be observed in Fig. 6.42 (a) and Fig. 6.42 (b), one of which is caused by the debonding of grain boundaries, and the other is induced by the debonding of TiBw-Ti interface. High GND density is observable near the cavities and the grain junctions (as pointed by the arrows), while the in-grain GND density

stays low. On the contrary, A high density of GNDs can be seen in STP-Ti and STP-980AC deformed at 750 °C/0.001 s^{-1} (Fig. 6.42 (d) – (i)). In STP-Ti, small recrystallization grains are observable near the grain boundaries and near the cavity. Regions of zero-solutions are seen inside the lamellae of STP-980AC, massive ultra-fine recrystallization grains are also observable in the zero-solution regions through band contrast maps. The zero-solutions are obtained because the size of recrystallization grains is too fine to be recognized by EBSD.

Comparing Fig. 6.42 (b), (e), and (h), it can be observed that the GND density in the necking region of STP-Ti specimens after high-temperature tensile testing at 800 °C / 0.0003 s^{-1} is significantly lower than those in STP-Ti and STP-980AC specimens produced at 750 °C / 0.001 s^{-1}. From Fig. 6.42 (c), (f), and (i), it can be seen that the average GND density in the necking region of STP-Ti specimens at 800 °C / 0.0003 s^{-1} is approximately 1.5×10^{14} m^{-2}, only slightly higher than the initial density in STP-Ti (approximately 1.4×10^{14} m^{-2}). This indicates that the plastic deformation of STP-Ti under this condition is governed by grain boundary sliding. In contrast, the GND density obtained from STP-Ti and STP-980AC specimens after tensile deformation at 750°C / 0.001 s^{-1} is 6.8×10^{14} m^{-2} and 6.4×10^{14} m^{-2}, respectively, which is significantly higher than that of STP-Ti at 800 °C / 0.0003 s^{-1}. It is worth noting that although the tensile specimens of STP-Ti and STP-980AC at 750 °C / 0.001 s^{-1} have similar GND density, the fracture strain of STP-Ti is approximately 2.7 times higher than that of STP-980AC under this condition. This indicates that the high-temperature plastic deformation of STP-980AC under the same condition is more dependent on dislocation movements, which is consistent with its higher tensile stress.

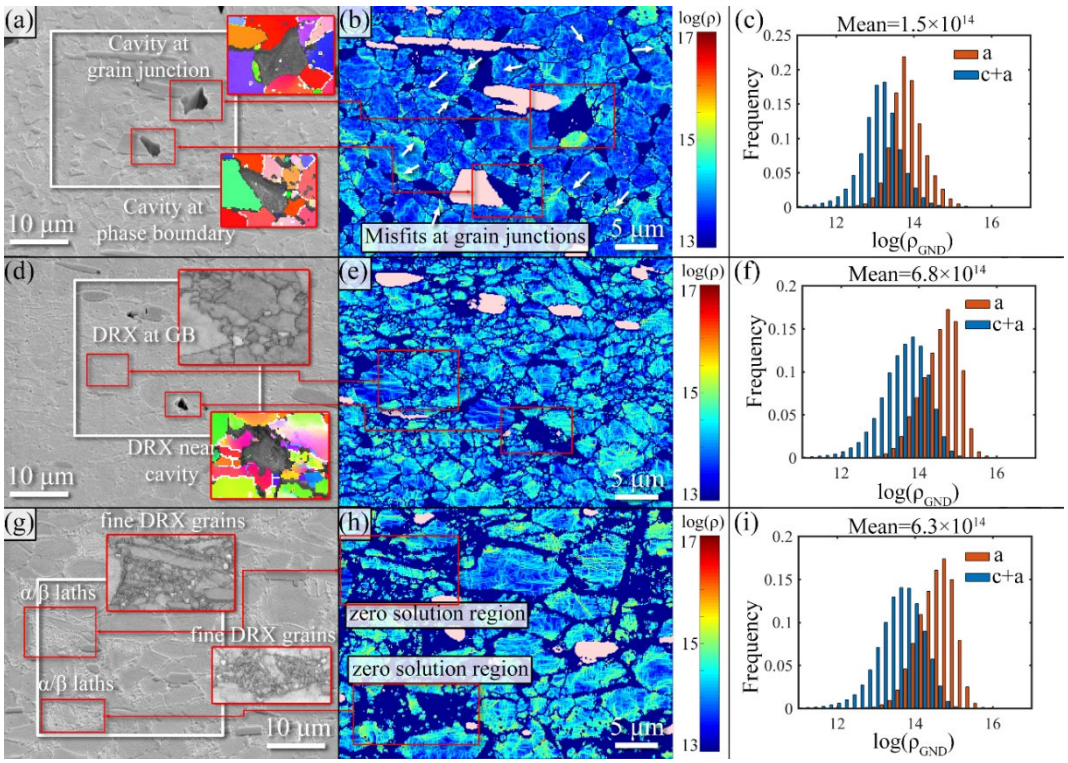

Fig. 6.42 Second-electron images, GND density maps and distribution histograms of samples tested with different conditions, (a) – (c) STP-Ti, 800 °C / 0.0003 s^{-1}, (d) – (f) STP-Ti, 750 / 0.001 s^{-1}, (g) – (i) STP-980AC, 750 °C / 0.001 s^{-1}

Based on the aforementioned analysis, it can be concluded that the high temperature tensile deformation behaviors and defect types of STP-Ti and STP-980AC change with deformation temperature and strain rate. At low temperatures and high strain rates, the deformation of the tensile specimen is primarily accommodated through the deformation of grain, resulting in significant elongation of the grain and lamellar structures within the fractured specimen. Due to the high stress levels under these conditions, TiBw reinforcements experience extensive fracture, and voids form at the stress concentration regions at the ends of TiBw and at fracture sites. As the deformation temperature increases and the strain rate decreases, dynamic recrystallization occurs during the tensile process, and the rapid consumption of dislocations leads to a rapid decrease in tensile stress after reaching its peak. At this stage, a large number of fine recrystallized grains can be observed in the microstructure, with STP-Ti exhibiting primarily dynamic recrystallization within equiaxed α grains, and STP-980AC shows dynamic recrystallization and decomposition within the lamellar microstructure. Due to the decrease in tensile stress, TiBw reinforcements almost cease to fracture, but the interfacial bonding strength between the reinforcements and the matrix decreases with increasing

temperature, leading to the cavitation through interface debonding. When the deformation temperature reaches 800 °C and the strain rate decreases to 0.001 s^{-1} and below, the tensile strain of the material significantly increases. The microstructure of STP-Ti remains unchanged after deformation, while the lamellar microstructure in STP-980AC disappears completely, and β-phase forms as thin sheets distributed around equiaxed α grains. In this case, plastic deformation in is governed by grain boundary sliding. The decrease in dislocation density reduces the stress at the TiBw interfaces, thereby reducing the occurrence of interface debonding. Meanwhile, due to significant deformation incompatibility, cavities primarily form along triple junctions. Compared to STP-Ti, STP-980AC, with coarsened grains and the presence of the lamellar microstructure, exhibits greater difficulty in grain boundary sliding. Therefore, under the same conditions, the tensile deformation of STP-980AC relies more on dislocation motion, resulting in higher tensile stress.

6.5.3 Activation energy and strain rate sensitivity of TiBw/TA15(Si) composites

Strain rate sensitivity and deformation activation energy are important indicators to describe the superplastic deformation behavior of a material. The strain rate sensitivity characterizes the capability of a material to hinder strain localization and sustain the deformation stability [164], the deformation activation energy describes the deformation resistance of a material, both giving hints to the deformation and softening mechanisms of the material.

For materials with viscous behavior, the strain rate sensitivity exponent can be calculated with the following equation [165]:

$$m = \frac{\partial \ln \sigma}{\partial \ln \dot{\varepsilon}} \tag{6-15}$$

Where σ is the tensile stress and $\dot{\varepsilon}$ is the strain rate at a certain temperature and strain. In the present work, the strain rate sensitivity exponent *m* is calculated with the peak stress obtained in the tensile test. Linear regression is done to the logarithm stress $\ln\sigma$ and the logarithm strain rate $\ln\dot{\varepsilon}$ for each composite at each temperature, to find the corresponding strain rate sensitivity. The deformation

activation energy of each composite is calculated with the Arrhenius equation of hyperbolic-sine law shown in Eq. 5-3. The temperatures, strain rates and peak stresses used for calculation are given in Table 6.7. The fitted strain rate sensitivity of each material at different temperatures are plotted in Fig. 6.43, the results of strain rate sensitivity m and deformation activation energy Q are shown in

Table 6.9. To compare the deformation mechanisms of TiBw/T15(Si) composites and TA15 alloys, the resulted obtained by Wang et al. [166] (TA15 alloy, equiaxed microstructure, grain size ~4 μm) is also added.

According to Fig. 6.43, the relationship between the peak stress and strain rate sensitivity of STP-Ti and STP-980AC at different temperatures exhibits good linearity in logarithmic coordinate, indicating that the strain rate sensitivity obeys Eq. 6-15. The strain rate sensitivity of both STP-Ti and STP-980AC increases with temperature, besides, the strain rate sensitivity of STP-Ti increases faster than that of STP-980AC with the increasing of temperature.

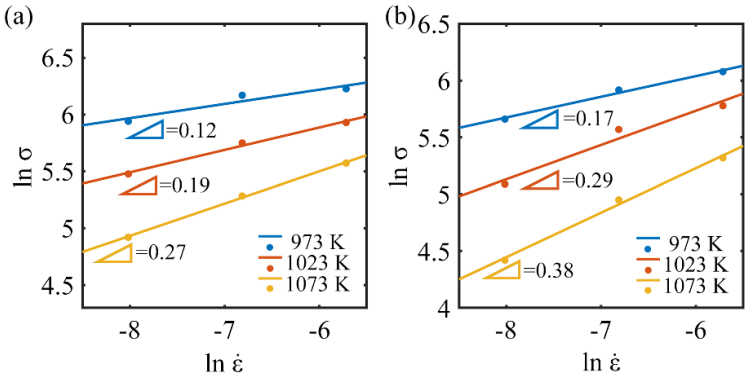

Fig. 6.43 Strain rate sensitivity of composites at different temperatures, expressed in line slopes, (a) STP-Ti, (b) STP-980AC

Table 6.9 Strain rate sensitivities and apparent activation energies of different materials [166]

Materials	Temperature / °C	*m*	*Q* / kJ/mol
STP-Ti	700	0.17	
	750	0.29	310
	800	0.38	
STP-980AC	700	0.12	
	750	0.19	390
	800	0.27	
S-Ti	800	0.21	—
TA15[166]	700	0.15	
	750	0.23	320
	800	0.31	

Unsurprisingly, a strong dependence between the elongation and the strain rate sensitivity is found by comparing Table 6.7 and

Table 6.9. The processed composites show significantly higher *m* than S-Ti under 800 °C, while the strain rate sensitivities of STP-Ti are always higher than that of STP-980AC under the same deformation conditions. The value of *m* gives hint to the deformation mechanism of metallic materials, Ideally, the strain rate sensitivity m is about 0.5 when the deformation is predominated by GBS, and about 0.2~0.3 when the deformation is predominated by dislocations creep [128]. The strain rate sensitivities of metal matrix composites, however, are reported to be lower than their unreinforced counterparts. The microstructural evidences of GBS dominated deformation were observed at m≥0.3 in pre-existing literatures [167,168], which is reasonable considering the m of metal matrix composites is determined not only by the viscose flow of the metal matrix, but also by the strengthening effect of ceramic reinforcements. For both STP-Ti and STP-980AC, the values of *m* increase gradually with the deformation temperatures, indicating the dominating mechanism changes gradually from dislocation-dominated to diffusion-dominated. The value of *m* of STP-Ti is always higher than that of STP-980AC under the same temperature, indicating the deformation of STP-980AC is more dependent on dislocation-related process, which agrees well with the microstructure observations and EBSD results. It is worth mentioning that the strain rate sensitivity of STP-Ti at 800 °C (*m*=0.38) is comparable to the m of other TMCs at around 900 °C (*m*=0.3 – 0.4), as documented in literatures [129,130,156]. The high *m* value shows the temperature of TMCs achieving superplasticity can be significantly decreased via properly designed processing routes.

Compared to the TA15 alloy reported by Wang et al. [166], the STP-Ti in this study exhibits higher strain rate sensitivity, while the STP-980AC demonstrates lower strain rate sensitivity. The smaller grain size of STP-Ti compared to the TA15 alloy used by Wang et al. enhances the significance of grain boundary sliding as a deformation mechanism in STP-Ti, resulting in increased strain rate sensitivity. On the other hand, although the grain size of STP-980AC is similar to that of the TA15 alloy used by Wang et al., as indicated by the microstructure analysis results mentioned earlier, the lamellar microstructure in STP-980AC favors dislocation movement as the predominant plastic deformation mechanism, leading to reduced strain rate sensitivity. However, despite the lower strain rate sensitivity of the TA15 alloy used by Wang et al. compared to STP-Ti, the absence of TiBw reinforcements

in the alloy makes it more prone to strain accommodation, resulting in higher elongation than STP-Ti under the same conditions.

The deformation activation energy of STP-Ti and STP-980AC are determined to be 310 KJ/mol and 391 KJ/mol, respectively. These values are relatively low for titanium matrix composites, of which the apparent activation energies vary from 360 KJ/mol to 620 KJ/mol in α+β region [34, 129, 130], indicating the deformation resistance of STP-Ti and STP-980AC is effectively reduced by the isothermal forging. The activation energy for hot deformation of the TA15 alloy used by Wang et al. is similar to that of STP-Ti in this study, but significantly lower than that of STP-980AC, indicating the lamellar structure in STP-980AC is the main factor contributing to the increase in deformation activation energy in the material.

6.5.4 Tensile deformation mechanism of TiBw/TA15(Si) composite

Fig. 6.44 schematically summarizes the damaging and deformation mechanism of the composite. Basically, the plastic deformation of STP-Ti and STP-980AC is predominated by two mechanics, depending on the deformation conditions: By dislocation movement under temperatures below 800 °C and 800 °C at high strain rate, or by GBS under 800 °C at low strain rate. For deformation dominated by dislocation movement, the accumulation of dislocations and the stress concentration on TiBw lead to the cavitations near TiBw reinforcements. Specifically, if the deformation is carried out under low temperature and high strain rate, DRX will be limited, bring about stretched microstructure and stress-strain curves of type 1. Otherwise, DRX will be triggered by the high dislocations density, resulting in microstructures with massive recrystallization grains and stress-strain curves of type 2. In this case, α grains are recrystallized homogeneously in STP-Ti since the dislocation accumulation rate in different grains are similar. While for STP-980AC, the recrystallization mainly takes place in lath microstructure, decomposing β phase into particles. The recrystallization significantly relieves stress concentration on TiBw, resulting in TiBw with better intactness after deformation.

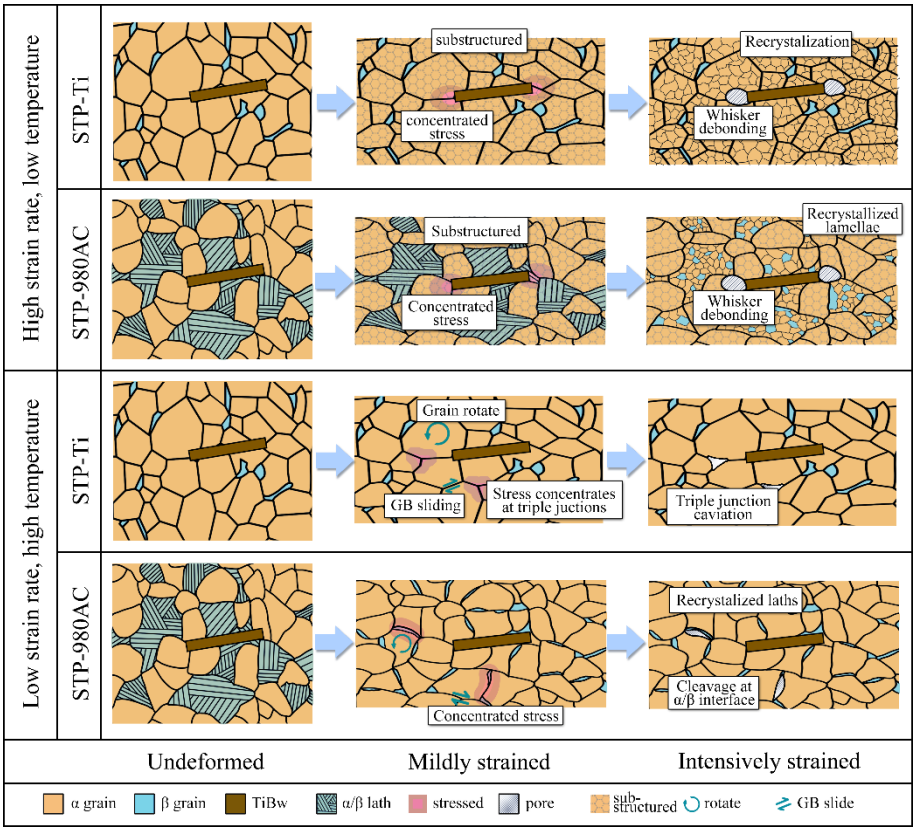

Fig. 6.44 Schematic diagram of the mechanisms of plastic deformation and defects nucleation for composites with different initial microstructures at different conditions.

Further elevate the deformation temperature and decrease the strain rate changes the predominating mechanism from dislocation movement to grain boundary sliding, leading to equiaxed microstructure and stress-strain curves of type 3. In this case, strain in the composite is not accommodated by the deformation of grains, but by the rotation and the relative displacement of grains via the sliding of grain boundaries. Therefore, no stretch nor obvious substructures can be observed in post-deformation grains. For STP-Ti, the strain mismatch is mainly concentrated on triple junctions and TiBw/Ti interfaces, leading to cavitations at these locations. For STP-980AC, lath microstructure has to be dissolved into equiaxed α grains and film-like β phase prior to the activation of GB sliding, leading to higher deformation resistance.

6.6 Summary

In this chapter, the microstructure of TiBw/TA15(Si) composite was refined through solid solution treatment and isothermal hot pressing in dual-phase region, the resultant microstructure was then regulated with heat treatment under different

conditions. The mechanical properties and deformation behaviors of different composites were investigated with tensile tests under room temperature and high temperatures. The substantial results are summarized as follows:

(1) By performing solid solution treatment in the single-phase region and isothermal hot pressing in the dual-phase region, the TiBw/TA15(Si) composite with equiaxed α grains of 1.6 μm in size and dispersed silicide particles of 70 nm in size were successfully achieved, leading to a dual-refinement of both titanium matrix and silicide. The solid solution treatment significantly improved the efficiency of α grain refinement, altered the distribution of silicides, suppressed silicide growth, reduced dislocation density in the matrix, and enhanced the uniformity of the material by reducing the required diffusion distance. The microstructural refinement and dispersed silicide distribution resulted in a yield strength of 1100 MPa, which was 200 MPa higher than that of the as-sintered composite and 86 MPa higher than that of the material without solid-solution treatment.

(2) Bimodal microstructures were obtained after the heat treatment of STP-Ti in the dual-phase region, while a fully lamellar microstructure was obtained after the heat treatment in the single-phase region. Increasing the heat treatment temperature resulted in the increased grain size of the titanium matrix, the increased content of lamellar microstructure, and the reduced texture intensity. The lamellar microstructure formed by air cooling has a lamellar width of 1 μm – 2 μm, while the lamellar microstructure formed by water cooling has a lamellar width of approximately 100 nm. Heat treatment followed by air cooling reduced the yield strength of the material by approximately 100 MPa, scarcely changed the ultimate strength, but significantly improved the elongation. After heat treatment at 1010 °C followed by water cooling, the ultimate strength of the material increased to 1350 MPa, while the elongation suffered only slight decrease.

(3) After heat treatment, the room temperature uniform elongation of STP-Ti decreased, but its resistance to local plastic deformation increased. The room temperature plastic deformation of the material is primarily achieved through dislocation slip, which can be assisted by twinning when slip is hindered. At room temperature, prismatic slip is the most activated system, followed by basal slip and <a> type pyramidal slip, while <c+a> type pyramidal slip is the least activated.

Equiaxed α grains are prone to multi-system slip, which facilitates uniform strain distribution. In the lamellar microstructure, prismatic slip is suppressed by BOR, leading to single system slip and localized deformation. The transformed β phase obtained by water cooling primarily accommodates plastic deformation through the prismatic slip in the primary α laths.

(4) Within the temperature range of 700 °C to 800 °C, the increase in deformation temperature, decrease in strain rate, refinement of grain size in the matrix, and reduction in lamellar content all prompts the high-temperature deformation behavior of TiBw/TA15(Si) composites from dislocation dominated to GBS dominated. This transition leads to improved elongation and reduced flow stress. When deformation is dominated by dislocations, fracture of reinforcements and interfacial debonding result in cavitations. When deformation is dominated by grain boundary sliding, cavities are primarily formed due to the strain incompatibility across triple junctions. TiBw/TA15(Si) composites with fine equiaxed grains exhibit an elongation of 348% at 800 °C / 0.0003 s^{-1}, showing a potential for superplastic forming at a temperature 50°C lower compared to documented TMCs.

Chapter 7 Conclusions and perspectives

TMCs exhibit excellent high-temperature strength and durability but suffer from poor room temperature plasticity and difficulties in grain refinement and microstructure regulation. In the present PhD work, a TiBw/TA15(Si) composite with network architecture was prepared. Utilizing solid solution treatment in the single-phase region and thermo-mechanical processing in the dual-phase region, a significant refinement of the microstructure of the TiBw/TA15(Si) composite was achieved. The hot deformation behaviors of the material, as well as the room temperature and high temperature tensile properties and deformation behaviors after microstructure regulations through heat treatment were investigated. The main conclusions of the present work are drawn as follows:

(1) TiBw/TA15(Si) with different compositions were fabricated using thermodynamic calculation to design chemical compositions and element diffusion calculation to design sintering parameters. The chemical composition of the fabricated composites was optimized based on room temperature tensile properties and the dissolution temperatures of silicide particles. It was found that the composite with a composition of 3.4 vol.% TiBw/TA15-0.3 wt.% Si exhibited excellent room temperature strength and ductility, with a tensile strength of 1060 MPa and an elongation of 6.7%. Moreover, silicide in the composite fully dissolved at 960°C, making it suitable for microstructure control by thermo-mechanical processing and heat treatment in dual-phase region.

(2) After treated with solid solution at 1050 °C, the hot compression stress-strain curves of TiBw/TA15(Si) composite shows dynamic recrystallization features in the dual-phase region. Lower deformation temperatures and higher strain rates result in higher compression stress. Solid solution treatment increases the peak stress but reduces the steady-state flow stress. During deformation, the lamellae distortion and dislocation accumulation first occur, followed by interface formation in the lamellae due to dynamic recovery or recrystallization. Ultimately, lamellae undergo terminal migration, leading to the formation of equiaxed grains. The activation energy for hot deformation of the TiBw/TA15(Si) composite after solid solution treatment is 623 kJ/mol, which is higher than the untreated material. Based

on the processing map, the ideal parameters for the thermo-mechanical processing of composite after solid solution is determined to be 900 °C to 950 °C at strain rates of 0.1 s^{-1} to 0.001 s^{-1}.

(3) The orientation of TiBw reinforcements in the TiBw/TA15(Si) composite changes with high temperature plastic deformation. The principal direction of the strain determines the principal direction of the covariance matrix for TiBw orientation, while the magnitude of the principal strain determines the parameters in the probability density function of the reinforcement orientation distribution. The local plastic strain in the TiBw/TA15(Si) composite can be calculated from the TiBw orientation distribution, simulative error analysis shows a good accuracy is achievable at the compressive strain between 20% to 80%. A non-uniform strain distribution in the high temperature compression specimens of TiBw/TA15(Si) composite is revealed using the orientation distribution of TiBw, with VME strain in the central region reaching three times the average. Comparing the calculated results with the TiBw network deformation confirms the accuracy of the calculations.

(4) Utilizing solid solution treatment in the single-phase region and isothermal hot pressing in the dual-phase region, TiBw/TA15(Si) composite with equiaxed α grains sized 1.6 μm and dispersed silicide particles sized 70 nm is obtained, resulting in a dual-refinement of both titanium matrix and silicide particles. Solid solution pretreatment significantly improved the efficiency of α grain refinement, altered the distribution of silicides, suppressed their growth, reduced dislocation density in the matrix, and enhanced the microstructure uniformity. The microstructure refinement and dispersion of silicide contribute to a yield strength of 1100 MPa. Heat treatment near the β transformation temperature enables complete silicide dissolution and the formation of bimodal microstructures. Increasing the heat treatment temperature increases the lamellar microstructure content, while higher cooling rates lead to finer lamellae. Subsequent air cooling after heat treatment leads to a decrease in room temperature yield strength by approximately 100 MPa, while the tensile strength remains unchanged, and the elongation significantly increases. Water quenching after heat treatment significantly improves the strength, with only a slight decrease in elongation. Using the 1010°C / 30 min / WQ process, excellent

room temperature tensile properties can be achieved with a tensile strength of 1350 MPa and an elongation of 6.7%.

(5) The TiBw/TA15(Si) composite that subjected to solid solution and isothermal hot pressing exhibits excellent uniform deformability at room temperature. However, the uniform deformability decreases after heat treatment, while the endurance to local plastic deformation significantly improves. The presence of equiaxed α grains in the material promotes multi-system slip, thus inhibiting strain localization. Prismatic slip in the lamellar microstructure is suppressed by BOR, while slip-induced interface misalignment leads to softening, resulting in deformation dominated by single system slip, and subsequently strain localization. The transformed β phase obtained through water quenching exhibits strong dislocation hindrance, hence the plastic deformation is primarily accommodated by the prismatic slip in coarse primary α lamellae.

(6) Within the temperature range of 700 °C to 800 °C, the increase in deformation temperature, decrease in strain rate, refinement of grain size in the matrix, and reduction in lamellar content all prompts the high-temperature deformation behavior of TiBw/TA15(Si) composites from dislocation dominated to grain boundary sliding dominated. This transition leads to improved elongation and reduced flow stress. When deformation is dominated by dislocations, fracture of reinforcements and interfacial debonding result in the formation of cavities. When deformation is dominated by grain boundary sliding, cavities are primarily formed due to the strain incompatibility across triple junctions. TiBw/TA15(Si) composites with fine equiaxed grains exhibit an elongation of 348% at 800 °C / 0.0003 s^{-1}, showing a potential for superplastic forming at a temperature 50°C lower compared to documented TMCs.

Based on the findings of the present research, the following subjects are suggested to be carried out for further investigation.

(1) The mass production of TiBw/TA15(Si) composites with fine equiaxed α grains. In the present work, a fine grain TiBw/TA15(Si) composite was prepared by combining the solid solution treatment and isothermal hot pressing. However, the processing condition was strictly controlled, and the shape of the produced

composite was limited, making it hard to apply the proposed procedure for industrial purposes. Therefore, it is suggested to investigate the behaviors of the solution-treated composites during thermo-mechanical processing procedures like forging, rolling and extruding, to reduce the cost and improve the efficiency for the production of TiBw/TA15(Si) composite with equiaxed fine grains.

(2) Heat treatment regulation of TiBw/TA15(Si) composite with equiaxed fine grains. It has been proven in the present work that the microstructures and mechanical properties of TiBw/TA15(Si) composites with equiaxed fine grains can be easily manipulated with heat treatment. However, the microstructures and properties responses of the composites to different heat treatment conditions such as temperature, holding period, and cooling rate is not yet clear. It is suggested to systematically investigate the influence of the heat treatment conditions to the microstructures and mechanical properties of the composite, to optimize the heat treatment parameters for different applications.

(3) The local strain distribution in metal matrix composites reinforced with short fibers. In the present work, the method to calculate the local strain in TiBw/TA15(Si) composite by the orientation distribution of TiBw reinforcements have been established and proven to possessing good accuracy. However, the proposed method requires a random initial reinforcements orientation, the applicable reinforcement is limited to TiBw, and the investigation method is limited to EBSD. In the future works, it is suggested to expand the method to the composites with arbitrary initial orientation distribution of reinforcement, examine the accuracy of the present method in composites with different matrices and reinforcements, and using multiple method like computer aided tomography (CT) for investigation.

Reference

[1] Peters M, Kumpfert J, Ward C H, et al. Titanium Alloys for Aerospace Applications[J]. Advanced Engineering Materials, 2003, 5(6): 419–427.

[2] Elias C N, Lima J H C, Valiev R, et al. Biomedical Applications of Titanium and Its Alloys[J]. The Journal of The Minerals, Metals & Materials Society, 2008, 60(3): 46–49.

[3] Dai J, Zhu J, Chen C, et al. High Temperature Oxidation Behavior and Research Status of Modifications on Improving High Temperature Oxidation Resistance of Titanium Alloys and Titanium Aluminides: A Review[J]. Journal of Alloys and Compounds, 2016, 685: 784–798.

[4] Williams J C, Boyer R R. Opportunities and Issues in the Application of Titanium Alloys for Aerospace Components[J]. Metals, 2020, 10(6): 705.

[5] Wang Y, Hao E, Zhao X, et al. Effect of Microstructure Evolution of Ti6Al4V Alloy on Its Cavitation Erosion and Corrosion Resistance in Artificial Seawater[J]. Journal of Materials Science and Technology, 2022, 100: 169–181.

[6] Williams J C, Starke E A. Progress in Structural Materials for Aerospace Systems[J]. Acta Materialia, 2003, 51(19): 5775–5799.

[7] Zhang X, Chen Y, Hu J. Recent Advances in the Development of Aerospace Materials[J]. Progress in Aerospace Sciences, 2018, 97: 22–34.

[8] Zhao Q, Sun Q, Xin S, et al. High-Strength Titanium Alloys for Aerospace Engineering Applications: A Review on Melting-Forging Process[J]. Materials Science and Engineering: A, 2022, 845: 143260.

[9] Dai J, Zhu J, Chen C, et al. High Temperature Oxidation Behavior and Research Status of Modifications on Improving High Temperature Oxidation Resistance of Titanium Alloys and Titanium Aluminides: A Review[J]. Journal of Alloys and Compounds, 2016, 685: 784–798.

[10] Narayana P L, Kim S W, Hong J K, et al. Tensile Properties of a Newly Developed High-Temperature Titanium Alloy at Room Temperature and 650 °C[J]. Materials Science and Engineering: A, 2018, 718: 287–291.

[11] Guo R, Liu B, Xu R, et al. Microstructure and Mechanical Properties of Powder Metallurgy High Temperature Titanium Alloy with High Si Content[J]. Materials Science and Engineering: A, 2020, 777: 138993.

[12] Zheng Z, Kong F, Chen Y, et al. Effect of Nano-Y2O3 Addition on the Creep Behavior of an As-Cast Near-α Titanium Alloy[J]. Materials Characterization, 2021, 178: 111249.

[13] Li X, Peng X-Y, Duan Y-L, et al. Thermal oxidation behavior of commercial purity titanium at high temperature[J]. Zhongguo Youse Jinshu Xuebao/Chinese Journal of Nonferrous Metals, 2013, 23(8): 2190–2199.

[14] Wang D, Li H, Zheng W. Oxidation Behaviors of TA15 Titanium Alloy and TiBw Reinforced TA15 Matrix Composites Prepared by Spark Plasma Sintering[J]. Journal of Materials Science and Technology, 2020, 37: 46–54.

[15] Liu Y, Guo Q, Li C, et al. Recent progress on evolution of precipitates in Inconel 718 superalloy[J]. Zhongguo Youse Jinshu Xuebao/Acta Metallurgica Sinica, 2016, 52(10): 1259–1266.

[16] Perrut M, Caron P, Thomas M, et al. High Temperature Materials for Aerospace Applications: Ni-Based Superalloys and γ-TiAl Alloys[J]. Comptes Rendus Physique, 2018, 19(8): 657–671.

[17] Xu Q, Yang C, Yan X, et al. Development of Numerical Simulation in Nickel-Based Superalloy Turbine Blade Directional Solidification[J]. Zhongguo Youse Jinshu Xuebao/Acta Metallurgica Sinica, 2019, 55(9): 1175–1184.

[18] Wu H, Liu M, Wang Y, et al. Experimental Study and Numerical Simulation of Dynamic Recrystallization for a FGH96 Superalloy During Isothermal Compression[J]. Journal of Materials Research and Technology, 2020, 9(3): 5090–5104.

[19] Sun Y, Wan Z, Hu L, et al. Characterization of Hot Processing Parameters of Powder Metallurgy TiAl-Based Alloy Based on the Activation Energy Map and Processing Map[J]. Materials & Design, 2015, 86: 922–932.

[20] Wu X. Review of Alloy and Process Development of TiAl Alloys[J]. Intermetallics, 2006, 14(10–11): 1114–1122.

[21] Genc O, Unal R. Development of Gamma Titanium Aluminide (γ-TiAl) Alloys: A Review[J]. Journal of Alloys and Compounds, 2022, 929: 167262.

[22] Leyens C, Hausmann J, Kumpfert J. Continuous Fiber Reinforced Titanium Matrix Composites: Fabrication, Properties and Applications[J]. Advanced Engineering Materials, 2003, 5(6): 399–410.

[23] Geng L, Huang L. High Temperature Properties of Discontinuously Reinforced Titanium Matrix Composites: A Review[J]. Acta Metallurgica

Sinica (English Letters), 2014, 27(5): 787–797.

[24] Jiao Y, Huang L, Geng L. Progress on Discontinuously Reinforced Titanium Matrix Composites[J], Journal of Alloys and Compounds, 2018, 767: 1196–1215.

[25] Tjong S C, Mai Y W. Processing-Structure-Property Aspects of Particulate- and Whisker-Reinforced Titanium Matrix Composites[J]. Composites Science and Technology, 2008, 68(3–4): 583–601.

[26] Gorsse S, Chaminade J P, Le Petitcorps Y. In Situ Preparation of Titanium Base Composites Reinforced by TiB Single Crystals Using a Powder Metallurgy Technique[J]. Composites Part A: Applied Science and Manufacturing, 1998, 29(9–10): 1229–1234.

[27] Huang L, Geng L, Peng H. Microstructurally Inhomogeneous Composites: Is a Homogeneous Reinforcement Distribution Optimal?[J]. Progress in Materials Science, 2015, 71: 93–168.

[28] Morsi K, Patel V V. Processing and Properties of Titanium-Titanium Boride (TiBw) Matrix Composites - A Review[J]. Journal of Materials Science, 2007, 42(6): 2037–2047.

[29] Huang L, Geng L, Peng H, et al. Room Temperature Tensile Fracture Characteristics of in Situ TiBw/Ti6Al4V Composites with a Quasi-Continuous Network Architecture[J]. Scripta Materialia, 2011, 64(9): 844–847.

[30] Huang L, Geng L, Peng H, et al. Effects of Sintering Parameters on the Microstructure and Tensile Properties of in Situ TiBw/Ti6Al4V Composites with a Novel Network Architecture[J]. Materials & Design, 2011, 32(6): 3347–3353.

[31] Jiao Y, Huang L, Geng L, et al. Nano-Scaled Ti_5Si_3 Evolution and Strength Enhancement of Titanium Matrix Composites with Two-Scale Architecture Via Heat Treatment[J]. 2017, 701: 359–369.

[32] Jiao Y, Huang L, Wei S, et al. Constructing Two-Scale Network Microstructure with Nano-Ti_5Si_3 for Superhigh Creep Resistance[J]. Journal of Materials Science and Technology, 2019, 35(8): 1532–1542.

[33] Huang L, An Q, Geng L, et al. Multiscale Architecture and Superior High-Temperature Performance of Discontinuously Reinforced Titanium Matrix Composites[J]. Advanced Materials, 2021, 33(6): 2000688.

[34] Zhang R, Huang L, An Q, et al. The Hyperbolic Constitutive Equations and Modified Dynamic Material Model of TiBw/Ti-6.5Al-2.5Zr-1Mo-1V-0.5Si Composites[J]. Materials Science and Engineering A, 2019, 766: 138329.

[35] Lu C J, Huang L, Geng L, et al. Mechanisms Behind the Superplastic Behavior of As-Extruded TiBw/Ti6Al4V Composites with a Network Architecture[J]. Materials Characterization, 2015, 104: 139–148.

[36] Qiu P, Li H, Sun X, et al. Reinforcements Stimulated Dynamic Recrystallization Behavior and Tensile Properties of Extruded (TiB+TiC+La_2O_3)/Ti6Al4V Composites[J]. Journal of Alloys and Compounds, 2017, 699: 874–881.

[37] Wei J, Yang F, Qi M, et al. The "Pinning" Effect of in-Situ TiB Whiskers on the Hot Deformation Behavior and Dynamic Recrystallization of (10vol%) TiB/Ti–6Al–4V Composites[J]. Journal of Materials Research and Technology, 2023, 22: 1695–1707.

[38] Xiang J, Han Y, Li J, et al. Microstructure Characteristics of ECAP-Processed (TiB+La_2O_3)/Ti-6Al-4V Composites[J]. Journal of Alloys and Compounds, 2017, 726: 57–66.

[39] Zhao P, Ma F, Liu P, et al. Evolution of the Strengthening Effects of In Situ TiB Fibers in a Ti Composite with Various Levels of Thermal Processing[J]. Materials 2023, Vol. 16, Page 2472, 2023, 16(6): 2472.

[40] Warlimont H. Springer Handbook of Materials Data[M]. New York: Springer, 2003: 195–206.

[41] Lutjering G. Titanium[M]. New York: Springer, 2007, 15–52.

[42] Bridier F, Villechaise P, Mendez J. Analysis of the Different Slip Systems Activated by Tension in a α/β Titanium Alloy in Relation with Local Crystallographic Orientation[J]. Acta Materialia, 2005, 53(3): 555–567.

[43] Feaugas X, Clavel M. Cyclic Deformation Behaviour of an α/β Titanium Alloy—I. Micromechanisms of Plasticity Under Various Loading Paths[J]. Acta Materialia, 1997, 45(7): 2685–2701.

[44] Flowers J W, O'Brien K C, McEleney P C. Elastic Constants of Alpha-Titanium Single Crystals at 25°C[J]. Journal of the Less Common Metals, 1964, 7(5): 393–395.

[45] Niinomi M, Nakai M, Hieda J. Development of New Metallic Alloys for Biomedical Applications[J]. Acta Biomaterialia, 2012, 8(11): 3888–3903.

[46] Zhong C, Liu J, Zhao T, et al. Laser Metal Deposition of Ti6Al4V—A Brief Review[J]. Applied Sciences 2020, Vol. 10, Page 764, 2020, 10(3): 764.

[47] Lipowitz J, Barnard T, Bujalski D, et al. Fine-Diameter Polycrystalline SiC Fibers[J]. Composites Science and Technology, 1994, 51(2): 167–171.

[48] Minus M L, Kumar S. The Processing, Properties, and Structure of Carbon Fibers[J]. JOM, 2005, 57(2): 52–58.

[49] Hausmann J, Schurmann H, Peters P, et al. Recent Developments in SIC-Fibre Reinforced Titanium Shaft[C]. International Congress on Innovative Solutions for the Advancement of the Transport Industry TRANSFAC '06. Pittsburgh: TMS Publications, 2006: 242.

[50] Loretto M H, Konitzer D G. The Effect of Matrix Reinforcement Reaction on Fracture in Ti-6Ai-4V-Base Composites[J]. Metallurgical Transactions A, 1990, 21(6): 1579–1587.

[51] Poletti C, Balog M, Schubert T, et al. Production of Titanium Matrix Composites Reinforced with SiC Particles[J]. Composites Science and Technology, 2008, 68(9): 2171–2177.

[52] Ranganath S, Subrahmanyam J. On the in Situ Formation of Tic and Ti2C Reinforcements in Combustion-Assisted Synthesis of Titanium Matrix Composites[J]. Metallurgical and Materials Transactions A, 1996, 27(1): 237–240.

[53] Li S, Sun B, Imai H, et al. Powder Metallurgy Titanium Metal Matrix Composites Reinforced with Carbon Nanotubes and Graphite[J]. Composites Part A: Applied Science and Manufacturing, 2013, 48(1): 57–66.

[54] Chaudhari R, Bauri R. A Novel Spark Plasma Sintering Route to Process High-Strength Ti–4Al–2Fe/TiB Nano-Composite[J]. Materials Science and Technology, 2018, 34(16): 2008–2017.

[55] Ni D, Geng L, Zhang J, et al. Fabrication and Tensile Properties of in Situ TiBw and TiCp Hybrid-Reinforced Titanium Matrix Composites Based on Ti-B4C-C[J]. Materials Science and Engineering A, 2008, 478(1–2): 291–296.

[56] GrüTzner S, KrüGer L, Radajewski M, et al. Characterization of in-Situ TiB/TiC Particle-Reinforced Ti-5Al-5Mo-5V-3Cr Matrix Composites Synthesized by Solid-State Reaction with B4C and Graphite Through Sps[J]. Metals, 2018, 8(6): 377.

[57] Cai C, Song B, Qiu C, et al. Hot Isostatic Pressing of in-Situ TiB/Ti-6Al-4V Composites with Novel Reinforcement Architecture, Enhanced Hardness and Elevated Tribological Properties[J]. Journal of Alloys and Compounds, 2017, 710: 364–374.

[58] Ma Z, Tjong S C, Geng L. In-Situ Ti-TiB Metal–Matrix Composite Prepared by a Reactive Pressing Process[J]. Scripta Materialia, 2000, 42(4): 367–373.

[59] You D, Wang Y, Yang C, et al. Comparative Analysis of the Hot-Isostatic-Pressing Densification Behavior of Atomized and Milled Ti6Al4V Powders[J]. Journal of Materials Research and Technology, 2020, 9(3): 3091–3108.

[60] Cao Y, Zeng F, Lu J, et al. In Situ Synthesis of TiB/Ti6Al4V Composites Reinforced with Nano TiB Through SPS[J]. Materials Transactions, 2015, 56(2): 259–263.

[61] Wei S, Zhang Z, Wang F, et al. Effect of Ti Content and Sintering Temperature on the Microstructures and Mechanical Properties of TiB Reinforced Titanium Composites Synthesized by SPS Process[J]. Materials Science and Engineering A, 2013, 560: 249–255.

[62] Li J, Han Y, Yang D, et al. Effect of Heat Treatment on Creep Properties of in Situ Synthesized (TiB+La_2O_3)/Ti Composite[J]. Frontiers in Materials, 2019, 6: 492995.

[63] Huang L, Chen Y. A Study on the Microstructures and Mechanical Properties of Forged Trace-Boron-Modified Ti-B20 Alloy[J]. Materials and Design, 2015, 66(PA): 110–117.

[64] Wang J, Li L, Lin P, et al. Effect of TiC Particle Size on the Microstructure and Tensile Properties of TiCp/Ti6Al4V Composites Fabricated by Laser Melting Deposition[J]. Optics and Laser Technology, 2018, 105: 195–206.

[65] Wang J, Li L, Tan C, et al. Microstructure and Tensile Properties of TiCp/Ti6Al4V Titanium Matrix Composites Manufactured by Laser Melting Deposition[J]. Journal of Materials Processing Technology, 2018, 252: 524–536.

[66] Fereiduni E, Ghasemi A, Elbestawi M. Selective Laser Melting of Hybrid Ex-Situ/in-Situ Reinforced Titanium Matrix Composites: Laser/Powder Interaction, Reinforcement Formation Mechanism, and Non-Equilibrium Microstructural Evolutions[J]. Materials and Design, 2019, 184: 108185.

[67] Attar H, BöNisch M, Calin M, et al. Selective Laser Melting of in Situ Titanium-Titanium Boride Composites: Processing, Microstructure and Mechanical Properties[J]. Acta Materialia, 2014, 76: 13–22.

[68] Niu H Z, Yin B, Zhang H, et al. Multiphase Polymorphic Nanoparticles Reinforced Titanium Matrix Composite Produced by Selective Electron Beam Melting of a Prealloyed Composite Powder[J]. Scripta Materialia, 2021, 200: 113916.

[69] Huang L, Geng L, Li A, et al. In Situ TiBw/Ti–6Al–4V Composites with Novel Reinforcement Architecture Fabricated by Reaction Hot Pressing[J]. Scripta Materialia, 2009, 60(11): 996–999.

[70] Jiao Y, Huang L, Duan T, et al. Controllable Two-Scale Network Architecture and Enhanced Mechanical Properties of (Ti_5Si_3+TiBw)/Ti6Al4V Composites[J]. Scientific Reports, 2016, 6: 32991.

[71] Liu B, Huang L, Geng L. Elastic and Plastic Behaviors of Laminated Ti-TiBw/Ti Composites[J]. Journal Wuhan University of Technology, Materials Science Edition, 2015, 30(3): 596–600.

[72] Chen J, Li S, Xu S, et al. Impact Behavior of in-Situ TiB/Ti6Al4V Composite with Tailored Gradient-Layered Network Structure[J]. Vacuum, 2023, 216: 112434.

[73] Jiao Y, Huang L J, Wang S, et al. Effects of First-Scale TiBw on Secondary-Scale Ti_5Si_3 Characteristics and Mechanical Properties of in-Situ (Ti_5Si_3+TiBw)/Ti6Al4V Composites[J]. Journal of Alloys and Compounds, 2017, 704: 269–281.

[74] Wang S, Jin J Y, Liu W, et al. High Temperature Performance of TiB/(Ti-6.5Al-2Zr-1Mo-1V-0.5Si) Composites Affected by the TiB Architecture[J]. Composites Part A: Applied Science and Manufacturing, 2023, 174: 107735.

[75] Li Z, Chen Y, Kang Q, et al. Differences in Mechanical Properties and High Temperature Deformation Behavior Between TiBw/Ti65 and TiBw/TA15 Composites with Network Structure[J]. Journal of Materials Research and Technology, 2023, 26: 9169–9189.

[76] Huang L, Wang L, Qian M, et al. High Tensile-Strength and Ductile Titanium Matrix Composites Strengthened by TiB Nanowires[J]. Scripta Materialia, 2017, 141: 133–137.

[77] Liu B, Huang L, Geng L, et al. Fabrication and Superior Ductility of

Laminated Ti–TiBw/Ti Composites by Diffusion Welding[J]. Journal of Alloys and Compounds, 2014, 602: 187–192.

[78] Wang S, Huang L, An Q, et al. Dramatically Enhanced Impact Toughness of Two-Scale Laminate-Network Structured Composites[J]. Materials and Design, 2018, 140: 163–171.

[79] Shishkovsky I, Kakovkina N, Sherbakov V. Graded Layered Titanium Composite Structures with TiB_2 Inclusions Fabricated by Selective Laser Melting[J]. Composite Structures, 2017, 169: 90–96.

[80] Murray J L, Liao P, Spear K E. The B-Ti (Boron-Titanium) System[J]. Bulletin of Alloy Phase Diagrams, 1986, 7(6): 550–555.

[81] Huang L, Geng L, Peng H X, et al. Effects of Sintering Parameters on the Microstructure and Tensile Properties of in Situ TiBw/Ti6Al4V Composites with a Novel Network Architecture[J]. Materials & Design, 2011, 32(6): 3347–3353.

[82] Le J, Han Y, Fang M, et al. A Universal Shear-Lag Model for Accurate Assessment of Whisker Load-Transfer Strengthening in Metal Matrix Composites[J]. Composites Part B: Engineering, 2022, 247: 110317.

[83] KöHler U, Herzig C. On the Anomalous Self-Diffusion in B.C.C. Titanium[J]. Physica Status Solidi (B), 1987, 144(1): 243–251.

[84] KöPpers M, Herzig C, Friesel M, et al. Intrinsic Self-Diffusion and Substitutional Al Diffusion in α-Ti[J]. Acta Materialia, 1997, 45(10): 4181–4191.

[85] Seshacharyulu T, Dutta B. Influence of Prior Deformation Rate on the Mechanism of β→α+β Transformation in Ti–6Al–4V[J]. Scripta Materialia, 2002, 46(9): 673–678.

[86] Hua K, Zhang Y, Gan W, et al. Hot Deformation Behavior Originated From Dislocation Activity and β to α Phase Transformation in a Metastable β Titanium Alloy[J]. International Journal of Plasticity, 2019, 119: 200–214.

[87] Fan X, Yang H, Yan S, et al. Mechanism and Kinetics of Static Globularization in TA15 Titanium Alloy with Transformed Structure[J]. Journal of Alloys and Compounds, 2012, 533: 1–8.

[88] Gao P, Fu M, Zhan M, et al. Deformation Behavior and Microstructure Evolution of Titanium Alloys with Lamellar Microstructure in Hot Working Process: A Review[J]. Journal of Materials Science & Technology, 2020, 39:

56–73.

[89] Germain L, Gey N, Humbert M, et al. Texture Heterogeneities Induced by Subtransus Processing of Near α Titanium Alloys[J]. Acta Materialia, 2008, 56(16): 4298–4308.

[90] Wang S, An Q, Zhang R, et al. Microstructure Characteristics and Enhanced Properties of Network-Structured TiB/(TA15-Si) Composites Via Rolling Deformation at Different Temperatures[J]. Materials Science and Engineering: A, 2022, 829: 142176.

[91] Guo X, Wang L, Wang M, et al. Effects of Degree of Deformation on the Microstructure, Mechanical Properties and Texture of Hybrid-Reinforced Titanium Matrix Composites[J]. Acta Materialia, 2012, 60(6–7): 2656–2667.

[92] Ma F, Lu S, Liu P, et al. Evolution of Strength and Fibers Orientation of a Short-Fibers Reinforced Ti-Matrix Composite After Extrusion[J]. Materials & Design, 2017, 126: 297–304.

[93] Huang Z, Guo W, Huang H, et al. Tensile Strength Prediction of Short Fiber Reinforced Composites[J]. Materials, 2021, 14(11): 2708.

[94] Le J, Han Y, Qiu P, et al. The Impact of Matrix Texture and Whisker Orientation on Property Anisotropy in Titanium Matrix Composites: Experimental and Computational Evaluation[J]. Composites Part B: Engineering, 2021, 212: 108682.

[95] Ma F, Liu P, Li W, et al. The Mechanical Behavior Dependence on the TiB Whisker Realignment During Hot-Working in Titanium Matrix Composites[J]. Scientific Reports, 2016, 6: 36126.

[96] Ma F, Lu S, Liu P, et al. Microstructure and Mechanical Properties Variation of TiB/Ti Matrix Composite by Thermo-Mechanical Processing in Beta Phase Field[J]. Journal of Alloys and Compounds, 2017, 695: 1515–1522.

[97] Kelly A, Tyson W R. Tensile Properties of Fibre-Reinforced Metals: Copper/Tungsten and Copper/Molybdenum[J]. Journal of the Mechanics and Physics of Solids, 1965, 13(6): 329–350.

[98] Wang B, Huang L, Geng L, et al. Compressive Behaviors and Mechanisms of TiB Whiskers Reinforced High Temperature Ti60 Alloy Matrix Composites[J]. Materials Science and Engineering: A, 2015, 648: 443–451.

[99] Zhang R, Wang D, Yuan S. Effect of Multi-Directional Forging on the Microstructure and Mechanical Properties of TiBw/TA15 Composite with

Network Architecture[J]. Materials and Design, 2017, 134: 250–258.

[100] Liu P, Han Y, Qiu P, et al. Isothermal Deformation and Spheroidization Mechanism of (TiB + La_2O_3)/Ti Composites with Different Initial Structures[J]. Materials Characterization, 2018, 146: 15–24.

[101] Wang S, Huang L, Zhang R, et al. Enhancing Ductility of Titanium Matrix Composites by Multimodal α-Grains[J]. Scripta Materialia, 2019, 170: 161–165.

[102] Sun S, Zhao E, Hu C, et al. Deformation Behavior and Softening Mechanism of TiB Reinforced Near-α Titanium Matrix Composite During Hot Compression[J]. Journal of Materials Research and Technology, 2020, 9(6): 13250–13263.

[103] Wang S, Huang L, Jiang S, et al. Microstructure Evolution and Tensile Properties of As-Rolled TiB/TA15 Composites with Network Microstructure[J]. Materials Science and Engineering: A, 2021, 804: 140783.

[104] Sun Q, Xie X. Microstructure and Mechanical Properties of TA15 Alloy After Thermo-Mechanical Processing[J]. Materials Science and Engineering: A, 2018, 724: 493–501.

[105] Prasad Y V R K, Gegel H L, Doraivelu S M, et al. Modeling of Dynamic Material Behavior in Hot Deformation : Forging of Ti-6242[J]. Metallurgical Transactions A, 1984, 15: 1883–1892.

[106] Ziegler H. Progress in Solid Mechanics[M], New York: John Wiley & Sons, Ltd, 1963: 93–193.

[107] Management E. Processing Maps : A Status Report[J]. Journal of Materials Engineering and Performance, 2003, 12: 638–645.

[108] Sun X, Li H, Han Y, et al. Compressive Response and Microstructural Evolution of Bimodal Sized Particulates Reinforced (TiB+La_2O_3)/Ti Composites[J]. Journal of Alloys and Compounds, 2018, 732: 524–535.

[109] Lin X, Huang H, Dong F, et al. Hot Deformation Behaviors in Ti-6Al-4V/(TiB + TiC) Composites[J]. Acta Metallurgica Sinica (English Letters), 2021, 34(12): 1747–1757.

[110] Cao Y, Liu Y, Li Y, et al. Hot Deformation Behavior of Nano-Sized TiB Reinforced Ti-6Al-4V Metal Matrix Composites[J]. Mechanics of Materials, 2020, 141: 103260.

[111] Wang B, Huang L, Geng L, et al. Compressive Behaviors and Mechanisms

of TiB Whiskers Reinforced High Temperature Ti60 Alloy Matrix Composites[J]. Materials Science and Engineering: A, 2015, 648: 443–451.

[112] Zhang C, Lian Y, Chen Y, et al. Hot Deformation Behavior and Microstructure Evolution of a TiBw/Near α-Ti Composite with Fine Matrix Microstructure[J]. Metals, 2019, 9(4): 481.

[113] Sen I, Kottada R S, Ramamurty U. High Temperature Deformation Processing Maps for Boron Modified Ti–6Al–4V Alloys[J]. Materials Science and Engineering: A, 2010, 527(23): 6157–6165.

[114] Lin X, Dong F, Zhang Y, et al. Hot-Deformation Behaviour and Hot-Processing Map of Melt-Hydrogenated Ti6Al4V/(TiB+TiC)[J]. International Journal of Hydrogen Energy, 2019, 44(16): 8641–8649.

[115] Jianhui Y, Shulong X, Chen Y, et al. The Tensile and Fracture Toughness Properties of a (TiBw + TiCp)/Ti–3.5Al–5Mo–6V–3Cr–2Sn–0.5Fe Composites After Heat Treatment[J]. Materials Science and Engineering A, 2018, 729: 21–28.

[116] Zherebtsov S, Ozerov M, Klimova M, et al. Mechanical Behavior and Microstructure Evolution of a Ti-15Mo/TiB Titanium–Matrix Composite During Hot Deformation[J]. Metals, 2019, 9(11): 1175.

[117] Li H, Zhao Z, Ning Y, et al. Characterization of Microstructural Evolution for a Near-α Titanium Alloy with Different Initial Lamellar Microstructures[J]. Metals 2018, Vol. 8, Page 1045, 2018, 8(12): 1045.

[118] Zhao Z, Li H, Fu M, et al. Effect of the Initial Microstructure on the Deformation Behavior of Ti60 Titanium Alloy at High Temperature Processing[J]. Journal of Alloys and Compounds, 2014, 617: 525–533.

[119] Guo X, Wang L, Qin J, et al. Microstructure and Mechanical Properties of (TiB+La_2O_3)/Ti Composites Heat Treated at Different Temperatures[J]. Transactions of Nonferrous Metals Society of China, 2014, 24(6): 1737–1743.

[120] Zhang Z, Qin J, Zhang Z, et al. Effect of β Heat Treatment Temperature on Microstructure and Mechanical Properties of in Situ Titanium Matrix Composites[J]. Materials & Design, 2010, 31(9): 4269–4273.

[121] Wang P, Wang L, Lu W, et al. The Effect of Heat Treatment on Mechanical Properties of in Situ Synthesized 7715D Titanium Matrix Composites[J]. Materials Science and Engineering: A, 2010, 527(16–17): 4312–4319.

[122] Huang L, Geng L, Wang B, et al. Effects of Extrusion and Heat Treatment on the Microstructure and Tensile Properties of in Situ TiBw/Ti6Al4V Composite with a Network Architecture[J]. Composites Part A: Applied Science and Manufacturing, 2012, 43(3): 486–491.

[123] Wang S, An Q, Liu W Q, et al. Towards Strength-Ductility Enhancement of Titanium Matrix Composites Through Heterogeneous Grain Structured Ti Matrix Design[J]. Journal of Alloys and Compounds, 2022, 927: 167022.

[124] KöHler U, Herzig C. On the Anomalous Self-Diffusion in B.C.C. Titanium[J]. Physica Status Solidi B-Basic Solid State Physics, 1987, 144(1): 243–251.

[125] Iijima Y, Lee S, Hirano K I. Diffusion of Silicon, Germanium and Tin in β-Titanium[J]. Philosophical Magazine, 2006, 68(5): 901–914.

[126] Araki H, Minamino Y, Yamane T, et al. Pressure Dependence of Anomalous Diffusion of Zirconium in β-Titanium[J]. Metallurgical and Materials Transactions A: Physical Metallurgy and Materials Science, 1996, 27(7): 1807–1814.

[127] Ramachandra C, Singh V, Rama Rao P. Characterization of Silicides in High Temperature Titanium Alloys[J]. Defence Science Journal, 1986, 36(2): 207–220.

[128] Takai R, Kimura S, Kashiuchi R, et al. Grain Refinement Effects on the Strain Rate Sensitivity and Grain Boundary Sliding in Partially Solidified Al–5 Wt%Mg Alloy[J]. Materials Science and Engineering: A, 2016, 667: 417–425.

[129] Li L, Lu W, Qin J, et al. Superplastic Deformation of in Situ Synthesized TiC/7715D Matrix Composite[J]. Materials Science and Engineering: A, 2009, 513–514(C): 384–388.

[130] Huang L, Lu C, Yuan B, et al. Comparative Study on Superplastic Tensile Behaviors of the As-Extruded Ti6Al4V Alloys and TiBw/Ti6Al4V Composites with Tailored Architecture[J]. Materials and Design, 2016, 93: 81–90.

[131] Li J, Li F, Cai J. Constitutive Model Prediction and Flow Behavior Considering Strain Response in the Thermal Processing for the TA15 Titanium Alloy[J]. Materials, 2018, 11(10): 1985.

[132] Zener C, Hollomon J H. Effect of Strain Rate Upon Plastic Flow of Steel[J]. Journal of Applied Physics, 1944, 15(1): 22–32.

[133] Pantleon W. Resolving the Geometrically Necessary Dislocation Content by Conventional Electron Backscattering Diffraction[J]. Scripta Materialia, 2008, 58(11): 994–997.

[134] Gibbs G B, Graham D, Tomlin D H. Diffusion in Titanium and Titanium—Niobium Alloys[J]. The Philosophical Magazine: A Journal of Theoretical Experimental and Applied Physics, 2006, 8(92): 1269–1282.

[135] Neumann G, Toelle V. Impurity Diffusion in Body-Centred Cubic Metals. Analysis of Experimental Data[J]. Zeitschrift Fuer Metallkunde/Materials Research and Advanced Techniques, 1991, 82(10): 741–744.

[136] Zang M, Niu H, Yu J, et al. Cryogenic Tensile Properties and Deformation Behavior of a Fine-Grained Near Alpha Titanium Alloy with an Equiaxed Microstructure[J]. Materials Science and Engineering: A, 2022, 840: 142952.

[137] Saba F, Zhang F, Liu S, et al. Reinforcement Size Dependence of Mechanical Properties and Strengthening Mechanisms in Diamond Reinforced Titanium Metal Matrix Composites[J]. Composites Part B: Engineering, 2019, 167: 7–19.

[138] Wang N, Chen Y, Wu G, et al. Non-Equivalence Contribution of Geometrically Necessary Dislocation and Statistically Stored Dislocation in Work-Hardened Metals[J]. Materials Science and Engineering: A, 2022, 836: 142728.

[139] Ashby M F. The Deformation of Plastically Non-Homogeneous Materials, The Philosophical Magazine: A[J]. Journal of Theoretical Experimental and Applied Physics, 1970, 21: 399–424.

[140] Zhi H, Zhang C, Antonov S, et al. Investigations of Dislocation-Type Evolution and Strain Hardening During Mechanical Twinning in Fe-22Mn-0.6C Twinning-Induced Plasticity Steel[J]. Acta Materialia, 2020, 195: 371–382.

[141] Le J, Han Y, Qiu P, et al. The Impact of Matrix Texture and Whisker Orientation on Property Anisotropy in Titanium Matrix Composites: Experimental and Computational Evaluation[J]. Composites Part B: Engineering, 2021, 212: 108682.

[142] Hansen N. Hall–Petch Relation and Boundary Strengthening[J]. Scripta

Materialia, 2004, 51(8): 801–806.

[143] Zhang Z, Chen D. Consideration of Orowan Strengthening Effect in Particulate-Reinforced Metal Matrix Nanocomposites: A Model for Predicting Their Yield Strength[J]. Scripta Materialia, 2006, 54(7): 1321–1326.

[144] Castro S F, Gallego J, Landgraf F J G, et al. Orientation Dependence of Stored Energy of Cold Work in Semi-Processed Electrical Steels After Temper Rolling[J]. Materials Science and Engineering: A, 2006, 427(1–2): 301–305.

[145] Jones I P, Hutchinson W B. Stress-State Dependence of Slip in Titanium-6Al-4V and Other H.C.P. Metals[J]. Acta Metallurgica, 1981, 29(6): 951–968.

[146] Dyakonov G S, Mironov S, Semenova I P, et al. Strengthening Mechanisms and Super-Strength of Severely Deformed Titanium[J]. Nanocrystalline Titanium, 2019, 123–143.

[147] Kikuchi S, Tamai S, Kawai T, et al. Effect of TiB Orientation on Near-Threshold Fatigue Crack Propagation in TiB-Reinforced Ti-3Al-2.5V Matrix Composites Treated with Heat Extrusion[J]. Materials, 2019, 12(22): 3685.

[148] Zherebtsov S, Salishchev G, Lee Semiatin S. Loss of Coherency of the Alpha/Beta Interface Boundary in Titanium Alloys During Deformation[J]. Philosophical Magazine Letters, 2010, 90(12): 903–914.

[149] Mataya M C, Carr M J, Krauss G. Flow Localization and Shear Band Formation in a Precipitation Strengthened Austenitic Stainless Steel[J]. Metallurgical Transactions A, 1982, 13(7): 1263–1274.

[150] Tan C, Sun Q, Xiao L, et al. Characterization of Deformation in Primary α Phase and Crack Initiation and Propagation of TC21 Alloy Using in-Situ SEM Experiments[J]. Materials Science and Engineering: A, 2018, 725: 33–42.

[151] Zheng Z, Waheed S, Balint D S, et al. Slip Transfer Across Phase Boundaries in Dual Phase Titanium Alloys and the Effect on Strain Rate Sensitivity[J]. International Journal of Plasticity, 2018, 104: 23–38.

[152] Ambard A, GuéTaz L, Louchet F, et al. Role of Interphases in the Deformation Mechanisms of an α/β Titanium Alloy at 20 K[J]. Materials Science and Engineering: A, 2001, 319–321: 404–408.

[153] Banerjee D, Williams J C. Microstructure and Slip Character in Titanium Alloys[J]. Defence Science Journal, 1986, 36(2): 191–206.

[154] Taoka T, Takeuchi S, Furubayashi E. Slip Systems and Their Critical Shear Stress in 3% Silicon Iron[J]. Journal of the Physical Society of Japan, 1964, 19(5): 701–711.

[155] Williams J C, Baggerly R G, Paton N E. Deformation Behavior of HCP Ti-Al Alloy Single Crystals[J]. Metallurgical and Materials Transactions A: Physical Metallurgy and Materials Science, 2002, 33(3): 837–850.

[156] Lu J, Qin J, Lu W, et al. Effect of Hydrogen on Superplastic Deformation of (TiB + TiC)/Ti–6Al–4V Composite[J]. International Journal of Hydrogen Energy, 2009, 34(19): 8308–8314.

[157] Lu J, Qin J, Chen Y, et al. Superplasticity of Coarse-Grained (TiB+TiC)/Ti–6Al–4V Composite[J]. Journal of Alloys and Compounds, 2010, 490(1–2): 118–123.

[158] Mirzadeh H, Parsa M H. Hot Deformation and Dynamic Recrystallization of NiTi Intermetallic Compound[J]. Journal of Alloys and Compounds, 2014, 614: 56–59.

[159] Yanagida A, Yanagimoto J. A Novel Approach to Determine the Kinetics for Dynamic Recrystallization by Using the Flow Curve[J]. Journal of Materials Processing Technology, 2004, 151(1–3): 33–38.

[160] Zhang C, Kong F, Xu L, et al. Temperature Dependence of Tensile Properties and Fracture Behavior of As Rolled TiB/Ti Composite Sheet[J]. Materials Science and Engineering A, 2012, 556: 962–969.

[161] Cai C, He S, Li L, et al. In-Situ TiB/Ti-6Al-4V Composites with a Tailored Architecture Produced by Hot Isostatic Pressing: Microstructure Evolution, Enhanced Tensile Properties and Strengthening Mechanisms[J]. Composites Part B: Engineering, 2019, 164: 546–558.

[162] Mosleh A O, Kotov A D, Vidal V, et al. Initial Microstructure Influence on Ti–Al–Mo–V Alloy'S Superplastic Deformation Behavior and Deformation Mechanisms[J]. Materials Science and Engineering: A, 2021, 802: 140626.

[163] Alabort E, Kontis P, Barba D, et al. On the Mechanisms of Superplasticity in Ti–6Al–4V[J]. Acta Materialia, 2016, 105: 449–463.

[164] Nazzal M A, Khraisheh M K, Abu-Farha F K. The Effect of Strain Rate Sensitivity Evolution on Deformation Stability During Superplastic

Forming[J]. Journal of Materials Processing Technology, 2007, 191(1–3): 189–192.

[165] Hedworth J, Stowell M J. The Measurement of Strain-Rate Sensitivity in Superplastic Alloys[J]. Journal of Materials Science 1971 6:8, 1971, 6(8): 1061–1069.

[166] Wang K, Liu G, Huang, K, et al. Effect of Recrystallization on Hot Deformation Mechanism of TA15 Titanium Alloy Under Uniaxial Tension and Biaxial Gas Bulging Conditions[J]. Materials Science and Engineering: A, 2017, 708: 149–158.

[167] Zhao S, Zhang H, Cui Z, et al. Superplastic Behavior of an in-Situ TiB_2 Particle Reinforced Aluminum Matrix Composite Processed by Elliptical Cross-Section Torsion Extrusion[J]. Materials Characterization, 2021, 178: 111243.

[168] Hu H, Zhen L, Imai T. Strain Rate Sensitivity of a High Strain Rate Superplastic TiNp/2014 Al Composite[J]. Journal of Materials Processing Technology, 2010, 210(5): 734–740.